UNIVERSITÀ DEGLI STUDI DI MILANO

Dottorato di Ricerca in Scienze della Terra
Ciclo XXXI

High-pressure behavior of microporous materials: crystal-fluid interactions and deformation mechanisms at the atomic scale

Tesi di Dottorato / Ph.D. Thesis

Davide Comboni
I.D nr. R11249

Tutor
Prof. Giacomo D. Gatta

Academic Year
2017-2018

Coordinator
Prof. ssa Elisabetta Erba

Co- Tutor
Dr. Paolo Lotti

Index

Abstract

Zeolite are crystalline, hydrated aluminosilicates characterized by a tetrahedral framework of TO_4 units connected in such a way that sub-nanometric channels and cages occur. These structural cavities host the so-called extra-framework population, which mainly consists of alkali and alkaline-earth cations and small molecules, such as H_2O. In the last decades, the scientific community showed a rising interest on the behavior of microporous and mesoporous compounds (*e.g.,* zeolites) at high-pressure conditions, and in particular on the crystal-fluid interaction phenomena occurring at extreme conditions. As zeolites could act as an ideal carrier of H_2O and others small molecules or monoatomic species (*e.g.*, CO_2, CH_4, H_2S, He, Ar, Kr, Xe,…), experiments on zeolites compressed (and ambient to low/high *T*) in aqueous mixtures have important implications in the Earth Sciences. Furthermore, high-pressure experiments on synthetic zeolites may pave the way for new routes of tailoring new functional materials (made by hybrid host-guest architecture), bearing a potentially relevant technological impact. In this experimental thesis, after an overall introduction and a section on the high-pressure experimental techniques (Chapter 1 and 2 , respectively), the high-pressure behavior and the crystal-fluid interaction at the atomic scale of a selected series of natural and synthetic zeolites (*i.e.*, $AlPO_4$-5, leonhardite, laumontite, phillipsite) and a zeolites-like mineral (*i.e.*, armstrongite) have been investigated by means of *in-situ* single-crystal X-ray diffraction, using "penetrating" and "non-penetrating" pressure-transmitting fluids. Into details:

1. $AlPO_4$-5 (Chapter 3): the high-pressure behavior of $AlPO_4$-5 has been studied by single crystal XRD using synchrotron radiation and a diamond anvil cell (DAC), with crystals compressed in *silicone oil* and *methanol:ethanol:water* =16:3:1 (*m.e.w.*) mixture. The high-pressure evolution of the crystalline structure and the deformation mechanism at atomic scale have been described on the basis of high-quality structure refinements, revealing adsorption phenomena of H_2O (and likely methanol) already at 2 Kbar. Moreover, evidence of an incommensurately modulated structure of $AlPO_4$-5 have been found.
2. Leonhardite and laumontite (Chapter 4): the H_2O adsorption kinetics, at ambient pressure and temperature, of leonhardite to give laumontite has been investigated using single crystal XRD techniques. *In-situ* high-pressure XRD experiments, using synchrotron radiation and a DAC, have been performed in order to obtain the *bulk moduli* of the two minerals (previously unknown). A detailed description of the atomic deformation mechanisms has been addressed.
3. Phillipsite (Chapter 5): the pressure-induced deformation mechanisms, at the atomic scale, have been studied *via* single crystals XRD-experiments, using synchrotron radiation and a DAC. Despite no pressure-induced adsorption was observed, the experimental findings suggest a change in the deformation mechanisms induced by a re-arrangement of the extra-framework population.
4. Armstrongite (Chapter 6): the high-pressure evolution of this zeolite-like mineral has been studied in the *m.e.w.* as nominally penetrating fluid. A first-order phase transition has been detected between 4 and 5 GPa.

In the Chapter 7 a detailed discussion of the aforementioned experimental findings has been addressed, along with their technological and geological implications. The results of the present studies have been published in peer-reviewed journals.

CHAPTER 1: INTRODUCTION

1.1 Zeolites: general overview

The name 'zeolite' was introduced by the Swedish mineralogist Cronstedt in 1756 for some given silicate minerals on the basis of their behavior on heating in a borax bead (Greek *zeon* = boil; *lithos* = stone) (Coombs et al. 1998). Zeolite minerals are crystalline, hydrated aluminosilicates of alkali and alkaline earth cations (mostly Li^+, Na^+, K^+, Ca^{2+}, Ba^{2+}, Sr^{2+}), characterized by an ability to hydrate/dehydrate reversibly and to exchange some of their constituent cations in aqueous solutions, without significant change of their structure (Pabalan and Bertetti 2001). From a classification point of view, zeolites and zeolite-like materials do not comprise an easily definable family of crystalline solids (Baerlocher et al. 2007). The very first classifications of zeolites were based on crystal morphology and proved to be of considerable value in directing the attention of structural crystallographers to zeolites with related structures. Those classifications were, in some cases, very effective: for instance, relying on morphology criteria, the morphologists suspected (correctly) phillipsite and harmotome to be isostructural. Smith (1963) introduced, for the very first time, structural features at atomic level, in order to classify a natural mineral as zeolite:

a) a three-dimensional framework of tetrahedra occupied for more than 50% by Si and Al;
b) an "open" structure with a framework density (*i.e.* number of tetrahedral atoms per 1000 $Å^3$) lower than 20 (Brunner and Meier 1989) and hence enclosing cavities connected by windows larger than regular six-membered rings of tetrahedra; and
c) an extra-framework content represented by cations and H_2O molecules (Passaglia and Sheppard 2001).

It is worth to note that the aforementioned criteria exclude feldspathoids, beryllo-phosphates, beryllo-silicates and zinc-silicates. As pointed out by Rinaldi (1983), this definition is still acceptable, when loosely applied, for any zeolitic material, both natural and synthetic. There are some cases of violation of this definition, which mainly occur for synthetic materials such as silicalite (the pure silica end member) which is Al-free and thus does not show ion exchange capacity (and, being hydrophobic, no spontaneous hydration and/or dehydration occur) and the $AlPO_4$-5 class of compounds (aluminophosphates) (Rinaldi 1983). Furthermore, there are some natural minerals very similar to a zeolite but with an "interrupted" framework structure (*e.g.,* roggianite, chiavennite, wenkite,…). Considering also that there is a number of heat-modified zeolites that have structures different from that of a "true" zeolite and may also be classified as "interrupted" framework structure, it is clear that

the definition proposed by Smith (1963) is not completely satisfactory. For these reasons, the *International Mineralogical Association– Commission on New Minerals and Mineral Names* (IMA CNMMN) has proposed the following definition of zeolite:

"A zeolite mineral is a crystalline substance with a structure characterized by a framework of linked tetrahedra, each consisting of four O atoms surrounding a cation. This framework contains open cavities in the form of channels and cages. These are usually occupied by H_2O molecules and extra-framework cations that are commonly exchangeable. The channels are large enough to allow passage of guest species. In the hydrated phases, dehydration occurs at temperatures mostly below 400°C and is largely reversible. The framework may be interrupted by (OH,F) groups; these occupy a tetrahedron apex that is not shared with adjacent tetrahedra." (Coombs et al. 1998)

As already pointed out by Rinaldi (1983), from a structural point of view, a simple criterion for distinguishing zeolites and zeolite-like materials from denser tectosilicates is based on the framework density (FD), *i.e.,* the number of tetrahedrally coordinated framework atoms (commonly referred as *T*-atoms) per 1000 $Å^3$. Baerlocher et al. (2007) plotted the FD of zeolite species and dense tetrahedral framework structures arguing that a clear gap between the two occurs. For zeolites, the FD ranges between 12 and 19 T-atoms per 1000 $Å^3$, whereas for denser non-zeolitic materials FD > 21 T-atoms per 1000 $Å^3$. As a fact, the most general physical property of a zeolite is the low bulk density and specific gravity, which lays somewhere between 2 and 2.4 g/cm^3 (Bhagwanjee and Devendra 2016). The bulk density correlates well with the structural porosity (*i.e.*, the measure of the pore volume in zeolite) and the cation exchange capacity (CEC).

Referring to a general chemical formula for zeolites, it is possible to adopt the one proposed by Gottardi (1978):

$$(M_x^{+},M_y^{2+})\,[Al_{(x+2y)}\,Si_{n-(x+2y)}O_{2n}]\cdot mH_2O \qquad (1.1)$$

where M^+ represents monovalent cations, M^{2+} represents divalent cations and (usually) $m < n$. In the Equation (1.1) is possible to distinguish two parts:

(i) In square brackets is represented the tetrahedral framework, characterized by an overall negative charge which increases as the Si/Al ratio decreases. Every TO_4 tetrahedron (where T is either Si^{4+} or Al^{3+} for natural zeolites) shares every atom of oxygen with an adjacent tetrahedron.

(ii) The part outside the square brackets represents the extra-framework population which consists of cations and H_2O molecules.

The $Si^{4+} \leftrightarrow Al^{3+}$ substitution gives an overall negative charge to the framework. This is balanced by the presence of extra-framework charge-balancing cations located within the channels and the cages of the tetrahedral framework. The extra-framework cations are coordinated to the framework atoms of oxygen. In the framework of zeolites, both natural or synthetic, the Si/Al ratio obeys to the Löewenstein's rule, namely that Si and Al must be present in such a way that a maximum Si to Al ratio equal to 1:1 occurs (Löewenstein 1954). Usually, the Si-O and Al-O bond distances are 1.61 and 1.73 Å, respectively, with O-T-O angles close to the ideal tetrahedral angle (≈ 109.4˚, Liebau 1985). As far as the T-O-T bond angles are concerned, the average angle vary between 135 and 180˚ (at ambient conditions). The TO_4 tetrahedrons are considered as "primary building units" and, they are connected in such a way that "secondary building units" (SBU) occur. These secondary building units are made of linked tetrahedra and may contain up to 16 T-atoms (Baerlocher et al. 2007). It should be pointed out that SBU's are invariably non-chiral and that a unit cell always contains an integral number of them. A complete list and description of all the zeolite SBU is given in Van Koningsveld (2007). Zeolites, according to the size of pores, can be classified as microporous materials (aperture diameter less than 2 nm). Xu et al. (2007) reported that over 20 elements may be introduced into zeolite frameworks, and taking into account the diversity of structural types with unique microporous frameworks, the number of unique zeolites structures might be enormous. As a fact, the International Zeolite Association (IZA) database shows that the number of structural types of unique microporous frameworks has been growing quickly, from 27 in 1970, to 38 in 1978, to 64 in 1988, to 98 in 1996, to 133 in 2001 and to 174 in 2007, whereas currently (April 2018), the number is 228. As a matter of fact, during the past half century, a great number of microporous compounds with diverse compositional elements (and different framework structure) have been synthesized thanks to the development of synthesis techniques (Xu et al. 2007). Such an increase was mainly related to the great industrial potential of microporous materials, of which further information are given in the Chapter 1.4 (*The economic importance of zeolites*)**.**

1.2 Properties of Zeolites

Zeolites have many interesting as useful features which had determined their success in a number of industrial applications. More in detail, zeolites are known for:

- cationic exchange capacity and molecular sieving;
- reversible dehydration;
- catalytic properties.

These properties arise from their unique structure features, with channels and cages large enough to contain exchangeable extra-framework cations, or/and to allow the reversible uptake of molecules up to *ca.* 1 nm in size, even without a major change in structure (Pabalan and Bertetti 2001). In this view, zeolites should not be considered "inert", but rather "responsive" especially in response to changes in temperature and pressure.

1.2.1 Cation exchange capacity and molecular sieving

The regular pore size distribution of zeolites enables separations based on the molecular-sieve effect. This effect promotes separation of molecular mix according to differences in their molecular sizes. Channel size, shape and other properties (*e.g.,* polarity) of zeolites are critical factors to govern molecular sieving. Moreover, the large surface areas of zeolites and their control over host-sorbate interactions, especially at low vapor pressure, determine that zeolites selectively adsorb or reject molecules. Therefore, zeolites can be used as "membranes". A membrane is defined as an intervening phase separating two other phases and/or acting as an active or passive barrier to the transport of matter between phases adjacent to it under a driving force (Tavolaro & Drioli 1999).

As zeolites are porous, cations can migrate in and out of zeolite structures. The highly-selective ion exchange capacity makes zeolites valuable in a number of industrial applications which will be described in the Chapter 1.3 (*Current utilizations of zeolites*). The cation exchange capacity of zeolites varies strongly from structure to structure, both in terms of selectivity and extent of ions exchange. This is mainly due to effects of the framework on cation exchange. In addition, the entering ion does not necessarily takes the position of the leaving ion (Pabalan and Bertetti 2001 and reference within). In a zeolite, the theoretical cation-exchange capacity (CEC) is primarily a function of the degree of $Si^{4+} \leftrightarrow Al^{3+}$ substitution in its tetrahedral framework. This is because greater the fraction of Al^{3+} in the structure, higher has to be the cationic content into the channels in order to balance the negative charge of the framework. However, Barrer (1978) underlined that the ion-exchange capacity of zeolites depends also on other factors, including:

(1) the framework topology (channel configuration and dimensions);
(2) ion size, shape (polarizability) and charge;
(3) charge density of the anionic framework;
(4) concentration of the external electrolyte solution.

In fact, both the spatial configuration of the zeolitic channels and the ion dimension control whether or not the ion itself can be adsorbed. For instance, Breck (1974) found that chabazite could not adsorb

La^{3+}, $(CH_3)4N^+$, and $(C_2H_5)4N^+$, due to the large size of these cations (or groups). Said that, it should be considered that zeolites usually contain several crystallographically distinct sets of sites that can be occupied by different (exchangeable) cations: each site will have a different ion-exchange behavior and a different ion selectivity. Furthermore, significant variations in both pressure (*P*) and temperature (*T*), which affect the ionic radius, have also a great importance in the process: increasing the *P-T* conditions, the adsorption process may or might not be enhanced. Surprisingly enough, the ion concentration (of a given ionic species) in the solution in which a given zeolite is immersed, does not have an extreme control on the selectivity of the zeolite if the exchange ions have equal charges (*e.g.,* K^+ and Na^+). Nevertheless, if the exchange ions have different charges (*e.g.,* K^+ and Ca^{2+}), the process is critically effected by the total concentration of the aqueous solution: the selectivity of the zeolite for the ion with higher valence number becomes progressively greater with increasing dilution.

Every zeolites has its own thermodynamic affinity for different metal ions which influences whether or not the exchange of a ion is thermodynamically encouraged or even possible. Overall, zeolites often have a particular affinity for alkaline/alkaline-heart elements and for NH^+_4. For instance, Barrer and Klinowski (1974), found that for mordenite the thermodynamic affinity sequence is $Cs^+ > K^+ > NH^+_4 > Na^+ > Ba^{2+} > Li^+$, whereas Tsitsishvili et al. (1999) found that for clinoptilolite the sequence is $Cs^+ > Rb^+ > K^+ > NH^+_4 > Ba^{2+} > Sr^{2+} > Na^+ > Ca^{2+} > Fe^{2+} > Al^{3+} > Mg^{2+} > Li^+$. A number of papers were devoted to the exchange capacities of zeolites for heavy metal ions under different experimental conditions (*e.g.,* Mier et al. 2001, Motsi et al. 2009, Taffarel and Rubio 2009, Ostroski et al. 2009). Clinoptilolite is the most frequently studied natural zeolites, due to its selectivity for heavy metal: for instance, it was reported by Doula (2009) that a modified clinoptilolite was successfully employed in the removal of Cu, Mn and Zn from drinking water. Clinoptilolite is reported also to effectively uptake Cs^+, Co^{2+}, and Sr^{2+} from aqueous solution, neutralizing the pH, indicating that clinoptilolite acts also as a proton acceptor or as a proton donor depending on pH itself (Smičiklas et al. 2006). Some practical applications of zeolite with an high cation-exchange capacity and/or with a particular affinity for specific elements will be presented in the Chapter 1.3 (*Current utilizations of zeolites*).

1.2.2 Reversible dehydration

The remarkable property of zeolites to dehydrate reversibly upon heating has led to an extensive study of this phenomenon using a large variety of methods and techniques. Most zeolites may be dehydrated without major alteration of their crystal structure; they may subsequently be rehydrated, namely adsorb H_2O molecules from the surrounding vapor or liquid phase (Cruciani 2006). The dehydration process is enhanced mainly increasing temperature, but it can also be triggered by decreasing the relative

humidity (RH) of the atmosphere surrounding the zeolite. This was observed, for example, in laumontite, which in its fully hydrated form contains 18 H_2O molecules per unit formula but, if exposed to atmosphere at low humidity rate (< 50%), up to 4 H_2O molecules per unit formula are lost (Yamazaki et al. 1991). However, most zeolites are relatively stable at the ambient conditions (in terms of *P*, *T*, and RH), and the common way to dehydrate them is usually by heating. Cruciani (2006) underlined that zeolites, upon heating, may undergo different kinds of structural changes including:

(i) unit-cell volume contraction due to the escape of H_2O and/or templating organic molecules (dehydration and calcination), which should not be confused with negative thermal expansion (NTE);
(ii) displacive or reconstructive phase transformation(s) to more or less metastable phase(s);
(iii) negative thermal expansion;
(iv) structural collapse (not *in strincto sensu*, but in the sense of Bish and Carey, 2001, *i.e.,* 'collapsed' zeolites may retain some sorption properties and a recognizable X-ray diffraction - XRD pattern); and,
(v) structural breakdown (*i.e.,* complete amorphization or recrystallization).

Among the factors that control the hydration/dehydration (and also the high-temperature behavior of zeolites), the main are related to (i) the framework Si/Al ratio, (ii) the framework topology, (iii) the ionic potential and size of exchangeable (charge-compensating) cations; (iv) the coordination of the extra-framework cations after H_2O expulsion (Cruciani 2006).

The dehydration and the response of zeolites to changes in temperature has a critical importance in many industrial applications. For instance, numerous zeolites are used in gas adsorption, as selective catalysts, and as molecular sieves, and a detailed understanding of their *short-term* (*e.g.*, overnight) thermal behavior and appropriate activation temperatures is crucial (Bish and Carey 2001). From a scientific point of view, short-term thermal behavior has also been suggested as a means to distinguish between similar zeolites, such as clinoptilolite from heulandite, and barrerite from stellerite (Bish and Carey 2001 and reference within).

If extreme structure modification(s) (*i.e.,* structural breakdown) does not occur, zeolites can re-adsorb the H_2O molecules previously lost. There are some zeolites (*e.g.,* clinoptilolite and faujasite) that dehydrate continuously upon heating (Armbruster and Gunter 1991, Johnson et al. 2003), others (*e.g.,* laumontite) show distinct steps in their dehydration behavior (Yamazaki et al. 1991, Fridriksson et al. 2003). Such differences in the dehydration/hydration process is related to the presence of different "types" of H_2O molecules. Into detail, Bish and Carey (2001) have clarified and classified the H_2O-types present in zeolites in 3 groups:

1. H_2O molecules which vary continuously with temperature and pressure: these H_2O molecules "loosely held", also defined as "high-energy H_2O", reflect the observation that most zeolites loose or gain H_2O in response to small changes in temperature or pressure over an extended temperature range;
2. H_2O molecules changing discontinuously at a given temperature (for a given pressure). This causes a dehydration process over a narrow temperature interval;
3. H_2O molecules sorbed to external surfaces. This type is present in very small amounts and most researchers believe that it does not contribute significantly to thermal analysis data.

It should be pointed out that not all the H_2O sites in a given zeolite behave in the same way. For instance, in Ca-laumontite, the H_2O W1 site dehydrates continuously in function of the relative humidity and temperature, whereas the H_2O W5 site is unaffected at least up to 640 K. This is due to the different energy of the bonds between the H_2O molecules and the extra-framework cations, along with the framework oxygen sites (if potential H-bonds occur). Rehydration experiments to establish the regeneration capabilities of zeolites and their metaphases have been included in thermogravimetric experiments (Pécsi-Donàth 1965, 1968, Aumento 1966 and Van Reeuwijk 1971). Depending on the zeolite species and the temperature reached in the experiment, there is a hysteresis effect that might take a considerable time before the rehydration process concludes. Hysteresis appears to be modest in the cases where no drastic lattice transformations are involved (Van Reeuwijk 1974 and reference within). Usually, if the temperature reached during the experiment is moderate (*i.e.,* < 500 K) a complete rehydration occurs, higher temperatures may cause reduced rehydration capability as reported by Pécsi-Donàth (1968). Interestingly enough, Pécsi-Donàth (1968) found that moderate heating sometimes causes such an activation of the zeolite that more than the original H_2O content is sorbed.

1.2.3 Catalytic properties

Zeolites are widely used as solid catalysts or catalyst components in petroleum refining and chemical synthesis, because it is possible to tailor nature and concentration of catalytically active sites in their cavities (Lercher and Jentys 2011). The use of zeolites as catalysts is related to their unique structure, consisting principally in a three-dimensional network of Si-Al-oxygen tetrahedra that provides a regularly sized micropore structure (Lercher and Jenty 2011). Because of the $Si^{4+} \leftrightarrow Al^{3+}$ substitution in the zeolite framework, which gives an overall negative charge to the framework, a cation is required in order to satisfy the framework electro-neutrality. The charge can be balanced also by a proton; in that case, the proton becomes a Brönsted acid site. Overall, the number of Brönsted acid sites (if all the

cation sites are populated by protons) is correlated to the degree of the $Si^{4+} \leftrightarrow Al^{3+}$ substitution in the framework. However, each acid site becomes somehow a weaker Brönsted site as the population of protons increases, due to protons crowding in the zeolite pores. Additionally, in zeolites there is also the presence of the so-called Lewis acid sites. These sites form generally as a result from extra-framework aluminum, meaning that they require aluminum to be not tetrahedrally coordinated. Such an extra-framework aluminum is often an artifact of the synthesis process, caused by an excess of aluminum in the synthesis mixture (Kazansky 1994). While Brönsted acid sites are used for most of the large-volume refining applications, also (redox active) Lewis acid sites have considerable importance for chemical transformations and emission clean up (Lercher and Jenty 2011). From a practical point of view, the use of microporous compounds as zeolites has only a major disadvantage: the size of molecules that can react in the channel is restricted by the diameter of the channel itself. Moreover, the transport to the Brönsted sites may become the rate limiting factor, although molecules are claimed to be able to react at the pore entrance, when being too bulky to enter (Lercher and Jenty 2011 and references within). Overall, the success of zeolites as key catalyst component relies on three main properties of zeotype molecular sieves:

(i) In comparison with mixed oxides, zeolites have an high concentration of active sites;

(ii) The diameter of the pores controls the size of reactants and products, and consequently allows only preferred reactants from being converted and/or products to be formed;

(iii) It is possible to change, at the atomic level, the active site and the environment, for instance by ion exchange or chemical functionalization of the framework.

1.3 Current utilization of zeolites

"One can safely say that the impact of zeolites in science and technology in the last 50 years has no precedents in the field of materials and catalysis" (Čejka et al. 2010)

Zeolites, in particular in the last half century, have been intensively employed in a number of practical applications to the environmental remediation and restoration. Most of these applications are based on their ion-exchange properties (Misaelides et al. 2011), to remove harmful substances from wastewater by adsorption and ion exchange processes. When the concentration of the pollutants exceeds law limits, *i.e.,* when their concentration endangers the environment and the human health, remediation actions are necessary. Remediation can be obtained either through the extraction of the pollutants from the soils or aqueous systems, either working on the reduction of their mobility and/or their stabilization *in-situ* (Misaelides et al. 2011, Shi et al. 2009). Zeolite can be valuable in the selective catching of toxic species (radioactive nuclides or others hazardous chemicals) which than have to be recovered

from the zeolites and secured. For instance, the cation exchange properties of zeolites have been intensively studied to reduce the level of dangerous isotopes, as ^{90}Sr and $^{135,137}Cs$, in the low level radioactive waste waters (LRW) as well as in the treatment of municipal and industrial wastewaters, acid mine, and in the remediation of soils contaminated with heavy metals (Pabalan and Bertetti 2001 and references within). As a fact, natural zeolites such as clinoptilolite, mordenite, erionite, and chabazite gained worldwide attention in radioactive waste applications after the studies of Ames in the late 1950s (*e.g.,* Ames 1960). Clinoptilolite, in particular, has a high cation-exchange capacity (CEC equal to 2.2 meq/g, according to Pabalan and Bertetti 2001) and along with mordenite has a high selectivity for alkali and earth-alkali cations (*i.e.,* $Cs^+ > K^+ > Na^+ > Li^+$ and $Ba^{2+} > Sr^{2+} > Ca^{2+} > Mg^{2+}$), so that they can be successfully employed to uptake Cs^+, Ba^{2+}, and Sr^{2+} from solutions even when the concentration of these cations is low and with significant concentrations of others competing cationic species. However, Borai et al. (2007), studying the uptaking of ^{134}Cs, found that Na-chabazite has the higher distribution coefficients and capacity towards Cs ion compared with other zeolites, including Na-clinoptilolite and both natural or synthetic mordenite. It should be pointed out that the half-lives of the most common radionuclides (^{137}Cs, ^{90}Sr) is ~30 years, meaning that the man-made containment at any radioactive waste repository is expected to outlive these radionuclides (Bish et al. 2003). Zeolites can retard the migration of dangerous radioactive nuclides, but cannot stop their migration because most of the cation-exchange reactions involving natural zeolites are reversible (Bish et al. 2003). Nevertheless, zeolites play an important role in the security of radioactive waste repository site. In fact, the emplacement of radioactive waste changes the temperature and P_{H2O} conditions of large volumes of rocks. Zeolites, in this case, act as important sources and sinks of H_2O molecules, as well as of thermal energy during heating and cooling in the vadose zone. These considerations are not trivial as, for instance, they were one of the reasons for which Yucca Mountain (Nevada) was approved by the U.S. Congress as the site of the first high-level radioactive waste repository in the U.S. (Bish et al. 2003).

As catalysts, the success of zeolite is related from the one hand to the ability to catalyze the conversion of alkanes and alkenes with a higher efficiency than amorphous mixed oxides (Plank and Rosinski 1967) and, on the other hand, to be environmental friendly. Moreover, their microporous dimensionality (either in 1, 2 or 3D) allows molecular selection and high reaction surface areas, their robustness and high thermal stability lead to easy regeneration at elevated temperatures, and, finally, zeolites have an "adjustable nature", so they can match the needs for the chemical transformations (Ennaert et al. 2016). As a fact, zeolites have replaced low-selective and harmful mineral acids and chloro-containing catalysts in several industrial processes (Millini 2011). The petrochemical industry is the one which takes the most advantage from the employment of zeolites as more than 90% of the

industrial zeolite catalysts are produced for this utilization (Millini 2011). In the oil refinery, one of the principal process is the chemical transformation (*e.g.*, coking, hydrocraking, FCC, alkylations, *etc*.) of the hydrocarbons, which is necessary to efficiently transform the feedstock in useful products. Zeolites are employed in the Fluid Catalytic Cracking (FCC) and in the synthesis of *cumene*, the intermediate product in the production of phenol (Plank and Rosinski 1964). Essentially, the importance of zeolites in the FCC is due to the H-transfer reaction, which favors the redistribution of hydrogen among the saturated (or partially saturated) and unsaturated molecules, which in turn is related to the Brönsted acid sites. In the catalytic processes that follow FCC, the different fractionated oil and gas streams are further upgraded. Besides monofunctional Brönsted acidic sites, also bifunctional or multifunctional catalytic properties are employed, usually by the addition of metallic nanoparticles (Ennaert et al. 2016). These particles can easily be introduced in zeolites with high metal dispersions. A fourth less-studied functionality is caused by the introduction of alkali metals providing the zeolite with basic properties (Ennaert et al. 2016). Since 1964, crystalline zeolite-based catalysts began to be employed in substitution of amorphous silica-alumina catalysts, also because zeolites can be easily regenerated several times before being disposed which is, at the industrial level, a major (economic) advantage (Millini 2011).

If the oil industry is actually the main consumer of synthetic zeolites, these microporous materials are also advantageously employed as catalyst in many others industrial sector. Recently, researchers are focused on investigations of small- and medium pore-type microporous/zeolitic catalysts suitable for the methanol conversion to hydrocarbons. For example, MFI-synthetic zeolites are presently employed as catalyst in the production of olefins (fundamental building blocks in the production of plastics, rubbers, or polymers) starting from methanol. This process is one of the most prominent alternative way for producing olefins avoiding the use of oil derivatives (Stöcker 1999; Olsbye et al. 2012).

For molecular sieving application, Gascon et al. (2012) highlights the progress made on synthesis and application of zeolitic membranes and coatings during the last few years (Tavolaro & Drioli 1999). Despite remarkable lab tests and researcher's efforts until 2000, only one type of zeolite membrane has been commercialized: LTA membranes are used in the dehydration of different solvents because of their strong hydrophilicity and suitable pore size (Tavolaro & Drioli 1999). The employment of zeolites as membranes differs generally in the pre-treatments of the stable or temporary supports, impregnation techniques for these supports, or in their post-synthesis treatments. Although only small surfaces of membranes, made by aligned zeolite crystals, have been synthesized, the lab tests indicate that such zeolites membranes could be valuable as sensors (Tavolaro & Drioli 1999).

In the treatment of wastewaters, most technologies using natural zeolites are based on their cation-exchange capacity, so that dissolved cations can be removed from the solution (Pabalan and Bertetti

2001). In wastewaters, the most common pollutant is NH_4^+. Such chemical compound has to be exchanged with more biologically acceptable cations such as Na^+, K^+, Ca^{2+}, which are hosted in the zeolite channels (Kalló 2001). Moreover, the most common natural zeolites employed in these cases (clinoptilolite and mordenite) are also very selective for transition metals (*e.g.,* Cu^{2+}, Ag^+, Zn^{2+}, Cd^{2+}, Hg^{2+}, Pb^{2+}, Cr^{3+}, Mo^{2+}, Mn^{2+}, Co^{2+}, Ni^{2+}). Considering that metals have often been found in industrial waters (*e.g.,* coke manufacturing industry, photographic material processing, tannery processing, the electroplating industry, *etc*.) and that these elements can be toxic even in concentration of mg/L, the employment of relatively cheap and common minerals, as natural zeolites, represents a very appealing solution. Adsorption of heavy metals from wastewater-graphic industry using clinoptilolite zeolite as adsorbent has been object of a number of studies. For instance, Zanin et al. (2017) showed the efficiency of the use of clinoptilolite as an adsorbent for treating printing industry effluent (containing mainly Cu^{2+}, Cr^{3+} and Fe^{3+}), showing no toxic and genotoxic potential, contrary to untreated effluent. The removal of heavy metals is also a critical aspect of the recovery of soils affected from acid mine drainage; phillipsite and faujasite were successfully used to stabilize lead, cadmium and nickel in contaminated soils while clinoptilolite was studied as sorbent of lithium for the protection of poplar plants grown in the contaminated soil (Harbottle et al. 2007). While clinoptilolite is often the natural zeolite most used, a wide variety of synthetic zeolites have been synthetized and treated with chemical solution, in order to enhance their cation selectivity towards particular pollutants. To enhance the simultaneous adsorption capacity of zeolite toward specific hydrophilic and hydrophobic solutes (adsorbates), several researchers have developed an amphiphilic adsorbent by adsorption of certain substances, *e.g.,* cationic surfactants, often quaternary ammonium salts with chloride or bromide onto its external surface (Tran et al. 2018 and reference within). The cationic surfactants are amphiphilic molecules that generally contain a hydrophilic head (usually quaternary ammonium and a counter-anion such as Cl–, Br–, or SO_3^{2-}) positively charged and a relatively long (8–24 carbon atoms) hydrophobic tail. These surfactant-modified zeolite (SMZ) have been employed in a number of applications. For instance, Tran et al. (2018) treated with sodium hydroxide a hydrophilic Y zeolite to enhance its cation exchange capacity (Na-zeolite). Adsorption performances on several pollutants (*e.g.,* Pb^{2+}, Cu^{2+}, Ni^{2+}, $Cr_2O_7^{2-}$ as well as propylbenzene, ethylbenzene, toluene, benzene, and phenol) indicated that Na-H zeolites can simultaneously adsorb the metal cations (on the surface not covered by hexadecyltrimethylammonium, HDTMA) and oxyanions (on the surface covered by HDTMA). The use of modified zeolites (*i.e.,* natural zeolite combined with proper chemicals) is drastically growing. For instance, novel impregnated zeolite material (ISM) was prepared by loading calix [4] arene bis (-2,3 naphtho-crown-6) onto synthetic mordenite to combine the high removal uptake of the mordenite with the high selectivity of calix [4] arene towards Cs-radionuclides (Borai et al. 2007), strongly

enhancing the distribution coefficients of Cs^+ ion (from 0.52 to 27.63 g/L) of the chabazite employed in the uptaking of ^{134}Cs. It has to be considered that zeolites, unfortunately, have channels too small to adsorb organic molecules such as complex hydrocarbons, oxygen-containing compounds, halogenated derivatives, amines, humic acids, proteins, and lipids, which are the other category of polluting compounds commonly found in wastewaters. Nevertheless, it has been proved (Tarasevich 1994, Baykal and Guven 1997) that materials containing zeolites, thanks to their high surface area/mass ratio, can trap colloids, enzymes and microorganisms as large as bacteria within their intra-particle pores. In this case, natural zeolitic materials can become effective biofilters when compared with particles having smaller total surface areas such as quartz sand beds (Kalló 2001 and reference within). The use of zeolites in this particularly utilization is also promoted thanks to their great recover capacity. For instance, NH_4^+-exchanged zeolite can be regenerated using 1N NaCl or KCl solutions, repopulating the exchange sites with either Na^+ or K^+ (the efficiency is even increased by high pH), removing the NH_4^+ groups and making the zeolites able to be employed again (Kalló 1990). Overall, the uptake of metal cations from solutions by zeolites depends on the aqueous chemistry and is affected by a numbers of factors such as temperature, pH, presence of competing cations, dimensions of the hydrated dissolved species compared to the diameters of their channels and the external surface activity. Recently, surfactant-modified zeolites (SMZ) have been proposed in environmental remediation. A SMZ combines the enhanced cation sorption properties of natural zeolites with the ability to sorb anionic species, non-polar organic species and pathogens from aqueous streams (Misaelides et al. 2011). Investigations have shown that natural zeolites modified by surfactants can successfully bind anionic species of metals (*e.g,.* arsenates, chromates, iodides, nitrates, perchlorates, antimonates, *e.g.,* Guan et al 2010, Li et al. 2007, Wingenfelder et al. 2006), so that they have been sucsessfully employed also in the treatment of oilfield wastewaters.

Significant progresses have also been made in the last years in the use of zeolites in aquaculture. Zeolitic materials improve the quality of fish farms and fish transportation tanks by selective capturing of ammonia and toxic heavy metals. Indeed, NH_4^+ is the major waste ions of aquatic animals in modern intensive fish farms and it is produced by de-amination of protein in aquaculture (unused) feeds and faeces. Ammonia can be toxic to fish when its concentration in the fish exceeds 0.02 ppm; ammonia, if seldom accumulates to lethal level, nevertheless can have sublethal effects namely slower growth rate, pooring feed conversion and reduce the fish resistance to different diseases (Ghasemi et al. 2018). Zeolites, added to the fish diet, are proven to enhance fish growth and promote its health and nutritional parameters (Ghasemi et al. 2018). In agronomy and horticulture, zeolites have been used to improve plant productivity and their uses in a variety of applications ranging from soil conditioners to slow-release fertilizers and remediation agents in contaminated soils have been deeply investigated. In

agronomy, the use of zeolites is mainly focused on improving soil physical and chemical properties including infiltration rate, saturated hydraulic conductivity (Ks), water holding capacity (WHC) and cation exchange capacity resulting in an increase of the soil's nutrient-holding capacity (Ming and Allen 2001, Nakhli et al. 2017). Using zeolites as slow-release fertilizer, decreases the leaching of nutrients into ground water. Moreover, zeolites due to their commonly low density may affect the bulk density of the soil which is related to the total porosity and topsoil stability (Ramesh et al. 2011).

Due to the wide worldwide distribution of zeolites-rich volcanic tuffs, these materials have been used intensively as low-cost building materials. The actual production of zeolitic tuff is difficult to estimate for a number of factors (see the Chapter 1.4: *The economic importance of zeolites*); an estimate of the worldwide consumption of zeolitic tuffs in the cement industry is at least one order of magnitude higher than that estimated for building stone production (which in 2000 was about $3 \cdot 10^6$ tons/year) (Colella et al. 2001). The use of zeolitic tuffs as cement additives is nowadays a common practice in Bulgaria, China, Cuba, Germany, Jordan, Russia, Turkey, United States, and in the ex-Yugoslavia countries.

Natural zeolites have been also employed in the production (at industrial scale) of warm mix asphalt (WMA), at least in France and U.S. In fact, foaming techniques offer high potential in terms of decreasing production temperature (by approximately 20-40 °C) and can be obtained using additives, like zeolites, which do not involve the use of expensive additives (Woszuk and Franus 2017). The foaming techniques need a material able to release H_2O at a given temperature, leading to a decrease of temperature production; as a consequence of such a decrease, the energy consumption and the harmful compound emissions in the atmosphere is reduced significantly. Furthermore, it is possible to transport the mix so created over longer distances which, in turn, means that the area of operation of companies with stationary asphalt plants is increased (Woszuk and Franus 2017). The crystal structure of zeolites do not change after adsorbing or desorbing vapor (reversible hydration-dehydration), making them eligible as storages of mechanical energy and in desiccation processes. As a desiccant, zeolites are very effective in controlling moisture levels especially in low humidity ranges (Fikri 1999).

Zeolites have also been used in biotechnology and medicine: as components of scaffolds for bone tissue, engineering zeolites can deliver oxygen to cells, stimulate osteogenic cell differentiation or inhibit bone resorption. Zeolites can also act as oxygen reservoirs, and can improve cell performance in vascular and skin tissue engineering and wound healing (Bacakova et al. 2018). In a very recent review, Bacakova et al. (2018) lists all the present or potential application of zeolites in frontier medical applications.

It is worth to mention that natural zeolites (and SMZ) have been successfully used as excipients in the pharmaceutical industry e.g., natural clinoptilolite has been employed as a carrier-releaser of zinc and

erythromycin for topical application against acne (Cerri et al. 2004, Bonferoni et al. 2007). Cappelletti et al. (2017) underlines the necessity of a thorough characterization of the zeolite-rich rocks in order to test a possible occurrence of potentially toxic chemical elements, but also to verify a reliable use on the basis of their chemical, mineralogical, and technological features (mostly referring to their surface properties). For applications in the pharmaceutical field, nowadays natural clinoptilolite is the most widespread and marketed zeolite in the world. In a recent study, de' Gennaro et al. (2016) paved the way for new scenarios at industrial scale of zeolites as potential carrier of active ingredients of diclofenac and ibuprofen sodium, two active ingredients widely used in pharmaceutical industry. However, recent papers have suggested that also superficially modified phillipsite (one of the zeolites studied in this thesis) and, to a lesser extent, chabazite, can be employed as carriers and slow releasers of diclofenac sodium (DS) (Serri et al. 2016). This may lead to new studies in order to consider not only others zeolites species as drugs carriers but also to extend the number of ingredients carried by zeolites (clinoptilolite and phillipsite in particular).

1.3.1 Potential application of zeolites: storage of mechanical energy

As previously mentioned, zeolites have high heat of adsorption and also the ability to hydrate and dehydrate; these properties enable them to be used in energy storage applications. The use of zeolites as heat storage was already suggested by Shigeishi et al. (1979). This follows the testing of Close and Dunkle (1977), which observed an increase of 25% in heating storage capacity of an Australian solar home with a gravel storage bed when humid air was circulated through (and so H_2O adsorbed by) the gravel bed. Shigeishi et al. (1979) than proposed the use of synthetic zeolites due to their high latent heat of adsorption. Compared to silica gel, the use of zeolites would be also meaningful in spite of the fact that the storage weight is significantly reduced. Indeed, silica gel has to be cooled down to <30°C (whereas zeolites not), limiting a lot its practical use. More details are present in Tchernev (2001). More interesting it is the application of zeolites as energy storage enhanced by pressure. Indeed, since 1990, effort has been made in order to investigate the possibility to accumulate, restore, and dissipate mechanical energy by means of the use of hydrophobic zeolites water (Eroshenko et al. 2001). In fact, a thermodynamic system consisting of a liquid and a lyophobic porous matrix has the property to accumulate, restore or dissipate energy (Eroschenko et al. 2002). Considering a closed physics system consisting of a zeolite and a liquid, at a given critical pressure P_c, the molecules of the liquid can penetrate or being expelled from the cavities. The intrusion of the liquid molecules into the pores is observed when the pressure P becomes equal to or higher than the capillary pressure P_L (Eroshenko and Acad 1990). According to Eroschenko (1996), the intrusion of the liquid molecules inside

microporous channels leads to the generation of a large interface Ω which leads to an increase in the Gibbs energy ($\Delta G > 0$). Doing that, there is a transformation of mechanical energy into interfacial energy and, indeed, a certain amount of mechanical energy is stored into zeolite cavities. In this process, the ratio $\Delta V/m$ (where m indicates the mass of the system and ΔV is the normalized difference between the final and the initial volume) of the whole closed system decreases (Fig 1.3.1). When the stress, in decompression, is progressively suppressed, the whole heterogeneous system spontaneously expands as a result of the extrusion of the extra-framework molecules and then constitutes a real molecular spring. If, after decompression, the volume of the whole system {liquid + zeolite} is lower than that before the compression, the system acts instead as a bumper. A complete recovery of the initial volume may be achieved after a large hysteresis loop, in this case the system behaves as a shock adsorber. A spring system may be used in engineering for devices where short-range molecular forces occur to induce important efforts and large displacements such as, for instance, the spreading of solar panels of satellites (Eroshenko et al. 2001 and reference within). The liquid employed could be, potentially, every liquid with molecules small enough to be adsorbed by the zeolites. In this particular application, H_2O is well suited as a mobile phase: it is a polar liquid, not polluting, easy to obtain as a pure phase, not expensive, and (more important) characterized by a high surface tension. Moreover, H_2O has a small diameters (~2.8 Å) and is able to access very small micropores.

If the potentialities of zeolites in the storage of mechanical energy could be of massive economic importance, the practical application has actually to overcame some critical issues. Ievtushenko et al. (2013) demonstrates the energetic performances of the system {silicalite-1 + H_2O} in the 10°C-80°C temperature range, highlighting the decreasing in efficiency after only 5 cycles of compression-decompression in the whole temperature range investigated. The system, while continuing to act as a spring, subjected a continuous degradation of the H_2O amount entering into the microporous. The decrease of the volume of embedded H_2O molecules, with the number of cycles, reduces the value of the intrusion–extrusion work and therefore the capacity of the whole system in the storage of mechanical energy. The authors suggested that such a reduction was probably induced by the generation of silanol defects in the structure of the porous matrix (Ievtushenko et al. 2013). Nevertheless, it should be pointed out that, in these particular applications, the knowledge of the bonding-topology of the adsorbed molecules of the liquid is critical. As a fact, if cluster of molecules are generated, less molecules would be in contact with the surface of the zeolitic channels and, therefore, less mechanical energy is “stored”. Thus, while high-pressure experiments on synthetic zeolites in penetrating fluids could be interesting for potential applications, X-ray diffraction experiments can also reveal the bonding configuration of the adsorbed molecules.

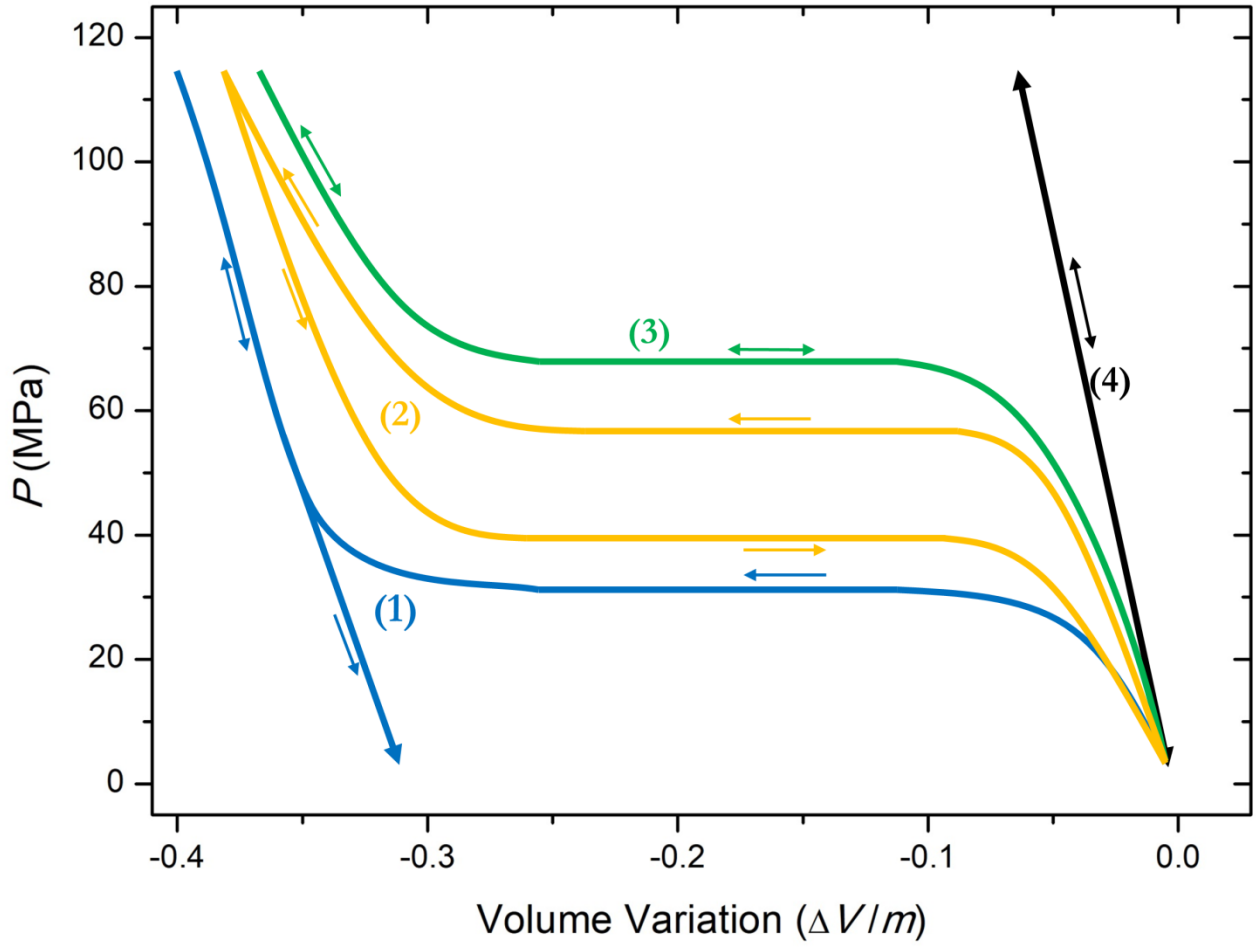

Figure 1.3.1: Example of pressure-volume isotherm of the various "water-hydrophobic zeolite" systems. (1) Bumper: energy is not restored (*e.g.*, "water-zeolite β (F^-)" system); (2) Shock adsorber: (*e.g.*, "water-silicalite-1 (OH^-)" system); (3) Spring: (*e.g.*, "water-silicalite-1 (F^-)" system); (4) Common material behavior (*e.g.*, "water-Na-ZSM-5" system). (from Eroshenko et al. 2001, modified).

1.4 The economic importance of zeolites

Additionally to the features listed in the Chapter 1.2 (*Properties of Zeolites*), zeolites have good mechanical strength and thermal stability and, as Si-Al tectosilicates, are resistant to most acids, bases and organic solvents. These features have determined the incredible success of this class of minerals. Already in the first years of the 20th century, studying the exploitation of ion-exchange capacity of some soils, it was found that natural zeolites exhibited similar properties and could exchange their cationic extra-framework content with other metal cations. Furthermore, the discovery that chabazite can adsorb H_2O, methanol, ethanol, and formic acid vapor, busted further the research on zeolites as scientists (and businessmen) began to realize the importance of such features and their potential use as adsorbents and desiccants (Xu et al. 2007). In spite of the first claim to have synthesized a zeolite (levynite) in the laboratory was that of St. Claire Deville in 1862, it was only in the 1940s that low-silica zeolites were synthesized (Xu et al. 2007, Cundy and Cox 2003). Interestingly enough, the major

clues to synthesize zeolites were found thanks to fieldwork papers. During a study on Triassic rocks, it was found that zeolites were in a chemical equilibrium state when they were formed and the *P-T* conditions were very similar to that of low-temperature hydrothermal synthesis reactions (Cundy and Cox 2003). The use of low-temperature hydrothermal techniques facilitated the extensive industrial production of zeolites. The utilization of zeolites at the industrial scale really began with the synthesis (at low temperature) of the zeolites mordenite, zeolite L, erionite, chabazite and clinoptilolite leaded by U.S. companies such as Linde, UCC, Mobil, and Exxon (Cundy and Cox 2003). From that point, the economic importance of zeolites increased and, at some extent, it can be argued that it still growing over the last decades. For instance, the majority of the world's gasoline is produced by the fluidized catalytic cracking (FCC) of petroleum using zeolite catalysts (Cundy and Cox 2003, Millini 2011). The increasing global zeolite market size, which was valued at USD 29.08 billion in 2016, is expected to grow at a CAGR (compound annual growth rate) of ~ 2.5% over the coming years (until 2022), as a result of growing demand for detergents, rising hygiene awareness among consumers, and rising refining output (online report, Zion Research). In addition, high demand for catalysts, adsorbents, and detergent builders have resulted in a significant growth in the trade (and thereby in the production) of both natural and synthetic zeolites. Nowadays, the worldwide zeolites market is dominated by the developing economies: if the mature markets of the West countries have not recently posted any large scale growth rates, the highest growth in the demand for zeolites is expected to be witnessed in APAC (Asia- Pacific countries) and the Middle East (Zion Research). Nevertheless, also in West Countries, natural zeolites are considered an important bulk commodity. For instance, since 2011, in the annual U.S. Geological Survey, a section is entirely dedicated to this mineral group. The U.S. zeolite market, estimated at USD 3.89 billion in 2014, is expected to grow at a CAGR of 2.1% from 2015 to 2022. The natural product industry, in the U.S., employed natural zeolites mainly in animal feed applications and, as pet litters. Even if these products are employed as low-cost materials, they require easy-to-operate technologies and, therefore, they are an attractive option for various industries. However, factors including low purity, divergent crystal size and competition from other (synthetic) products are likely going to hamper demand (U.S. Geological Survey 2017).

Overall, the world production of natural zeolites is increasing but an accurate estimate is currently unavailable as most countries either do not report production of natural zeolites or the production is reported with a 2- to 3-year lag time (U.S. Geological Survey 2017). This occurs because countries, in which large tonnages of natural zeolites are mined, typically use these as low-value construction materials (*e.g.,* lightweight aggregate, pozzolanic cement). As a result, production data do not accurately indicate (basically underestimated) the effective amount of natural zeolites employed and the available estimates of the domestic production regard only zeolites used in high-value applications.

Despite large deposits occur in many countries, world reserves of natural zeolites have never been estimated. An accurate estimate of the world reserves is prevented mainly by two factors: 1) companies rarely (if never) publish reserves data and 2) on the other hand, some reported zeolite deposits are, basically, volcanic tuffs with low to moderate concentrations of zeolites. At least those deposits with a very low content of zeolites, used in high-volume construction applications, should be excluded from reserves estimates as it is the rock itself and not its zeolite content that makes the deposit valuable (U.S. Geological Survey 2017). Nevertheless, even if there are not global estimates, the reserves of natural zeolites are considerable: only in the U.S.A., resources (and only of chabazite, clinoptilolite, erionite, mordenite, and phillipsite) are estimated to be 120 million of tons in near-surface deposits in the Basin and Range province (U.S. Geological Survey 2017, Deffeyes 1968).

1.5 Occurrence of zeolites: general consideration

The genesis mechanisms and the occurrence of zeolites are wide and complex topics and a detailed description is unnecessary to the purposes of the present thesis. However, because phillipsite and laumontite are two of the minerals studied at high-pressure (H*P*) conditions, a brief description on the general conditions that lead to the formation of natural zeolites is presented. Specific sections pertaining the natural occurrence of laumontite and phillipsite will be addressed in the Chapter 4 (*High-pressure behavior and crystal-fluid interactions in laumontite*) and 5 (*High-pressure behaviour of the zeolite phillipsite*), respectively.

Zeolites have been classified from their discovery (18th century) as minerals occurring primarily in fracture fillings and amygdules in igneous rocks, particularly basaltic lava flows (Hay and Sheppard 2001); only in the last century zeolites have been recognized as important rock-forming constituents, commonly authigenic, in low-grade metamorphic rocks and in a variety of sedimentary rocks. As pointed out in the Chapter 1.1 (*Zeolites: general interview*), the open structure of zeolites, with the capacity of hosting diverse cations, make zeolites a mineral group that currently counts hundreds of species, but only eight zeolites are largely diffused. These are analcime, chabazite, clinoptilolite, erionite, heulandite, laumontite, mordenite, and phillipsite (Hay and Sheppard 2001). In order to interpret correctly the mineral-forming processes, which give rise to nucleation and growth of a specific zeolite, it is necessary to consider (Langella et al. 2001):

1- the composition of starting materials;
2- the composition of solutions interacting with them;
3- the hydrologic conditions;
4- kinetic factors.

These conditions and features largely depend on the geological environments in which zeolites occur; the highest concentrations of zeolites are generally found in glass-rich volcaniclastic deposits but zeolites are also widespread in tephra deposits of saline alkaline lakes (pH = 9.5–10), in hydrothermally altered rocks, in lava flows and ignimbrites, in petroleum and natural gas reservoirs and, even if rare, in soils (Hay and Sheppard 2001, Sheppard and Hay 2001, Utada 2001a, Utada 2001b, Ming and Bottiger 2001, Iijima 2001). Moreover, zeolites from sedimentary rocks, in terms of areal extent of deposits and abundance of certain zeolite species, represent the most important occurrence (Langella et al. 2001). However, from a broader perspective, zeolite deposits can be classified into two main groups depending on the way in which water flows in the geologic system, namely "closed hydrologic systems" and "open hydrologic systems" (Langella et al. 2001). In open hydrologic systems, aqueous solutions move through tephra deposits (or deposits containing the feeding minerals) and change progressively by the same water-rock reactions as in closed systems, in which the alteration of tephra proceed without substantial ionic diffusion or interchange of pore fluids from outside the reacting system (Hay and Sheppard 2001). In theory, closed systems require an impermeable layer that limits the deposit but the concept can be broadly applied to hydrologic systems of low permeability (induced, for example, by a bentonitic mudstone layer). The main difference from the point of view of the mineralogical phases occurring in the two systems is that in closed systems both early and late-stage reaction products are present in the same areas, whereas in open systems the early formed phases, such as smectite, should be concentrated near the entry of fluid to the system, and the zeolites should be concentrated farther along the flow path (Hay and Sheppard 2001). Either in open and closed hydrologic systems, hydrolysis of volcanic glasses represents the main process through which zeolites can form. The dissolution of other phases as smectite, kaolinite, feldspars, other zeolites and feldspathoids is usually of secondary importance and, interestingly enough, also biogenic silica can be a significant pre-constituent of zeolite (*e.g.,* of clinoptilolite and phillipsite). The dissolution of these mineralogical phases leads to the formation of aluminosilicate gels, very rich in H_4SiO_4, and $Al(OH_4)^-$, which in theory can promote the growth of either clay minerals or zeolites, depending on the $(Na^+ + K^+ + Ca^{2+})/H^+$ ratio. If this ratio is high, zeolites can form, whereas if it is low clay minerals are favored. In both cases, the nature and proportions of extra-framework cations are critical in determining which cationic types of the secondary minerals will form. Overall, any glass-to-zeolite transformation is characterized by a silica loss and this can be applied either in open or closed systems (Langella et al. 2001). The difference is that, in open systems, the leached silica is removed from the system, whereas in closed systems silica remains in solution. The higher pH, typical of closed systems, increases silica solubility and the resulting zeolites display lower Si/Al ratios (Langella et al. 2001). If the $(Na^+ + K^+ + Ca^{2+})/H^+$ ratio is high and zeolites form, usually the one early formed alter to

other zeolites (Hay and Sheppard 2001). This may be the case of phillipsite and clinoptilolite: the first one is present in shallower burial depths than clinoptilolite and, although replacement textures have not been demonstrated, clinoptilolite is believed to be the product of the dissolution and re-precipitation of phillipsite (Couture 1977; Boles and Wise 1978). If the presence of high ($Na^+ + K^+ + Ca^{2+}$)/H^+ ratio is a critical requirement to form zeolites, there are other factors controlling the formation of zeolites: pH, water activity, temperature and pressure. The pH affects zeolite-forming reaction rates which are much more quick at a pH above 9 than at lower pH values; Taylor and Surdam (1981) attributes such an increase to the increased solubility of SiO_2 and Al-species above a pH of about 9. Langella et al. (2001) underlines that the alkalinity in many cases is primarily a consequence of the hydrolysis of the mineralogical phases, such as the volcanic glass. For instance, in saline-alkaline lakes, if the Ca^{2+} – HCO_3^- equilibria in solution is the most important factor which can control the precipitation of calcite, the determination of the overall pH of the lake waters is also dependent on reaction such as :

$$Na^+_{(s)} + H_2O_{(l)} \Leftrightarrow H^+_{(s)} + Na^+_{(l)} + OH^-_{(l)} \qquad (1.2)$$

High pH favors the alkaline attack of the glass framework as suggested by de' Gennaro et al. (1988) and contributes to form the gel-like phase, which evolves with time to hydrated aluminosilicates such as zeolites (Langella et al. 2001). Such reactions occur in the presence of an aqueous solution, therefore the water activity plays a main role in determining zeolite stability. In particular, the salinity of the solution controls the temperature of dehydration reactions, and consequently, the temperatures at which the less hydrous zeolites are stable (Hay 1966). Temperature and pressure exert a major control on both the rates of reaction and the species of formed zeolite: elevated pressures should favor the zeolites with higher density, which are also the less hydrous phases, such as laumontite, analcime, and wairakite that are stable at higher temperatures than the more hydrous zeolites, such as clinoptilolite, chabazite, and stilbite (Hay and Sheppard 2001). In volcanic arcs, in which plutonic masses have been intruded in sediments, the thermal effects induce zeolitization within the surrounding sediments but with a differentiation depending on the proximity to the pluton. A detailed description about the effect of temperature is given in Utada (2001a) and Seki et al. (1969).

1.6. Zeolite at high pressure

During the last 20 years, a series of experiments on zeolites at high pressure have been carried out mainly by two experimental techniques:

- *in-situ* single-crystal and powder X-ray diffraction (XRD) and infrared/Raman spectroscopy adopting the Merrill-Bassett (or modified Merrill-Bassett) diamond-anvil cell (DAC) (Merrill and Bassett 1974; Miletich et al. 2000),
- *in-situ* neutron powder diffraction using the large-volume Paris-Edinburgh press (*i.e.*, Besson et al. 1992; Colligan et al. 2005; Seryotkin et al. 2005).

Neutron diffraction studies play an important role in structural solid-state chemistry, making possible the location of light atoms, particularly hydrogen (Cheetham and Wilkinson 1992).

About the high-pressure X-ray experiments on zeolites, *in-situ* single-crystal diffraction data usually allow to perform structural refinements, thus investigating the structure evolution at increasing pressure. In contrast, the lower quality of the H*P* powder-diffraction data usually allow the refinement of the lattice parameters, but often they are not sufficiently high in quality for structural refinements. The nature of fluid employed as *P*-transmitting medium is critical: the *P*-transmitting fluid employed must not dissolve the sample, and should behave hydrostatically within the investigated *P*-range. As will be later discussed (section 2.3.4, *Pressure media*), in high-pressure experiments with microporous or mesoporous materials it is possible to observed a crystal-fluid interaction, with the molecules of the *P*-transmitting fluid. Such an interaction can affect drastically the compressional behavior and the deformation mechanisms at the atomic scale of a given porous material. The *P*-transmitting fluid in which the crystals are compressed are therefore distinguished as "nominally penetrating" or "nominally non-penetrating" fluids (Gatta 2008, 2010a).

Experiment at high pressure on zeolites (with or without crystal-fluid interactions) have shown that microporous materials accommodate the volume compression mainly by *tilting*, *distortion* and *contraction* of the primary building units: the TO_4 units (Gatta et al. 2018):

- *Tilting* of the TO_4 units occurs around the bridging oxygen atoms that act as "hinges", without any significant distortion of the tetrahedra themselves. This means that the O-T-O angles of the tetrahedra are almost unaffected during compression, maintaining the T-O distances constant, whereas the major distortion involves the T–O–T angles, thus tilting the TO_4 units.
- *Distortion* of tetrahedra is reflected by changes in the intra-tetrahedral O–T–O angles, preserving the average T–O bond length.
- Bond shortening (*contraction*), is observed in all substances at high pressure and it is therefore always responsible, at least in part, for any reduction in volume. As pointed out in Hazen and Finger (1985), bond shortening dominates compression in structures in which polyhedra are joined by shared edges or faces. This is not the case of zeolites and, at least at low pressure, the compression of the TO_4 units (which is expressed by contraction of the T–O bond distances) is modest.

The deformation mechanisms are dictated by the topological configuration of the tetrahedral framework and are not influenced by the Si/Al/P distribution or by the extra-framework population (Gatta et al. 2018). *Tilting*, *distortion* and *contraction* act simultaneously at any pressure. However, tilting is an energetically less-costly mechanism if compared to distortion or contraction and therefore it is, at low-*P* regime, the dominant deformation mechanism (Gatta 2010a, b, Gatta and Lee 2014, Gatta et al. 2018). On the other hand, at higher pressure distortion and contraction become dominant because the tilting cannot accommodate anymore the effect of pressure. Such a "hierarchy" of the deformation mechanisms (as defined by Gatta 2010a) implies that up to ~ 3-5 GPa tetrahedra can be considered as "rigid-units", at least to a first approximation (see also Zhang et al. (1998) about the compressibility of the SiO_4 polyhedron). The secondary building units (SBU) of the zeolitic framewok made by "open forms", which consist in 4-, 5-, 6-, 8-, 10- and 12-membered rings of tetrahedra, for the effect of the TO_4 tilting tend to increase monotonically with *P* their ellipticity, defined as the ratio between the shorter and the longer diameter of the given ring. This is observed in every zeolitic structure unless a phase transition occurs (Gatta et al. 2018).

Hydration in zeolites occurs also at ambient pressure; for example laumontite hydrates (and dehydrates) continuously if it is submerged in pure H_2O or even if it is kept in air at a high humidity rate (Yamazaki et al. 1991, Fridriksson et al. 2003). However, pressure can enhance the hydration of zeolites: the first study that showed unambiguously the *P*-induced ''overhydration effect" in natural zeolites was that on natrolite-like minerals (Lee et al. 2002a, b), which adsorb H_2O molecules from the *P*-transmitting fluid between 0.8 and 1.5 GPa. Natrolite (*i.e.,* $Na_{16}Al_{16}Si_{24}O_{48}\cdot 16H_2O$ at room pressure) can double its H_2O content at 1.2 GPa. These experiments opened the way for a wide number of studies which investigated the penetration of molecules (or atoms) in both natural and synthetic zeolites (*e.g.,* Lee et al. 2004a, b, Colligan et al. 2005, Seryotkin et al. 2005, Likhacheva et al. 2006). It should be underlined that natural zeolites do not adsorb only H_2O molecules: for instance, Lee et al. (2010), compressing a natural natrolite ($Na_{16}Al_{16}Si_{24}O_{48}\cdot 16H_2O$) in Ar, showed that there is a significant (6 Ar atoms p.f.u) incorporation of Ar under moderate pressure (and at room *T*). Natrolite have been also compressed in CO_2 as penetrating *P*-medium, adsorbing 8 CO_2 molecules p.f.u. at 1.5 GPa (Lee et al. 2013). If natural zeolites usually do not adsorb alcohols, synthetic zeolites can adsorb also larger molecules (*e.g., n*-hexane, Wloch 2003, or methanol, Kortunov et al. 2005).

The channel population (*i.e*., H_2O molecules and cations) have a control on the compressibility of the cavities and therefore influences the compressibility of the unit-cell volume. Indeed, the adsorption of "penetrating" molecules, enhanced by pressure, affects the structure deformation and can be detected by a change (that can be drastic) in the *bulk modulus* (*i.e.,* $K_0 = -V\frac{\partial P}{\partial V}$) value. As a matter of fact, one of

the main effect of the intrusion of molecules (or atoms) in the zeolitic cavities is a change in the elastic parameters. For instance, Arletti et al. (2010) reports the results of an *in-situ* high-pressure synchrotron powder-diffraction investigation on boggsite (ideally $Ca_8Na_3Al_{19}Si_{77}O_{192}\cdot 70H_2O$) using both penetrating (mix methanol:ethanol:water = 16:3:1 – *m.e.w.*, up to 7.6 GPa) and non-penetrating (*i.e., silicon oil*, up to 5.9 GPa) *P*-transmitting fluids. The continuous adsorption of H_2O molecules (13 p.f.u. in the pressure range between 0.3 and 2.9 GPa) does not lead to any unit-cell-volume expansion but the compressibility of boggsite is higher when compressed in a non-penetrating *P*-fluid (K_0 ~ 31 and ~37 GPa in s.o. and *m.e.w.*, respectively) (Arletti et al. 2010). In this case, the intrusion of guest molecules leads to the so-called "pillar effect": to an increase of the *bulk modulus* with respect to that of the same zeolite compressed in a non-penetrating pressure fluid. This is a rather common effect and can lead to a significant change in the bulk compressibility. For instance, Colligan et al. (2004) reported a *bulk modulus* of 38(2) and 208(19) of a purely siliceous zeolite Y (faujasite) compressed in silicone oil and in *m.e.w.* (16:3:1), respectively. In the same paper, preliminary experiments have also been conducted on a sample of Na-X zeolite which is reported to have a *bulk modulus* of 91(2) GPa if compressed in an alcohols/water mixture whereas only 35(2) if compressed in silicone oil. The change in compressibility depends on the nature of the molecules that are adsorbed by the zeolite. For instance, Na-4A zeolite is reported to change dramatically its compressibility depending on the molecular size of the hydrostatic pressure medium which is 140, 70, 22 GPa in H_2O, alcohols and glycerol respectively (Hazen 1983, Hazen and Finger 1984). The decrease of the bulk compressibility, in response to the penetration of *m.e.w.* molecules is not a rule. One example could be gismondine which was studied by Ori et al. (2008) and Betti et al. (2007). Gismondine has a *bulk modulus* of K_0 = 80(2) GPa in the 0.4-2.8 GPa pressure range if compressed in silicone oil, whereas, in the same pressure range, it has a *bulk modulus* of 54(3) GPa if compressed in *m.e.w.* (16:3:1). It has to be said that in the case of gismondine, compressed in *m.e.w.*, at 0.6 GPa the H_2O content is slightly higher than at ambient pressure, as a result of a moderate over-hydration. Moreover, at about 2 GPa, a significant H_2O-molecules system re-arrangement occurs, characterized by an ordering of part of the molecules from four partially occupied sites to only two fully occupied ones. For that reason, Ori et al. (2008) recalculated the *bulk modulus* in different *P*-range, which results to be K_0 = 69(5) and K_0 = 74 (9) GPa in the 0.6–1.6 and 1.9–2.8 GPa pressure range. In all the cases, the *bulk modulus* of gismondine seems to be higher in silicone oil than in *m.e.w.*, in which gismondine adsorbs H_2O. Ori et al. (2008) suggests that the lower K_0 of gismondine in *m.e.w.* is ascribable to the re-organization of the H_2O molecules, which leaves a larger free volume inside the pores and hence allows a higher compressibility in the penetrating aqueous medium. The same phenomenon was observed also in Na-

ZSM-5, investigated by Arletti et al. (2011), which compressed in silicone oil and in *m.e.w.* has a *bulk modulus* of K_0 = 28.9(5) and 18.2(6), respectively. As previously explained, the effects of the *P*-induced penetration depend on the nature of the penetrating atoms (or molecules) through the zeolitic channels. Further details can be found in the review paper of Gatta et al. (2018), who divides the adsorption of monoatomic species from small molecules and larger molecules. Overall, it should be pointed out that not all the zeolites experience a *P*-induced intrusion of monoatomic species or molecules from the *P*-transmitting fluids. In this respect, experiments are needed in order to establish whether or not a given zeolite can adsorb molecules (or atoms) at high pressure. A general rule is that zeolites with well stuffed channels at ambient conditions (which is the case of most natural zeolites) tend to hinder the penetration of new species through the channels (Gatta et al. 2018).

1.7 Aim of the project

The main aim of this study is to investigate the crystal-fluid interaction of four natural and synthetic zeolite and zeolite-like minerals: phillipsite $K_2(Na,Ca_{0.5})_3[Al_5Si_{11}O_{32}]\cdot 12H_2O$, laumontite $[(Ca_{4x}Na_x)K_x][Al_8Si_{16}O_{48}]\cdot(H_2O)_n$, synthetic $AlPO_4$-5 and armstrongite $CaZr[Si_6O_{15}]\cdot 2H_2O$. Phillipsite and laumontite are two of the most common zeolites in nature and they are widespread in a lots of geological environments. The investigation of mineral behavior under extreme conditions is the basis for predicting the properties of multi-phase systems of geological interest. For instance, the interaction between laumontite and phillipsite with H_2O-based mixture at moderate pressure can provide valuable information at a geological level. Understanding the actual content of H_2O in the structure of natural zeolites under moderate pressure and in presence of a acqueous fluids is important in order to define their role as water-carrier in the first kilometers of the Earth crust. Furthermore, before the begin of this Ph.D. research program, there were no single-crystal X-ray diffraction (XRD-SC) data available at high pressure of these two minerals and important thermodynamic parameters, and the isothermal *bulk modulus* and *P*-derivative of leonhardite was missing.

Experiments in high-*P/T* mineralogy often have implications beyond the Earth sciences, for example in material sciences or metallurgy. $AlPO_4$-5 is an excellent synthetic target for high-pressure experiments because it represents a completely different scenario with respect to both laumontite and phillipsite. In fact, $AlPO_4$-5 is a zeolite with (nominally) empty channels, whereas laumontite and phillipsite have both cations and H_2O molecules. $AlPO_4$-5 is an object of a growing research interest, as proved by the large number of recent studies mainly focused on the adsorption of simple and complex molecules with potential technological applications (*e.g.,* spring and bumper systems; see Chapter 1.3, *Current utilizations of zeolites*). Armstrongite was selected because it is a zeolite-like mineral: its framework is

not only made by TO_4 units, but it has channels in which cations and H_2O molecules are hosted. Up to now, very little is known on this class of minerals at non-ambient conditions and this is one of the very first study of heterosilicates at high pressure. In this regard, the study of armstrongite is to be considered as an ultimately evolution of the project, aimed to provide a broad look-out on the crystal-fluid interaction at high pressure in open-framework materials.

CHAPTER 2:
BEHAVIOR OF MATERIALS UNDER EXTREME CONDITIONS AND EXPERIMENTAL METHODS

This is a two-fold Chapter. In the first part, the theory of elasticity is summarized; the main elastic parameters, including the compliance coefficient and the *bulk modulus*, are defined. A particular attention is devoted to the definition and the different of Equation of States for solids. In the second part of this Chapter, a description of the devices employed during the X-ray single crystal diffraction experiments, including the diamond anvil cells and the synchrotron radiation, is provided.

2.1. Elastic behavior at extreme conditions

Over the last sixty years, *in-situ* X-ray and neutron powder diffraction experiments have enabled the study of matter in response to "intensive" thermodynamic variables, in particular pressure and temperature. The range of pressure or temperature at which diffraction experiments can be conducted currently is vast: from a few degrees Kelvin to kiloKelvin or from a few bars to Mbars, reflecting the extraordinary developments in high-temperatures and high-pressure techniques of the last decades Altomare et al. (2017).

The unit cell parameters of every crystalline material (synthetic or natural) depend on (and vary with) pressure and temperature. The crystal system of the crystalline compound governs how its shape and size change in response to an uniform variation in temperature or hydrostatic pressure. The deformations induced by the application of hydrostatic pressure can be described with the so-called "stain ellipsoid", a fictitious ellipsoid in which the three main axes are mutually orthogonal. If the symmetry of the crystal is cubic, trigonal, hexagonal, tetragonal or orthorhombic, the axes of the "stain ellipsoid" are parallel to the unique crystallographic axes. In monoclinic crystals, only the 2-fold crystallographic axis is always co-axial with one of the principal strain axes of the "strain ellipsoid" (the other two axis are dispersed on the (010) plane), whereas in triclinic crystals none of the main strain axes is parallel to the crystallographic ones. This implies that, in monoclinic and triclinic crystal, the changes in length of the unit-cell edges along the crystallographic axes are not sufficient to entirely describe orientation and magnitude of the unit-strain ellipsoid, caused by a finite and isotropic change in temperature and pressure, but even the inter-axial angles of the unit-cell (*i.e.,* α, β and γ) concur to describe the strain ellipsoid.

2.1.1 Compressibility

Under a linear elastic regime, the strains in a crystal are linearly dependent upon the applied stress (Hook's Law). The stress is describable by a second-rank tensor (s_{ij}), and the stress-strain relationship is the following tensor equation (Nye 1985):

$$\varepsilon_{ij} = S_{ijkl}\sigma_{kl} \quad (2.1)$$

where S_{ijkl} is the elastic compliance fourth-rank tensor. As an alternative to the previous equation, the stress-strain relationship can be expressed as:

$$\sigma_{kl} = c_{ijkl}\varepsilon_{kl} \quad (2.2)$$

here c_{ijkl} is the elastic stiffness fourth-rank tensor (Altomare et al. 2017).

Any given compound, compressed by an external force, will contract accordingly to the magnitude of the force itself. The work (W), volume (V) and pressure (P) are related by:

$$W = -P\Delta V \quad (2.3)$$

Considering that both work and pressure are positive, this implies that ΔV must be negative in all materials under compression. The magnitude of the changes is governed by the interatomic forces. Compressibility (usually expressed in GPa^{-1}) and stiffness (usually in GPa) are reciprocal in nature, but individual components of the two tensors are not (Altomare et al. 2017). Under hydrostatic conditions, the off-diagonal components of the stress tensor are zero (which means that there are no shear stresses) and the diagonal terms of the tensor are all equal to the applied pressure (P), so that:

$$\sigma_{kl} = P \quad (2.4)$$

This is true only if $k = l$, otherwise for $k \neq l$, $\sigma_{kl}=0$. Thus, the hydrostatic conditions lead to:

$$\varepsilon_{ij} = -Ps_{ijkl} \quad (2.5)$$

It is possible to define the volumetric and linear compressibility coefficient, β_V and β_l [GPa^{-1}], as:

$$\beta_V = \frac{1}{V} \cdot \left(\frac{\partial V}{\partial P}\right)_T = \partial \ln V/\partial P, \quad (2.6)$$

$$\beta_l = \frac{1}{l} \cdot \left(\frac{\partial l}{\partial P}\right)_T \quad (2.7)$$

It is worth to underline that the volume compressibility (β_V) is defined as the proportional decrease in volume of a crystal when subjected to unit *hydrostatic* pressure. Especially in Geosciences, it is commonly used the volume *bulk modulus* K_V [GPa], and the linearized bulk moduli (K_l), defined as

$$K_{V0_{P_0,T_0}} = \beta_V^{-1} = V_0(\partial P/\partial V)_{P_0,T_0} \quad (2.8)$$

$$K_l = 3 \cdot \beta_l^{-1} \quad (2.9)$$

Where V_0, P_0 and T_0 refer respectively to the ambient V, P and T. In order simplify the notation, hereafter the *bulk modulus* will be indicated only as K_{V0}. While linear elasticity can describe successfully the elastic response of a material to a small increment in pressure, it cannot address the

total response of the material to a large pressure change. For that, the concept of an equation of state is required (Altomare et al. 2017). The equation of state for solid compound are particularly useful in Geosciences, where the crystalline compounds are often compressed out of the field of their linear elasticity. Because of that, at a first level of approximation, an equation of state can be viewed as an extension of linear elasticity. In fact, although normally it is defined in terms of volume variation with pressure, it can also be seen in term of *bulk modulus* variation with pressure (Angel 2000).

2.1.2 Equation of state

An equation of state (thereafter EoS) is a thermodynamic equation relating state variables, which describes the state of matter under a given set of physical conditions. An equation of state provides a mathematical relationship between two or more state functions (*e.g., T*, *P*, *V*, *p*) associated with the matter. The very first example of EoS is the Boyle's law :

$$PV = \text{constant} \quad (2.10)$$

Although, perhaps, the most notorious EoS is the combined gas law (for ideal gases):

$$\frac{PV}{T} = k \quad (2.11)$$

where *k* is a constant and *P*,*V*, *T* stand for pressure, volume and temperature, respectively. All EoS are based on a number of assumptions and therefore they cannot be applied in any given condition; for instance, the combined gas law (8) fails to predict the behavior of a gas at very high/low temperatures. Nowadays, there is no single EoS that accurately predict the behavior of any substance under all conditions.

Moreover, in the case of solids (*i.e.,* crystalline and amorphous compound) there is not even a thermodynamic basis that allows to derive a "unique" EoS, as is the case for ideal gases. As a consequence, a number of semiempirical equations have been proposed, starting from different assumptions, but no one can be considered as universally valid. The reliability of these equations of state has to be validated through the reproducibility of experimental data (Angel 2000). The latter aspect introduces an element of subjectivity to the interpretation of *P*-*V*-*T* data (in solid material). Duffy and Wang (1998) underlines that a full *P*-*V*-*T* EoS is needed in order to characterize the state of a solid compound, although the equation can also be simplified assuming constant one of the state variables (*T* or *P*). As a consequence, isothermal $(P, V)_T$ and thermal EoS are defined.

2.1.3 Isothermal EoS

In the case of solid compounds, a number of semi-empirical isothermal EoS have been formulated, each one based on a different set of assumptions. These EoS relate volume with pressure at a given temperature; isothermal equations of state are usually parameterized in terms of the values of the isothermal *bulk modulus* (K_{V0}) and its pressure derivatives:

$$K_{V0}' = \left(\frac{\partial K}{\partial P}\right)_T \quad (2.12)$$

$$K_{V0}'' = \left(\frac{\partial^2 K}{\partial^2 P}\right)_T \quad (2.13)$$

Both K_{V0}' and K_{V0}'' are evaluated at a reference pressure, normally at *ambient P;* In order simplify the notation, hereafter the *bulk modulus* derivatives will be indicated as *K' and K''.* Among the EoS, the most used in Geosciences are the Murnaghan and the Birch-Murnaghan EoS. Because of that, these EoS are here presented whereas the other isothermal EoS (*e.g.,* Vinet EoS, natural strain EoS…) will be only introduced. The Murnaghan EoS (Murnaghan 1937) well describes compression up to $\eta = V/V_0$ down to 0.9 (Angel 2000). This EoS is based on the assumption that K_V has a linear dependence to pressure (Angel 2000), and this leads to a *V(P)* relation formulized as:

$$V = V_0\left(1 + \frac{K'P}{K_{V0}}\right)^{-1/K'} \quad (2.14)$$

or

$$V = \frac{K_{V0}}{K'}\left[\left(\frac{V_0}{V}\right)^{K'} - 1\right] \quad (2.15)$$

The Murnaghan EoS, due to its simple functional form, is commonly incorporated into thermodynamic databases in order to model phase equilibria (*e.g.,* Holland and Powell 1998, Chatterjee et al. 1998). However, because of its limited η interval of reliability, it is often preferable to use other EoSs at high compression regimes, among which the most widespread one is the Birch-Murnaghan EoS (Birch 1947). This EoS is based on the assumption that the strain energy of a solid, under compression, can be expressed as a Taylor series in the finite strain (*f*). In the Birch-Murnaghan EoS, it is used that the finite Eulerian strain (f_E), equal to:

$$f_E = \left[\left(\frac{V_0}{V}\right)^{2/3} - 1\right]/2 \quad (2.16)$$

Ideally, the Birch Murnaghan EoS is a polynomial equation with infinite terms. The expansion of the Birch-Murnaghan EoS to the fourth order (in energy) leads to the expression:

$$P = 3K_{V0}f_E(1 + 2f_E)^{5/2}\left(1 + \frac{3}{2}(K' - 4)f_E + \frac{3}{2}\left(K_{V0}K'' + (K' - 4)(K' - 3) + \frac{35}{9}\right)f_E^2\right) \quad (2.17)$$

It is worth to say that, as the Birch-Murnaghan EoS is defined as a Taylor's series, it can also be truncated to lower orders, decreasing the number of refinable parameters. The Birch- Murnaghan EoS truncated to the third order implies the refinements of 3 parameters (*i.e.*, V_0, K_0 and K'), whereas K''(Anderson 1995) is derived as:

$$K'' = -\frac{1}{K_{V0}}\left[+(4-K')(3-K') + \frac{35}{9}\right] \quad (2.18)$$

Furthermore, sometimes it is useful to fix the value of K' to 4. The resulting second-order Birch-Murnaghan EoS is expressed as:

$$P = 3K_{V0}f_E(1+2f_E)^{5/2} \quad (2.19)$$

Contrarily to the Murnaghan EoS, here there is a mathematical basis for which the K' is fixed to 4 (*i.e.,* the simplification of the Taylor's series which leads to the refinement of only V_0 and K_0).

Poirier and Tarantola (1998) elaborated an EoS based upon a logarithmic (natural) expression of the strain:

$$f_N = \ln\left(\frac{l}{l_0}\right) \quad (2.20)$$

This leads to a different mathematical formulation of the Taylor's series expansion. Even in this expression, it is possible to truncate the equation to different orders, however the parameters K' and K'' have different absolute values with respect to the ones of the Birch-Murnaghan EoS.

The accuracy of previous EoS fails in the case of very high compression (*i.e.,* $\eta < 0.6$). In this cases, it is advisable the use of the Vinet EoS (Vinet et al. 1986). This EoS is derived from a general inter-atomic potential.

2.1.4 The f_E-F_e Plot

For the majority of dataset, a visual assessment of the quality of an EoS fit is very difficult to obtain directly from a *P-V* plot. Moreover, there would be no indication on whether or not truncate the Taylor's expansion series on a specific order. For an isothermal EoS based upon Eulerian finite strain, an useful tool is the f_E-F_e plot. For instance, in the case of a Birch-Murnaghan EoS, Stacey at al. (1981) defined a normalized pressure, F_E, expressed as:

$$Fe = \frac{P}{3f_E(1+2f_E)^{5/2}} \quad (2.21)$$

This allows to re-write the Birch-Murnaghan EoS in a simple polynomial expression:

$$F_e = K_{V0} + \frac{3K'}{2}(K' - 4)f_E + \frac{3K_0}{2}\left(K'\,K'' + (K' - 4)(K' - 3) + \frac{35}{9}\right)f_E^2 + \ldots \quad (2.22)$$

If the values of f_E and F_e are plotted in a diagram respectively in abscissa and in ordinate, the intercept represents the value of K_{V0}. Furthermore, if the slope of the obtained plot is horizontal, the trend suggests the use of a 2nd order Birch Murnaghan EoS . In this scenario, it is reasonable to fix the K' to 4. If the plot has a non-horizontal slope with a linear trend, the use of a 3rd Birch-Murnaghan EoS is suggested. Finally, a parabolic trend suggests a 4th order truncation. However, for a reasonable evaluation of the f_E-F_e plot, the uncertainties σ_{F_E} and σ_{fe}have also to be taken into account (Angel 2000). σ_{F_E} and σ_{fe} can be expressed as:

$$\sigma_{fe} = \frac{1}{3}\sigma_\eta\left(\eta^{-\frac{5}{3}}\right) \quad (2.23)$$

$$\sigma_{F_E} = F_e\sqrt{\left(\frac{\sigma_P}{P}\right)^2 + (\sigma')^2} \quad (2.24)$$

In which η is the compression V/V_0 , σ_η its uncertainty and σ' the uncertainty in $f_E(1 + 2f_E)^{5/2}$ defined as:

$$\sigma' = \frac{\left[7\left(\eta^{-\frac{2}{3}}\right) - 5\right]\sigma_\eta}{3\left(1 - \eta^{-\frac{2}{3}}\right)\eta} \quad (2.25)$$

Because η decreases with pressure, σ_{fe} is inversely proportional with P itself. Moreover, the term $\left(\frac{\sigma_P}{P}\right)^2$ also decreases with pressure and this means that, the lower the pressure, the higher the uncertainties in both $\sigma_{fe}$and σ_{F_E}. The f_E-F_e plot requires *a-priori* knowledge of V_0.

2.2- X-ray Diffraction instrumentations for single crystal experiments: devices and methods

The art and science of crystal chemistry lies in the interpretation of three-dimensional electron and nuclear density data from diffraction experiments in terms of interatomic bonding and forces; these data essentially reveal the nature of the atomic species as well as their distribution within the unit cell. But for a complete description of the crystal structure, the spatial and temporal distributions of all

atoms in the crystal itself are not the only needed parameters. In order to describe a crystalline structure, others parameters (*e.g.,* atomic radii, bond distances, packing indices, polyhedral representations, distortion indices) are needed, which are often model-dependent: namely, they are all based on interpretations of the primary diffraction data (Hazen at al. 2000). By definition, the crystal has periodicity, and the spatial terms can be represented by (1) the size and shape of the unit cell, (2) the space group, and (3) the fractional coordinates of all symmetrically distinct sites along with their associated elemental compositions (Hazen et al. 2000). X-ray or neutron diffraction experiments are particularly useful for *in-situ* investigation which have a number of advantages over other techniques. *In-situ* experiments allow studying the selected compound at given *P-T* conditions, meaning that the structural modifications induced by a finite change in *P* or *T* can be followed in real time. In the case of zeolites, the structural data (*e.g.,* lattice parameters, nature and distribution of the atoms in the unit cell, bond distances, coordination shell, …) obtained at non-ambient conditions allows not only to calculate the coefficients of the EoS, but provides also useful indication on many other aspects such as phase stability field, *P*- induced over-hydration, structural changes related with the migration of molecules (*e.g.,* H_2O) and so on. Overall, the refinements of a crystal structure is possible by a least-squares minimization and from the integration of the collected diffraction data. In the structure refinement, the X-ray intensities, diffracted from a large number of planes, is converted into a set of amplitudes, |**F**(**s**)|. This set is then compared to another set of amplitudes calculated with the equation (23):

$$F(s) = \sum_{J=1}^{n} f_j^h(s)\, e^{2\pi i r_j \cdot s} \quad (2.26)$$

Where n is the number of atoms in the unit cell, $\boldsymbol{r}_j$ represents the positional vector of the j^{th} atom in the direct space, and $\boldsymbol{r}_j \cdot s$ is equal to $h\frac{x}{a} + k\frac{y}{b} + l\frac{z}{c}$. The value $f_j^h(s)$ is the atomic displacement factor and represents the effect that the electron distributions, from the center of gravity of all atoms in the structure, have on X-ray scattering (Downs 2000).The two set of amplitudes are then compared with the intent of minimize the difference between them by varying $\boldsymbol{r}_j$ and $f_j^h(s)$. At the end of the minimization process, the value of $\boldsymbol{r}_j$ will represent the refined positional vector of the j^{th} atom in the direct space (and therefore it will give the atomic fractional position of the j^{th} atom in the unit cell). For further details, refer to Downs (2000). In this thesis, the high-pressure behavior and the structure evolution of the selected zeolites have been investigated using single-crystal X-ray diffraction methods. Conventional X-ray diffractometer and synchrotron facilities have been employed.

2.2.1 Conventional and unconventional X-ray devices

All the crystals employed for the present research project were selected *via* optical investigation and tested using an Xcalibur Oxford Instruments diffractometer equipped with a CCD, using graphite-monocromatized Mo*K*α radiation, and operating at 50 kV and 30 mA at the Earth Science Department of Milan (ESD-MI). For natural and synthetic compounds, with relatively small unit cell, the use of a Mo*K*α X-ray (0.7107Å) source is preferable with respect to Cu*K*α (1.5418Å), because it allows a larger 2/λ radius of the limiting sphere. This is particularly critical in high-pressure experiments as it counterbalances (partially) the loss of reflections due to the limited portion of the explorable reciprocal space, because of the shadowing effect promoted by the high-pressure devices. The area detector allows the maximum coverage of the reciprocal space, coupled with reduced data collection time. In order to maximize the number of reciprocal nodes intercepting the Ewald sphere, this diffractometer relies on the mutual rotation of the crystal and of the detector. The maximum coverage of the reciprocal space is obtained through the use of four goniometers: one (θ) moves the detector whereas the others three (φ, ω, and κ) allow the rotation of the sample (acing as an Eulerian cradle). Into detail, in this diffractometer, based on a "κ geometry", the 2θ goniometer rotates the detector about an axis perpendicular to the basal plane. The φ goniometer is co-axial to the goniometer head's axis, whereas the ω-goniometer is coaxial with 2θ. Finally, the axis of the κ goniometer is rotated of about 50° with respect to the basal plane in which 2θ rotates (Fig. 2.1). Usually, a data collection is based on one or more runs, in each one a rotation of one axis is performed while the other three are kept constant. The detector collects and records the frames in a stepwise method, where the step-angle and the collection-time per frame are selected parameters. This differs from a point detector where a θ or ω scan of each diffraction peak is performed, in order to define at best its 2θ position and integrate the diffraction density. For the experiments performed at the large scale facilities, data were collected at the ID09A and ID15b beamline of the European Synchrotron Radiation Source (ESRF), Grenoble, France, and at the Extreme Conditions Beamline P02.2 at PETRA III/DESY, Hamburg, Germany. These beamlines are entirely dedicated to high-pressure experiments using diamond anvil-cell devices. The beamline setup differs from beamline to beamline, although the common advantage is to operate by using a synchrotron radiation which has an extremely high brilliance (at least 10 magnitude order) with respect to the conventional X-ray diffractometers. This allows the study of very small-volumes crystals, decreasing the exposure time (which allows quicker data collections) and selecting a completely polarized and well suited beam wavelength.

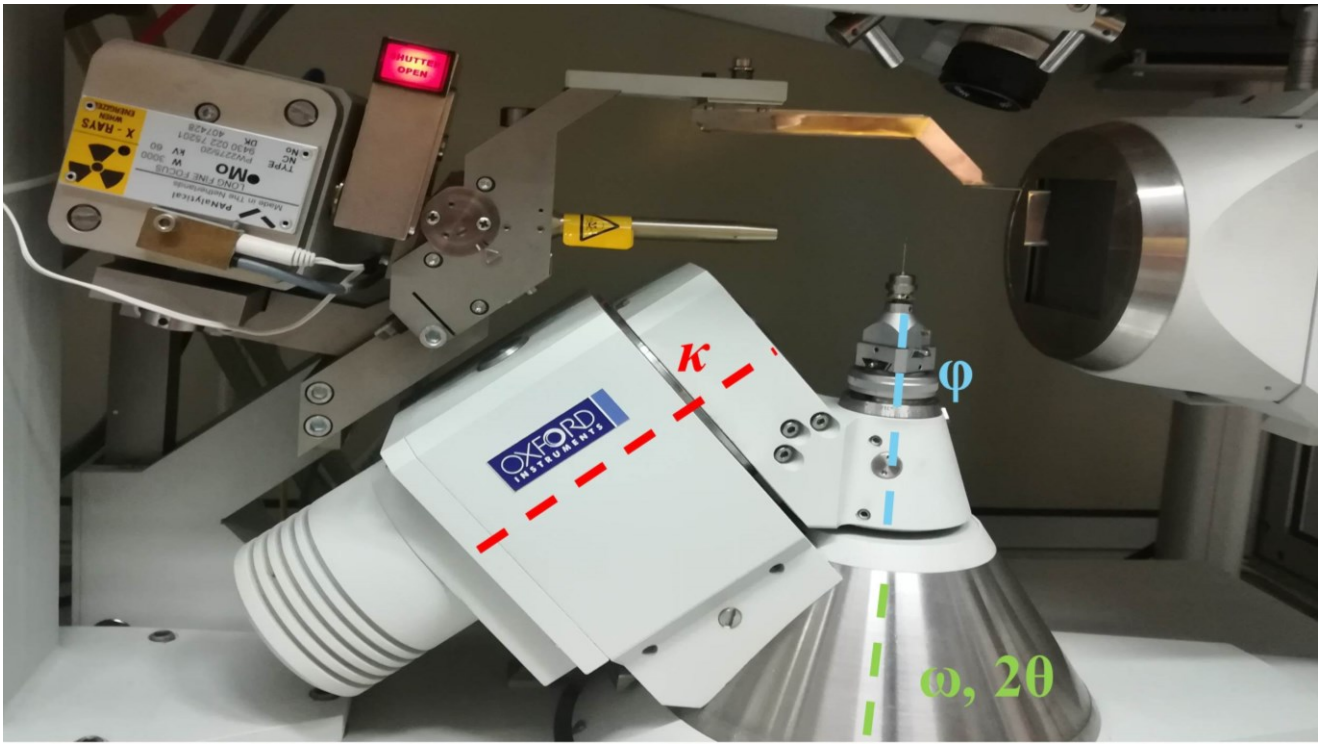

Fig. 2.1: CCD Xcalibur Oxford Diffraction based on the κ geometry: the goniometers axes are shown.

2.2.2 Synchrotron light

Synchrotron facilities (Fig. 2.2, 2.3) consist in circular storage ring where the electrons are forced to follow circular paths under the action of magnets placed along the circumference (bending magnets), in evacuated pipes. Usually, the electrons enter in the storage ring only after have been accelerated until their energy reaches several millions of electron volts (MeV) by a linear accelerator or 'LINAC'. Then, they enter in a booster ring that gives them a boost in energy from millions to billions of giga-electron volts (GeV); after that, electrons are transferred to the final circular accelerator (Fig. 2.3). The main properties of the synchrotron radiation are:

1. High intensity, which implies high brightness due to the small section of the electron beam
2. Very broad and continuous spectral range from IR to hard X-ray
3. Narrow angular collimation
4. High beam stability
5. Perfectly (or almost) polarized beam

When relativistic charged particles are forced to move along curved trajectories, by applied magnetic fields, they generate an electromagnetic radiation (called "Synchrotron Radiation") along the direction of their motion. The radiation so produced is extremely intense and extends over a broad energy range from the infrared through the visible and ultraviolet, up to soft and hard X-ray. The first time that it

was observed, in 1947 at the General Electric synchrotron in the USA by the physics Herb Pollock and Robert Langmuir, it was considered as a tedious problem since it represented the major source of energy loss in high energy particle accelerators. Only in the late sixties the true potential of Synchrotron Radiation was entirely realized. Nowadays, synchrotron facilities are fundamental to study the matter at atomic scale. Taking an electron moving at a speed much lower than the speed of light *c*, its emitted pattern does not depend on the electron speed and is similar to that of an oscillating dipole with its maximum of intensity in the direction perpendicular to the acceleration.

However, when the speed of electron is close to *c,* the radiation pattern results compressed into a narrow cone and the resulting emission is tangential to the particle orbit (Fig. 2.4). The vertical half opening angle ψ, is expressed by:

$$\psi \approx mc^2 \approx \gamma^{-1} \quad (2.27)$$

where m and E are the particle mass and energy and c is the speed of light. For electrons, $\gamma \sim 1957E$(GeV) which implies that, for a storage ring of E = 1GeV, $\psi \sim 0.029°$. This means that, not only the synchrotron radiation is extremely collimated, but also that, even at distances of tens meters (distance that usually separates an experimental hutch from the storage ring), the resulting beam will have an extremely high brightness. Thanks mainly to the very high brilliance of the beam, as well as to its narrow angular collimation, in a synchrotron beamline is possible to perform high-pressure experiments that would otherwise have taken several days or also weeks, within a few hours. Furthermore, the quality of the data is extremely high due to the very high I/σ_I ratio. Perhaps, the only disadvantage of working with synchrotrons is the limited time machine available, since the access is very competitive. With microporous or mesoporous material, such as zeolites that can adsorb small molecules at high *P-T* conditions, the short time machine available represent in a critical limitation. In fact, some hydration processes, for instance, may requires several days or also some weeks in order to complete. In these cases, the use of home-lab instrumentations (*i.e.,* common diffractometer) be preferred.

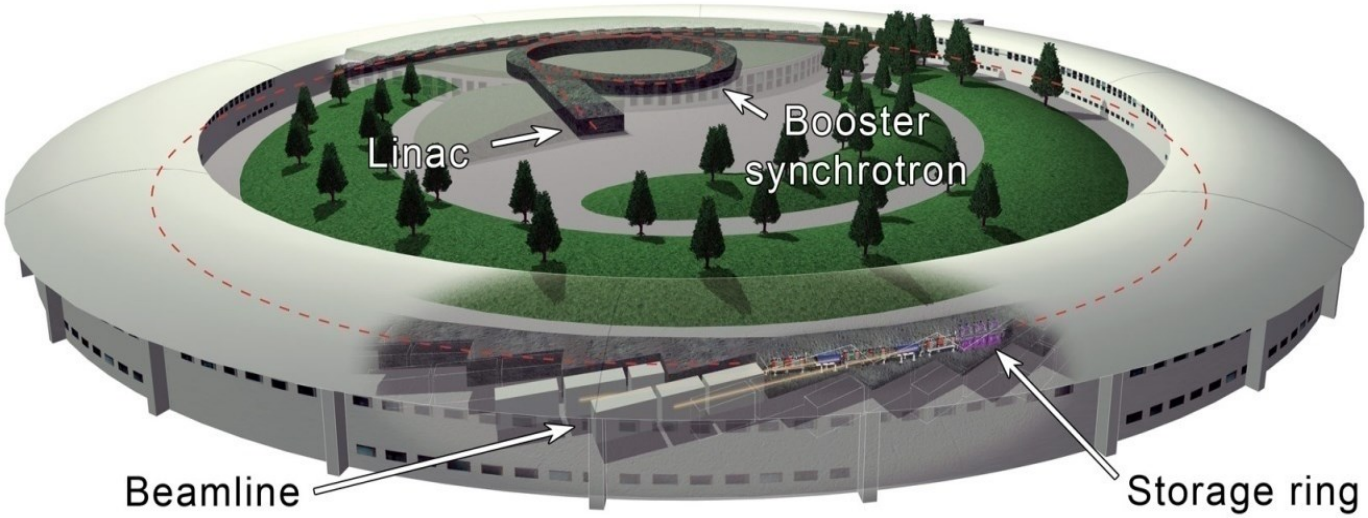

Fig. 2.2 : schematic representation of E.S.R.F. (http://www.esrf.eu).

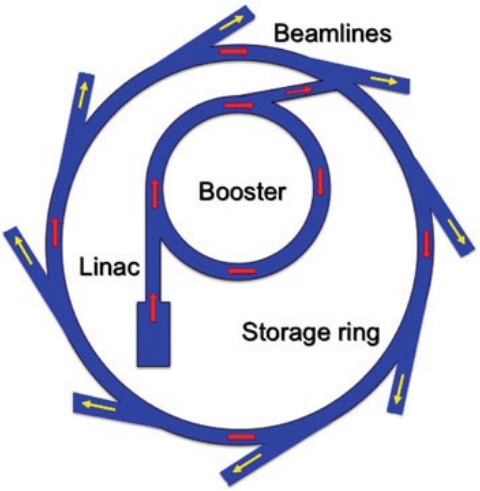

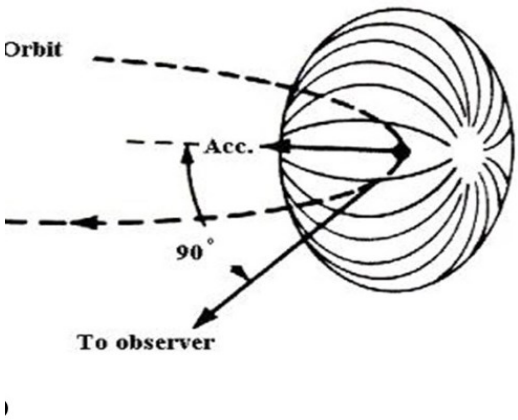

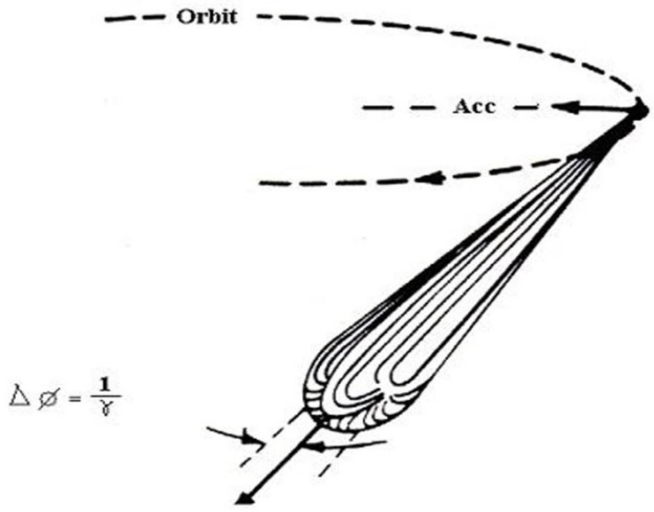

Fig. 2.2 and 2.3: (left) schematic representation of a synchrotron. (bottom) Visualization of the Lorentz transformation of emitted synchrotron radiation (Bartolini, public domain);

2.3 *In-situ* high pressure device: the diamond anvil cell

In order to compress the crystals hydrostatically for *in-situ* measurement, the high-pressure experiments of this research project have been performed using diamond anvil cells (DAC, Fig. 2.5). The experiments based on single crystal data collections allow an accurate description of the deformation mechanisms at an atomic level at high pressure. The sample, along with the pressure calibrant, is placed in a pressure chamber which is delimited on the top and on the bottom by flat parallel faces (culets) of two opposed diamond anvils. Laterally, the pressure chamber is confined by a metal foil, called "gasket". The pressure chamber is flooded with a pressure-transmitting fluid, a liquid which, ideally, exerts hydrostatic pressure onto the sample. The pressure is applied by forcing the diamonds together. This causes the extrusion of the gasket around the diamond culets, sealing in this way the pressure chamber. The extrusion of the gasket compresses the pressure-transmitting medium which, in turn, compresses both sample and pressure calibrant under hydrostatic conditions. One of the advantage of the diamond anvil cell is that the force required in order to reach even the highest pressure achievable by the DAC set up, can be easily generated by simple mechanical mechanisms. The X-ray beam penetrates across the first diamond, hits the crystal in the pressure chamber and the diffracted beams pass through the second diamond. It follows a detailed description of the main components of a diamond anvil cell.

2.3.1 Diamond backing plates

The **Backing plates** act as a support for the diamonds and must allow the incident beam to penetrate. In the firsts DAC model, Be plates seem the obvious solution since beryllium is practically transparent to X-rays. Although the improvements in both design and composition of Be-backing plates, beryllium has also a number of disadvantages, primarily its toxicity. Moreover, beryllium mechanical strength decreases rapidly at high/low temperature, meaning that experiments at non-ambient T conditions cannot be performed. Because of these reasons, other materials, such as tungsten carbide and boron carbide, have been used to produce the backing plates. These materials are not toxic, have a remarkable mechanical strength in a wide range of temperatures. Therefore, they are the best substitute for beryllium, although the support to the diamond table is reduced.

2.3.2 Diamonds

Diamonds are the fundamental components of the diamond anvil cell. Diamonds are used, over all the others natural or synthetic compounds, because of their unique properties. In fact, diamond is not only the hardest material on Earth but has also a low thermal expansion and it is relatively transparent to

many ranges of electromagnetic radiation, from infrared to X-ray (5 eV to 10 keV) (Miletich et al. 2000). Depending on the fraction of nitrogen impurity, diamonds are classified into two types (I and II). Type-I diamonds contain 0.1% of nitrogen, whereas the type-II diamonds have only a minor content in nitrogen and may also have some ppm of other impurities (Miletich et al. 2000). This chemical difference is critical for high- pressure spectroscopic studies, because *e.g.,* type-II diamonds do not show adsorption bands in the ultraviolet regions. However, Mao et al. (1979) have demonstrated that type-I diamonds, with platelet nitrogen impurities, are more resistant to plastic deformation. At a practical level, for the majority of high-pressure X-ray experiments, including the experiments of the present thesis, both types are suitable and can be employed, although type-II diamonds are more expensive. Diamond anvils typically used for X-ray diffraction studies are approximately 1/3 carat (1 carat = 0.2 gram), have a thickness of approximately 1.5 to 2 mm, and a table and culet diameter of about 3 mm and 0.6 mm respectively (Dunstan and Spain 1989, Miletich et al. 2000). Dimensions are perhaps the most critical factor for several reasons. The anvils has to be as thin as possible in order to minimize the Compton scattering. But reducing the thickness of the diamond, the tensile stresses increase, and this in turn would lead to diamond failing at lower pressures (Adams and Shaw 1982). The effect of the tensile stresses could be compensated by reducing the area of the diamond's table but this will lead to a reduction of the maximum pressure reachable in the pressure chamber. In fact, the P_{max} is related to the table/culet ratio: the higher is the ratio, the higher is the pressure that can be reached. The effective dimensions are generally the best possible compromise. The design of the diamond anvils is another critical factor because it determines the pressure that the diamond-anvil cell can achieve. In the first years, the standard design was based on modified brilliant cut which maximizes back reflections as well as spectral dispersion. In order to achieve higher pressure, it was developed a new design based on the so called Drukker-cut. In this particular design, the highly stressed shoulders of the brilliant cut have been removed, the table diameter enlarged and the anvil angle increased.

2.3.3 Gasket

The **gasket** (Fig. 2.5) is a metal foil which has a double role. Firstly, it is a support to the diamond anvils preventing a direct contact between the two culets (which could result in a breaking of the diamonds); secondly, it delimits the chamber where the pressure-transmitting medium compresses hydrostatically the sample. Indeed, when the diamond anvil are pressured one close to the other, the diamonds deform the gasket plastically. The metal foil can be made by different metal materials, such as stainless steel, rhenium, tungsten (Miletich et al. 2000), and it is usually 250 μm thick. Spain and

Dunstan (1989) reported also the possible use of special alloy such as the Inconel (Ni:Cr:Fe=72:16:8) or Cu-Be. However, the gasket has to be pre-intended in the DAC, giving the desired height for the pressure chamber. This operation has also another important effect: by reducing the gasket's thickness the gasket would deform less when compress by the anvils, thus increasing the pressure range reachable by the experiment. Once the gasket is pre-indented, the sample chamber is obtained by drilling a hole in the center of the pre-indented area, by using a spark eroder or a mechanical drill. The diameter of the hole is critical since defines the maximum pressure achievable during the experiment: bigger is the diameter, lower is the maximum achievable pressure (Miletich et al. 2000). In fact, at high pressure, there are two forces on the "wall" of the gasket hole: one acting outwards, caused by the pressure-transmitting fluid, and another, equal but opposite, acting inwards, caused by the shear strength of the gasket material and by the friction between the culets and the gasket surfaces they are in contact with. Until the surface area of the gasket "wall" is sufficiently small, the system is in equilibrium. When the outward force becomes dominant over the inward force, the gasket hole begin to expand dropping the pressure inside the chamber.

2.3.4 Pressure media

The **pressure transmitting medium** compresses both the sample and the pressure calibrant. This fluid must not dissolve the single crystal (or the polycrystalline material) employed in the experiment and should transmits the pressure hydrostatically, over the entire pressure range of the experiment. This allows that there are not differential stresses and thus induced shear strain (Angel et al. 2007). Non-hydrostatic stresses would generate inhomogeneous strain in the crystal which would result in a broadening of the diffraction peaks of the sample, reducing not only the signal-to-noise ratio of the measured diffraction signal, but also modifying the relative evolution of cell parameters with *P* (*e.g.,* Kenichi et al. 1999). Furthermore, non-hydrostatic media would bias the behavior of the pressure calibrant, leading to uncorrected pressure measurement (Miletich et al. 2000). This results in using mainly liquids, even though some solid soft material, for instance NaCl, KCl or KBr have been used for some experiments (Miletich et al. 2000). Klotz et al. (2009) and Angel et al. (2007) reported similar hydrostatic limits for the most commonly used pressure-transmitting media (Table 2.1.). Gaseous pressure media (*e.g.,* argon, neon, helium,…) transform to liquid already at relatively low pressure and preserve a quasi-hydrostatic behavior even after the *P*-induced solidification (Klotz et al. 2009).

Studying open framework materials, as zeolites, the potential adsorption of *P*-transmitting medium molecules should also been taken into account. Because pure liquids crystallize at relatively low

pressure (Miletich et al. 2000), the pressure-transmitting media commonly used are mixture of liquids, such as the 4:1 ethanol-methanol mixture, or the 16:3:1 methanol-ethanol-H_2O, hydrostatic up to 9.8 and 10.5 GPa, respectively (Angel et al. 2007, Klotz et al. 2009). In addition, silicone oil is commonly used, due to its polymeric nature, despite its low hydrostatic limit (0.9 GPa, Angel et al. 2007), in order to obtain the elastic parameters of zeolite that, otherwise, would adsorb molecules (*e.g.,* ethanol or H_2O) from the *P*-transmitting fluid. Indeed, in the specific case of porous materials, the use of ‘‘penetrating’’ or ‘‘non-penetrating’’ *P*-media (*sensu* Gatta, 2008) is critical for the final results of the experiments. “Non- penetrating’’ *P*-medium as glycerol, various grades of silicone-oils, isopropanol, perfluorether, fluorinert FC-75 (Angel et al. 2007; Klotz et al. 2009) are generally used in order to study the evolution at high pressure of the selected zeolite “as it is” (*e.g.,* Ori et al. 2008). In fact, they cannot be adsorbed by the zeolite, due to their molecular diameter, which is larger than the zeolites’ channel diameter. In contrast, “penetrating” *P*-media, as He, N, Ne, Ar, Xe and small molecules (*e.g.,* H_2O, CO_2), can be potentially adsorbed in response to the applied pressure (Gatta and Lee 2014). The *P*-induced penetrability is controlled by several variables and mainly, as already underlined, by the ‘‘free diameters’’ (Baerlocher et al. 2007) of the framework channels, along with the nature of the channel content (Gatta and Lee 2014) and the partial pressure of the penetrating fluid (if mixed with other non-penetrating compounds, *e.g.,* P_{H2O} in a mixture of methanol:ethanol:H_2O = 16:3:1, usually used as hydrostatic *P*-fluids up to 10 GPa).

Medium	Hydrostatic limit (GPa)
4:1 Methanol-ethanol	9.8
Anydrous 2-proponol	4.2
Argon	1.9
Nitrogen	3.0
Glycerol	1.4
Silicon-oil, viscosity 0.65 cSt	0.9
Silicon-oil, viscosity 37 cSt	0.9

Tab. 2.1: Nominal hydrostatic limits of pressure media (In: Angel et al. 2007).

2.3.5 *P*-generating mechanisms

The high pressure in the pressure chamber is generated by compressing the two diamonds anvils towards each other. The most common pressure generating mechanism widespread is the screw-bolts mechanism. In this case, the diamond anvil cell consists of two parts which are pushed together tightening the screws by Allen keys. In order to ensure the best homogeneous load possible, often the pressure generating mechanism employs the use of a circular membrane. The membrane (Fig. 2.5) can be loaded with a gas thanks to an online remote control, thus increasing pressure without removing the cell from the experimental conditions, improving overall both the pressure control and the homogeneously of compression (Miletich et al. 2000).

2.3.6 Pressure calibrations

The **pressure calibration** is probably the most critical aspect of any high-pressure experiment, as an inaccurate measurement of pressure could bias both the description on the *P*-induced behavior as well as the elastic parameters of the sample (Miletich et al. 2000). Because there is not a direct relation between the applied load and the pressure in the *P*-chamber, it is mandatory to use a pressure calibrant: a material whose properties change with pressure with a known function. Diamonds are relatively transparent to many ranges of electromagnetic radiation, from infrared to X-ray (5 eV to 10 keV). This property is exploitable by irradiating, with the proper radiation, fluorescent sensors. The pressure fluorescent sensors, once irradiated, will emit a radiation wavelength with a λ shifted as function of pressure. Because is the $\Delta\lambda$ that reveals the actual pressure in the pressure chamber, an accurate measurement of the emitted wavelength at room pressure has to be performed before every experiment. The fluorescent sensors (*e.g.,* ruby, $Sm:SrB_4O_7$) are placed inside the pressure chamber with the sample and irradiated with a laser beam, and the emitted radiation is collected and measured by a spectrometer. The most common pressure calibrants are ruby and REE-doped compounds, and they can be excited by visible radiations. The sensor have to be highly luminescent, with a small halfwidths of the peaks and with a pronounced $\Delta\lambda$ *vs P*. Ruby (a Cr^{3+} doped α-Al_2O_3) is probably the most widespread pressure calibrant, also because of its relatively low cost. Another advantage of ruby is that a few spheres of 10-15 μm in diameter provide an intensive signal. The spheres of Cr^{3+} doped α-Al_2O_3 are excited by visible light and emit two characteristic radiation at $\lambda \sim 694.2$ nm (R_1) and $\lambda \sim 692.8$ (R_2) nm at 1 bar. Barnett et al. (1973) and Piermarini et al. (1975) calibrated the wavelength shift of ruby against the equation of state of NaCl up to 19.5 GPa for the first time. Later, Mao et al. (1986) revised the ruby calibration compressing several metals up to 180 GPa finding the empirical quasi-linear function:

$$P_{T0} = 1904\left[\left(\frac{\lambda}{\lambda_0}\right)^{B} - 1\right] / \mathrm{B} \quad (2.28),$$

where λ_0 is the emitted radiation wavelength at room-*P*, λ is the emitted radiation wavelength at the pressure P_{T0} and B is a constant equal to 7.665 for quasi-hydrostatic condition and equal to 5 in non-hydrostatic conditions. The calibration was performed for the R_1 peak, although the R_1-R_2 distances remains almost constant under hydrostatic condition (Miletich et al. 2000). The major disadvantage in using ruby as pressure calibrant is the strong dependence of the $\Delta\lambda$ on temperature. For instance, a ΔT of only 6 K causes a shift equal to ΔP of 0.1 GPa (Miletich et al. 2000). Overall, typical uncertainties in the measured pressure by the ruby fluorescence method range between 0.05 and 0.1 GPa (Miletich et al. 2000). Alternatively, the pressure can be measured by the use of an internal diffraction standard, through the determination of its unit-cell parameters if its equation of state is well known. Quartz is the main calibrant used as internal pressure standard due to its chemical stability in the *P*- transmitting media commonly used; furthermore, quartz has a high symmetry, small unit-cell edges lenghts and strong diffraction peaks. Moreover quartz is highly compressible in a large *P*-range (K_0 = 37.12(9) GPa, K'= 5.99(4)) (Angel et al. 1997). The only practical recommendation using quartz, as internal pressure standard, is to load the crystal with the (100) face parallel to the DAC bisecting plane (see next paragraph). In the case of ultrahigh pressure, face-centered cubic (f.c.c.) and body-centered cubic (b.c.c.) metals serve as internal standard.

2.4 The accessible reciprocal lattice in high pressure DAC experiments

Considering a crystal in air, ideally, the accessible reciprocal lattice for diffraction is a sphere centered on the origin and of radius $2/\lambda$, in fact all the diffraction peaks can be moved to intersect the Ewald sphere by rotation of the crystal. However, in a high pressure experiment, X-ray access is only possible *via* the diamonds and/or through the transparent components of the DAC. Practically, the accessible reciprocal space volume during a high-pressure experiment is a function of the DAC's opening angle (2α) and of its orientation with respect to the incident and diffracted X-ray beam, defined respectively by the angles ψ_i and ψ_d. In a diffraction experiment in transmission geometry, such as all the experiments performed in the present thesis, it is accessible a toroidal volume of reciprocal space, where the rotation axis of the toroid is perpendicular to the bisecting plane of the DAC (*i.e.,* perpendicular to the gasket plane). In these particular conditions, the limiting diffraction conditions in 2θ are given by:

$$2\theta \leq \alpha + \psi_i \quad (2.29)$$

It is worth to underline that every [hkl] vector oriented parallel (or almost) to the toroid axis will be impossible to detect. This means that in dimetric crystal (*i.e.,* trigonal, tetragonal and hexagonal) the [001] axis should be taken parallel to the bisecting plane of the DAC in order to preserve the information along both a^* and c^*.

Fig. 2.5: (top) a membrane and a membrane anvil cell ready for the experiment; (bottom) components of an ETH-type diamond anvil cell with the four screws used to load to the diamonds.

a

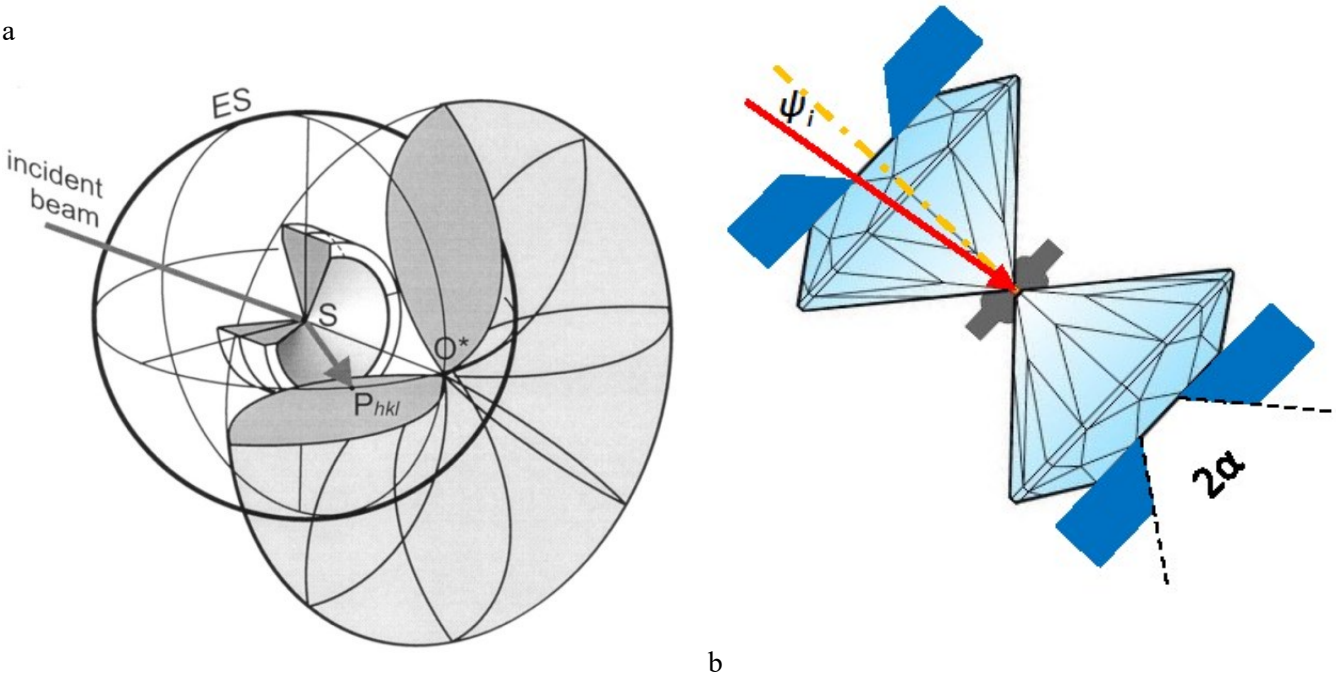

b

Fig. 2.6: (left) Cut-away view of the toroidal portion of the reciprocal space for a radially symmetric transmission geometry DAC with 2α = 90° (Miletich at al. 2000); (right) schematic representation of the angular restriction in a H*P* experiment (ψ_i and α are the maximum angles of the X-ray incident and diffracted beam respectevely).

CHAPTER 3:
HIGH-PRESSURE BEHAVIOR AND CRYSTAL-FLUID INTERACTION IN $AlPO_4$-5

The experimental findings reported in the following pages have been published in the paper:

Lotti P., Gatta G.D., **Comboni D.**, Merlini M., Pastero L., Hanfland M. (2016) $AlPO_4$-5 at high pressure: crystal-fluid interaction and elastic behavior. MICROPOROUS AND MESOPOROUS MATERIALS. Volume: 228, Pages: 158-167.

3.1 Introduction

$AlPO_4$-5 is a member of the aluminophosphate $(Al,P)_nO_{2n}$ compounds which are an important class of microporous materials currently employed as molecular sieves, catalysts, *etc* (Wilson et al. 1982; Flanigen et al. 1986, Lotti et al. 2016). Furthermore, $AlPO_4$-5 may have potential technological and industrial applications as underlined in (Liu et al. 2015; Chen et al. 2015; Yang et al. 2016). $AlPO_4$-5, *P6/mcc,* has an AFI-type framework, with ideal cell parameters a ~13.827 and c ~ 8.580 Å (Baerlocher et al. 2007). The whole structure of $AlPO_4$-5 may be described by an alternation, along the c-axis, of sheets made by isolated upward AlO_4 and downward PO_4 tetrahedra, respectively (Fig. 3.1). The TO_4 tetrahedra are connected in such a way that large channels made by 12-membered rings of tetrahedra (hereafter 12-mRs channels) occur. The 12-mRs channels are parallel to the [001] direction and centered to the sixfold axis (Fig. 3.1). Their largest free diameter (7.42 Å, Baerlocher et al. 2007) is defined by the two symmetry-independent O1-O1 and O3-O3 (Fig. 3.1) distances and can be, potentially, an ideal host for several molecules and polymers. The 12-mRs are connected to each other by the so-called "pseudo-cage" cavities, which are confined in the (001) plane by single six membered rings of tetrahedra centered on the 3-fold axis (hereafter 6-mRs [001], Fig. 3.1). The 6-mRs [001] and the 12-mRs share rings of six tetrahedra which lay almost parallel to the c-axis (hereafter 6-mRs $[hk0]_1$, Fig. 3.1). It is important to underline that, in order to diffuse from a channel to the neighboring ones, a molecule/ion needs to cross a second 6-mRs (hereafter 6-mRs $[hk0]_2$), independent from 6-mRs $[hk0]_1$ (Fig. 3.2). In the literature, there was an open debate about the true space group of $AlPO_4$-5, as the ordered distribution of Al and P reduces the symmetry of $AlPO_4$-5 from *P6/mcc* to *P6cc*, which leads to Al-O2-P interatomic angles close to 180° (Bordat et al. 2007).

Previous studies, based on the use of different *P*-transmitting fluids (*e.g.*, N_2, methanol:ethanol:water=16:3:1 - hereafter *m.e.w.*) showed that the channels system of $AlPO_4$-5 can adsorb external molecules, through selective sorption from the *P*-fluid, even at low pressure (*i.e.*, < 1

Figure 3.1: (*Left*) Alternation of the upward AlO_4 and downward PO_4 tetrahedra in $AlPO_4$-5 structure (in grey and light blue respectively), underlined in yellow the 6-mRs $[hk0]_1$; (*right*) secondary building units (6-mRs [001] and 12-mRs) shown down the *c* crystallographic axis. Some relevant interatomic distances as well as symmetry elements are shown (in Lotti et al. 2016).

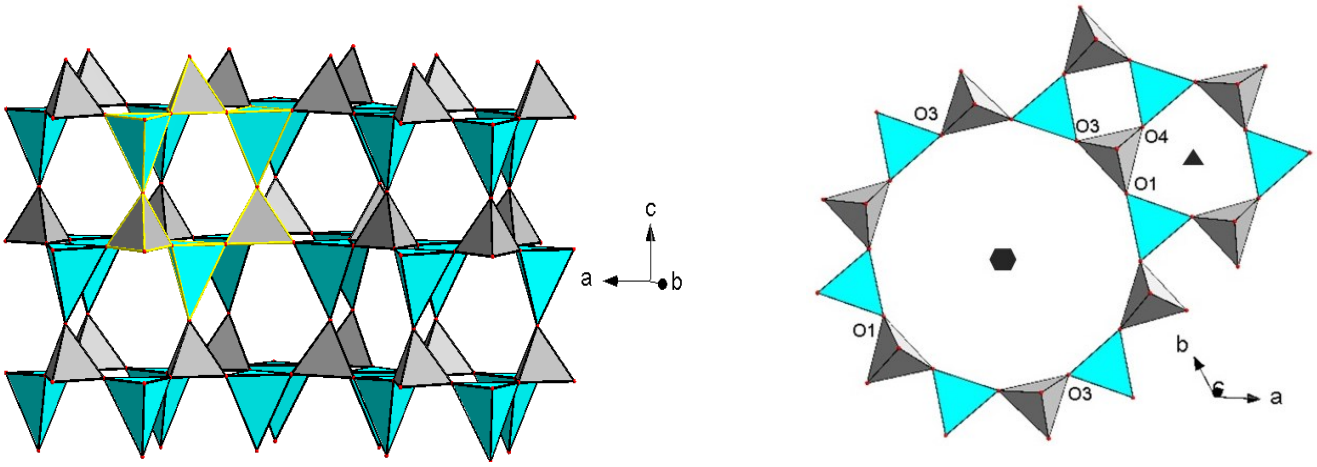

Figure 3.2: (*Left*) A view of the two symmetry-independent 6-membered rings windows of tetrahedra (S6R$[hk0]_{1,2}$) defining the access between neighboring 12R-channels. (*Right*) upward AlO_4 and downward PO_4 tetrahedra (in grey and light blue respectively), with the atomic sites represented with anisotropic displacement parameters are shown, based on the structure refinement with the crystal in air of this study (displacement probability factor: 50%) (in Lotti et al. 2016).

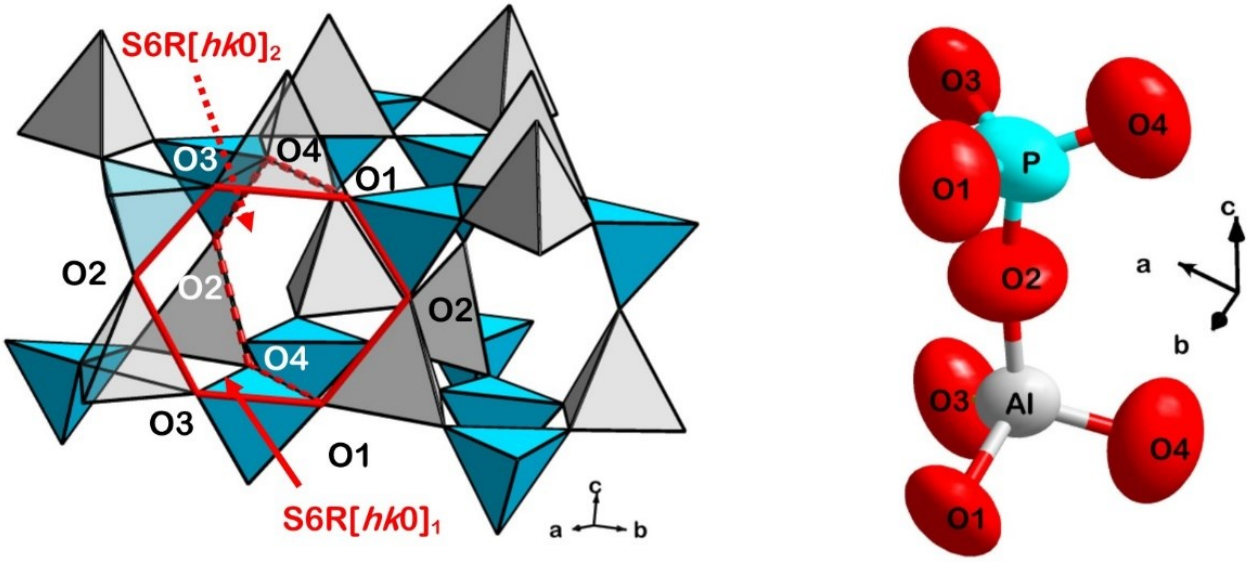

GPa) (Lv et al. 2012, Kim et al. 2013), making $AlPO_4$-5 an excellent candidate to explore the *P*-induced crystal-fluid interaction phenomena.

On the basis of the previous experimental findings, in this study we investigate, by *in-situ* single-crystal synchrotron X-ray diffraction, the high-pressure behavior of the zeolite $AlPO_4$-5 compressed in "non-penetrating" silicone oil and in the "penetrating" *m.e.w.* mixture. The "non-penetrating" silicone oil allows a description of the elastic behavior and of the deformation mechanisms when no interference from the *P*-transmitting fluid occurs. Due to the non-penetrating nature of silicone oil, the actual compressibility of $AlPO_4$-5 can be extrapolated from the related experimental data. In contrast, the compression in the penetrating *m.e.w.* allows the study of the *P*-induced intrusion of fluid molecules into the structural cavities of the zeolite $AlPO_4$-5, as well as the influence that this phenomenon plays on the elastic and structural response. In this light, the present investigation on the synthetic zeolite $AlPO_4$-5 aims to provide a comprehensive description of the deformation mechanisms at the atomic scale and of the intrusion phenomena in response to the applied pressure.

3.2 Experimental methods

The $AlPO_4$-5 crystals employed in this research project were synthesized following the protocol proposed by Li et al. (2012) and described by Lotti et al. (2016). The molar composition of the synthesis gel was modified as follows:

$$1Al_2O_3 : 1.33P_2O_5 : 0.6TEA : 100H_2O \quad (3.1)$$

Aluminum isopropoxide, phosphoric acid and trimethylamine were all Sigma analytical grade reagents. Ultrapurewater 18 MOhm was obtained using an Elga Flex3 water purification system. Aluminum isopropoxide and water were mixed on the basis of the molar ratios previously indicated and stirred for 4 h. Then, phosphoric acid was added and the suspension was stirred further for 1 h. TEA was then added and stirred vigorously for 10 min. The synthesis gel was kept at room temperature for 12 h and afterward it was heated at 210 °C for 4 days. The synthesis product was filtered, washed with ultrapure water and dried at room temperature. The as synthesized sample was then calcined up to 600 °C, in order to completely remove the template molecules from the zeolitic cavities. A thermogravimetric analysis of the calcined sample was carried out using a Seiko SSC 5200 thermal analyzer (Fig. 3.3). The sample was loaded in a Pt crucible and heated in an air flux (100 mL/min) from room temperature up to 880 °C (increment rate: 10 °C/min). A few single crystals showing hexagonal prismatic morphology (ca. $20 \cdot 20 \cdot 40$ μm^3 in size) were selected for the further experiments.

The X-ray diffraction experiments were performed at the ID09A beamline of the European Synchrotron Radiation Facility (ESRF) in Grenoble, France. A parallel monochromatic beam (E ~30 KeV, $\lambda \sim 0.414$

Figure 3.3 TG (*left*) and DTG (*right*) experimental patterns of the previously calcined $AlPO_4$-5 synthetic sample (in Lotti et al. 2016).

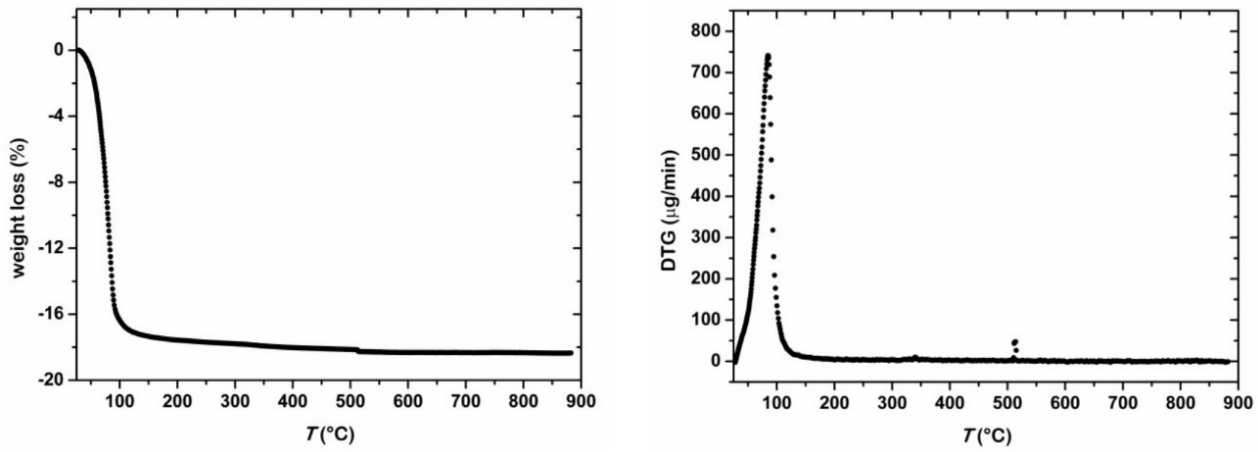

Å) was used for the diffraction experiments. The diffraction patterns were collected by a MAR555 flat-panel detector, positioned at 287.43 mm from the sample position. Further details on the beamline experimental setup are reported in Merlini and Hanfland (2013). A first data collection was performed with a crystal in air mounted on a glass fiber. A stepwise omega-rotation in the range ±45°, with 1° step width and 1s exposure time per step, was adopted as collection strategy.

Two high-pressure experiments were then performed using silicone oil and a 16:3:1 *m.e.w.*, as *P*-transmitting fluids, respectively. H_2O, methanol and ethanol molecules (kinetic diameters at ambient conditions ~2.65, ~3.76 and 4.46 Å, respectively) can potentially be incorporated into the large 12-mRs channels of $AlPO_4$-5 (~ 7.3 Å, Baerlocher et al 2007). For both the *P*-experiments, membrane driven diamond anvil cells (DACs), mounting Boehler-Almax designed diamonds (culet diameter 600 µm), were used. Two selected crystals of $AlPO_4$-5 (one for each H*P*-experiment) were loaded in *P*-chambers obtained drilling a hole (~ 250 mm), by spark erosion, in a T301 stainless steel foil, previously pre-indented to ca. 70 µm and used as a gasket. Along with the zeolite crystals, the *P*-chambers were filled with the *P*-fluids and a few ruby spheres as pressure calibrant (pressure uncertainty ± 0.05 GPa, Mao et al. 1986). At any pressure point of both the ramps, the following data collection strategy was adopted: a stepwise omega-rotation of the DAC between -30 and +30°, with 1° step width and 1s exposure time per step.

3.3 Strategy of structure refinements

One of the new findings of the present experiment was to observe diffraction patterns typical of incommensurately modulated structures, with modulation vector **q** ~ 0.37***c**** (Fig. 3.4); the low intensity of the satellite peaks did not allow the refinement of the incommensurate structure. The structure refinements were performed in the average *P*6*cc* space group structure using the *JANA2006* software (Petricek et al. 2014). A challenging aspect was the low number of "observed" reflections, due to the DAC components and to a sudden decrease of the *I*/sig(*I*) ratio of the diffraction peaks, observed in all datasets for d_{hkl} < 1 Å. Moreover, large anisotropic displacement parameters were obtained for all the oxygen sites of the framework. The O1, O3 and O4 sites show an elongated shape roughly parallel to ***c***, whereas a flattened [on the (001) plane] oblate shape was obtained for the O2 site, which connects the AlO_4 and PO_4 tetrahedra (Fig. 2b), in fair agreement with the findings of Klap et al. (2000). Such large displacement parameters reflect a static or dynamic disorder, likely induced by the presence of rigid-unit modes or structural microdomains (see Chapter 3.5, *Discussion*), which persists even at high pressure. For the structure refinement based on the intensity data collected with the crystal in air, the position and the anisotropic displacement parameters of the framework sites were refined. The Al-O and the P-O distances were restrained to 1.74(±0.02) and 1.52(±0.02) Å, respectively. Difference- Fourier maps of the electron density were calculated, in order to locate H_2O molecules into the zeolitic channels, revealing a rather diffuse distribution of the electron density in specific portions of the 12-mRs and in the 6-mRs close to the trigonal axis.

Figure 3.4 A fraction of the reconstructed (*h*1*l*) * reciprocal lattice plane, based on the P_1 (0.25 GPa) dataset in silicone oil. The incommensurately modulated satellite diffraction spots, with modulation vector (α ~ 0.37) parallel to ***c****, are shown (in Lotti et al. 2016).

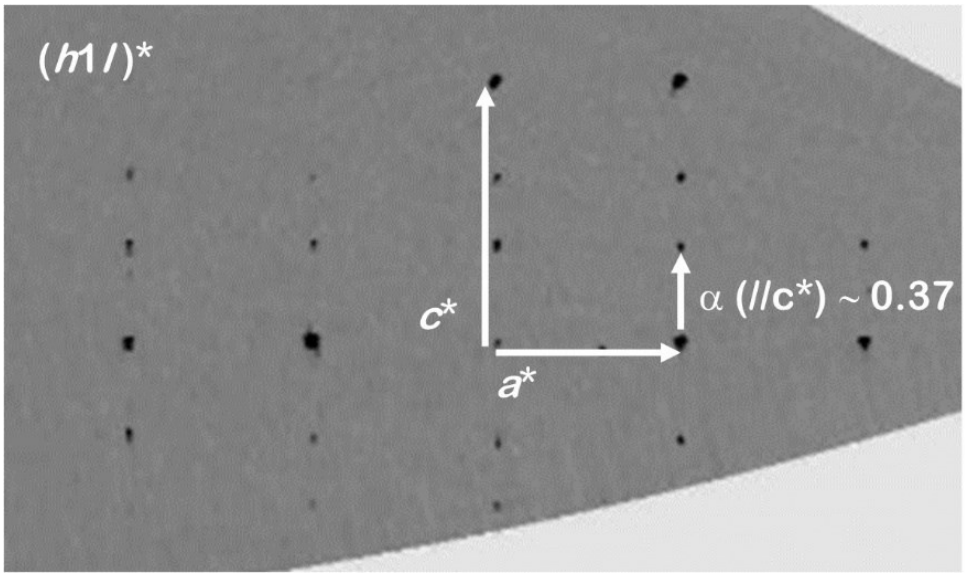

Consequently, coordinates and occupancies of five oxygen sites were refined to model the extra-framework population, assuming high isotropic displacement parameter (U_{iso} = 0.08 Å^2). Such a constrain on the U_{iso} implies that the occupancy of the H_2O molecules refined in this way has to be considered as merely qualitative rather than quantitative.

The same strategy was applied to refine the structure models based on the high-pressure intensity data. However, due to the limited portion of the reciprocal space accessible at high pressure (which reduces the number of reflections detected), an independent refinement of the anisotropic displacement parameters of the framework sites was not possible. As commonly done in high-pressure studies, isotropic displacement parameters were refined in order to reduce the number of variables. However, in this case, constraining large and highly anisotropic displacement (which are the result of the incommensurately modulated structure) parameters to a spherical distribution, decreased significantly the refinement quality. Therefore, we opted to refine, one by one, anisotropic displacement parameters for the framework oxygen sites, while all the atomic coordinates and the H_2O-oxygen occupancies were always refined. This (not conventional) strategy allowed a significantly better fit between observed and calculated structure model, with a pronounced decrease of the R_1 factors of the refinements. The structure refinements were possible for the datasets up to 1.43 (P7) and 2.44 (P9) GPa in silicone oil and *m.e.w.*, respectively. At higher pressures, the low number of observed reflections did not allow reliable refinements.

Table 3.1 reports the *P*-induced evolution of the unit-cell parameters of $AlPO_4$-5 compressed in silicone oil and *m.e.w.* (see Fig. 3.5). Relevant interatomic distances and structural parameters are reported in Table 3.2. Details on the structure refinements, refined site coordinates, occupancies and displacement parameters are deposited in Tables 3.3, 3.4 and 3.5.

3.4 Results

3.4.1 Thermogravimetric analysis

The thermogravimetric analysis of the calcined $AlPO_4$-5 sample shows a total weight loss, at 880 °C, of 18.35% (Fig. 3.3). Assuming that the loss is completely due to zeolitic H_2O, the chemical formula of the $AlPO_4$-5 used in this experiment is assumed to be: $AlPO_4 \cdot 1.52H_2O$ (post-calcination). This leads to 18.24 H_2O molecules per unit cell, in fair agreement with previous TG-analyses (*e.g.,* Malla and Komarneni 1995; Kim et al. 2013) and isotherm adsorption experiments (*e.g.,* Newalkar et al. 1998; Floquet et al. 2004). As can be seen in Fig. 3.4, the TG- and DTG-data show that the dehydration mainly occurs in a single step, in the range 50-100 °C, with the maximum of the DTG at 85 °C.

Figure 3.5. (*A*). High-pressure evolution of the normalized unit-cell volume of the zeolite $AlPO_4$-5 compressed in silicone oil and *m.e.w.* (*B*). Comparison of the experimental V/V_0 *vs*. *P* patterns of the zeolite $AlPO_4$-5 compressed in *m.e.w.*, based on *in-situ* single-crystal (round symbols, this study) and powder (diamond symbols, Kim et al. (2013)) X-ray diffraction data. (*C* and *D*). *P*-induced evolution of the normalized unit-cell *a* and *c* parameters of the zeolite $AlPO_4$-5 compressed in silicone oil and *m.e.w.*. The Birch-Murnaghan equations of state, fitting the experimental data (Table 3.6), are reported as solid lines in *A*, *C* and *D*. Data related to the silicone oil experiments have been normalized to the V_0, a_0 and c_0 refined by the BM-EoS fits (in Lotti et al. 2016).

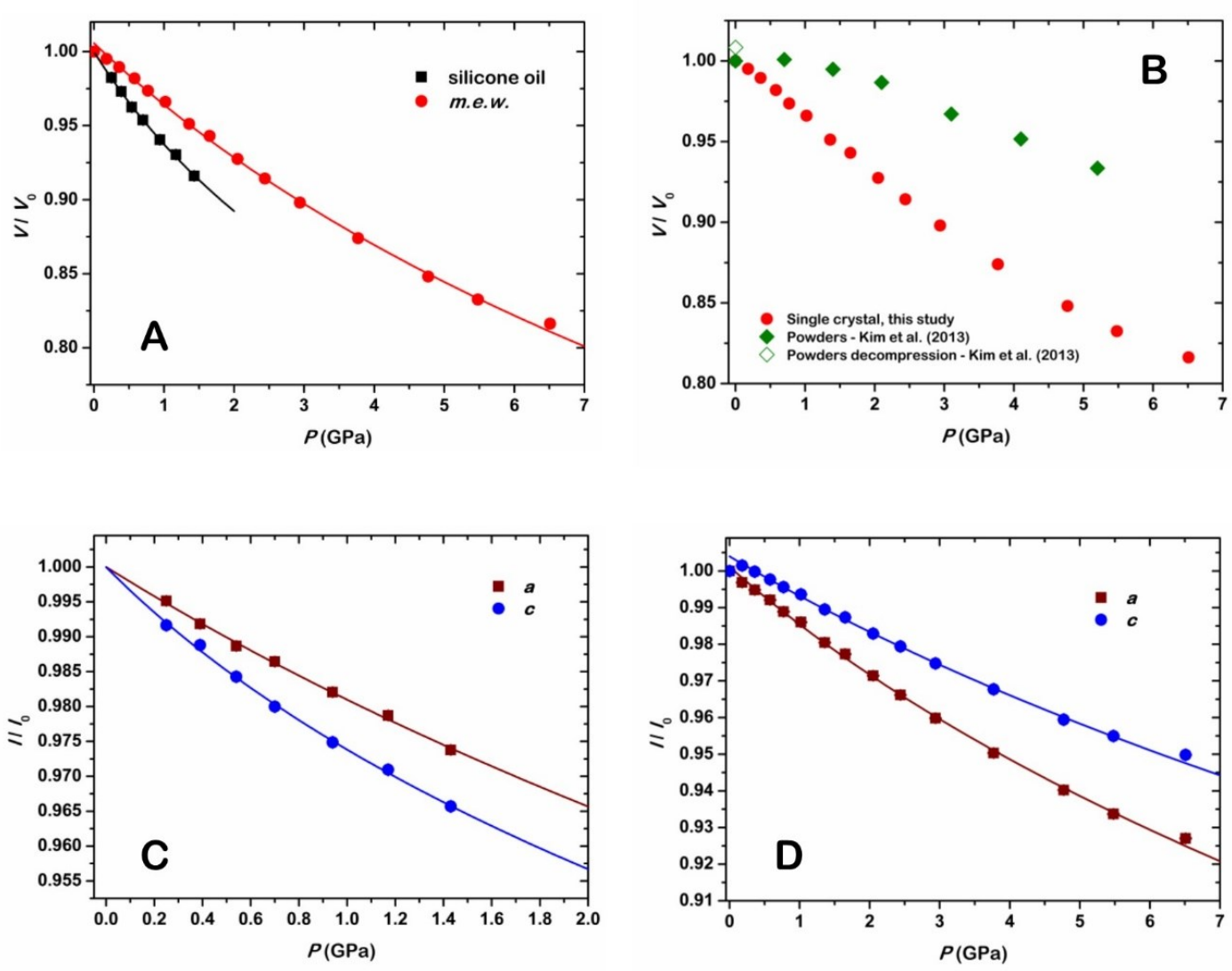

3.4.2 Compressibility

For the high-*P* experiment in silicone oil, diffraction data up to 2.97 GPa were collected (fourteen data points), along with one point in decompression at 1.43 GPa. The intensity of the Bragg reflections decreased steadily with increasing pressure to the extent that a reliable refinement of the unit-cell parameters was possible only up to 1.65 GPa (*i.e. P*8). Intensities in the diffraction pattern were not recovered in decompression, suggesting that the average long-range order of the crystal was irreversibly lost by compression. For the ramp in *m.e.w.,* seventeen *P*-points up to 6.51 GPa were collected, along with two points in decompression at 0.82 and 0.75 GPa. Also in this case, a decrease in the intensity of the diffraction peaks was observed with increasing pressure; however, contrarily to the experiment in silicone oil, the refinement of the unit-cell parameters was possible for all the datasets. Overall, the unit cell parameters *a*, *c* and *V* of the $AlPO_4$-5 compressed in silicone oil decrease steadily with no evidence of phase transitions or change in the compressional behavior. Unit-cell volumes *vs. P* were fitted to a third-order Birch-Murnaghan Equation of State (III-BM-EoS) (Murnaghan 1937; Birch 1947) using the EOS-FIT7 program (Angel et al. 2014). As already described in the section 2.1 (*Elastic behavior at extreme conditions*), this EoS of state is widely used in order to describe the compressional behavior of crystalline materials in low/middle *P*-regimes (see Angel 2000 for a review), and allows to refine the isothermal *bulk modulus* of a given material and its *P*-derivatives. The refined elastic parameters are reported in Table 3.6. The linear elastic behavior along the ***a*** and ***c*** crystallographic axes was also described by the fit of linearized BM-EoS (Angel 2000). However, in this case, the simultaneous refinement of three variables (namely: l_0, K_{l0} and K_l') was unstable and did not reach the convergence. Therefore, $K_l' = \partial K_l / \partial P$ was kept fixed to the value that provided the best figure of merit. For the ***a***-axis, the best fit was obtained with $K_a' = 4$, whereas for the ***c***-axis the best figure of merit was obtained with $K_c' = 7$. The other refined elastic parameters are reported in Table 3.3.

On the other hand, the *P*-induced evolution of the unit-cell parameters of $AlPO_4$-5 compressed in *m.e.w.* shows an increase of the ***c*** unit-cell parameters between room-*P* and 0.18 GPa (Fig. 3.5, Table 3.1). Furthermore, the *P*-*V* data suggests a significantly lower compressibility of the $AlPO_4$-5 compressed in *m.e.w.* with respect to the sample compressed in silicone oil. The penetration of H_2O molecules into zeolitic channels will be discussed in the following sections; nevertheless, a III-BM Equations of State (Angel 2000) were fitted to the experimental *V*-*P*, *a*-*P* and *c*-*P* data in the range P_1-P_{14} (0.18-6.51 GPa, Fig. 3.6), leading to the refined elastic parameters reported in Table 3.6. The unit-cell parameters refined from the data collected in decompression at 0.82 (P_{15d}) and 0.75 (P_{16d}) GPa (Table 3.1) reveal that the bulk compression is not fully recovered at these pressures.

Figure 3.6. A view of the deformation mechanisms with pressure of the 6-mRs $[hk0]_1$ window of zeolite $AlPO_4$-5 (in Lotti et al. 2016).

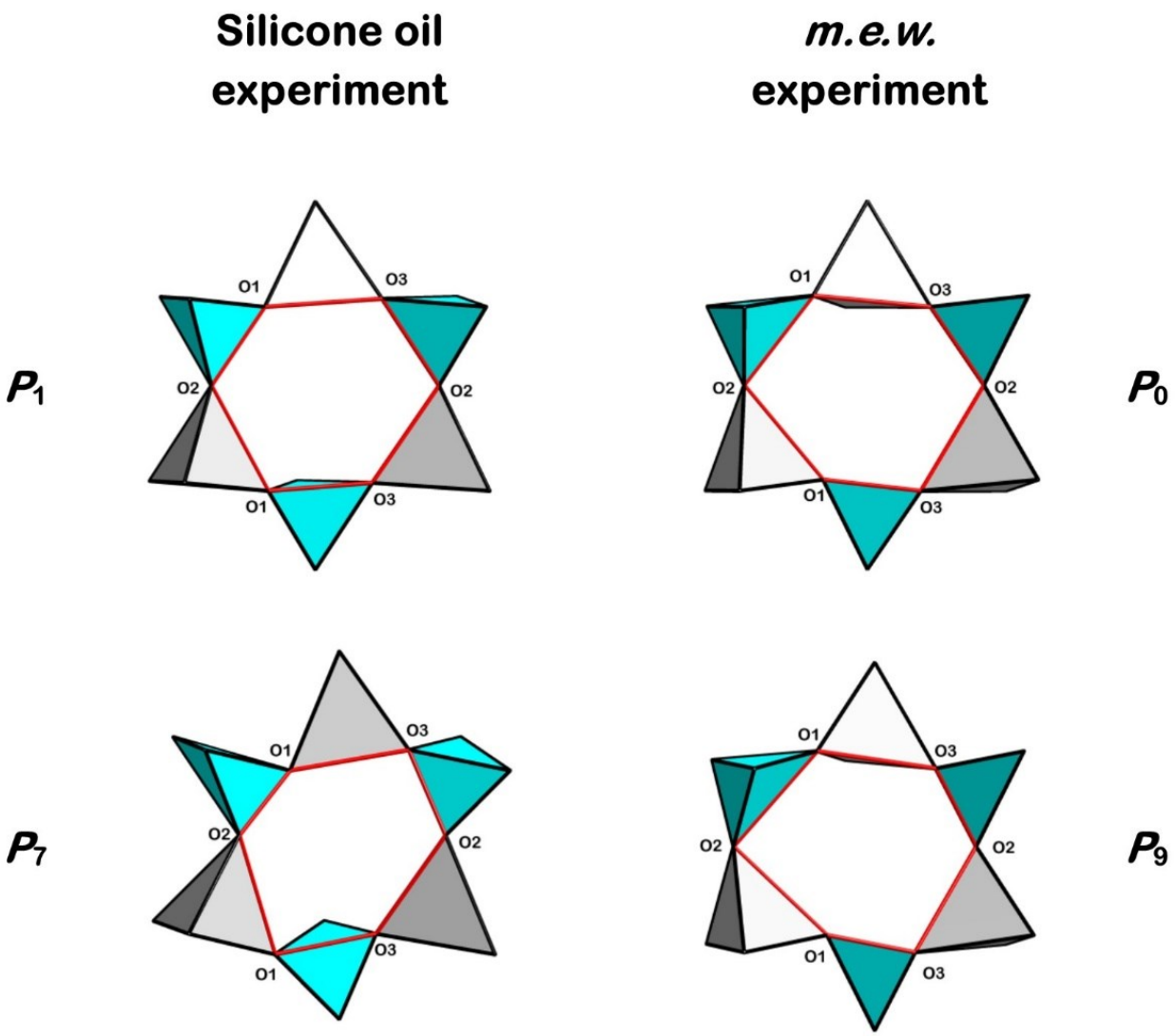

3.4.3 High-pressure structure evolution of $AlPO_4$-5 compressed in silicone oil

The structure refinements were performed in the average *P6cc* space group using the *JANA2006* software (Petricek et al. 2014), allowing a description of the *P*-induced deformation of the AlPO4-5 average structure. Coherently with Gatta et al. (2010a), the bulk compression is mainly accommodated by tilting of the quasi-rigid (framework) tetrahedra, which leads to a compression of the structural cavities. Such a behavior is predominant to the distortion of the TO_4 units as well as to the contraction of the T-O bonds. The *tilting* of the AlO_4 and PO_4 tetrahedra induces a framework deformation which mainly affects the SBUs: the 4-mRs undergo a compression along both the O3–O3 and O4–O4 diameters (Fig. 3.1), coupled with a distortion of the planarity on (001), which can be described as $\Delta z_{4R} = (|(z\text{O3} - 0.5) - z\text{O4}| \times c)$ (Table 3.2). Such a deviation from planarity, on the (001) plane, is experimented also by the 6-mRs [001]. The deviation here described as $\Delta z_{S6R[001]}$ is reported in Table 3.2. As can be seen in Fig. 3.6, the 6-mRs $[hk0]_{1,2}$ clearly deform with increasing pressure (as also suggested by the ε_1 and ε_2, Table 3.2).

The *tilting* can also be analyzed by two geometrical models which were arbitrarily defined for the large 12mRs-channels and the pseudo-cage cavities centered on the 3-fold axis (Figs. 3.1 and 3.2). A cylinder with height equal to the *c*-cell parameter and base diameter D = (O1–O1 + O3–O3)/2 was chosen to model the compression of the 12-mRs, since O1-O1 and O3-O3 are the two independent diameters of this SBU. The pseudo-cage was modeled as a prism of height equal to the *c*-edge and triangular basis of side O4–O4 (see Fig. 3.1). In this way, although qualitative, it was possible to provide a description of the high-pressure behavior of the structural voids of $AlPO_4$-5. The *V vs*. *P* evolution of the so-modelled 12-mRs-channel and pseudo-cage is reported in Table 3.2 and shown in Fig. 3.7, where it can be seen that the compressibility of the pseudo-cage increases with pressure.

As reported in the section 3.3 (*Strategy of structure refinements*), while the coordinates of the H_2O sites represent an average position of a likely locally-disordered distribution, their refined occupancies are biased by the constrained displacement parameter fixed to 0.08Å^2. However, an analysis of the high-pressure evolution of the W1 H_2O-site shows a continuous decrease of the refined occupancy parameter up to 0.70 GPa (P_4) (Table 3.4). At higher pressures, the analysis of the difference-Fourier maps of the electron density revealed the absence of a clear residual peak close to the former W1 position. Therefore, the W1 site was not included in the structural model in the *P*-range between 0.94 and 1.43 GPa (P_5-P_7). This can be explained considering an increase in the disorder of the H_2O molecules which, at low pressure, are relatively close to the average W1 position. Alternatively, a *P*-induced migration of H_2O molecules from the pseudo-cages to the larger 12-mRs- channels (*i.e.,* a *P*-induced extrusion of H_2O from a structural micropore to another) may also explain this phenomenon. However, a *P*-induced migration of

extra-framework H_2O molecules among different structural micropores was not, to the best of our knowledge, reported in the literature without the effect of temperature.

Figure 3.7. High-pressure evolution of the calculated volumes of the 12-mRs -channels (*A*) and pseudo-cage cavities (*B*). (*C*) *P*-induced evolution of the total number of extra-framework H_2O molecules per unit cell, deduced from the structure refinements related to the *m.e.w.* experiment (in Lotti et al. 2016).

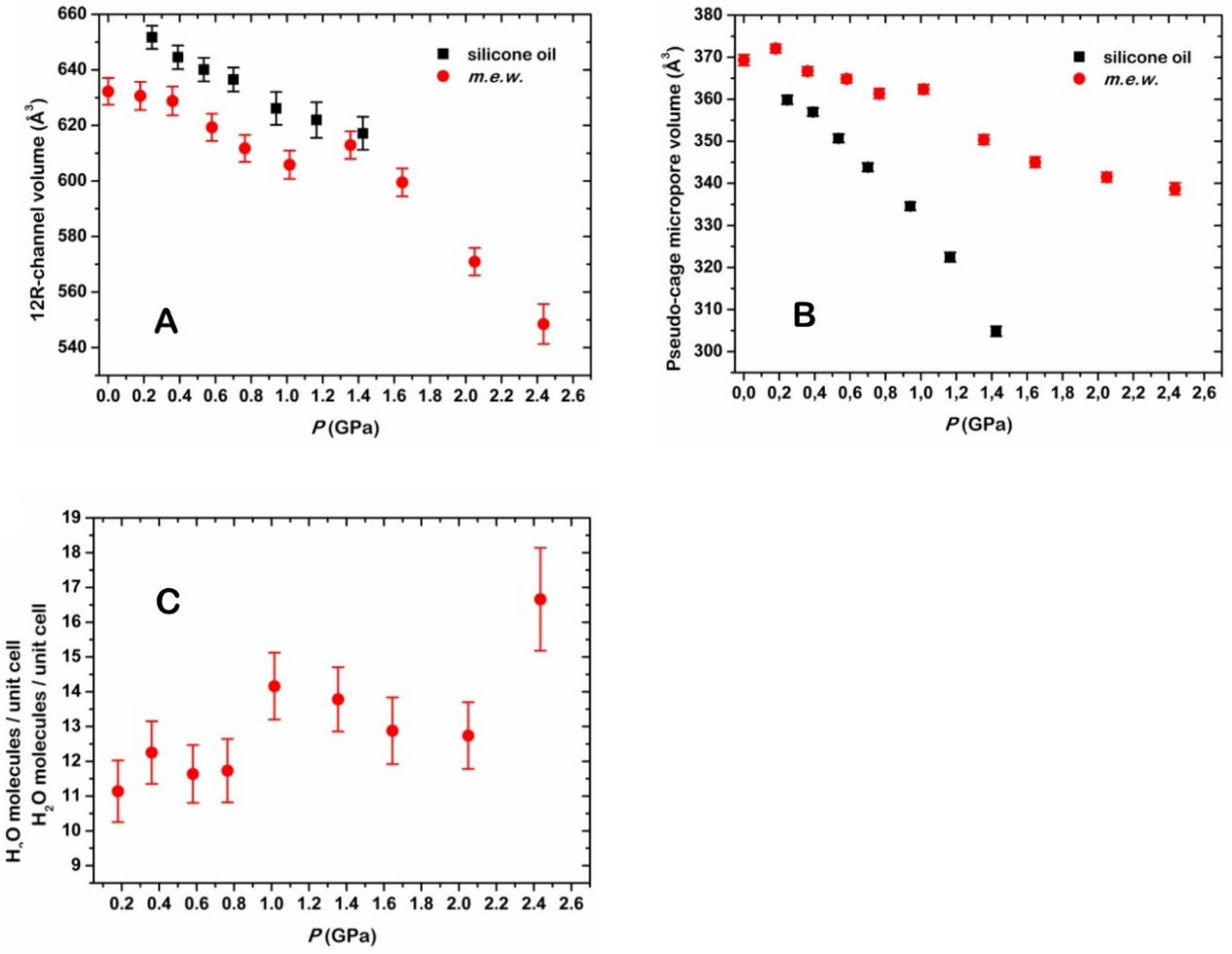

3.4.4 High-pressure structure evolution of $AlPO_4$-5 compressed in *m.e.w.*

Contrarily to the sample compressed in silicone oil, the *P-V* patterns of the 12mRs-channel and pseudo-cage (Fig. 3.7, Table 3.2) show that the two types of cavities of the sample compressed in *m.e.w.* deform approximately in the same way. The Δz_{4R} aplanarity parameter is significantly lower with respect to the values observed in silicone oil compression, whereas the O3–O3 and O4–O4 diameters of the 4-mRs remain practically undeformed (Table 3.2). Also the ellipticity parameters ε1 and ε2 of the 6-mRs undergo only a minor deformation with increasing pressure (Fig. 3.6, Table 3.2). No major changes of the refined coordinates of the H_2O sites, detected at room-*P*, were observed up to 2.44 GPa (P9). Although with a given uncertainty, due to the constrain on the dislacement parameters, the evolution of the site occupancy factors of the H_2O sites (Table 3.4, Table 3.5) suggests an increase of the total number of the H_2O molecules (Fig. 3.7).

3.5 Discussion

3.5.1 $AlPO_4$-5 structural model

As reported in the section 3.1 (*Introduciton*), in the literature there is an open debate about the real space group of $AlPO_4$-5. For instance, Klap et al. (2000) proposed a splitting of the framework oxygen sites into three mutually exclusive positions, leading to 3 coexistent structural microdomains with local symmetry *P*6 (which give rise to the average *P*6*cc*-structure). Liu et al. (2002) and Berlie et al. (2015) proposed the existence of several rigid-unit modes of distortion in the AFI-framework, which lead to a dynamical (or static in case the RUMs condense at ambient temperature) local disorder of all the framework atoms. Both these models reduce significantly the Al-O2-P angle, which is very close to 180° in the average structure, to a value that rages between 140° and 150°(Klap et al. 2000; Liu et al. 2003; Berlie et al. 2015). Liu et al. (2002) investigated the SiO_2 analogue of $AlPO_4$-5, zeolite SSZ-24, finding the presence of incommensurately modulated diffraction spots with a wave vector $\alpha \sim 0.38$, parallel to $\boldsymbol{c}^*$. This value is close to the one calculated for $AlPO_4$-5, $\alpha \sim 0.37$, for the satellite spots showed in Fig. 3.3. Our findings represent the first experimental evidence of an incommensurately modulated diffraction pattern in crystals of the zeolite $AlPO_4$-5. The low intensity of the satellites diffraction spots did not allow the refinement of the incommensurate structure. However, as the observed orientation and magnitude of the modulation vector α for the zeolites $AlPO_4$-5 and SSZ-24 are very similar, and considering that the SSZ-24 zeolite is the SiO_2 analogue of $AlPO_4$-5, it is reasonable to assume the same structural origin of the satellites. As pointed out by Berlie et al. (2015), the modulated static disorder has as a direct consequence: anomalously large anisotropic displacement parameters of the framework sites in the average *P*6*cc*

structure. This explains the "cigar-like" shape of the electron density around the center of gravity of the O1, O3 and O4 framework oxygen sites, elongated along [001], as well as the "discoidal-like" shape of the electron density of the O2 site, lying approximately on (001) (Fig. 3.2; Table 3.4, Table 3.5). It is worth to underline that shapes and orientations of the framework's oxygen atoms are consistent with what observed in the SSZ-24 zeolite (Liu et al. 2002).

Despite the aluminophosphate framework of $AlPO_4$-5 is electrically neutral, several experimental data (*e.g.,* Malla and Komarneni 1995; Tsutsumi et al. 1999; Newalkar et al. 1998; Floquet et al. 2004) showed that a steep adsorption of H_2O molecules occurs at partial pressures of water higher than 0.3, up to 18 molecules per unit cell (Floquet et al. 2004). Our TGA analysis leads to a total amount of 18.24 H_2O molecules per unit cell. However, the refined occupancies of the five H_2O oxygen sites, detected by the difference-Fourier maps of the electron density, lead to a total amount of 6.4(4) molecules per unit cell, which significantly underestimates the H_2O content if compared to that derived from the TG-analysis. These aspects can be explained considering that:

- the calcined $AlPO_4$-5 crystals adsorb H_2O molecules from the atmosphere after the calcination.
- The location of the H_2O sites based on the diffraction data was not straightforward: the occupancies are biased by the constrained displacement parameters to U_{iso}= 0.08Å^2.
- Dynamical and/or static disorder has to be considered, as suggested by the difference-Fourier maps of electron density pertaining to the extra-framework population, likely influenced by the disorder of the framework sites.

The latter two points may lead to an underestimation of the content of H_2O molecules, which occupy the 12-mRs, and are connected each other *via* H-bonds. It has also been proposed a double-helix configuration of the H_2O molecules, similar to that of the hexagonal ice (Floquet et al. 2004; Demontis et al. 2012).

Overall, the refined structure model of this study confirms the presence of clusters of H-bonded H_2O molecules into the 12-mRs channels, which can give rise to helical configurations along the *c*-axis (Table 3.4), in fair agreement with the results of Floquet et al. (2004) and Demontis et al. (2011). Although the number and position of the H_2O sites in the two crystals used for the high-*P* ramps was found to be slightly different, their structural configuration is substantially consistent to that described above for the crystal collected in air.

3.5.2 *P*-induced adsorption of *m.e.w.* molecules and effects on the high-pressure behavior of $AlPO_4$-5

Silicone oil is a non-penetrating *P*-transmitting fluid due to its polymeric nature. Therefore, the experimental data of the silicone oil *P*-ramp allow the description of the intrinsic compressibility of the zeolite $AlPO_4$-5. Table 3.6 reports the elastic parameters of $AlPO_4$-5, which has a K_{V0} (= $1/\beta_V$) of 13.2(11) GPa (β_V = 0.076(6) GPa^{-1}), and a *K'* value of 5.1(14). This makes $AlPO_4$-5 one of the softest zeolites reported so far. The largest compressibility is observed along the *c*-crystallographic axis, *i.e.,* along the large channels direction (Fig. 3.1). The bulk compressibility of zeolite $AlPO_4$-5, when compressed in the methanol:ethanol:water (16:3:1) mixture, is unambiguously lower if compared to that in silicone oil, as shown in Fig. 3.5 and by the refined elastic parameters reported in Table 3.6. Interestingly enough, the decrease in stiffness concerns mainly the *c*-axis, which becomes the less compressible direction in the sample compressed in *m.e.w.,* whereas is the most compressible direction in the sample compressed in silicone oil. Between *P*0 and *P*1 (0.18(5) GPa) a clear increase of the *c*-axis length is observed (Fig. 3.5; Table 3.1). This suggests a *P*-induced intrusion of the fluid molecules of the *m.e.w.* medium into the structural micropores of the zeolite $AlPO_4$-5. A careful analysis of the difference-Fourier maps of the electron density reveals a weak electron density peak which can be attributed to a H_2O site located near the trigonal axis of the 6-mRs[001]. If the total number of molecules per unit cell is calculated from the refined occupancies of the H_2O-oxygen sites at any pressure-point, a clear increasing trend is shown (Fig. 3.6).

The intrusion of (at least) H_2O molecules is also corroborated by the difference in the *P*-induced framework deformation using penetrating and non-penetrating fluids. In the sample compressed in silicone oil, a major distortion of the SBU occurs, especially for the 6-mRs$[hk0]_{1,2}$ and the 4-mRs-joint units (Fig. 3.6; Table 3.2). On the contrary, the same units are basically undistorted when the crystal is compressed in *m.e.w.* (Fig. 3.6; Table 3.2); even the *P*-induced deviation from planarity on the (001) plane (Δz) of the 6-mRs [001] and 4-mRs is less pronounced, with respect to the compression in silicone oil (Table 2). These data support the intrusion of the fluid molecules, which act as fillers decreasing the *P*-induced tilting of the framework tetrahedra, and thus the deformation of the whole framework (the so called "pillar effect"), which is ultimately reflected in a lowering of the compressibility of $AlPO_4$-5 zeolite in *m.e.w.*.

Fig. 6 shows a drastic difference in the H*P*-behavior of the modeled pseudo-cage volume: this structural cavity shows a higher compressibility in silicone oil than in *m.e.w.*, suggesting that at least a fraction of the *P*-intruded molecules are likely located in the pseudo-cage, where they act as fillers. The largest free diameter, controlled by O2–O2 (Fig. 3.6), is *ca.* 3.3 and 2.8 Å (with no significant change with pressure) in the two 6-mRs$[hk0]_{1,2}$ windows, suggesting that only H_2O molecules can have access to these

structural voids. If we can presume that only H_2O can be intruded into the pseudo-cages (its diameter is ~2.65 Å, shorter than the diameter of the two 6-mRs[*hk*0]$_{1,2}$ windows), we cannot exclude that methanol and even ethanol (kinetic diameters 3.76 and 4.46 Å, respectively) may be intruded into the large 12-mRs-channels (diameter ~7.4 to 6.8 Å in the range *P*0-*P*9), though a clear picture in this respect is still missing.

Overall, the comparative high-*P* behavior of $AlPO_4$-5 in silicone oil and *m.e.w.* is a further evidence that pressure can be used for the incorporation and hyper-confinement of molecules in this zeolite. In this view, a comparison between the high-pressure behavior of a single crystal of $AlPO_4$-5 compressed in *m.e.w.* (this study) with that of a polycrystalline sample compressed in the same fluid (Kim et al. 2013) could be also fruitful. In Fig. 3.5 the *P*-evolution of the (normalized) unit-cell volume of the polycrystalline sample employed by Kim et al. (2013) can be compared with the experimental findings of this study (crystal compressed in silicone oil and in *m.e.w.*). The polycrystalline sample shows a significantly lower compressibility, which is confirmed also by the reported *bulk modulus* (50.5(7) GPa Kim et al. 2013). No structure refinements are available for the crystalline powder; therefore, a direct comparison of the deformation mechanisms at the atomic scale cannot be drawn. However, it is highly likely that such a discrepancy in compressibility is governed by a stronger intrusion of H_2O molecules into the structural cavities of the polycrystalline material, enhanced by the higher surface/volume ratio of the powder with respect to single crystals. Moreover, in a single crystal, local defects may generate occlusions of the structural voids, hindering the intra-crystalline diffusion of the intruded molecules. The different behavior of polycrystalline *vs.* single crystal immersed in the same *P*-fluid was already reported in previous studies (*e.g.,* Lotti et al. 2015a, b) and shows that the particle size of the zeolite samples strongly influences the magnitude of the H*P*-intrusion of fluid molecules in the structural voids.

Overall, the results here reported suggest that the zeolite $AlPO_4$-5 is a promising material for the penetration, at high-pressure, of a relatively high number of (small) molecules per unit cell. In this respect, the next step would be the engineering of the results in systems for the mechanical energy storage/dissipation (Eroshenko et al. 2001; Soulard et al. 2004), already described in the Chapter 1.3.1 (*Potential application of zeolites: storage of mechanical energy*).

CHAPTER 4:
HIGH-PRESSURE BEHAVIOR AND CRYSTAL-FLUID INTERACTIONS IN LAUMONTITE

The experimental findings reported in the following pages have been published in the paper:
Comboni D., Gatta G.D., Lotti P., Merlini M., Hanfland M. (2018) Crystal-fluid interactions in laumontite. MICROPOROUS AND MESOPOROUS MATERIALS. Volume: 263, Pages: 86-95.

4.1. Introduction

Laumontite, $[(Ca_{4-x}Na_x)K_x][Al_8Si_{16}O_{48}]\cdot(H_2O)_n$ ($0 \leq x \leq 2$ and $12 \leq n \leq 18$), space group $C2/m$, is one of the most common natural zeolites, adopted as a reference mineral for the "zeolite facies" of low-grade metamorphism (Coombs et al. 1959). Laumontite occurs in a wide range of natural environments, including sedimentary deposits or volcanoclastic sequences interested by burial diagenesis/metamorphism, as well as in hydrothermal vugs of intrusive and volcanic rocks (Sheppard 1973, Hay and Sheppard 2001, Passaglia and Sheppard 2001, Richard and Sheppard 2001, Koporulin 2013 and references therein). According to Jove and Hacker (1997), laumontite can represent up to 20% in volume of the rocks forming oil reservoirs, where, due its cementing action, it can dramatically decrease the porosity of the host rock (Galloway 1979, Surdam and Boles1979). Authigenic laumontite is present in sedimentary sequences differing in age, lithology, genesis, tectonic setting, and stratigraphic depth: for instance, laumontite has been reported from the Archean tuffs, tuffites, and tectonized metamorphic rocks (Koporulin 2013). The formation of this mineral is always accompanied by the different-scale replacement of other minerals as aluminosilicates (less commonly carbonates + silicates) and others zeolites. For instance, the transformation reaction of heulandite to laumontite can be written as (Utada 2001):

$$Ca(Al_2Si_7O_{18})\cdot 6H_2O \Rightarrow Ca(Al_2Si_4O_{12})\cdot 4H_2O + 3SiO_2 + 2H_2O \quad (4.1)$$

Heulandite laumontite quartz

In fact, zeolites, such as laumontite, analcime, and wairakite, are stable at higher temperatures than the more hydrous zeolites, such as clinoptilolite, chabazite, and stilbite (Utada 2001). In marine sequences, laumontite occurs in vein or in amygdaloidal, in both coarse-grained and fine-grained aggregates (Liou 1979) or as monocrystalline aggregates. In this case, laumontite contains only minor amount of K/Na and is mainly enriched of Ca, due to the leaching of Ca-rich mineral of the basaltic rocks (Bohlke et al. 1980; Alt and Honnorez, 1984, Liou 1979, Juan and Lo 1971). At (relatively) high *P-T* conditions, laumontite is replaced by wairakite; since the laumontite→ wairakite reaction requires temperatures >

300 °C and pressure > 3 Kbar (Liou 1971); this transformation in marine sequences has been related to abnormally high geothermal gradients caused by localized heat sources, and more in general, to basaltic magma (*e.g.,* Vitali et al. 1995).

The aluminosilicate framework of laumontite (Baerlocher et al. 2007) is characterized by chains of four- and six-membered rings (hereafter 4-mRs and 6-mRs, respectively), also referred to as secondary building units (SBU 4-6, Fig. 4.1). The Si and Al atoms are ordered among three distinct tetrahedral sites (namely Si1, Si2 and Al) leading to a constant Si:Al = 2:1 ratio in most of the natural laumontite samples. The 4-mRs/6-mRs chains, running along the *c* axis, form ten-membered rings (Fig. 4.1), hereafter 10-mRs, which host Ca and other cations, mainly K and Na (Armbuster and Gunter 2001). The main difference between (Na,K)- and Ca-laumontite is the presence, in the former, of an additional cation position (M2) occupied by K^+ or Na^+, whereas the tetrahedral framework and the H_2O molecules arrangement (at least at room-*P*) are almost identical in both the varieties. Fully hydrated laumontite contains 18 H_2O molecules per unit formula (Yamazaki et al. 1991, Lee et al. 2004b), but if it is exposed to atmosphere at low humidity rate (< 50% of relative humidity, RH), up to 4 H_2O molecules per unit formula are lost. This partially-dehydrated laumontite (*i.e.,* $Ca_4Al_8Si_{16}O_{48}\cdot 14H_2O$) is formally referred to as "leonhardite" (Coombs 1952, Yamazaki et al. 1991, Artioli and Ståhl 1993, Ståhl and Artioli 1993). Following this nomenclature, hereafter the term leonhardite will refer to a partially-dehydrated laumontite (LAU·$14H_2O$), for which the W1 crystallographic site is missing and a partial occupancy is found for the W2 and W5 H_2O sites.

Artioli et al. (1989), in a single-crystal neutron diffraction experiment performed at 15 K, identified 11 H_2O sites. However, some of these sites were found to merge with increasing temperature. Based on a single crystal X-ray diffraction experiment at 100 K, Armbruster and Kohler (1992), identified 7 H_2O sites, whereas only four (referred to as W1, W2, W5, W8) can be distinguished in the fully hydrated Ca-laumontite at ambient conditions (Artioli and Ståhl 1993; Ståhl and Artioli 1993, Ståhl et al. 1996). The W2 and W8 oxygens are bonded to the Ca^{2+} ion, whereas W1 and W5 are hydrogen-bonded to the framework oxygen atoms and to other H_2O molecules. Yamazaki et al. (1991), based on X-ray powder diffraction data, investigated the hydration process of Ca-laumontite reporting a final unit-cell volume of about 1388 $Å^3$ at RH > 80%. Fridriksson et al. (2003) studied the response of a quasi-stoichiometric Ca-laumontite to hydration/dehydration paths by controlling the partial pressure of H_2O (P_{H2O}) at ~301.7 K, reporting that the dehydration of W1 allows W2 to move off the special position and split in two half-occupied subsites. White et al. (2004), using computational methods, hypothesized that fully hydrated laumontite (LAU·$18H_2O$) is stable up to ~ 5.5 GPa, whereas leonhardite only up to ~3.5 GPa. Above these pressures, the simulations showed that both the structures undergo a phase transition. The high-pressure behavior of Ca-laumontite was experimentally investigated by Lee et al. (2004b), by

Fig. 4.1. Configuration of the 6-mRs at ambient pressure (*a*) and at 7.5 GPa (*b*) and of the 10-mRs, as viewed down [100] in Ca-leonhardite (*c, d*) and Ca-hydrated laumontite (*e, f*) based on the structural refinements at ambient and high pressure (7.5 and 2.7 GPa for Ca-leonhardite and Ca-hydrated laumontite, respectively), (from Comboni et al. 2018)

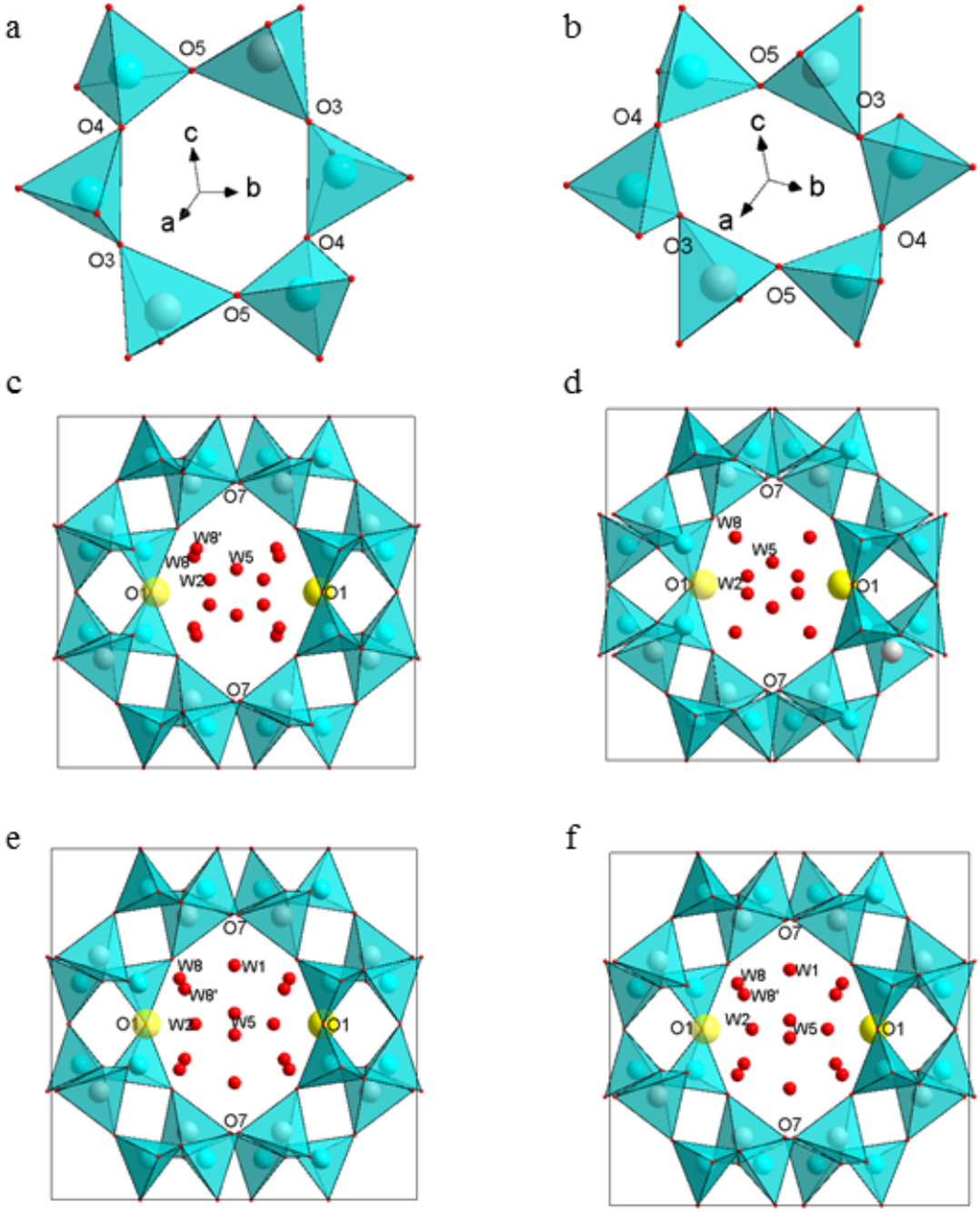

means of a synchrotron powder diffraction experiment using a diamond anvil cell with a 16:3:1 *m.e.w.* mixture as pressure transmitting fluid. These authors observed that the partially-hydrated Ca-laumontite with ~12 H_2O per formula unit used in their experiment (V_0 ~1356 $Å^3$ at room pressure), underwent a full hydration already at 0.2 GPa. In that experiment, an order–disorder transition of the hydrogen- bonded H_2O molecules, followed by a tripling of the *b* axis above 3 GPa, was observed. The latter phenomenon has been interpreted as a result of a different ordering of either the H_2O molecules or the Ca cations in the channels along the *b*-axis. Such a phase transition, occurring above 3 GPa, could be related to the predicted transition theorized by White et al. (2004). More recently, the hydration of a partially hydrated (Na,K)-rich laumontite has been investigated either at room pressure (at different RH rates) and at high pressure using pure water as pressure-transmitting medium (Rashcenko et al. 2012a, b). Rashcenko et al. (2012a) observed that (Na,K)-rich laumontite hydrates continuously if exposed to increasing RH rates, in contrast to Ca-laumontite, in which the hydration or dehydration of the W1 site induces an abrupt increase or decrease of the unit-cell volume (Fridriksson et al. 2003, Yamazaki et al. 1991). Rashcenko et al. (2012b) investigated the high-pressure behavior of the same (Na,K)-rich laumontite observing a continuous hydration up to 0.75 GPa.

Comparing their results with the data of Lee et al. (2004b), Rashchenko et al. (2012b) suggested that Ca-laumontite becomes fully hydrated only between 0.3 GPa and 0.6 GPa. This is partially in contrast with the findings of the previous studies (*e.g.,* Yamazaki et al. 1991, Fridriksson et al. 2003) in which an almost instantaneous response to the increase/decrease of T/P_{H2O} was found. However, a possible explanation could be the low H_2O activity of the used pressure-transmitting medium, as in a 16:3:1 *m.e.w.* mixture the amount of H_2O is only 5 vol.%. As an example, Likhacheva et al. (2007), in an high-pressure study on thomsonite, reported an expansion of the structure in response to selective sorption of additional H_2O molecules (with ΔV = 4.5 % at 2.0 GPa) only if the fraction of H_2O in the *P*-fluid was > 25 vol.%. This could also be the case of laumontite.

To the best of our knowledge, no single crystal study has been performed on Ca-laumontite at high-pressure conditions. In addition, the elastic behavior and the *P*-induced structure evolution of leonhardite is still unknown, despite thermodynamic calculations, as well as experimental and geological observations, suggest that it should be the stable form of laumontite at diagenetic and low-grade metamorphic conditions (*e.g.,* Neuhoff and Bird 2001, Coombs et al. 1959, Cho et al.1987). For these reasons, we have studied, by means of *in-situ* single-crystal synchrotron X-ray diffraction using a diamond anvil cell (DAC), the:

1) elastic compressional behavior,
2) the structural re-arrangement occurring at the atomic scale and

3) the crystal-H_2O interactions induced by pressure on natural samples of Ca-laumontite and leonhardite.

A comparative description of the high-*P* behavior of Ca-laumontite and Ca-leonhardite is provided. In addition, in order to better constrain our knowledge of the hydration process in laumontite, the kinetics of molecules sorption by single crystals of leonhardite immersed in water-based mixtures at ambient (*P,T*)-conditions has been investigated by means of single crystal X-ray diffraction.

4.2. Experimental methods

4.2.1 Chemical analysis

Crystals of leonhardite from a natural rock sample from Nashik (India), were selected for the experiments of this study. Preliminary single-crystal X-ray diffraction data collections were performed using a KUMA-KM4 four-circle diffractometer, equipped with a point-detector and MoKα radiation, at the Earth Sciences Department of the University of Milano (ESD-MI). All the selected crystals had similar size and shape (prismatic, ~400 × 200 × 200 μm^3) and were found to be free of twinning and optical defects. The chemical compositions of the selected crystals have been determined by electron-microprobe analysis in wavelength dispersive mode (EPMA-WDS), using a Jeol JXA-8200 microprobe at the ESD-MI (Fig. 4.2). The system was operated with an accelerating voltage of 15 kV, a beam current of 5 nA, a counting time of 30 s on the peaks and 10 s on the backgrounds and a beam diameter of 10 μm. Natural mineral samples (grossular for Si, Al and Ca; K-feldspar for K and omphacite for Na) were used as standards. The raw data were corrected for matrix effects using the φρZ method as implemented in the JEOL suite of programs. Overall, the selected crystals were found chemically homogeneous; only minor differences were found in the amount of Na and K, which were anyway negligible. The samples were always significantly enriched in Ca and the average chemical formula (based on 10 crystal fragments and 100 point analyses), calculated on the basis of 48 oxygen atoms, is:

$$[Na_{0.04}K_{0.04}Ca_{3.80}]_{\Sigma 3.88}[Al_{7.95}Si_{16.11}]_{\Sigma 24.06}O_{48} \cdot 13.85H_2O \quad (4.2)$$

In order to perform the high-pressure experiment on a fully hydrated laumontite, and based on the results obtained at ambient pressure (see section 4.2.2, *Hydration of leonhardite at ambient (P,T) conditions* and 4.4.1, *Hydration of leonhardite at ambient conditions*), a few crystals have been immersed in pure H_2O for six months.

Fig. 4.2. The Electron microprobe at the Sciences Department of the University of Milano (ESD-MI).

4.2.2 Hydration of leonhardite at ambient (*P,T*) conditions

Single crystals with prismatic habit were selected to investigate the hydration process of leonhardite by means of *in-situ* single-crystal X-ray diffraction. The crystals were stuck (with epoxy resin) on a glass fiber, located in a 5 mm (in diameter) glass vial (Fig. 4.3). All the samples so prepared were mounted on a goniometer head for X-ray diffraction data collections (firstly) in air, performed with an Xcalibur Oxford Diffraction diffractometer equipped with a CCD detector, graphite-monochromatized Mo-*K*α radiation, and operating at 50 kV and 30 mA at the ESD-MI (see section 2.2.1. *Conventional and unconventional X-ray devices*, Fig. 2.1). A combination of ω and φ scans, in order to maximize the reciprocal space coverage, with a step size of 1° and an exposure time of 25 s per frame, was adopted. Data reductions, including Lorenz-polarization and absorption correction based on the implemented semi-empirical

ABSPACK routine, were performed using the software CrysAlis (Agilent Technologies 2011). After the measurement in air, aimed to obtain the initial cell parameters, the vials were flooded with a H_2O-ethanol

Fig. 4.3. A leonhardite (partially dehydrated laumontite) crystal stuck with epoxy resin on a glass capillary and in a glass vial (from Comboni et al. 2018).

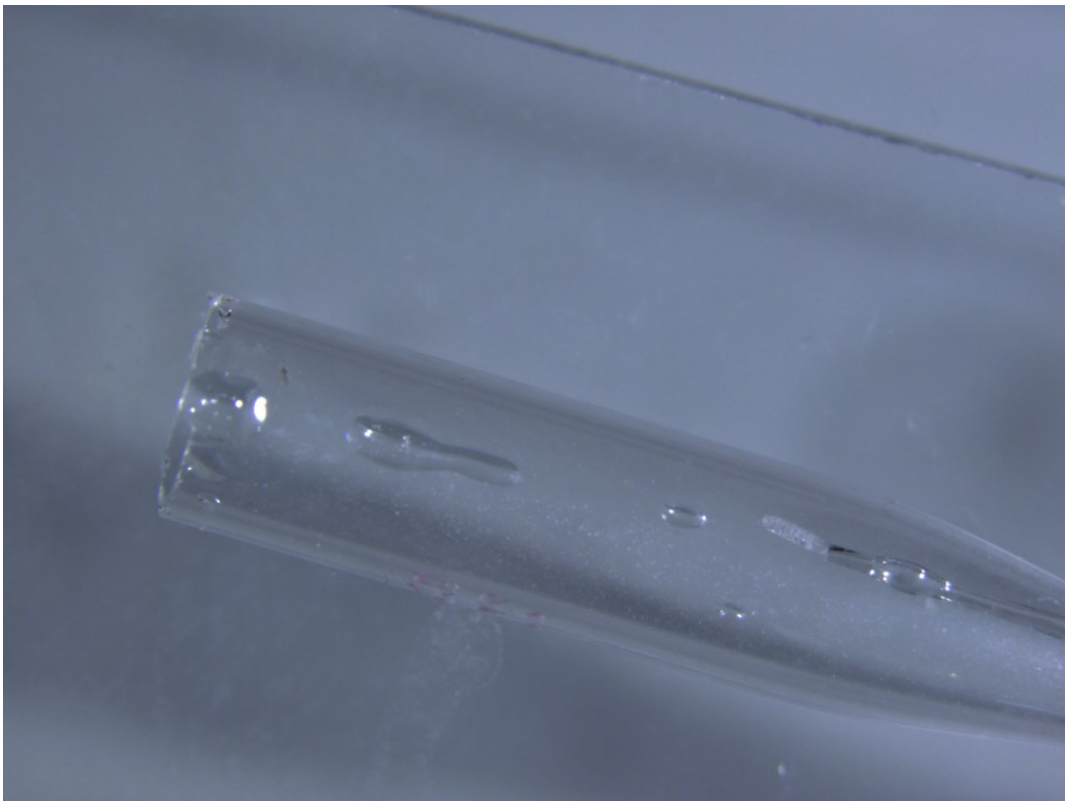

mixture containing 100%, 15%, 10% and 5% of H_2O, the samples being named Wat100, Wat15, Wat10 and Wat5, respectively. The open side of each vial was carefully closed with a plastic cap stuck with epoxy resin, in order to avoid a change in the H_2O-ethanol ratio, due to different vapour pressures of ethanol and H_2O. In order to primary investigate the role of the fraction of H_2O in the fluid, in which leonhardite is immersed during the hydration process, the selected samples were chosen with similar size and habit, to minimize the effects induced by shape, surface/volume ratio, *etc*. Consecutive short data collections were performed for the samples Wat100 and Wat5 adopting the following strategy: a 180° φ scan, with a step size of 1.5° and an exposure time of 20 s per frame. Such a data collection required only 120 min. In this way, it was possible to study the evolution of the unit-cell parameters as a function of the hydration process. On the other hand, for the samples Wat15 and Wat10, longer data collections (similar to those with the crystal in air) were performed, in order to obtain sufficient intensity data to perform structure refinements.

4.2.3 High-pressure ramps

In order to perform high-pressure experiments on laumontite and leonhardite, a few single crystals with a prismatic habit (~60×25×25 μm^3 in size) were selected on the basis of their optical quality. Some of the crystals were immersed in pure H_2O for *ca*. 6 months in order to fully hydrate to laumontite LAU·18H_2O (see Chapter 4.4, *Results*). The high-pressure diffraction experiments were performed at the ID15B beamline of the European Synchrotron Radiation Facility (ESRF) in Grenoble, France. A parallel monochromatic beam (E = 30.16 KeV, $\lambda \sim 0.411$ Å) was used.

In the case of leonhardite, the first data collection was performed with the crystal in the DAC without the *P*-transmitting fluid. In the case of hydrated laumontite, this was not possible as the data collections performed in air showed that the dehydration process starts as soon as the sample is exposed to the atmosphere (or even if the crystals are submerged into a mixture with a low content of H_2O), in fair agreement with the observations of Fridriksson et al. (2003). On this basis, a single crystal was selected from the batch immersed in pure H_2O, and immediately placed in a DAC along with a 1:1:2 methanol:ethanol:H_2O mixture. Pressure was increased only after the data collections and refinements (performed with the same protocol described in the section 4.3, *Structure refinement protocol*) revealed that the unit-cell volume was compatible with the one of fully hydrated laumontite (LAU·18H_2O)(coherently with Fridriksson et al. 2003 and Yamazaki et al. 1991). Due to the high H_2O content, the experiment with 1:1:2 methanol:ethanol:H_2O mixture was performed up to 2.7 GPa, in order to prevent the crystallization of ice, and five data collections were performed during the decompression. In the case of leonhardite, a nominally anhydrous methanol:ethanol mixture (4:1), which is hydrostatic up to 9.8 GPa (Angel et al. 2007), was used as *P*-transmitting fluid. In both the experiments, membrane-driven diamond anvil cells, mounting Boehler-Almax designed diamonds (culet diameter 600 μm), were used. A 250-μm-thick foil of stainless steel, which served as a gasket, was pre-indented to ~70 μm and then drilled using a spark-erosion device, leading to a *P*-chamber ~200 μm in diameter. The ruby fluorescence method was used for pressure calibration (Mao et al. 1986; pressure uncertainty ±0.05 GPa). A stepwise ω-rotation in the range ±32°, with 1° step width and 1s exposure time per step, was adopted for the data collection strategy at high pressure; the diffraction patterns were collected by a MAR555 flat-panel detector, at a 287.43 mm distance from the sample position. Further details on the beamline experimental setup are reported in Merlini and Hanfland (2013). Indexing of the diffraction patterns, unit-cell parameters refinement and integration of the intensity data were performed using the CrysAlis package (Agilent Technologies 2011). Corrections for absorption (due to the DAC components) and background were applied by the semiempirical ABSPACK routine implemented in CrysAlis (Agilent Technologies 2011).

4.3. Structure refinement protocol

All the structure refinements (pertaining to the hydration experiments at ambient conditions and to the high-*P* experiments) were performed using the software JANA2006 (Petříček et al. 2014) in the space group *C*2/*m*, as suggested by the diffraction patterns and by the reflection conditions. The fractional coordinates of the framework sites were obtained using the SUPERFLIP program (Palatinus et al. 2007), and found to be compatible with those previously reported (*e.g.*, Fridriksson et al. 2003, Lee et al. 2004). The positions of the extra-framework sites were obtained by a careful analysis of the difference-Fourier maps of the electron density. In the structure refinement based on the data collected in air, one Ca site along with four independent sites assigned to the H_2O-oxygen atoms were identified and named W2, W5, W8 and W8', respectively. This is reasonable considering the high Ca/ (Na+K) ratio obtained by the chemical microprobe analysis. As the Al:Si = 1:2 ratio, the tetrahedral sites Si1 and Si2 were modelled as fully occupied by Si, whereas Al1 by Al. This notation is consistent with that of Lee et al. (2004b) and Fridriksson et al. (2003), with the difference that W8, in the present study, is modelled as two mutually exclusive sites, namely W8 and W8'. Notably, Fridriksson et al. (2003) reported that refining W8 with anisotropic displacement parameters yielded to a significant improvement of the refined model and suggested that W8 could have been refined as 2 partially occupied sites. This is also consistent with the structure refinements reported by Armbruster and Kohler (1992) and Artioli et al. (1989). In order to reduce the number of the refined variables, the displacement parameters (D.P.) were restrained as isotropic, the H_2O-oxygen sites were restrained to share the same D.P. value, except for the structure refinement of leonhardite based on the X-ray data collected with the crystal in the DAC without *P*-medium, where two D.P.'s were refined (one for W8-W8' and one for W5-W2, respectively). In addition, due to mutual exclusiveness, the sum of the W8 and W8' occupancies was kept ≤ 1. The refined unit-cell parameters pertaining to the experiments at high pressure are listed in Tables 4.1 and 4.2. The unit-cell parameters of the H_2O-adsorption experiments performed at ambient conditions are listed in Table 4.3 and shown in Fig. 4.4, whereas relevant bond distances pertaining to the H_2O sites are reported in Tables 4.4 and 4.5. Further relevant structural parameters pertaining to leonhardite and hydrated laumontite are listed in Table 4.6. The principal statistical parameters of the structure refinements are listed in Table 4.7; atomic coordinates and site occupancies of selected structure refinements are given in Table 4.8.

Fig. 4.4. Evolution of the normalized unit-cell volume of leonhardite *vs.* time of immersion (Wat5 in black squares, Wat10 in blue triangles, Wat15 in green triangles and Wat100 in red circles) (from Comboni et al. 2018).

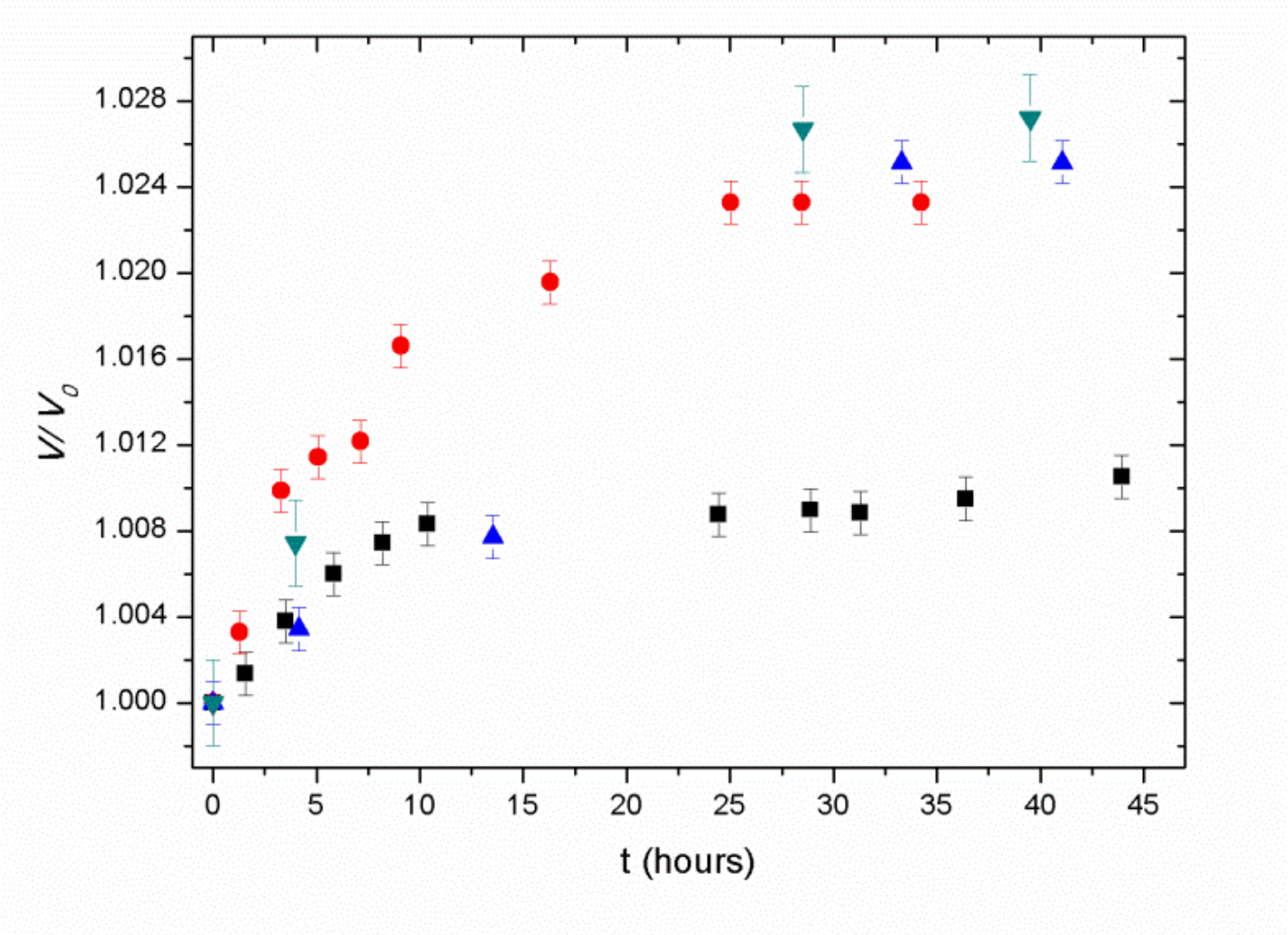

4.4. Results

4.4.1 Hydration of leonhardite at ambient conditions

The evolution of the unit-cell parameters as a function of H_2O fraction of the mixture and time (Fig. 4.4; Table 4.3) suggests that the adsorption rate of H_2O into the structural voids of laumontite is enhanced by increasing its concentration in the fluid interacting with the sample, in fair agreement with the observations reported in previous studies (*e.g.,* Fridriksson et al. 2003, Yamazaki et al. 1991). A *s.o.f* value ~ 0.85 of the W1 H_2O site was observed after ~ 40 hours of immersion in every mixture with at least 10% of water in the mixture. In order to perform the high-pressure ramp on a fully hydrated laumontite, a few crystals were selected after preliminary XRD analysis (same protocol described in the section 4.2.2, *Hydration of leonhardite at ambient (P,T) conditions*) and immersed in pure H_2O for six months.

4.4.2 High-pressure behavior of leonhardite and fully hydrated Ca-laumontite

The *P*-induced evolution of the unit-cell parameters of both leonhardite and fully-hydrated laumontite, shown in Figs. 4.5 and 4. 6, is monotonic, without any evidence of phase transition up to the highest pressure investigated. In both the cases, the unit cell edges *a* and *c* decrease over the entire *P*-range investigated, whereas the monoclinic β angle markedly increases. The *b* unit-cell edge of leonhardite, on the other hand, slightly increases between 2.38 GPa and 3.01 GPa, after which a significant stiffening along that direction occurs, leading to an almost uncompressible behavior (Fig. 4.6 and Table 4.1). This anomalous behavior was also observed for hydrated laumontite between 2.1 and 2.5 GPa. To describe the (isothermal) compressional behavior of leonhardite and hydrated-laumontite, the unit-cell volume *vs. P* data were fitted to a Birch-Murnaghan equation of state (BM-EoS) truncated to the third and to the second order, for leonhardite and hydrated laumontite, respectively. The experimental *V-P* data, weighted by their uncertainties, have been fitted to the BM EoS using the EoSFit 7.0 software (Angel et al. 2000, 2014), leading to the refined elastic parameters listed in Table 4.9. The refined *bulk modulus* at ambient conditions of the hydrated laumontite is K_{V0}=54.8(10) GPa, similar, but slightly lower, to that obtained for a powder sample by Lee et al. (2004b), who reported K_{V0} = 59(1) GPa, whereas the refined *bulk modulus* of leonhardite at ambient conditions was found to be K_{V0} = 36(1) GPa.

Both leonhardite and hydrated laumontite show a significant anisotropic compressibility with $K(c)_{P0,T0} < K(a)_{P0,T0} < K(b)_{P0,T0}$, even though in the case of leonhardite the anisotropy in particularly pronounced as $K(b)_{P0,T0}$ ~2.5 $K(a)_{P0,T0}$ ~ 5$K(c)_{P0,T0}$ whereas $K(b)_{P0,T0}$ ~1.3 $K(a)_{P0,T0}$ ~ 2$K(c)_{P0,T0}$ in the case of hydrated laumontite.

4.5. Discussion

4.5.1. Hydration of leonhardite at ambient conditions

The experiments on the hydration at ambient conditions of Ca-laumontite performed so far (*e.g.,* Fridriksson et al. 2003, Ståhl et al. 1996, Yamazaki et al 1991; Lee et al. 2004b) were based on the use of powder samples, which almost immediately increase or decrease their unit-cell volume in response to different RH rate or submersion in pure H_2O or hydrous mixtures. On the contrary, to the best of our knowledge, this is the first experiment that investigates the hydration of Ca-laumontite at ambient conditions by means of *in-situ* single-crystal XRD. The results reported in the section 4.4.1 (*Hydration of leonhardite at ambient conditions*) indicate that the adsorption of H_2O depends not only on the size of the crystals, or on the timescale of immersion, but also on the fraction of H_2O of the mixture, similarly to the results obtained with laumontite in air at varying the RH conditions (*e.g.,* Fridriksson et al. 2003, Yamazaki et al 1991). The hydration of leonhardite can take a few hours before affecting the unit-cell

Fig. 4.5. (*Top*) High-pressure evolution of the normalized (to P_0) unit-cell volume and axial parameters of leonhardite compressed in the 4:1 methanol:ethanol mixture. V/V_0 in *black squares*, a/a_0 *red circles*, b/b_0 *blue triangles*, c/c_0 *cyan triangle.* (B*ottom*) High-pressure evolution of the normalized (to P_0) β angle; black squares points taken during compression, red circle taken during decompression (from Comboni et al. 2018).

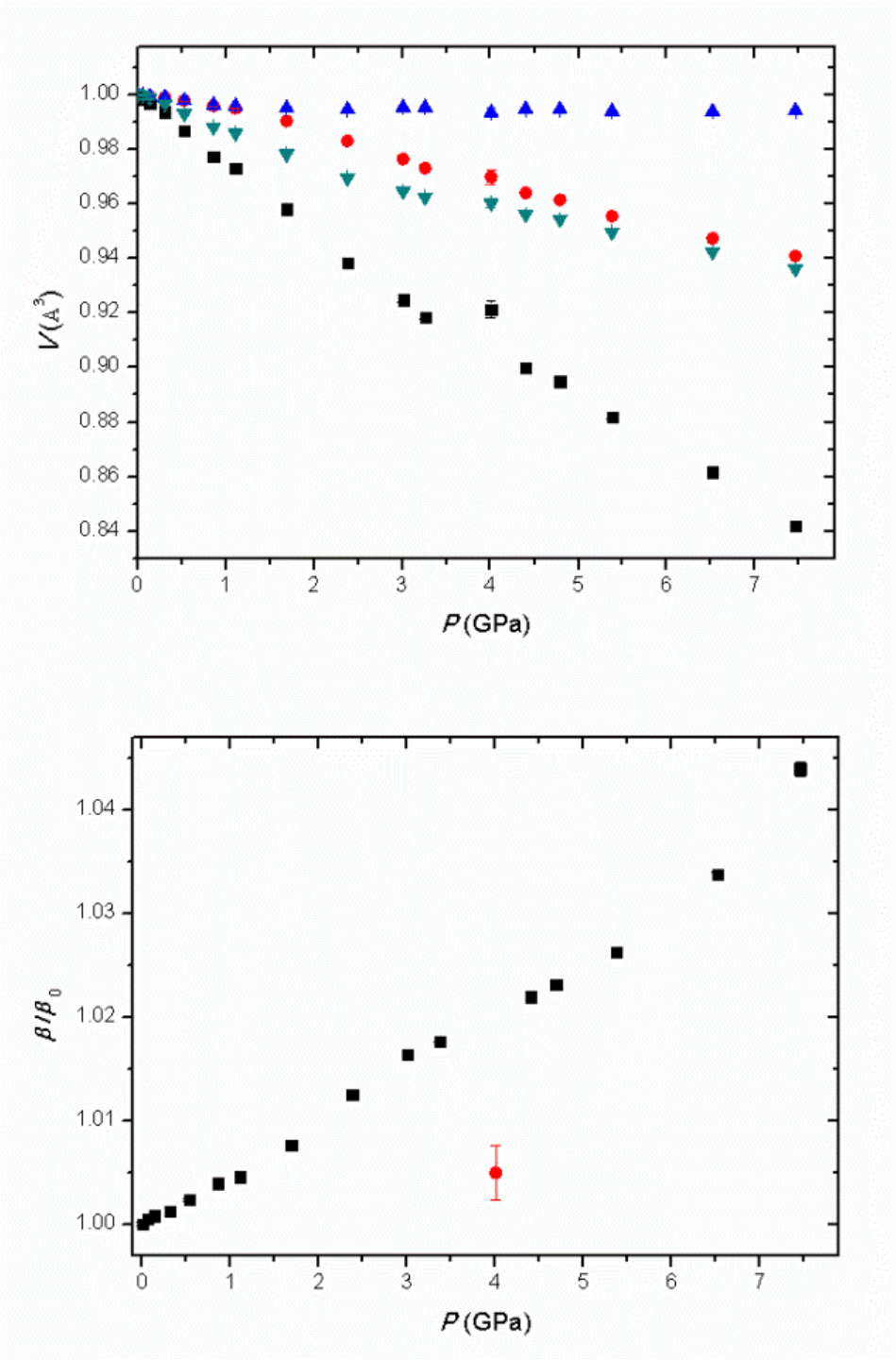

Fig. 4.6. (*Top*) High-pressure evolution of the normalized (to P_0) unit-cell volume and axial parameters of hydrated laumontite compressed in the 1:1:2 methanol-ethanol-H_2O mixture. V/V_0 in *black squares*, a/a_0 *red circles*, b/b_0 *blue triangles*, c/c_0 *cyan triangle.* (*Bottom*) High pressure evolution of the normalized (to P_0) β angle; black squares points taken during compression, red circle taken during decompression (from Comboni et al. 2018).

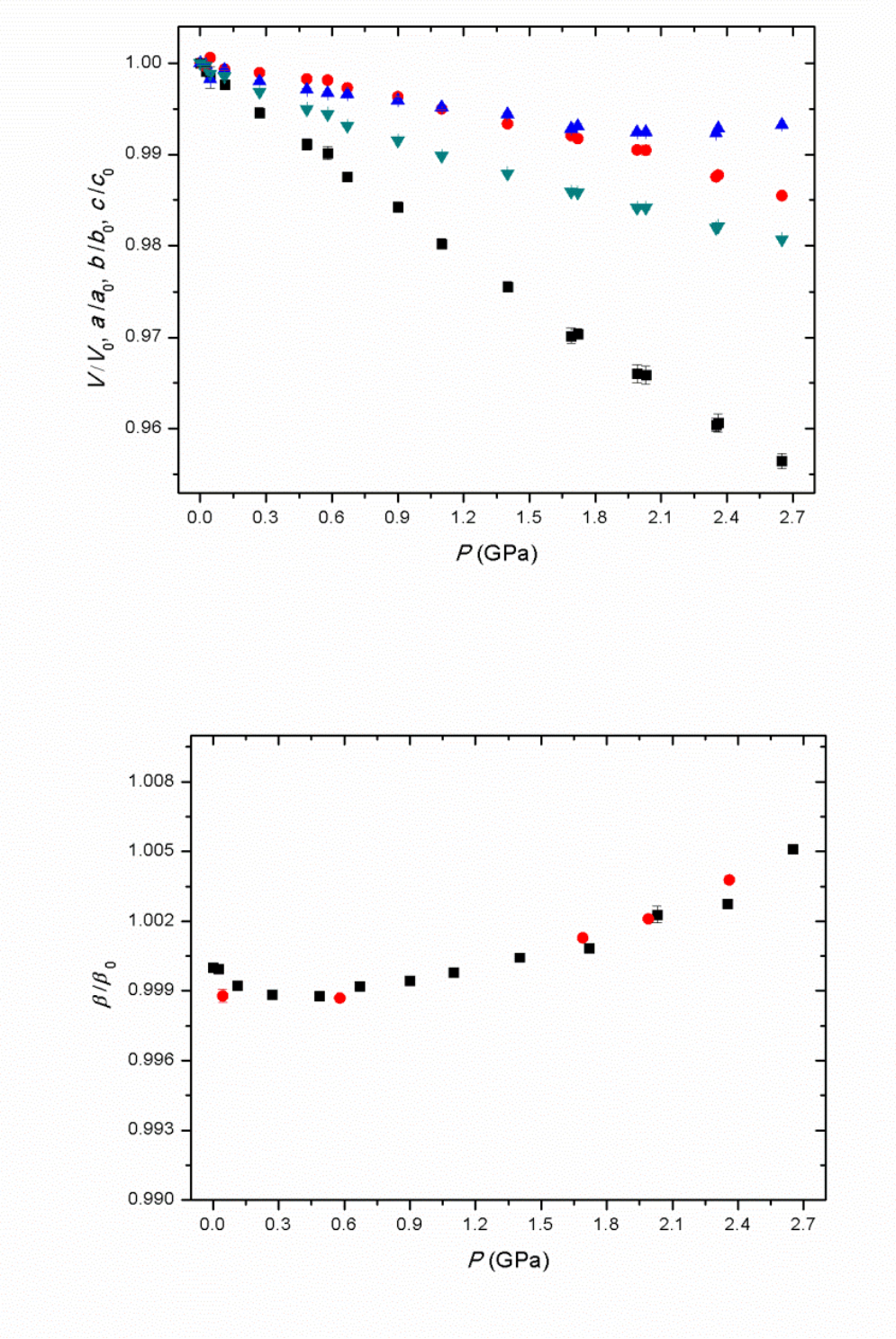

volume: for instance, the unit-cell volume of the sample Wat10 (*i.e.*, immersed in a 10% H_2O mixture) increases of only 5 $Å^3$ after 4 h. In addition, the results suggest that there is a critical fraction of H_2O under which the full occupancy of the H_2O-oxygen site W1 is not fulfilled (at least at the timescale of

the experiment). In fact, the sample Wat5, after a quick volume increase (identical within 3σ to that observed in the samples Wat10 and Wat15), does not complete the hydration process, with final unit-cell volume of 1364.3(4) $Å^3$ (Table 4.3). On the contrary, the unit-cell volumes of the samples Wat10 and Wat15 continuously increase up to 1385.7(4)$Å^3$ and 1384.1(3)$Å^3$, respectively (Table 4.3, Fig. 4.4).It is noteworthy to underline that the latters are consistent with the final unit-cell volume of the sample Wat100 (1383(1)$Å^3$), which was submerged in pure H_2O. As can be seen in Fig. 4.4, the higher the fraction of H_2O in the fluid interacting with the crystal, the quicker the hydration process. The structure refinements performed with the data collected from the sample Wat10 and Wat15, in which long data collections were performed for each point (see section 4.3, *Structure refinement protocol*), show that the volume variation is coupled with an increase of the W1 site occupancy, which is initially negligible. After 48 h, the occupancy of W1 site in the sample Wat10 (0.83(2)) and Wat15 (0.89(2)), reaches the saturation and, at the same conditions, the unit-cell volumes do not increase anymore (see Table 4.3 and Fig. 4.4).

After two days of immersion, the volume of the sample Wat100 (Tab. 4.3) is slightly lower than the volume of the Wat10 and Wat15 samples. This may be misleading. In order to settle this issue, a structure refinement of the sample Wat100 was done on the basis of a data collection performed after 40 hours of immersion in pure H_2O. Comparing the W1-*s.o.f* obtained for the samples Wat10, Wat15 and Wat100, the following trend was found: W1-$s.o.f_{(Wat15)}$ > W1-$s.o.f_{(Wat10)}$ ~ W1-$s.o.f_{(Wat100)}$ (Table 4.3). Moreover, if the W1-*s.o.f* values of the sample Wat10, Wat15 and Wat100 are plotted against the corresponding normalized unit-cell volumes, it can be seen that W1-$s.o.f_{(Wat100)}$ is in trend and that an almost perfect linear correlation occurs (Fig. 4.7).This means that the unit-cell volume is directly related to the W1-*s.o.f* : the higher is the *s.o.f* of this H_2O site, the higher is the unit-cell volume. The differences in the absolute unit-cell volume values of the samples could be very likely related to the different quality of the crystals, suggesting that the W1-occupancy is also influenced by other variables, such as the presence of structural defects hindering the molecules diffusion through the channels, the surface/volume ratio, *etc*…. In spite of any effort, these issues cannot be avoid unless using every time the same crystal for all the experiments.

During the hydration process, the *a* and *b* unit-cell edges increase whereas *c* decreases, although the hydration process mainly affects the *β* monoclinic angle (Table 4.3). It is interesting to note that, as the W1- occupancy increases, the H_2O-oxygen sites W2 and W5 move towards the mirror plane, reducing the W2-W2 and W5-W5 distances, respectively (Fig. 4.8). Based on the results at ambient pressure, several single crystals were submerged into pure H_2O and, after six months, the W1 site was found fully occupied within 1σ. A fragment of one of these crystals was then used for the high-*P* experiment on fully-hydrated laumontite.

4.5.2. High-pressure behavior of leonhardite and fully-hydrated Ca-laumontite

Due to its anhydrous nature and the high hydrostatic pressure limit (Angel et al. 2007), the methanol:ethanol 4:1 mixture has been adopted as *P*-transmitting fluid to investigate the high-pressure behavior of leonhardite. The higher compressibility shown by leonhardite (K_{V0}=36(1) GPa), with respect to the hydrated Ca-laumontite here studied (K_{V0} = 54.8(10) GPa) and that reported by Lee et al. (2004b) (K_{V0} = 59(1) GPa, based on the compression of a polycrystalline sample in the methanol: ethanol:H_2O 16:3:1 mixture), may be ascribed to the absence of the W1 H_2O-oxygen site, acting as a "filler" of the cavities, and to the partial occupancy of W2 in the crystal structure of leonhardite. Comparing the (slightly) different compressibility between the Ca-laumontite of this study and that reported by Lee et al. (2004b) is less trivial. However, we can note that:

1) contrary to the structure model reported by Lee et al. (2004b), the W5 H_2O-oxygen site of the Ca-laumontite of this study is only partially occupied (Table 4.8);
2) the larger surface/volume ratio of the powder sample used for the previous experiments may promote the *P*-induced intrusion of H_2O molecules, which is hindered in single crystals, as already observed in SiO_2-ferrierite and $AlPO_4$-5 zeolites (Lotti et al. 2015, 2016).

It is noteworthy that, compressing the sample in pure water, Rashchenko et al. (2012b) reported a higher compressibility (K_{V0} = 39(3) GPa) for the (Na, K) counterpart of laumontite. In both hydrated laumontite and leonhardite, a dramatic stiffening along the *b* crystallographic axis was detected at about 2.2–2.5 GPa, whereas no tripling of the same axis has been observed, in contrast to what reported by Lee et al. (2004b).

As common for open-framework materials (Gatta and Lee 2014; Gatta et al. 2018), the $(Si,Al)O_4$ tetrahedra behave as quasi-rigid units in response to pressure, and the bulk compression is mainly accommodated through the tilting of the TO_4 units around the shared oxygen hinges. This mechanism gives rise to a pronounced increase of the ellipticity of the 10-mRs with pressure. The ellipticity ratio ε, defined as the ratio between the shortest (O1-O1) and the longest (O7-O7) diameters of the ring (Fig. 4.1), is almost constant up to 2.38 GPa, whereas at higher pressures significantly decreases (Table 4.6), revealing that the bulk compression is initially accommodated isotropically by the 10-mRs channels and, in the higher pressure range, the deformation occurs mainly along the O1-O1 diameter parallel to the *a* crystallographic axis. Consistently, up to the highest pressure investigated of 2.65 GPa, no significant changes in the ε parameter of the 10-mRs of hydrated laumontite are observed, suggesting an isotropic compression of this channel (Table 4.6). One of the most relevant deformation mechanism induced by pressure consists in the distortion of the 6-mRs (Fig. 4.1). In leonhardite, this distortion is driven by a significant decrease of the O5-O5 diameter coupled with an increase of the O4-O4 one (Fig. 4.1, Fig. 4.9 and Table 4.6).The same distortion mechanism is observed also in the

fully hydrated laumontite, although less pronounced (Fig. 4.9 and Table 4.6). Overall, the higher H_2O content in laumontite induces an expansion of the unit-cell volume that is reflected in the tetrahedral framework. In leonhardite, as the absence of H_2O molecules acts as a sort of "chemical pressure", the ellipticity of the 10-mRs is higher and the pore diameters are shorter than in laumontite (Table 4.6).
The H_2O molecules act as fillers, partially counteracting the effect of pressure by leading, in hydrated laumontite, to a lower magnitude of the same deformation mechanisms observed in leonhardite, which is also reflected at the macroscopic scale by the different isothermal bulk moduli. The *P*-induced compression in leonhardite affects the extra-framework population mainly through the significant shortening of the W8-Ca, W8-O5, W8-O7, W2-Ca and W2-W5 interatomic distances (Table 4.5). On the contrary, it is worth to note that the W8'-O4 distance undergoes only a moderate contraction, whereas an expansion of the W8'-Ca distance is observed (Table 4.5). This is coupled with a reduction in the occupancy of the W8' H_2O-oxygen site at 1.69 GPa (Table 4.8), whereas at 2.38 GPa no peak could be detected in the difference-Fuorier synthesis of the electron density at the position formerly occupied by the W8' site. It is noteworthy that the disappearance of the W8' site is coupled with an increase in the occupancy of W8 (Table 4.8). A similar *P*-induced re-arrangement of the H_2O molecules, without any phase transition, was also observed in the natural zeolite phillipsite (see Chapter 5, *High-pressure behaviour of the zeolite phillipsite*). As pressure increases, a significant shortening in the W5-W2 interatomic distance is observed (Table 4.5). A different *P*-induced evolution of the extra-framework population has been observed in the hydrated laumontite, where a minor shortening (less than 1%) of the W8-O7, W2-Ca, W8'-Ca and W1-O7 interatomic distances occurs, along with a more pronounced compression of the W8-O5, W5-W2 and W1-W2 distances, which decrease by about 4%, 6% and 5%, respectively (see Table 4.5). It is worth to report that the W8' H_2O-oxygen site, in the crystal structure of fully hydrated laumontite, occupies a position slightly different with respect to that of leonhardite. Unfortunately, the low hydrostatic *P*-limit of the 1:1:2 methanol-ethanol-H_2O mixture, adopted as *P*-transmitting fluid for hydrated laumontite, prevented to investigate the behavior of this compound at higher pressures, where we cannot exclude that the merging of the W8' and W8 sites, similar site that observed in leonhardite, might occur.

4.6. Concluding remarks

The hydration process of Ca-leonhardite, a partially dehydrated form of Ca-laumontite, in aqueous solutions has been studied by *in-situ* single-crystal XRD. Overall, the results show that:

1) it is reasonable to assume that, in order to enhance a complete hydration process, a critical fraction of H_2O of the solution (between 5% and 10%) is required;

2) the higher the fraction of H_2O in the mixture, the quicker the hydration of the crystals;
3) additional factors (*e.g.,* quality of the crystals, density of crystalline defects, *S/V* ratio) concur to govern the hydration process.

The high-pressure behaviors of Ca-leonhardite and Ca-laumontite show that, despite a significant stiffening along the *b* axis at ~2.4 GPa, no phase transition occurs up to the highest pressure investigated. This is in contrast with the previous experimental findings of Lee et al. (2004b), and to what predicted by White et al. (2004). The lower compressibility of Ca-laumontite (β_{V0} = 0.0184(3) GPa^{-1}), with respect to Ca-leonhardite (β_{V0} = 0.0278(8) GPa^{-1}), highlights the "pillar effect" played by the extra-framework H_2O molecules, which counteract the *P*-induced framework deformation and, therefore, the bulk compression, similarly to what observed in $AlPO_4$-5 (Chapter 3, *High-pressure behavior and crystal-fluid interactions in $AlPO_4$-5*), even with a different (lower) magnitude. The hydration process here described underlines that laumontite behaves as an "open system" when immersed in an aqueous fluid, with a continuous uptake or release of structural H_2O molecules as a function of its relative abundance in the fluid (as well as of *T* and *P*). This observation bears a large relevance if we consider that laumontite can be a major component of oceanic sediments and basalts, where it forms as an alteration product of Ca-bearing aluminosilicate minerals at the conditions of burial diagenesis and low-grade metamorphism (Hay and Sheppard 2001, Utada 2001). Knowing how much H_2O is host in Ca-laumontite could be important in order to quantify the amount of water that is released when laumontite become unstable, as a consequence of the rising *P-T* conditions during the subduction of the oceanic crust. Modeling the stability of mineralogical assemblages by thermodynamic calculations can be largely biased by the choice of Ca-laumontite or Ca-leonhardite (Neuhoff and Bird 2001). The drastically different refined bulk compressibilities of the two forms (*i.e.,*Ca-laumontite and Ca-leonhardite), here reported, further confirm this conclusion. As the availability of consistent thermodynamic data has been the driving force for research into increasingly complex equilibria relating to natural rocks, the choice of suitable thermodynamic parameters is, therefore, fundamental for modeling the stability of these hydrous minerals, for example during the subduction process of the oceanic crust. Moreover, thermodynamic data as the K_{V0} are critical for predicting the occurrence of laumontite and leonhardite in geological environments of economic relevance, as oil reservoirs, where cementing laumontite degrades the potential of the country rocks for hosting hydrocarbons (Galloway et al. 1979, Surdam et al. 1979).

Figure 4.7 W1 *s.o.f vs.* V/V_0 pertaining the room pressure experiment; an almost perfect linear correlation links the volume increase to the W1 *s.o.f*, more details in the text. Sample Wat15 in black squares, Wat10 red circles, Wat100 in blue triangles.

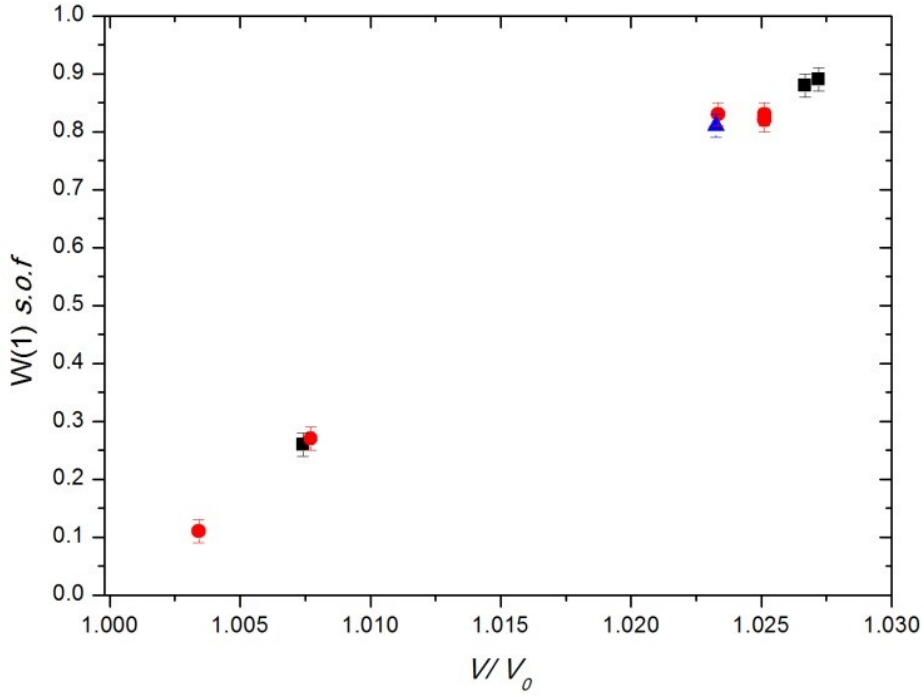

Fig. 4.8. W2 and W5 migration towards the mirror plane as a function of the W1 site occupancy. As W1 *s.o.f* increases, both W2 and W5 migrates towards the mirror plane (W2 in black squares, W5 in red circles) (from Comboni et al. 2018).

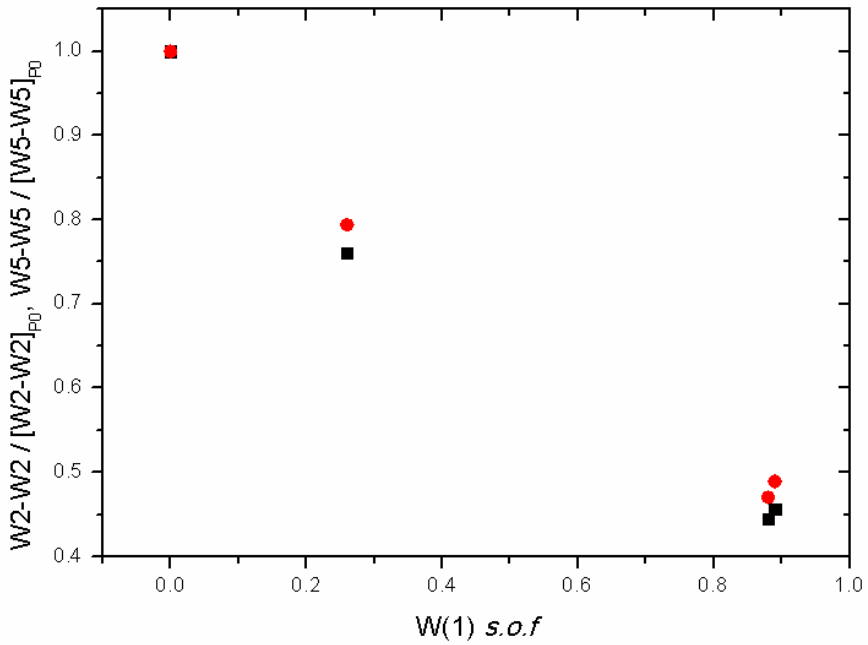

Fig. 4.9. Evolution of the normalized diameters (O5-O5 black squares, O4-O4 red circles, O3-O3 blue triangles) of the 6-mRs in leonhardite (*top*) and hydrated laumontite (*bottom*) (from Comboni et al. 2018).

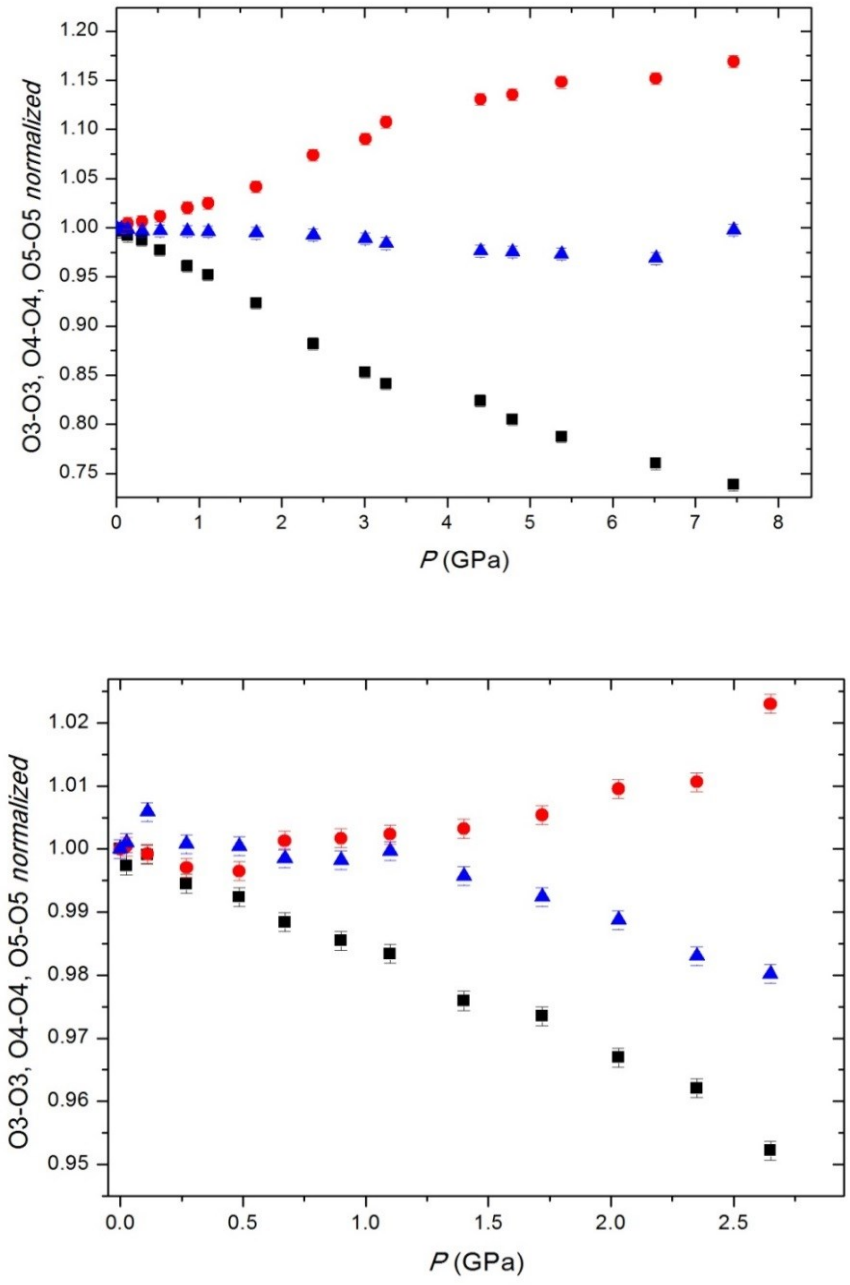

CHAPTER 5:
HIGH-PRESSURE BEHAVIOR OF THE ZEOLITE PHILLIPSITE

The experimental findings reported in the following pages have been published in the manuscript:
Comboni D., Gatta G.D., Lotti P., Merlini M., Liermann H.P. (2017) On the *P*-induced behavior of the zeolite phillipsite: an *in situ* single-crystal synchrotron X-ray diffraction study. PHYSICS AND CHEMISTRY OF MINERALS, 44, Pages: 1-20.

5.1. Introduction

Phillipsite is one of the most common natural zeolites with ideal composition $K_2(Na, Ca_{0.5})_3[Al_5Si_{11}O_{32}]\cdot 12H_2O$ (Passaglia and Sheppard 2001), commonly found in altered sediments in "closed" or "open" hydrologic systems, such as saline lakes, deep-sea sediments, hot spring deposits, as well as in vugs of basalt and in tuffs (Galli and Ghittoni 1972; Rinaldi et al. 1974; Gottardi and Galli 1985; Armbruster and Gunter 2001). Phillipsite is distributed in the low-silica and very low alkaline-earth region (Langella et al. 2001), as well as in alkali tephra deposits: several studies have shown that the trachytic glass in the lower part of the Neapolitan Yellow Tuff is altered to phillipsite and chabazite with minor analcime (*e.g.,* de' Gennaro et al. 1990, Passaglia et al. 1990). Phillipsite and chabazite are probably the most common zeolites in low-silica tuffs, but others low-silica zeolites such as natrolite, gonnardite and analcime, are commonly recognized (Sheppard and Hay 2001). In tephra deposits, the glass leaching produced a rise in pH, which leads to Na/K and Si/Al ratios in the solution favorable for phillipsite crystallization. Any glass-to-zeolite transformation is characterized by a silica loss, and this is valid either in open or closed systems. The only difference between open and close systems is that, in the former, the leached silica is removed from the system, whereas silica remains in solution in closed systems (Langella et al. 2001). The higher pHs, typical of closed systems, increase silica solubility and the resulting zeolites display lower Si/Al ratios, such as in phillipsite and chabazite. As the physico-chemical conditions of the system evolved, chabazite nucleation is favored, giving rise to chabazite overgrowths on phillipsite. These considerations were experimentally investigated by Wirsching (1976) and Höller and Wirsching (1980), who simulated open-system alteration in low-temperature hydrothermal experiments using, as starting material, rhyolitic glass and nephelinite, respectively. Phillipsite was found to be the first zeolite which formed from the glass (followed by mordenite, analcime and chabazite). Phillipsite formation requires a low silica activity, and this zeolite is concentrated in soil horizons (Langella et al. 2001). However, minor amount of authigenic phillipsite have been found associated

mainly with erionite and analcime, along with minor amounts of chabazite, clinoptilolite and mordenite. Phillipsite is monoclinic (space group *P*21/*m*, *a* ~9.865 Å, *b* ~14.300 Å, *c* ~8.693 Å, *β* ~124.92°), with framework density: 15.8 T/1000 $Å^3$ (Baerlocher et al. 2007). In nature, crystals are often found in spherical radiating aggregates, frequently twinned on [001], [021] and [110] (Rinaldi et al. 1974). Several examples of intergrowths with other zeolites (*e.g.,* faujasite, offretite, gismondine, garrionite and gobbinsite) are reported in the literature (Rinaldi et al. 1975, Passaglia and Sheppard 2001). Danisi et al. (2015) reported coherent twinned intergrowths of merlinoite and phillipsite in a sample originated from Monte Somma, Vesuvius (Italy). The framework of phillipsite (PHI topology, Baerlocher et al. 2007) is built up by four corner-shearing Si/Al tetrahedra, which form four- and eight- membered rings. The four-membered rings (hereafter 4-mRs) and the eight-membered rings (hereafter 8-mRs) are also referred as the secondary building units of PHI framework type (SBU, codes 4 and 8, respectively, Baerlocher et al. 2007). In PHI framework, the 4-mRs are connected to form double-crankshaft chains running parallel to [100]. The PHI framework contains two independent channel systems, running along [100] and [010] (hereafter: 8-mRs[100] and 8-mRs[010] channels, respectively) (Fig. 5.1). The two sets of channels intersect each other (Gatta and Lee 2007; Gatta et al. 2009a). The channel running along [100] is confined by two different 8-mRs, hereafter 8-mRs[100]-1 and 8-mRs[100]- 2. In the 8-mRs[100]-1, the distance O9–O8 < O7–O7, whereas, in the 8-mRs[100]-2, O9–O8 > O7–O7 (Fig. 5.1). The 4-mRs double-crankshaft chains form 8-mRs, here referred as 8-mRs(001) (Fig. 5.1). As pointed out by Rinaldi et al. (1974) and Gatta et al. (2009a, 2010, 2015), the Si/Al distribution between the tetrahedral sites is completely disordered in natural phillipsite. In phillipsite from Richmond, Victoria, Australia (*i.e.,* the same natural species used in this study), the extra-framework population (Fig. 5.1) is represented by two main cation sites in which Ca (or Na) and K lie. Viewing the structure perpendicular to (010), the Ca site lies above and below the mirror plane, where the two independent systems of channels intersect. As reported by Gatta et al. (2009a), the coordination shell of Ca site is complex, with a maximum distance of ~3 Å, and at least nine mutually excluding configurations are possible. The coordination number (CN) of the Ca sites is 6–7: three oxygen atoms of the tetrahedral framework (O4, O3, O7) and three or four H_2O molecules (among W1, W3, W4–W4′, W5, W6). The K site is actually split into two subsites, K1 and K2, only 0.5 Å apart. The two K sites lie close to the 8-mRs[100] channel wall. If a maximum bond length of 3.4 Å is considered, the CN of both sites is 9 (five oxygen atoms of the framework and four H_2O molecules) (Gatta et al. 2009a). As shown by Gatta et al. (2009a), the H_2O molecules are distributed over seven independent sites: Only W1 and W2 lie on the mirror plane, occupying the *Wyckoff* special position 2*e*; the others sites (*i.e.,* W3, W5, W6, W4, W4′ in Gatta et al. 2009a) occupy the general *Wyckoff* position 4*f*. W4 and W4′ are two subsites only 0.4 Å apart, and mutually exclusive. The sites W4, W4′, W5, W6 occupy central positions in the 8-mRs[010] channel, whereas the W3 site lies close to the

Figure 5.1. Configuration of the 8-mR[100]-1, 8mR[100]-2, 8-mR[010] and 8-mR(001) at *P*1 and of the extra-framework population in phillipsite, as viewed down [100], based on the structural refinements at 0.20 GPa (in Comboni et al 2017).

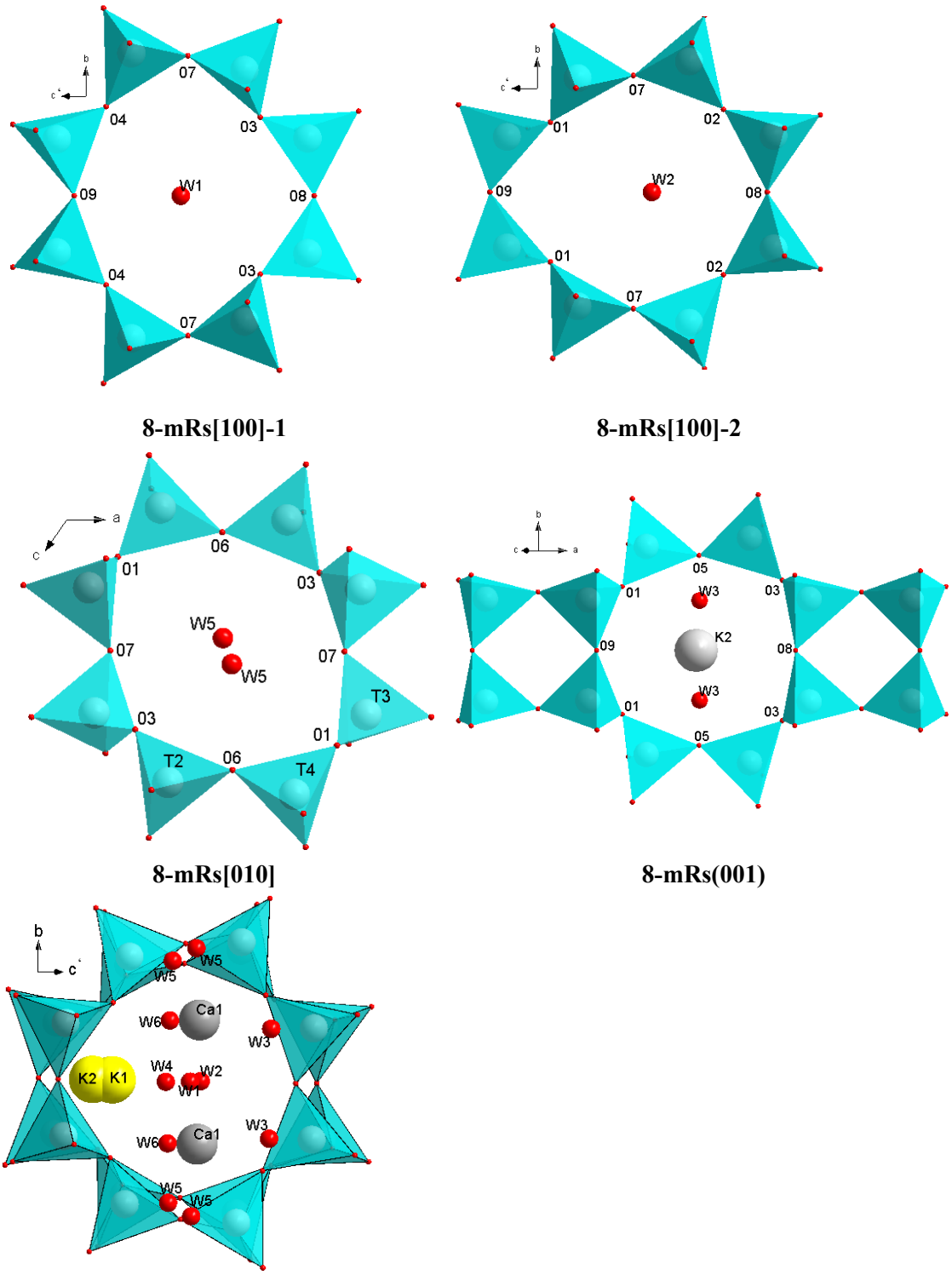

channel wall. Among them, W4, W4′ and W6 lie at the intersection of the two channels. The W1 and W2 sites lie approximately in the center of the 8-mRs[100] channel (Fig. 5.1).

The high-temperature behavior of natural and synthetic phillipsites has been the object of several investigations (*e.g.,* Steinfink 1962; Stuckenschmidt et al. 1990; Gualtieri et al.1999a, b, 2000; Passaglia et al. 2000; Sani et al. 2002). The thermal behavior and, in particular, the dehydration mechanisms are connected to the nature of the extra-framework population. Due to the lack of single crystals of phillipsite suitable for non-ambient conditions experiments, Gatta and Lee (2007) investigated the high-pressure behavior of a natural phillipsite powder from Richmond, Victoria, Australia, up to 3.64 GPa, by *in-situ* synchrotron X-ray powder diffraction with a diamond anvil cell, using the methanol:ethanol:water = 16:3:1 mix as *P*-transmitting fluid. Axial and volumetric bulk moduli were reported. No unambiguous evidence of phase transition was observed within the *P*-range investigated. Moreover, the quality of the high-*P* powder data, as well as the complex structure of phillipsite, prevented a fulfill discussion about the role played by the extra-framework population on the elastic behavior. Although the general aspects of the high-*P* behavior of the zeolite phillipsite were discussed by Gatta and Lee (2007), a comprehensive characterization of the mechanisms which involve framework and extra-framework population is still missing. In addition, the previous high-*P* study explored a modest *P*-range. In the framework of this thesis, phillipsite represents the second natural zeolite with channels already occupied (at room conditions) by both cations and H_2O molecules. In laumontite (see Chapter 4, *High-pressure behavior and crystal-fluid interactions in laumontite*) an intrusion of H_2O molecules was observed already submerging the sample in a water-ethanol mixture; unfortunately this was not the case of phillipsite. However, it cannot be exclude that pressure could enable and enhance the adsorption process. In light of this, the aim of this work is to reinvestigate the *P*-induced structural evolution of a natural phillipsite (using the same natural sample previously used by Gatta and Lee 2007) by *in-situ* single-crystal synchrotron X-ray diffraction, with a diamond anvil cell.

5.2. Experimental methods

The H*P*-synchrotron X-ray single-crystal diffraction experiments were conducted at the Extreme Conditions Beamline P02.2 at PETRA III/DESY, Hamburg, Germany. Data collections were performed with an incident beam of 42.7 keV in energy, and a focusing spot of ~8.5 (H) μm × 1.8 (V) μm originated from a compound refractive lenses system, consisting of 121 Be lenses with a radius of 50 μm (400 μm beam acceptance) and a focal length of 1221 mm. A single crystal of phillipsite (~50 × 50 × 20 μm), free of twinning under polarized light microscope and with lamellar morphology, was selected for the experiment. The crystal was loaded in a symmetric DAC equipped with Boehler–Almax design

diamonds/seats with a 70° opening and 300 μm culet size. A 250-μm-thick foil of stainless steel was used as gasket, which was pre-indented to ~60 μm and then drilled with a hole of ~200 μm in diameter, using a spark-erosion device. A few ruby spheres were added into the gasket hole for *P* measurement, by the ruby-fluorescence method (Mao et al. 1986; pressure uncertainty ±0.05 GPa). The mix of methanol:ethanol:water = 16:3:1 (hereafter *m.e.w.*) was used as hydrostatic *P*-transmitting fluid (Angel et al. 2007). This pressure medium is considered potentially "penetrating", as at least the molecules of H_2O (Ø ~ 2.65Å) and CH_3OH (Ø ~ 3.76 Å) may theoretically be incorporated into the 8-mRs[100] channels of phillipsite (diameter ~ 3.8 Å, Baerlocher et al. 2007). Pressure was increased (up to P_{max} = 9.4 GPa, Table 5.1) with an automated pressure-driven system from Sanchez Technology (Viarmes, France) and measured with the online ruby/alignment system powered by a 100 mW 458-nm laser. Diffraction images were collected with a PerkinElmer XRD 1621 flat-panel detector, using an in-house script for collecting step-scan diffraction images. The sample-to-detector distance (402.34 mm) was calibrated using a CeO_2 standard (NIST 674a). A few data collections were performed in decompression (Table 5.1). The diffraction images were then converted to conform to the "Esperanto" format of the program CrysAlis (Agilent 2012; Rothkirch et al. 2013). At all pressure points, the adopted data collection strategy consisted in a pure ω-scan ($-28° \leq \omega \leq +28°$), with a step size of 1° and an exposure time of 1 s/frame; then, Bragg peaks were indexed. Intensities of the diffraction peaks were integrated and corrected for Lorentz-polarization effects, using the CrysAlis package (Agilent 2012). Corrections for adsorption (due to the DAC components) were applied by the semiempirical *ABSPACK* routine implemented in CrysAlis. The refined unit-cell parameters are listed in Table 5.1.

5.3. Structure refinement protocol

All the structure refinements, at different pressures, were performed using the suite of softwares JANA2006 (Petříček et al. 2014) in the space group $P2_1/m$, as suggested by the reflection conditions. Reflections were "observed" down to an inter-planar distance *d* ~0.8 Å. At $P \geq 2.57$ GPa, an abrupt decrease in the number of observed reflections, with a consequent increase in the R_1 factor, was observed (Table 5.2). The isotropic structure refinements were possible up to 4.85 GPa (*P*11). For the first refinement (*P*1, 0.2 GPa), the input fractional coordinates of the framework sites were taken from Gatta et al. (2009a). The positions of the extra-framework sites were obtained by a careful analysis of the difference-Fourier maps of the electron density. At *P*1, one Ca site and two mutually independent K sites were identified, along with six independent sites assigned to the H_2O molecules, according to the structure model of Gatta et al. (2009a); the same sites' labeling scheme was used (*i.e.,* Ca, K1, K2 and W1-6, Table 5.3). Briefly, W1 and W2 sites lie in the center of 8-mRs[100]-1 and 8-mRs[100]-2,

respectively, whereas W3 and W5 occupy the 8-mRs[010] channel; the W4 and W6 sites lie at the intersection of the two channel systems. As the analysis of the difference-Fourier maps revealed only one strong peak lying on the mirror plane between the position of the sites W4–W4′ in Gatta et al. (2009a), in the structure model of this study, we refined only one site (labeled as W4, Table 5.3). No specific restraints were applied to the Ca site, whereas the K1–K2 sites were refined with the same displacing parameter (DP). The same restriction was applied to all the H_2O sites. This protocol was used in all the refinements at different pressures, with the following exceptions:

- The DPs of the H_2O sites were forced to have an U_{iso} value fixed to 0.075 $Å^2$. This value is arbitrary, although very reasonable: The refined U_{iso} of H_2O sites at $P1$ was ~0.079(4) $Å^2$ (Table 5.3).
- The occupancy of the Ca site was fixed to the one obtained from the refinement of $P1$. The sum of the K1 and K2 site occupancies, in all the refinements at $P > P1$, was forced to assume the value found at $P1$.
- The R_1 factors were all ≤10 % up to 2.56 GPa ($P8$). At $P > P8$, the R_1 values increased significantly; the last refinement which reached convergence is that at 4.85 GPa ($P11$). At $P > P8$, the occupancy of the H_2O sites showed an anomalous increase. As the adsorption of H_2O molecule at this pressure is not realistic (*i.e.,* all the previous experimental findings available in the literature reported *P*-induced over-hydration effects at $P < 1$ GPa, Gatta and Lee 2014, for a review), we introduced a further restraint: The *sum* of the H_2O site occupancies was fixed to the value obtained by the refinement at $P8$ (*i.e.,* 14.36 ± 1.16 molecules per formula unit, m.p.f.u.). The sum at $P8$ is equal, within 1σ, to that obtained at $P1$ (*i.e.,* 14.00 ± 0.84 m.p.f.u.).

For all the structure refinements, Table 5.2 lists the principal statistical parameters. Site coordinates and occupancies are given in Table 5.3. Refined bond distances are reported in Tables 5.4 and 5.5. Other relevant structural parameters are reported in Tables 5.6, 5.7, 5.8, and 5.9.

5.4. Results

5.4.1 High-pressure elastic behavior

The unit-cell parameters at eighteen *P*-points up to 9.44(5) GPa, and three points in decompression, are reported in Table 5.1. The *P*-induced evolution of the unit-cell parameters is shown in Fig. 5.2. The evolution of the unit-cell parameters shows at least two different compressional regimes. From $P1$ to $P6$ (1.82 GPa), phillipsite is stiffer than in the second regime [*i.e.,* from $P9$ (3.13 GPa) to $P19$ (9.44 GPa)]. Up to $P8$ (2.56 GPa), the value of the β angle decreases, whereas at $P \geq P9$, there is a clear inversion of the trend (Fig. 5.2). The evolution of the β angle is diagnostic for the change in the compressional

Figure 5.2. High-pressure evolution of the normalized (to *P*1) unit-cell volume and axial parameters of phillipsite compressed in *m.e.w.* V/V_0 in black squares, a/a_0 red circles, b/b_0 blue triangles, c/c_0 cyan triangles (in Comboni et al 2017).

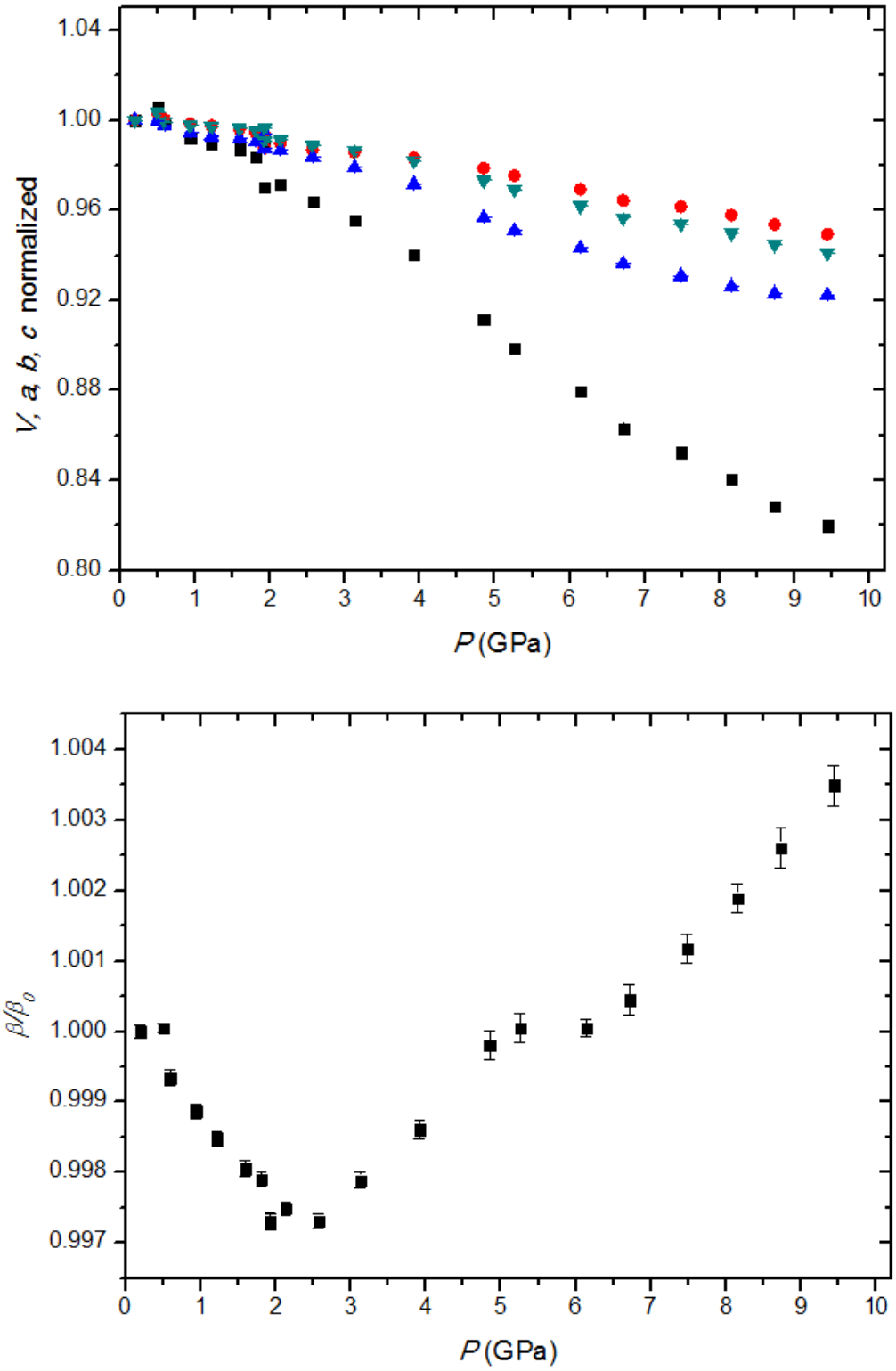

regimes. For the two regimes, a Birch–Murnaghan equation of state truncated to the second order was fitted to the experimental *P–V* data using the *EoSFit 7.0* software (Angel et al. 2000, 2014). We did not consider the unit-cell parameters of *P*7 (2.14 GPa) and *P*8 in the calculation of the elastic parameters, considering the *P*-range between *P*7 and *P*8 as a transitional interval between the two regimes. The refined elastic parameters are reported in Table 10. Bulk moduli, K_{V0}, K_a, K_b, K_c of the first regime (hereafter named K_x 1), are significantly higher than the ones obtained for the second regime (hereafter named K_x 2), suggesting that, at low pressure, phillipsite is "stiffer." In the second regime, the linear bulk moduli decrease drastically and anisotropically (*e.g.,* K_a decreases by about 2.5 times, whereas K_b and K_c decrease by about 5 times). The reasons of such changes in the elastic behavior, at the atomic level, will be discussed in the next sessions.

5.4.2 Pressure-induced structural evolution: deformation of the Si/Al framework

The intra-tetrahedral T–O distances (reported in Table 5.4) do not show drastic changes within the *P*-range investigated. The most significant changes in the inter-tetrahedral angles are those observed for the T1–O7–T3, T2–O8–T2, T4–O6– T2 and T4–O1–T3 angles, reported in Table 5.11. Figure 5.3 shows the trends of these T–O–T angles (normalized to the value at *P*1). At *P*7, all trends change markedly. The inter-tetrahedral tilting gives rise to a pronounced increase in the ellipticity of all the 8-mRs. In order to explain the behavior of the 8-mRs, we introduce the ε parameter (*i.e.,* the ellipticity ratio) as the *b/a* ratio, where *b* is the minor and *a* the major axis of any given ring (*e.g.,* Gatta and Lee 2007; Gatta et al. 2009a). The ε ratio for the 8-mRs[100]-1 (hereafter $\varepsilon_{8\text{- mRs}[100]\text{-}1}$) is defined as O9–O8/O7–O7 (with O7–O7 > O9–O8); for the 8-mRs[100]-2, the ε ratio (hereafter $\varepsilon_{8\text{-mRs}[100]\text{-}2}$) is defined as O7–O7/O9–O8 (as O7–O7 < O9–O8). For the 8-mRs[010] and the 8-mRs(001) (hereafter $\varepsilon_{8\text{-mRs}[010]}$ and $\varepsilon_{8\text{-mRs}(001)}$), the ε ratios are defined as O3–O3/O1–O1 and O9–O8/O5–O5, respectively. The trend of all the ε values of the 8-mRs is shown in Fig. 5.4. Every ring tends to increase its ellipticity with the pressure increase, as previously observed in several others zeolites (*e.g.,* Gatta et al. 2005, 2009b; Lotti et al. 2016). Contrarily to what was observed by Gatta and Lee (2007), the ε ratio of the 8-mRs[100]-2 is more pronounced than that of the 8mRs[100]-1. This feature is maintained at high-*P*, and, interestingly, the trends of $\varepsilon_{8\text{-mRs}[100]\text{-}1}$, $\varepsilon_{8\text{-mRs}[100]\text{-}2}$ and $\varepsilon_{8\text{-mRs}[010]}$ are practically parallel (Fig. 5.4). However, at a careful analysis from *P*7 to *P*11, $\varepsilon_{8\text{-mRs}[100]\text{-}2}$ decreases more pronouncedly than $\varepsilon_{8\text{-mRs}[100]\text{-}1}$ and $\varepsilon_{8\text{-mRs}[010]}$. In fact, in the considered *P*-range, the slope of $\varepsilon_{8\text{-mRs}[100]\text{-}2}$ is −0.059(2), whereas the slope of both $\varepsilon_{8\text{- mRs}[100]\text{-}1}$ and $\varepsilon_{8\text{-mRs}[010]}$ is −0.052(3): The 8-mRs[100]-2 is, therefore, more affected by the *P*-induced deformation than 8-mRs[100]-1 and 8-mRs[010]. If the normalized O3–O3 and O7–O7 diameters of the 8-mRs[010] are plotted versus *P*, the trend are almost parallel up to *P*7 (Fig. 5.5). At *P* > *P*7, the diameter O3–O3 begins to decrease abruptly,

Figure 5.2. High-pressure evolution of the normalized (to *P*1) unit-cell volume and axial parameters of phillipsite compressed in *m.e.w.* V/V_0 in black squares, a/a_0 red circles, b/b_0 blue triangles, c/c_0 cyan triangles (in Comboni et al 2017).

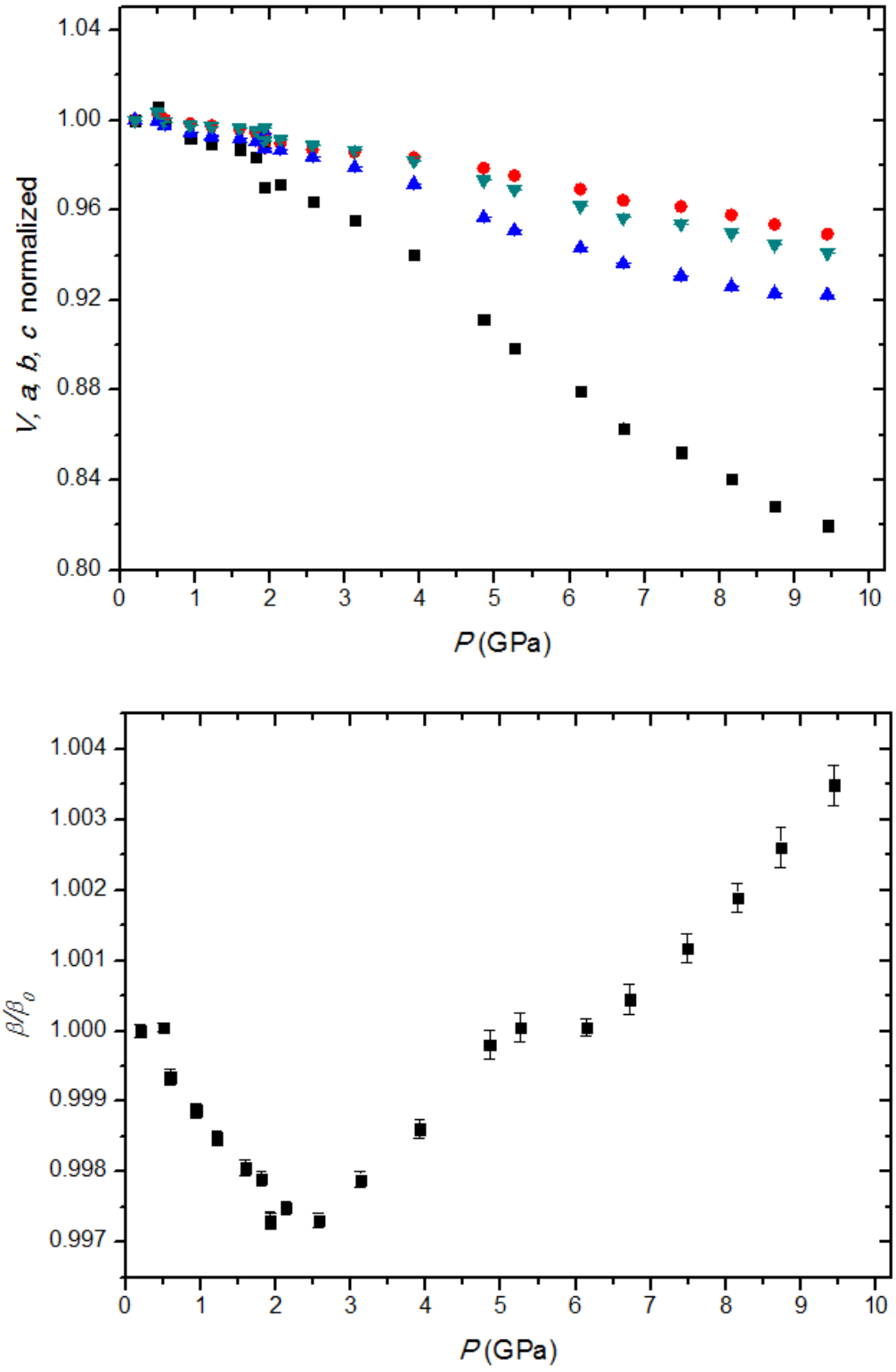

Figure 5.3. High-pressure evolution of some selected T-O-T angles (normalized to their P_0 values). T2-O8-T2 in black squares, T1-O7-T3 red circles; T4-O1-T3 in black squares, T4-O6-T2 red circles (in Comboni et al 2017).

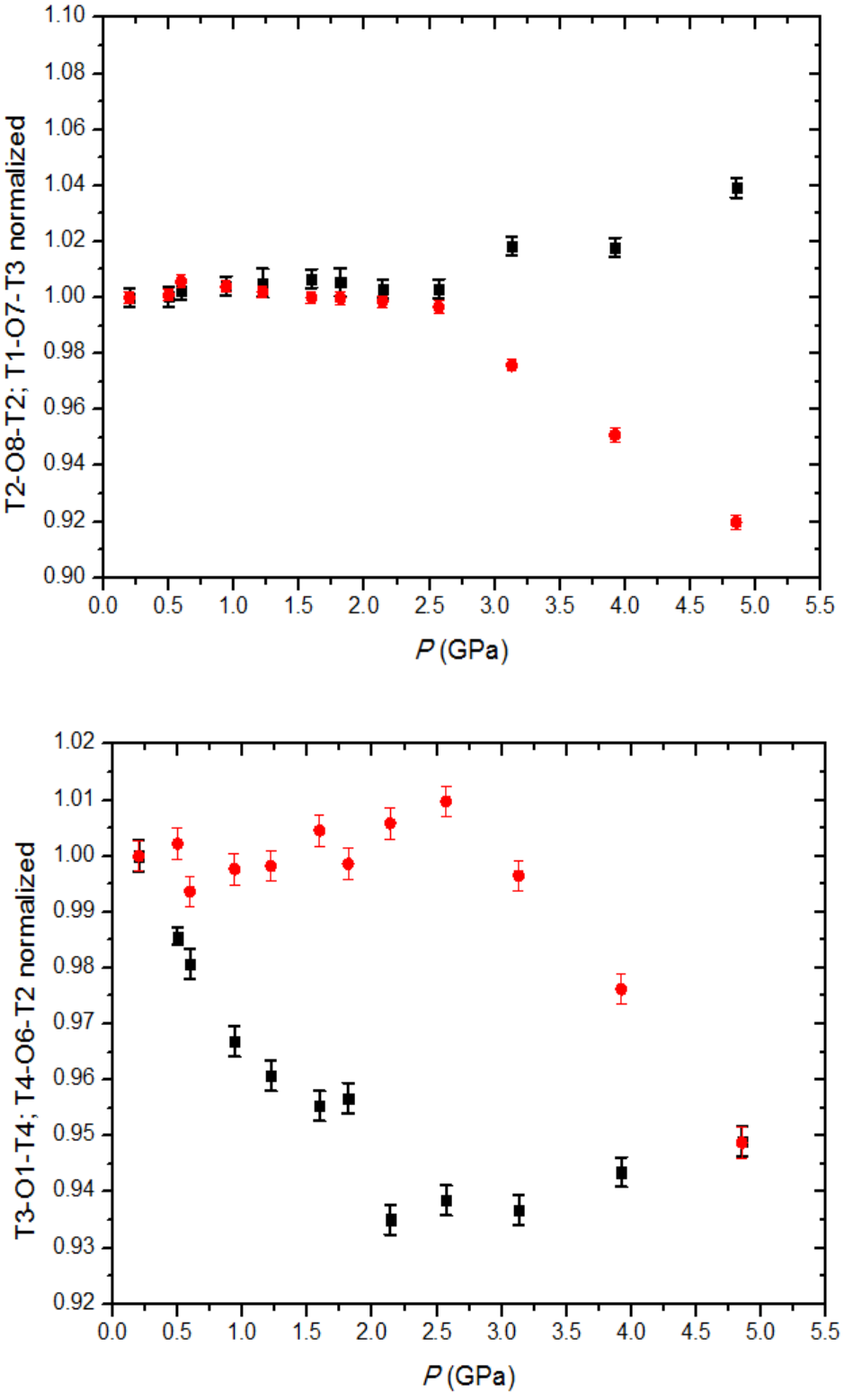

Figure 5.4. High-pressure evolution of the $\varepsilon_{8\text{-mRs}}$ parameters; $\varepsilon_{8\text{-mRs}}$[100]-1 in black squares, $\varepsilon_{8\text{-mRs}}$[100]-2 red circles, $\varepsilon_{8\text{-mRs}}$[010] blue triangle, and $\varepsilon_{8\text{-mRs}}$(001) cyan triangles (in Comboni et al 2017).

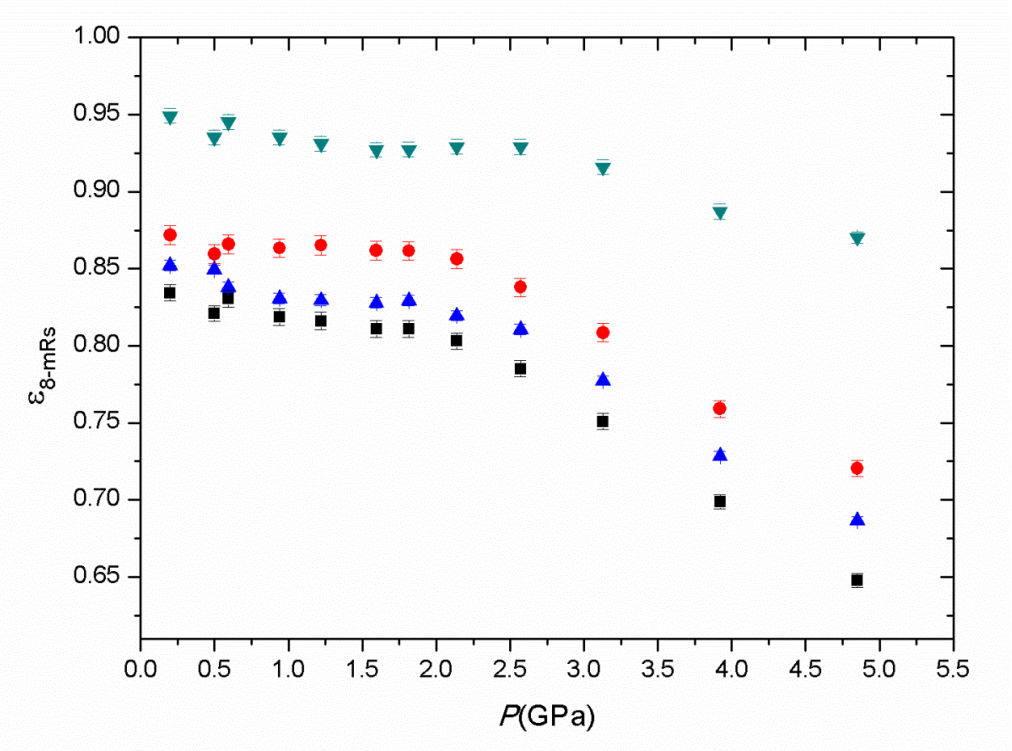

Figure 5.5. Evolution of the 8-mRs[010] diameters normalized to their P_0 values *vs*. pressure. O7-O7 in black squares, O3-O3 in red circles (in Comboni et al 2017).

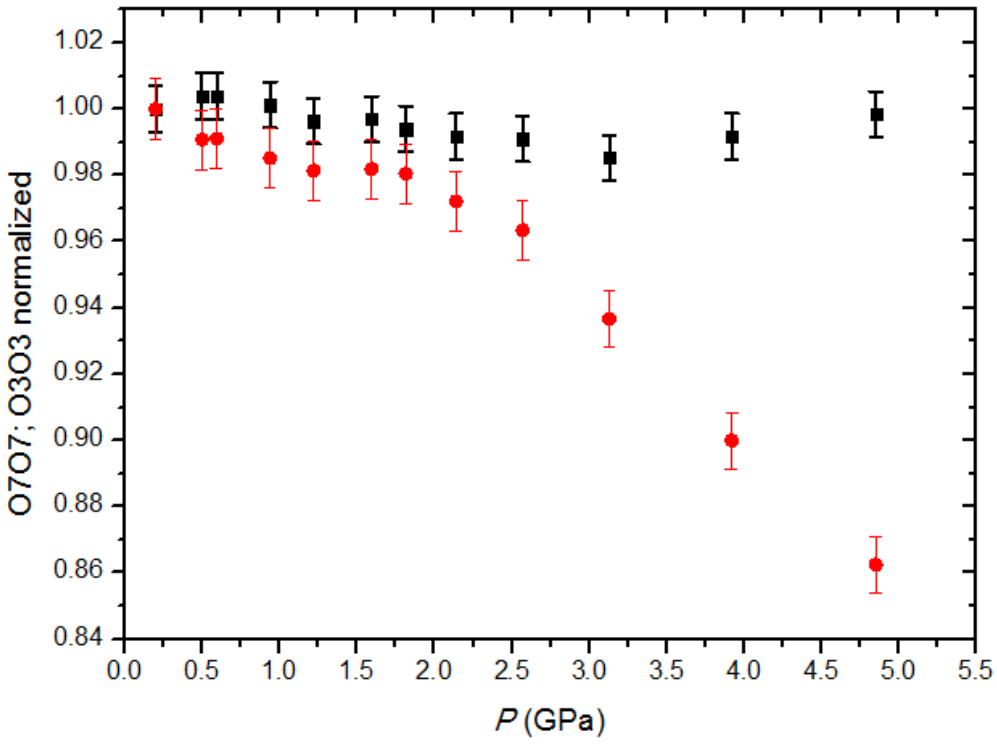

whereas O7–O7 slightly increases. As the diameter O7–O7 is parallel to [100] and O3–O3 almost parallel to [001], this can explain the observed $K_a > K_c$ at $P > P7$ (Table 5.10). It is also interesting to note that at $P8$, the β angle reverses its negative trend with P and begins to increase. The change in β is somehow related to some T–O–T angles. We expect that the evolution of β might depend on the evolution of the inter-tetrahedral angles of the 8-mRs[010] and, in particular, on a combination of the T3–O1–T4 and T2–O6–T4 angles (Fig. 5.1). More in detail, if T3–O1–T4 and T2–O6–T4 were lying on the same plane (perpendicular to [010]), an increase in their values would correspond to a decrease in β. They actually do not lie on the same plane; however, if the value of the difference [(T2–O6– T4) − (T3–O1–T4)] is plotted versus pressure (Fig. 5.6), an almost overlapped trend to that of β is observed. This finding suggests that the combined effect of the T3–O1–T4 and T2–O6–T4 angles evolution can play a role in the evolution of the β angle, and thus on the distortion of the (monoclinic) unit cell.

Figure 5.6. High-pressure evolution of the (normalized) difference between the inter-tetrahedral angles T3-O1-T4 and T4-O6-T2 (in Comboni et al 2017).

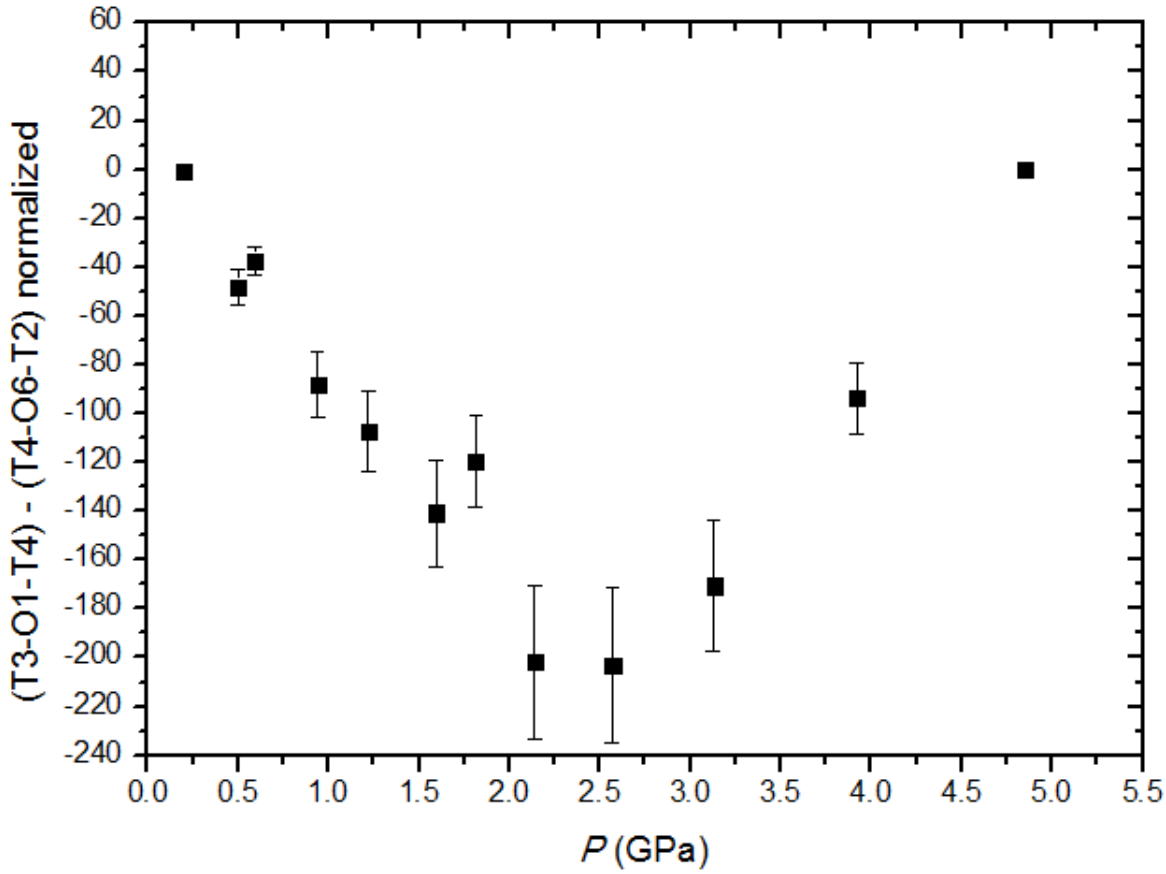

5.4.3 Pressure-induced structural evolution: evolution of the extra-framework population

W sites

The first changes in the evolution of the extra-framework population are already observed at low-*P* regime. At *P*2, the analysis of the difference-Fourier maps of the electron density showed the presence of a maximum close (but distinct) to the position of W2. This peak, labeled as W2' in this study, was not found in the analysis of the difference-Fourier maps at *P*1. Although we cannot exclude that the occupancies of the H_2O sites are influenced by the constrains adopted for the D.P. values, it is possible that the sum of the occupancies of W2 and W2' (which are mutually exclusive) at *P*2 is equal, within the *e.s.d*., to the occupancy of W2 site at *P*1. The distances W2'-O8 [*i.e.,* 2.878(3) Å] and W2'-O2 [*i.e.,* 2.893(3) Å] at *P*2 are shorter than the distances W2–O8 [*i.e.,* 3.205(3) Å] and W2–O2 [*i.e.,* 3.076(3) Å], and this suggests that the new W2' site is involved in an energetically more favorable H-bonding network if compared to W2. At *P*9, the two maxima ascribable to W2 and W2' were not distinctly observed anymore: only one distinct electron-density peak was found. As the distance between the two subsites decreases significantly from *P*6 to *P*8 (from ~1 to ~0.75 Å, respectively), it is highly likely that they converge to one site at *P*9 (3.13 GPa), here re-labeled as W2 (Table 5.3, Fig. 5.7). It is worth to point out that the occupancy of W2 at *P*9 is slightly lower than the sum of the W2 and W2' sites at *P*8 (Table 5.3). As pressure increases, the distance between W1 and Ca decreases (Table 5.5), toward non-realistic values expected for a Ca–W distance (Fig. 5.7). This finding suggests that Ca and W1 are actually two mutually exclusive sites, even in the low-*P* regime. An additional finding concerns the "migration" of W1 out of the 8-mRs[100]-1. Such a behavior implies a change in its H-bonding scheme. As reported in Table 5.5, at *P*1, the distances W1–O9 and W1– O3 are 2.940(3) and 3.081(3)Å, respectively. The same distances at *P*11 are 2.690(3) and 3.229(3) Å, respectively, which means that the distance W1–O9 decreases by ~9 %, whereas the W1–O3 increases by ~4.5 %. The analysis of the difference-Fourier maps, based on the refinements at *P*10 and *P*11, revealed the presence of two new maxima, here labeled as W'' and W1', lying in the 8-mRs[100]-2 and 8-mRs[100]-1 rings, respectively (Table 5.3, Fig. 5.7), with partial site occupancy and mutually exclusive with the co-respective W1 and W2 (Table 5.3). These new sites have distances with some framework oxygen sites ascribable to H-bond interactions (*e.g.,* W1'–O9 ~2.9 Å, W''–O8 ~2.5 Å, W''–O2 ~2.6 Å). Additional effects of H_2O migration among the W sites are observed at W4, W5 and W6. The fractional coordinates of the W3, W5 and W6 sites do not show any substantial change with the increase in pressure. The occupancy of the W4 sites decreases as pressure rises, whereas the occupancies of W5 and W6 increase. At $P > P9$, no evidence of the W4 site was found in the difference-Fourier maps, coupled with significantly higher densities at W5 and W6 than those observed at *P*1 (Fig. 5.8). A general view of the *P*-induced changes involving the extra-framework population is shown in Fig. 5.7.

Ca and K1–K2 sites

As reported in Table 5.5, the distance Ca–O7 increases with pressure, whereas the distances Ca–O4 and Ca–O3 decrease. This trend leads the Ca site toward the mirror plane located at y = ¼. This behavior might be correlated to the tilting of the TO_4 tetrahedra and, in particular, to the closure of the O4–O7–O3 angle in the 8-mRs[100]-1. The structural data show also a correlation between the distances K1/K2–O1 and K1/K2–O8 and the inter-tetrahedral angles T3–O1–T4 and T2–O8–T2, respectively. As explained in the previous section, the principal effect of the hydrostatic compression on the 8-mRs(001) is the tilting of the TO_4 tetrahedra, which leads to a reduction of the T3–O1–T4 and T2–O8–T2 angles with pressure. The decrease in the aforementioned angles leads to a shortening of the K1/K2–O1 and K1/K2–O8 distances (Table 5.5).

5.5. Discussion

This is the first experiment in which the high-*P* behavior of a natural phillipsite is described on the basis of single-crystal X-ray diffraction data (collected up to 9.4 GPa). The previous experiment on phillipsite was conducted on a polycrystalline sample up to 3.6 GPa (Gatta and Lee 2007). Gatta and Lee (2007) described the elastic behavior of phillipsite on the basis of powder data. However, the low quality of the powder data themselves, along with the modest *P*-range investigated (*i.e.,* P_{max} = 3.6 GPa), did not allow the authors to have a clear picture of the high-*P* behavior of this zeolite, and only one BM-EoS was used to model its compressibility. A potential change in the compressional behavior was already reported by Gatta and Lee (2007) at $P > 2$ GPa. In this study, we used the same natural sample previously used by Gatta and Lee (2007). In light of this, this work can be considered as an extension of the first study. Also in this case, we observe a change in the compressional behavior of phillipsite between 2.0 and 2.5 GPa, which is not apparently due to a potential penetration of the *P*-fluid molecules. The inversion of β-trend is likely the most evident effect of such a change. The diffraction patterns and the structure refinements confirmed that the space group $P2_1/m$ is preserved within the entire *P*-range investigated (*i.e.*, 0-9.4 GPa). Therefore, the change in the elastic behavior does not reflect a phase transition, but rather a change in the deformation mechanisms at the atomic scale. More specifically, phillipsite experiences a "softening" at $P > 2$–2.5 GPa, and the *bulk modulus* in the low-*P* regime is drastically higher than that of the high-*P* regime [*i.e.,* 89(8) *vs.* 18.8(7) GPa, Table 5.10]. A similar behavior was previously observed in other open-framework materials (*e.g.,* Gatta et al. 2006, 2008, 2009b, 2012). Moreover, also Ori et al. (2008) in a high-*P* X-ray powder diffraction experiment on gismondine observed a dependence between the K_{V0} and the arrangement of H_2O sites. In gismondine, at ambient conditions, the W4-W5 and the W6-W7 H_2O sites are two pair of

partially occupied sites. At 1.9 GPa, a significant H_2O system rearrangement and ordering was observed: the H_2O molecules partially occupying the W4, W5, W6, and W7 sites migrated to fully occupy only two of these positions (*i.e.,*W5 and W7), whereas the W4 and W6 sites disappeared (Ori et al. 2008). Such a rearrangement induced an abrupt volume decrease, and the larger free volume available in the cavities allows an easier framework contraction, leading to a change in the compressibility of gismondine. This is very similar to what observed in this study on phillipsite.

In phillipsite, the tetrahedral behave as rigid units (at least at a first approximation), the structure deformation is basically governed by tetrahedral tilting and by the rearrangement of the extra-framework population, as usually observed in zeolites (*e.g.,* Gatta et al. 2008, 2014; Gatta and Lee 2014; Lotti et al. 2016). The elastic anisotropic scheme of phillipsite is preserved within the *P*-range investigated, with K_a, $K_c >> K_b$. The structure is, therefore, more compressible along [010]. From the low- to the high-*P* regime, the linearized *bulk modulus* K_b decreases from 50(5) to 12(1) GPa. Such a behavior might be somehow influenced by a change in the extra-framework population and, more specifically, by the disappearance of the W4 site. W4 (along with W5 and W6) lies almost at the center of the 8-mRs[010] channel, in such a way that a helicoidal H_2O chain occurs. The lack of W4 implies a reduced "pillar effect" of the H_2O chain (Fig. 5.7, 5.8). As the H_2O chain is perpendicular to (010), its weakening does not affect significantly the compressibility along [100] or [001]. However, if the ratio O7–O7/ O3–O3 is plotted versus *P*, where O3–O3 and O7–O7 are two independent diameters of the 8-mRs[010] channel (Fig. 5.5), we observe an almost horizontal trend up to *P*7 and then a drastic increase at $P > P7$. Therefore, one of the reasons of the softening along [100] and [001] can be ascribed to the tilting of the 8-mRs[010]-tetrahedra, in response to the disappearance of W4. The tilting causes the deformation of the 8-mRs[010] channel and, in turn, the β-inversion. An additional cause of the elastic anisotropy may be correlated to the migration of W1. The lack of W1 at high-*P*, in the 8-mRs[100]-1, leads to a significant shortening of the O8–O9 diameter, which is perpendicular to [001]. Therefore, the migration of W1 cannot affect K_a or K_b but only K_c. There is not a unique explanation about the H_2O sites migration at high pressure and the occurrence of subsites, *e.g.,* W1', W2', W'' (Table 5.3). The lack of the proton positions does not allow a clear view of the H-bonding network. However, it appears that the framework deformation leads to energetically most favorable H-bonding connection with H_2O molecules located in a slightly different positions than the parent ones (at room conditions), promoting split and, in general, H_2O sites migration. It is interesting to note that despite phillipsite and leonhardite have both channels already occupied by H_2O and alkaline (or earth-alkaline) cations, phillipsite does not over-hydrate. This can be due to the different steric obstruction in the 8-mRs channels.

Figure 5.7(*a,b,c*)**.** Migration of W1 with *P* viewed down [010] and (*d,e*) general view of the *P*-induced changes into the structure. H_2O molecules in small red spheres, K cations in yellow and Ca in dark grey (in Comboni et al 2017).

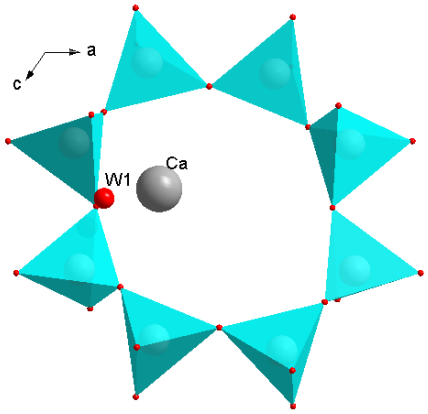

a) 8-mR[010] at *P*1 (0.20 GPa)

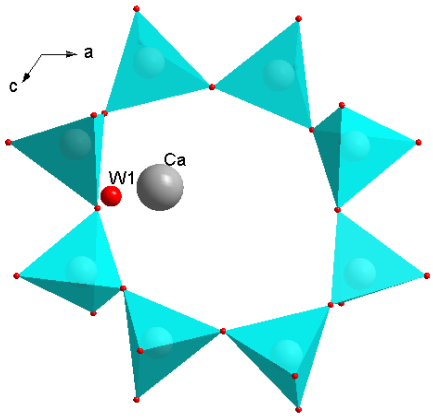

b) 8-mR[010] at *P*3 (0.94 GPa)

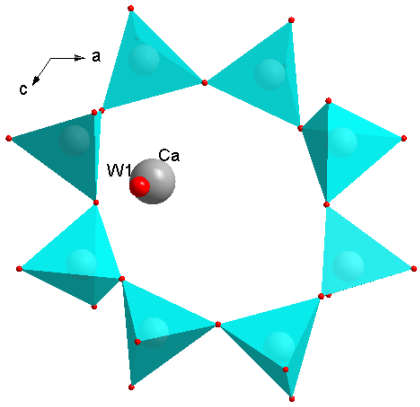

c) 8-mR[010] at *P*8 (2.56 GPa)

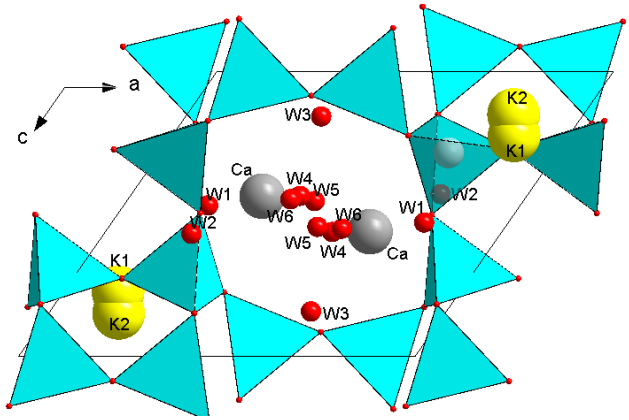

d) extra-framework configuration at *P*1 (0.20 GPa)

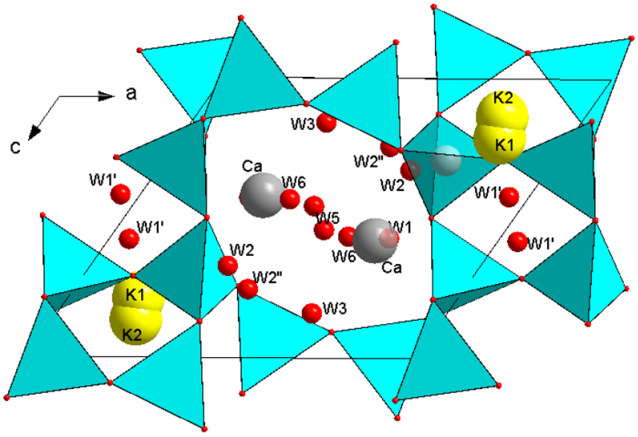

e) extra-framework configuration at *P*10 (3.92 GPa)

Figure 5.8. Helicoidally configuration of the H_2O molecule-chain in the low (*top*) and high (*bottom*) compressional regime.

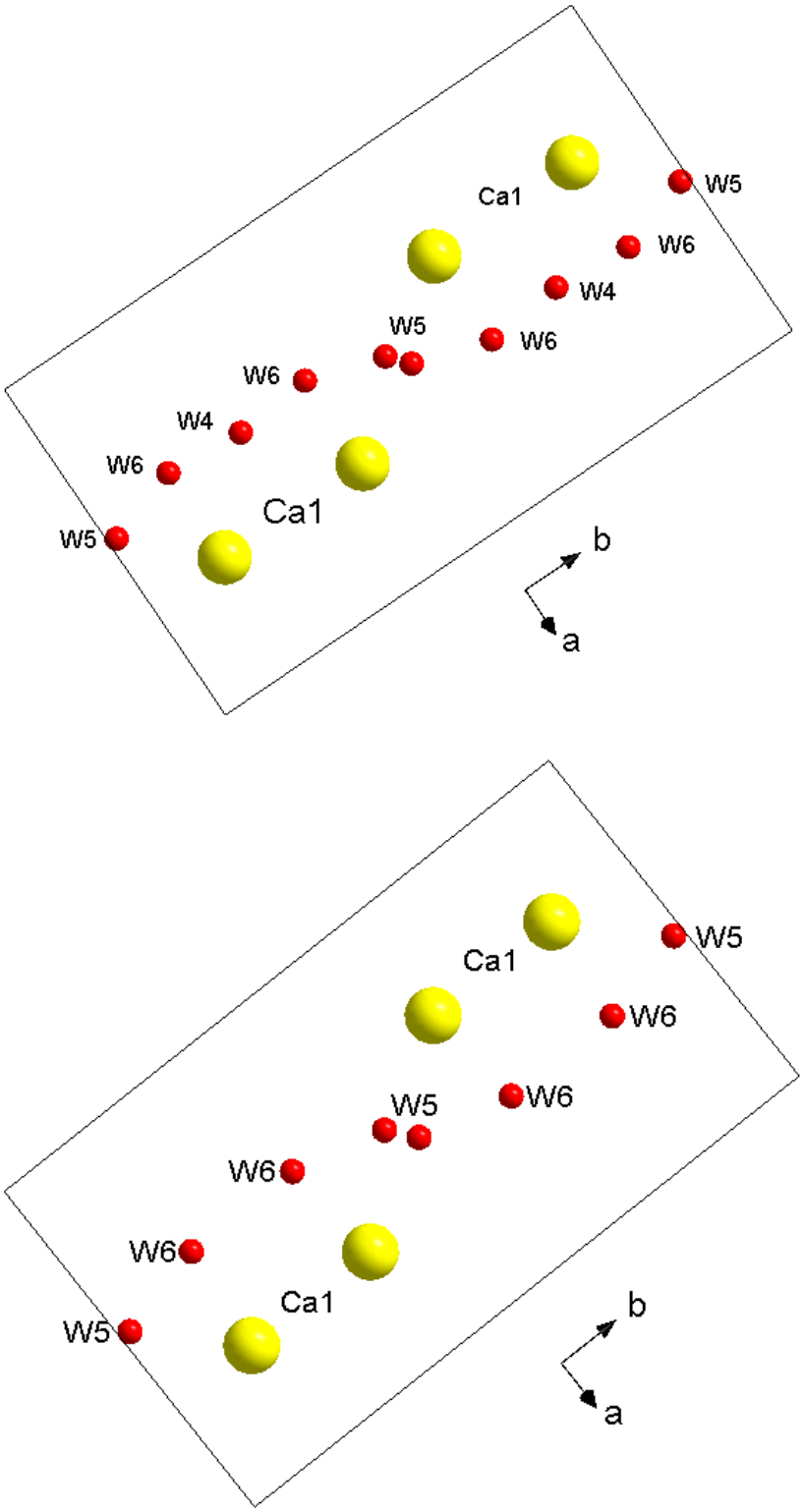

CHAPTER 6:
HIGH-PRESSURE BEHAVIOR OF ARMSTRONGITE

The experimental findings reported in the following pages have been reported in the following paper: **Comboni D**., Lotti P., Gatta G.D, Lacalamita M., Mesto E., Merlini M., Hanfland M. (2018). Armstrongite at non-ambient conditions: An *in-situ* high-pressure single-crystal X-ray diffraction study, MICROPOROUS AND MESOPOROUS MATERIALS, 274, Pages: 171-175.

6.1. Introduction

Armstrongite, ideally $CaZr[Si_6O_{15}]\cdot 3H_2O$, is a rare mineral discovered for the first time in granite pegmatites and alkine granites of the Khan Bogdo massif (Mongolia) and described by Vladykin et al. (1973), who indicated as possible space group *Cm*, *C*2 and *C*2/*m* and assigned to armstrongite the ideal formula $CaZr[Si_6O_{15}]\cdot 2.5H_2O$. Concerns regarding the true space group of armstrongite were discussed by Karashaev and Sapozhnikov (1978) and Jambor et al. (1987): on the basis of the reflection conditions (in particular $h + k + l \neq 2n$, *h0l* with $h + l \neq 2n$ and *0k0* with $k \neq 2n$), they reported the *I*-centered lattice with space group choices *I*2/*m*, *I*2 and *Im*. Kabalov et al. (2000) re-investigated the structure of armstrongite solving and refining the structure in the space group *C*2, with a Rietveld full-profile fit with R_{wp}= 2.75%, finding also the position of a new H_2O site and increasing the number of H_2O molecules up to 3 per formula unit (pfu). More recently, Mesto et al. (2014), solved and refined the structure of a twinned crystal of armstrongite in the space group *C*2/*m,* with *a*~14.03Å, *b*~14.14 Å, *c*~7.85 Å, and β~109.4°. The structure of armstrongite (Fig. 6.1) is characterized by a mixed framework of $[Si_6O_{15}]^{6-}$ silicate sheets, interlinked *via* ZrO_6 octahedra through vertex connection of octahedra and tetrahedra. Accordingly to Zubkova and Pushcharovsky (2008), the stability of such polyhedral topology depends on the formation of almost equivalent Si-O-Si or Si-O-Zr bonds. The $[Si_6O_{15}]^{6-}$ sheets are formed by a system of xonolite-like chains running along the *b* axis (Fig. 6.1) which, in turn, are generated by the condensation of two wollastonite-type chain (Haile and Wuensch 1997). Similar chains have been also found also in vlasovite and miserite (Sokolova et al. 2006; Kaneva et al. 2014).The condensation of the xonotlite-like-chains, running along *the b* axis, results into the arrangement of the tetrahedra in $[Si_6O_{15}]^{6-}$ sheets showing four- and six-member rings, alternating along [010], and four- and eight-member rings, alternating along [100] (hereafter 6-, 4-, 8-mRs, respectively) (Fig. 6.2). ZrO_6 octahedra are connected with the SiO_4 tetrahedra to give the $(ZrSi_6O_{15})^{2-}$ heterogeneous framework, in which $CaO_5(H_2O)_2$-sevenfold coordination polyhedra are edge-connected to ZrO_6 octahedra to form columns running parallel to

Fig. 6.1. (*Top*) Crystal structure of armstrongite viewed down [001], (*bottom, left*) the xonolite-like chain of armstrongite and (*bottom*, *right*) a column of ZrO_6 octahedra and $CaO_5(H_2O)_2$ polyhedra viewed perpendicular to the *bc* plane (SiO_4 tetrahedra in sky blue, ZrO_6 octahedra in green, Ca polyhedra and atoms in yellow, oxygen atoms in red spheres; in Comboni et al. 2018).

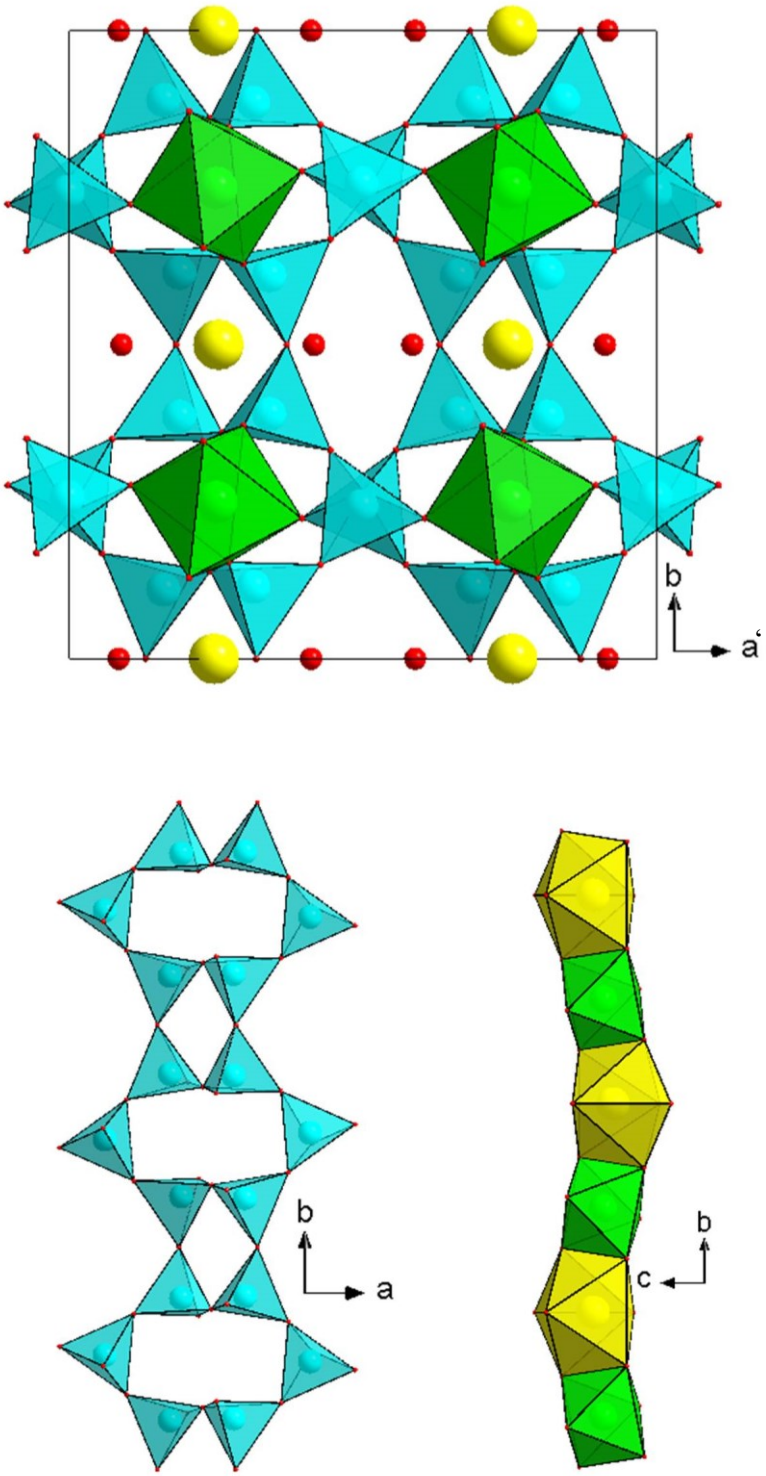

Fig. 6.2. Configuration of the 8-mRs (*top*), 6-mRs (*middle*) and 5-mRs (*bottom*) at ambient pressure (*left*) and at 4.01(5) GPa (*right*) (SiO_4 tetrahedra in sky blue, ZrO_6 octahedra in green; in Comboni et al. 2018).

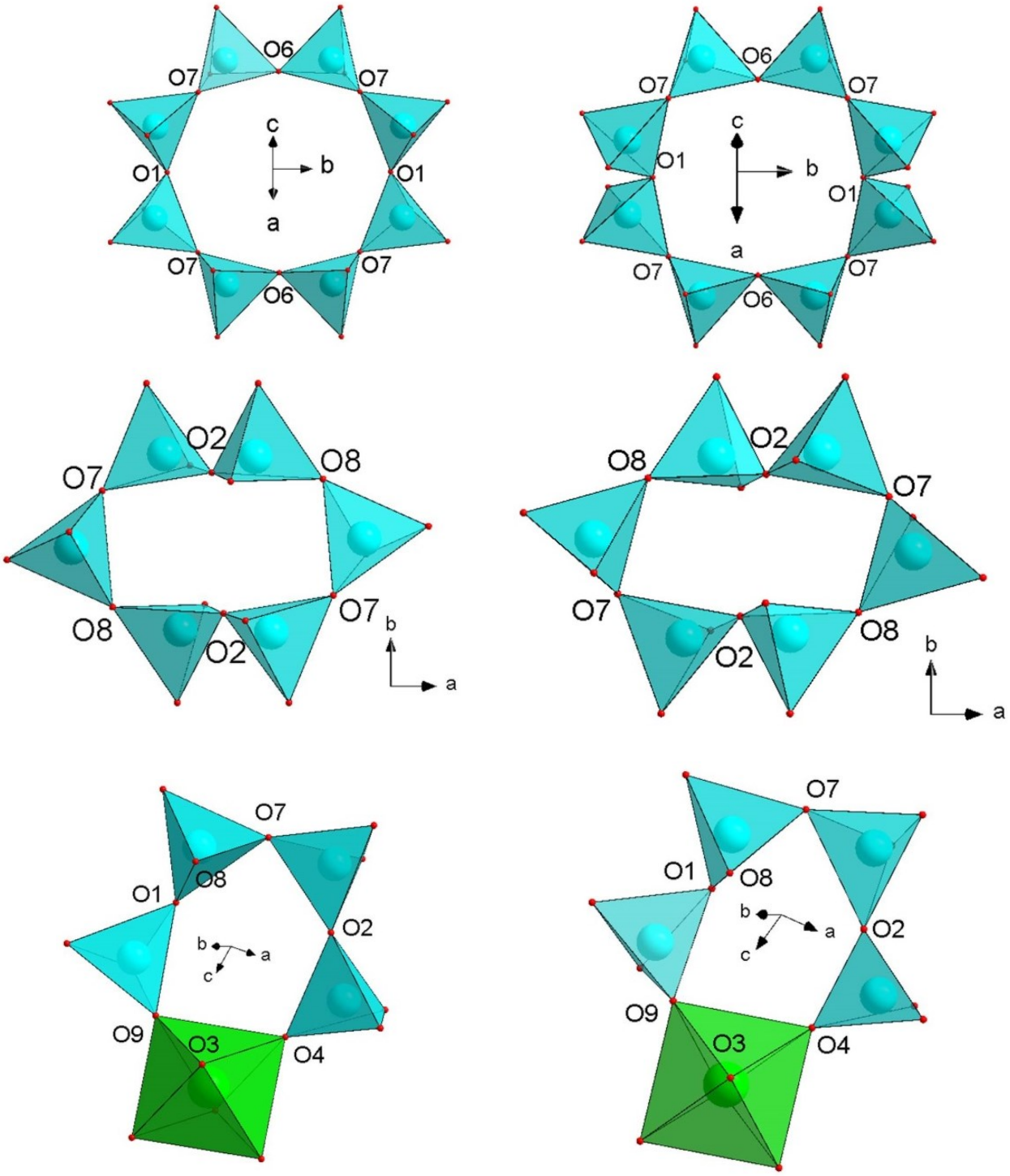

[010] (Fig. 6.1). Kabalov et al. (2000) recorded a notable elongation of shared Si-O bond lengths (*i.e.,* <Si-O_{sh}> ~ 1.63 Å) with respect to unshared ones (*i.e.,* <Si-O_{ush}> ~ 1.58 Å), but this feature is not consistent with the findings of Mesto et al. (2014) (*i.e.,* <Si-O_{sh}> ~ 1.62 Å, <Si-O_{ush}> ~ 1.59 Å) (Tab.6.4). Schingaro et al. (2018) investigated the dehydration process of armstrongite by means of thermal analysis, *in-situ* X-ray powder diffraction and Fourier-transform infrared spectroscopy. The structure of the fully dehydrated form of armstrongite has very recently been solved and refined by *in-situ* high-temperature single crystal X-ray diffraction by Lacalamita et al. (2018).

This study is aimed to extend the knowledge about the behavior of armstrongite under extreme conditions, with the description of its high-pressure behavior under hydrostatic compression. To date, no X-ray diffraction data at high pressure are available in the open literature and, consequently, the compressional parameters of this material are still unknown. Although armstrongite is a heterosilicate, its structure, with a framework density FD ~21.86 T/1000 $Å^3$ (lying in the range of zeolites), could be a potential candidate for molecular intrusion enhanced by increasing pressure. On this basis, we have investigated the high-pressure behavior of armstrongite up to 8 GPa by means of *in-situ* single-crystal synchrotron X-ray diffraction, using a diamond-anvil cell and a potentially penetrating *P*-transmitting fluid.

6.2. Experimental methods

A single crystal of armstrongite (same specimen described by Mesto et al. (2014) and in Lacalamita et al. (2018)) from Khan Bogdo, Mongolia, with a prismatic habit (~50x20x20 μm in size) was selected, on the basis of its optical quality, for the high-pressure experiment, performed at the ID15B beamline of the European Synchrotron Radiation Facility (ESRF) in Grenoble, France. A parallel monochromatic beam operating with an E = 30.16 KeV (λ ~ 0.411 Å) was used. The crystal was loaded in a membrane-driven DAC, with 600 μm Boehler-Almax design anvils, along with some ruby spheres for pressure determination (pressure uncertainty ±0.05 GPa Mao et al. (1986)). A stainless steel foil (with thickness ~ 250 μm) was pre-indented to 70 μm and then drilled by spark-erosion, leading to a *P*-chamber of ~200 μm in diameter. Before adding the methanol:ethanol:H_2O = 16:3:1 mix, used as hydrostatic *P*-transmitting fluid (Angel et al. 2007), a first data collection was performed with the crystal in the DAC without any *P*-fluid. The adopted data collection strategy consisted in a pure ω-scan (-32°≤ ω ≤ +32°), with 1° step width and 1s exposure time per step. The X-ray diffraction patterns were collected by a MAR555 flat-panel detector (at a distance of 287.43 mm from the sample position). Further details pertaining to the beamline experimental setup are reported in Merlini and Hanfland (2013). Indexing of the diffraction peaks and integration of their intensities (corrected for

Lorentz-polarization effects) was done using the CrysAlis package (Agilent Technologies 2012). Corrections for absorption (caused by the DAC components) and background were applied using the semi-empirical *ABSPACK* routine implemented in CrysAlis (Agilent Technologies 2012).

6.3. Structure refinement protocol

The structure refinements of the armstrongite structure at room and high pressure were performed using the software suite JANA2006 (Petříček et al. 2014). Starting with the structure model of Mesto et al. (2014), a series of structure refinements were performed up to 4 GPa, at which the material experiences a *P*-induced phase transition with a triplication of the unit-cell volume. In the structure refinements of the low-*P* polymorph, in order to reduce the number of the refined variables, the atomic displacement parameters (D.P.) were modelled as isotropic. For the high-*P* polymorph, unfortunately, the low (reflections/parameters to be refined) ratio hindered the structure solution of the crystal structure. The unit-cell parameters with *P* are listed in Tab. 6.1 and the principal statistical parameters of the structure refinements are listed in Tab. 6.2. Atomic coordinates, site occupancies and displacement parameters are given in Tab. 6.3. Si-O and Zr-O distances are listed in Tab. 6.4, whereas other relevant distances are reported in Tab. 6.5.

6.4. Results

6.4.1. Phase transition, elastic behavior, and equation of state

The evolution of the unit-cell parameters as a function of pressure is shown in Fig. 6.3 and Fig. 6.4. Overall, the unit-cell parameters decrease steadily up to 4.01(5) GPa (Table 6.1). In this *P*-range, the lengths of the *b*- and *c*-edges decrease by 3.5 and 3.2%, respectively, whereas along *a* the edge length decreases by only 1.5%; the unit-cell volume is reduced by about 8.8% (Fig. 6.3). Between 4 and 5 GPa, armstrongite undergoes a phase transition characterized by a triplication of the unit-cell volume (Table 6.1 and Fig. 6.4), as a result of the triplication of the *c* unit-cell edge (Table 6.1, Fig. 6.5). The associated volume discontinuity reflects a first-order phase transition. Comparing the unit-cell volume of the low-*P* polymorph at 4.01(5) GPa and the *V*/3 of the high-*P* one at 5.07(5) GPa, a difference of about 5.2% occurs. In order to maintain the metrical configuration, the lattice of the high-*P* polymorph is better described as *I*-centered, and the reflection conditions suggests the space group *I*2/*m* as highly likely. The metrical relationship between the lattice of the low-*P* (*C*2/*m*) and high-*P* (*I*2/*m*) polymorphs can be ideally expressed as: $\boldsymbol{a'} = \boldsymbol{a}$, $\boldsymbol{b'} = \boldsymbol{b}$, $\boldsymbol{c'} = 3\boldsymbol{c}$. The phase transition affects also the value of the monoclinic β angle: as shown in Fig. 6.3, in the low-*P* form, β progressively increases

from 109.37(1)° at ambient pressure to 110.38(4)° at 4.01(5) GPa; for the high-*P* polymorph, the β value appears to be nearly unaffected by *P* with an average value of 103.1° (± 0.2°) (Fig. 6.3, S2 SM). In order to describe the (isothermal) compressional behavior of both low- and high-*P* polymorph, the experimental *V*-*P* data, weighted by their uncertainties, were fitted to a third-order (BM3-EoS) and a second-order (BM2-EoS) Birch-Murnaghan Equations of State (Birch 1947, Murnaghan 1937), respectively, using the EoS Fit 7.0 software (Angel et al. 2014). The refined elastic coefficients of the fit are reported in Tab. 6.6. The high-*P* polymorph has a *bulk modulus* K_{V0} ~ 50% higher than that obtained for the low-*P* one, indicating a significant increase in stiffness in response to the phase transition. Moreover, a remarkable change of the "axial bulk moduli" (calculated simply by substituting the cube of the individual lattice parameter a^3, b^3, c^3 for the volume in the EoS) (Angel et al. 2000) occurs from the low- to the high-*P* polymorph: K_b and K_c increase from 23 to 50 GPa and from 26 to 46 GPa, respectively, whereas K_a falls from 78 to 35 GPa. Therefore, the phase transition leads to a pronounced decrease of the compressibility along [010] and [001] coupled with a marked increase along [100]. Data collected in decompression show a significant hysteresis loop, as the high-*P* phase is stable (at least) down to 2.91(5) GPa (Fig. 6.2, Tab. 6.1).

6.4.2. Structure evolution at increasing pressure

The Zr-O distances of the low-*P* polymorph (reported in Tab. 6.4) do not change drastically with *P*. Though the intra-tetrahedral Si-O distances (reported in Tab. 6.4) do not show drastic changes up to 3.27(5) GPa, it is worth noting that a considerable distortion of the Si1-O_4 and Si2-O_4 tetrahedra is observed in the structural model refined at 4.01(5) GPa. This distortion is mainly governed by the sharp decrease of the Si1-O2 distance coupled with an increase of the Si2-O2 distance (Tab. 6.4). Nevertheless, similarly to zeolites (*e.g.*, Lotti et al. 2016, Comboni et al. 2017, Comboni et al. 2018) and others open-framework materials (Gatta et al. 2018 and references therein), the bulk compression is mainly accommodated through the tilting of the TO_4 units around the shared oxygen hinges. In armstrongite, the effects of such a behavior affect especially the diameters of the 6-mRs and 8-mRs (reported in Tab. 6.5 and shown in Fig. 6.3). For the 6-mRs, for example, the extension of the O7-O7 diameter with *P* is coupled with the compression of the O8-O8 one, leading to a noticeable distortion of this building unit (Fig. 6.6). Likewise, the distortion of the 8-mRs at high pressure is mainly due to the increase of the O6-O6 diameter, coupled with the decrease of O7-O7 and O1-O1 (Fig. 6.6).

With increasing pressure, the rotation of the ZrO_6 octahedra is reflected by the change of the O1-O7-O2, O8-O1-O9, O1-O9-O3 and O2-O4-O3 angles (Tab. 6.7). The O1-O9-O3 and O2-O4-O3 angles, for example, increase respectively by about 10.6 and 10.3 % ($\Delta P \approx 4$ GPa). The distortion of the 5-

mRs is mainly governed by the decrease of the O1-O7-O2 and O8-O1-O9 angles (Fig. 6.6). Further (O-O-O) angles, related to the 5-mRs, are given in Tab. 6.8. Fig. 6.2 shows a 5-mR (formed by four SiO_4 tetrahedra and one ZrO_6 octahedra) at ambient pressure and at 4.01(5) GPa, respectively.

Fig. 6.3. High-pressure evolution of the normalized (to P_0) unit-cell volume and axial parameters of armstrongite (V/V_0 in *black squares*, a/a_0 *red circles*, b/b_0 *blue triangles*, c/c_0 *cyan triangles*) from ambient pressure to 4.01(5) GPa (*i.e.*, only for the low-*P* polymorph); *black squares* represent the compression path, whereas *red circles* the decompression path (*above the phase transition pressure, $V/3$ is reported) (in Comboni et al. 2018).

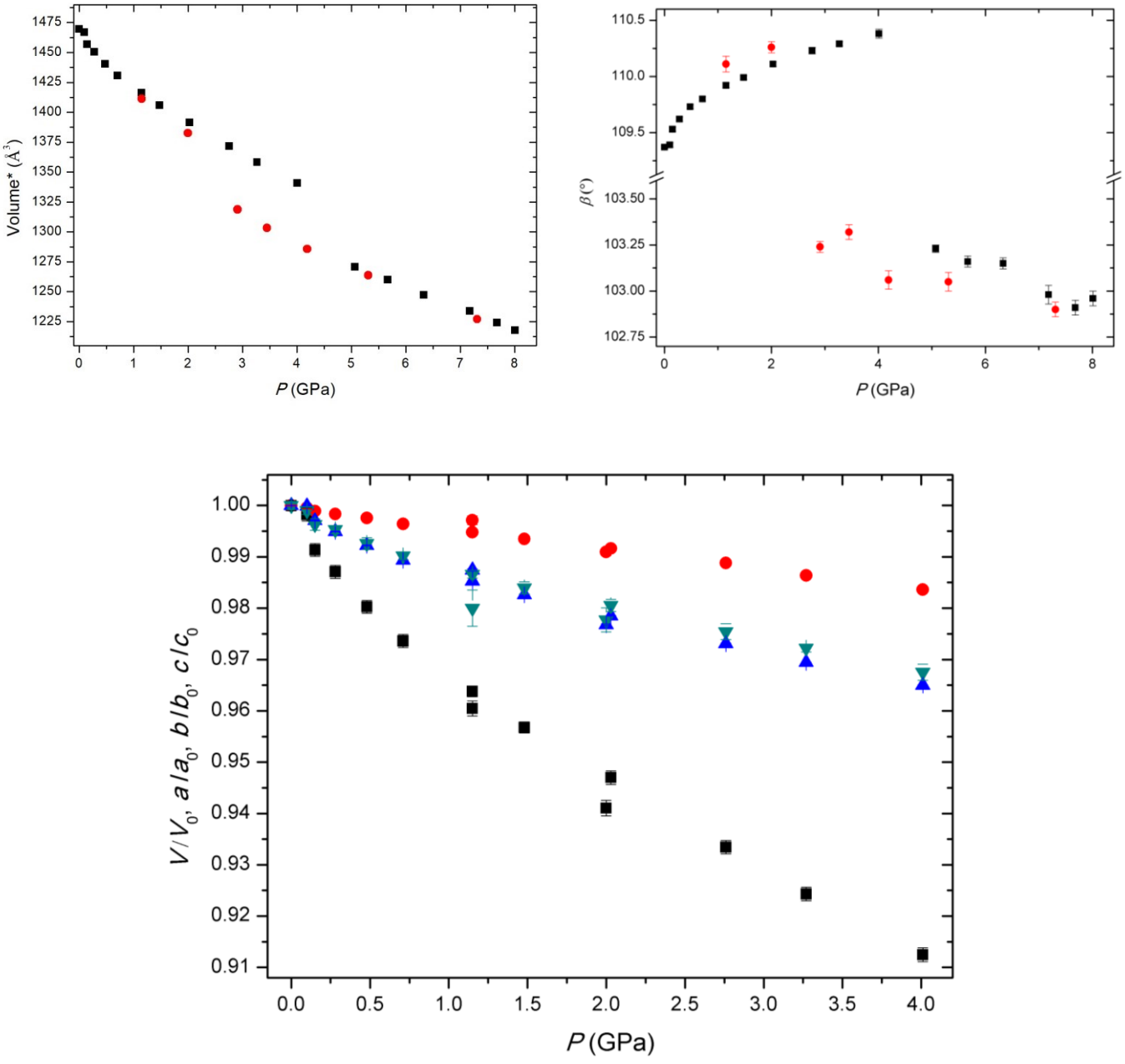

Fig. 6.4. Evolution with *P* of the axial parameters of the high-*P* polymorph of armstrongite (a/a_0 *black squares*, b/b_0 *red circles*, c/c_0 *blue triangles*) (in Comboni et al. 2018).

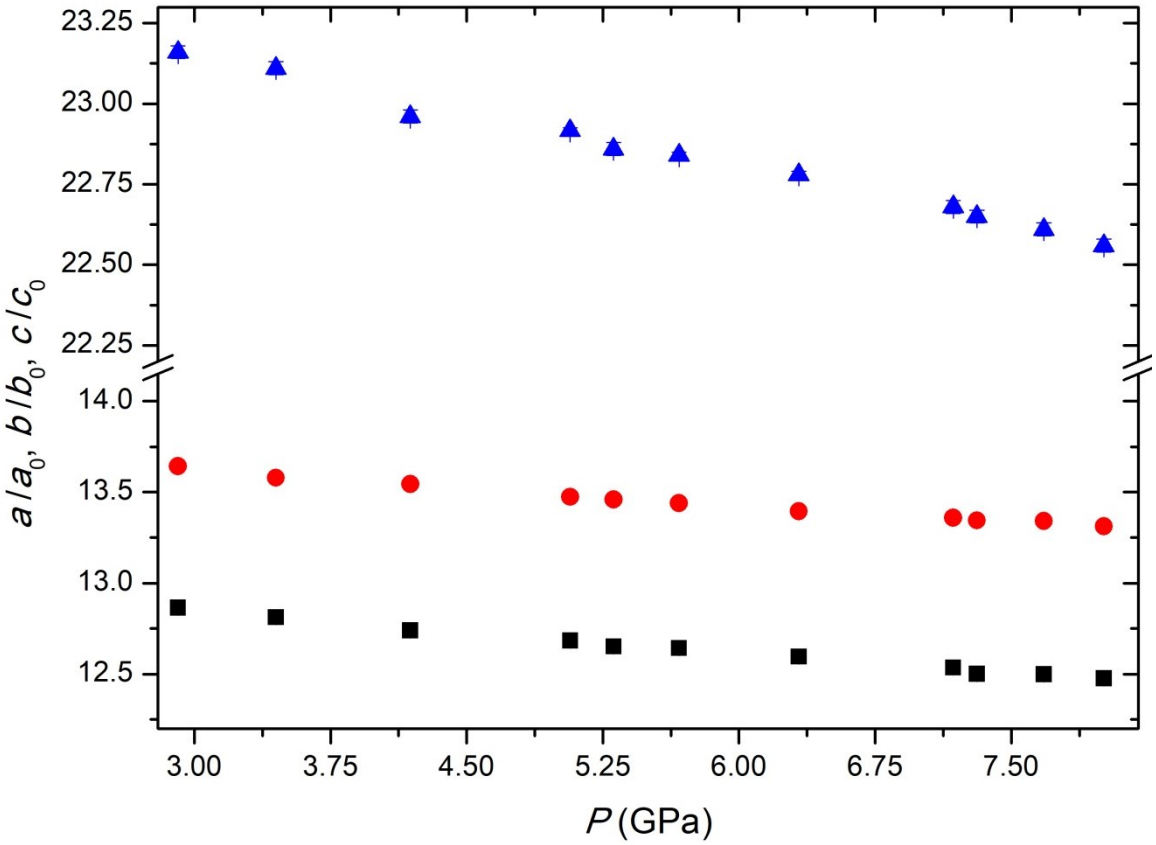

Fig. 6.5. Idealized metrical relationship between the unit cell of the low-*P* (continuous line) and high-*P* (dashed line) polymorphs of armstrongite (viewed down [010]) (in Comboni et al. 2018).

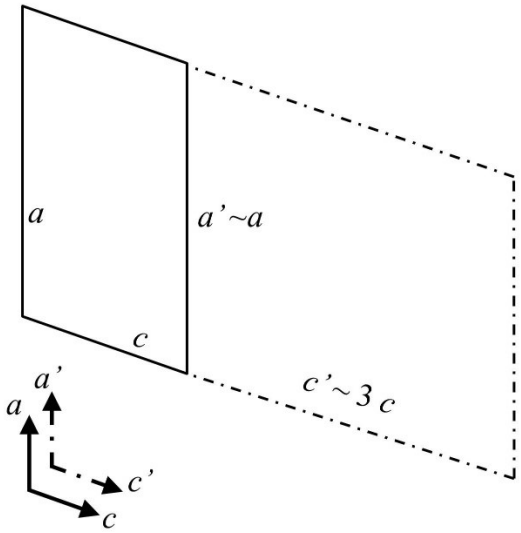

Fig. 6.6. Evolution of the (relevant) normalized diameters and angles of the 6-mRs (O7-O7 in *black squares*, O8-O8 in *red circles*), 8-mRs (O1-O1 in *black squares*, O6-O6 in *red circles*, O7-O7 in *blue triangles*) and 5-mRs (O1-O7-O2 in *black squares*, O8-O1-O9 in *red circles*, O1-O9-O3 in *blue triangles* and O2-O4-O3 in *green triangles*) with *P* (in Comboni et al. 2018).

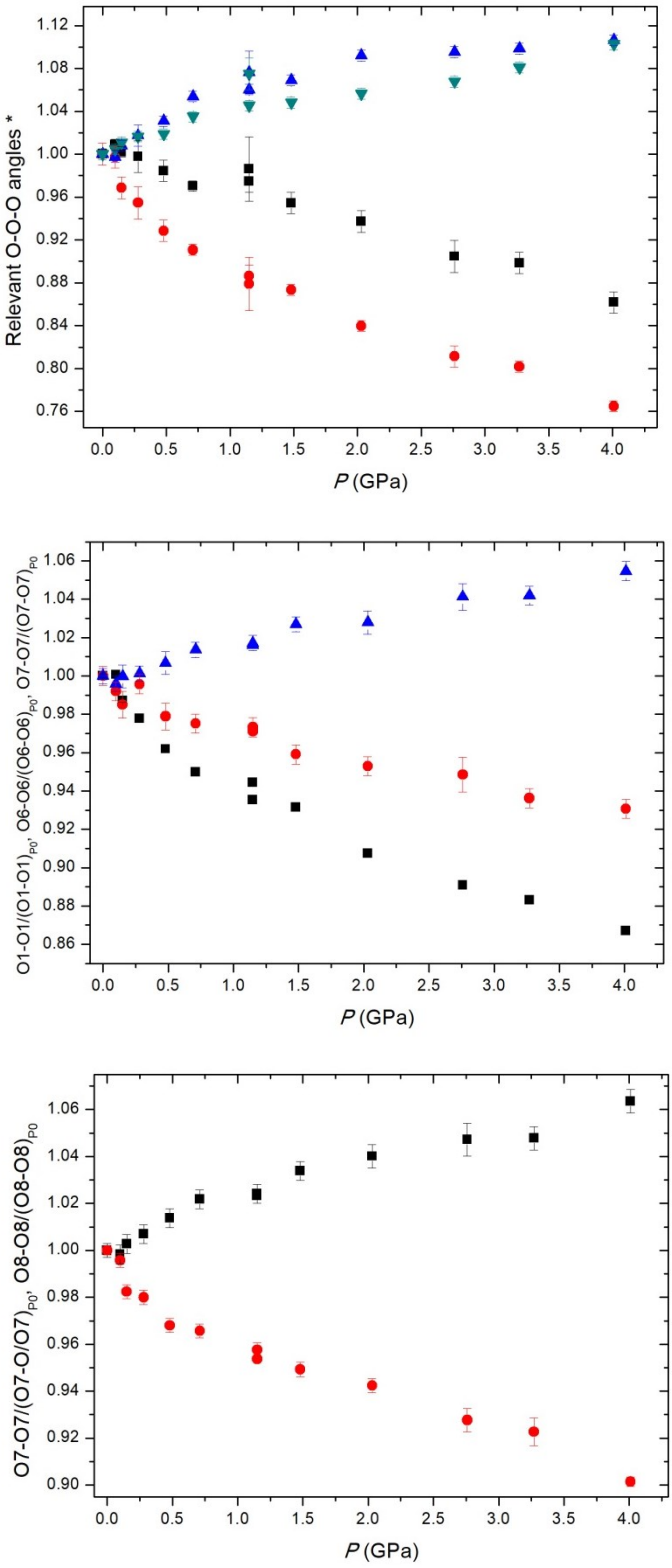

The role played by the $CaO_5(H_2O)_2$-sevenfold coordination polyhedra, in order to accommodate the effects of pressure, appears to be only secondary (Tab. 6.4) and subordinated to the tilting of Si-tetrahedra and Zr-octahedra.

6.5. Discussion

In this study, we have investigated, for the first time, the behavior of armstrongite at high pressure, on the basis of *in-situ* single crystal X-ray diffraction data collected up to 8.01 GPa. Data collected at high pressure show a first-order phase transition, bracketed between 4.01(5) and 5.07(5) GPa. The unit-cell volume of the high-*P* polymorph triplicates (Tab. 6.1). The bulk compression of the low-*P* polymorph is mainly accommodated through the tilting of both SiO_4 tetrahedra and ZrO_6 octahedra, around the shared oxygen hinges. In fact, these polyhedra behave as quasi-rigid units; in this respect, armstrongite behaves similarly to other microporous minerals, such as zeolites (*e.g.,* Lotti et al. 2016, Comboni et al. 2017, 2018, Gatta et al. 2018) or heterosilicates, such as its Na- analogue, elpidite ($Na_2ZrSi_6O_{15}$•$3H_2O$) (Seryotkin et al. 2014). In elpidite, one of the major distortion mechanisms in response to hydrostatic compression is represented by the opposite rotations of the Zr-octahedra. Also elpidite experiences a *P*-induced phase transition, between 1.2-1.9 GPa, with doubling of the *a* cell parameter (and consequently of the unit-cell volume). Tilting of the Zr-octahedra is the common deformation mechanism between elpidite and armstrongite (either at high temperature and high pressure; see Lacalamita et al. 2018, Seryotkin et al. 2014), whereas the role played by Ca (or Na) appears to be only secondary in armstrongite at high pressure but it is critical in elpidite at H*P* and in armstrongite at H*T* (Lacalamita et al. 2018, Seryotkin et al. 2014). Unfortunately, the triplication of the unit-cell volume prevented the structure solution of the high-*P* polymorph of armstrongite, hindering a comparison between the high-pressure structures of armstrongite and elpidite. However, armstrongite seems to be more stable to pressure with respect to its Na-analogue, which undergoes a (presumably) second-order phase transition between 1.2-1.9 GPa (Seryotkin et al. 2014).

The lack of the structure model of the high-*P* polymorph of armstrongite does not allow any speculation about the character of the first-order phase transition observed between 4.01(5) and 5.07(5) GPa: displacive or reconstructive? Overall, the high-*P* polymorph of armstrongite is found to be stiffer than the low-*P* one (*i.e.*, K_{V0} increases by about 50%, Tab. 6.6), and a remarkable change of the elastic anisotropic scheme occurs: $K_c \sim K_b \sim \frac{1}{3}K_a$ for the low-*P* form, $K_c \sim K_b \sim 1.4K_a$ for the high-*P* form (Tab. 6.6).

On the basis of the structure refinements of the low-*P* polymorph, we can infer that no evidence of crystal-fluid interaction, with a selective sorption of molecules of the *P*-transmitting fluid through the cavities, occurs. This kind of effect was observed in several open-framework materials when

compressed in fluids made by small molecules (*e.g.*, with kinetic diameter shorter than the free diameters of the structural cavities), recently reviewed by Gatta et al. (2018). It is highly likely that the channel population in armstrongite structure hinders the penetration of the new molecules (*e.g.*, H_2O) in response to the applied pressure.

CHAPTER 7:
DISCUSSION AND CONCLUSIONS

7.1. Comparative compressional behavior

Figure 7.1 shows the evolution of the unit-cell volumes and axial parameters with pressure, normalized to the room-*P* values, of the studied open-framework materials. The refined elastic parameters, based on second- or third-order Birch-Murnaghan equations of state fits, are reported in Table 7.1. The analysis of these parameters shows that the studied materials display a high diversity as far as the bulk compressibility (at ambient temperature) is concerned. The reported compressibility of zeolites (*e.g.,* Gatta et al. 2008) is quite variable, as their bulk moduli range between 18 and 70 GPa. $AlPO_4$-5 is the most compressible microporous material studied in this research project, with a K_{V0} of only 13.2(11) GPa, which makes it one of the softest zeolites reported so far. The other minerals species here studied, *i.e.,* laumontite, leonhardite, phillipsite and armstrongite, are far less compressible with respect to $AlPO_4$-5 (see Table 7.1).

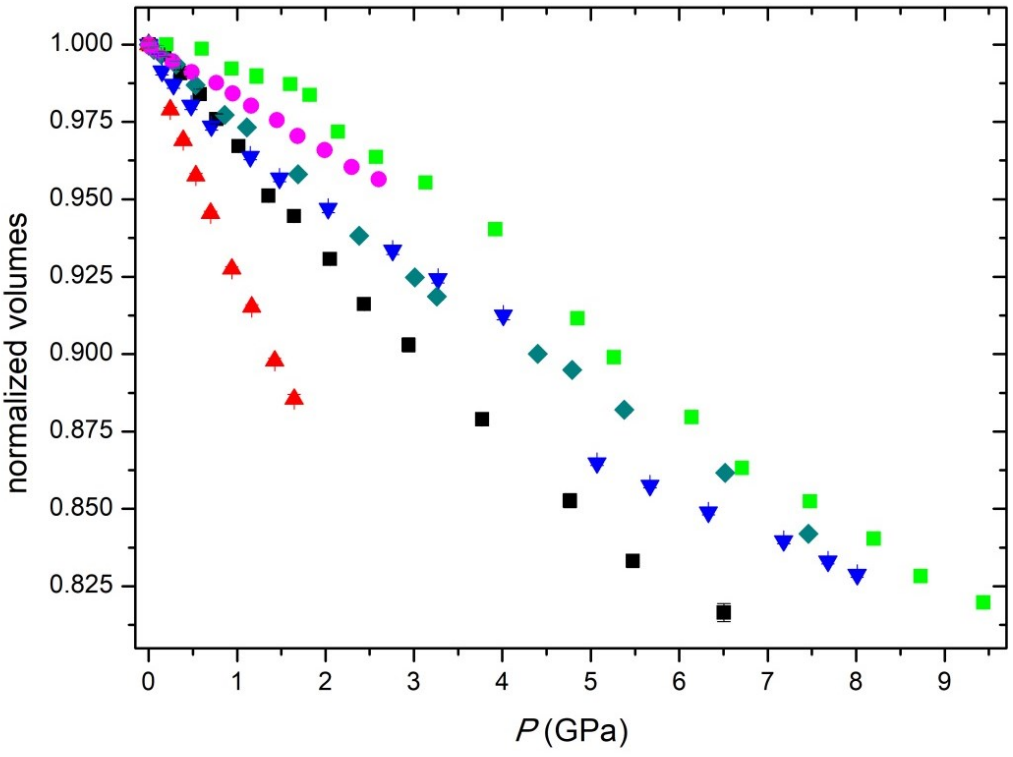

Fig. 7.1: Evolution of the normalized (to P_0) unit-cell volumes of $AlPO_4$-5 (s.oil in red triangles, *m.e.w.* in black squares), phillipsite (green squares), armstrongite (blue triangles), laumontite (purple circles) and leonhardite (dark green diamonds).

This behavior can be explained only if both framework and extra-framework populations are considered. The framework geometry somehow governs the *bulk modulus* of a given microporous material and, if only the framework is considered, it would be expected that the compressibility of a microporous compound is somehow related to its framework density (FD), *i.e.,* number of tetrahedral sites per 1000 Å^3. However, $AlPO_4$-5 has a FD of 17.3 T/1000 Å^3, whereas laumontite (and leonhardite), phillipsite and armstrongite have FD of 17.8, 15.8 and 21.86 T/1000 Å^3, respectively (Baerlocher et al. 2007, Mesto et al. 2014). Therefore, if the compressibility were directly related to the FD, we should expect that $K_{V0(\text{armstrongite})} > K_{V0(\text{laumontite})} \sim K_{V0(\text{leonhardite})} > K_{V0(\text{AlPO4-5})} > K_{V0(\text{phillipsite})}$, which is not experimentally proved (Table 7.1). One could argue that, if the FD is not linearly correlated with compressibility, at least the tetrahedra-ring configuration, which often represent the SBU forming the framework, should have an influence. In this respect, $AlPO_4$-5 has large 12-mRs, whereas laumontite (and leonhardite) have only 10-mRs and both phillipsite and armstrongite have 8-mRs. However, if the *bulk modulus* would be related (only) to the number of tetrahedra of the ring-SBUs, the following relation $K_{V0(\text{armstrongite})} \sim K_{V0(\text{laumontite})} \sim K_{V0(\text{leonhardite})} > K_{V0(\text{phillipsite})} > K_{V0(\text{AlPO4-5})}$ should be expected. The experimental findings of this research study show that there is no correlation between the order of the ring-SBUs or the FD and the compressibility of a microporous material.

7.2. Elastic anisotropy and difference between zeolite and zeolite-like materials

A visual inspection of Table 7.1 highlights that the studied materials are characterized by a pronounced elastic anisotropy. This is rather expectable since all the studied open-framework materials, with the only exception of $AlPO_4$-5, have low symmetry. Nevertheless, it is worth to note that such an anisotropy is usually not preserved when changes in the extra-framework configuration occur. In $AlPO_4$-5, for example, for the sample compressed in silicone oil, K_c is considerably lower than K_a (15.5(3) *vs.* 9.6(2) GPa, respectively). This reverses when the crystal is compressed in *m.e.w.* as, in response to the "pillar effect" induced by the adsorbed H_2O molecules, the *bulk modulus* along the *c* direction triplicates, whereas K_a only increases by 50% (*i.e.,* 19.7(7) and 29.3(10) GPa, respectively).

The considerable change in the elastic anisotropy scheme, as a consequence of the adsorption of H_2O molecules, occurs also in leonhardite but with a less dramatic effect. In this natural zeolite (*i.e.,* LAU·14H_2O), the refined linear bulk moduli K_a, K_b and K_c were found to be 37(2), 95(9) and 20(2) GPa, respectively. In fully hydrated laumontite (*i.e.,* LAU·18H_2O), on the one hand it is respected the relation $K_b > K_a > K_c$, but on the other hand K_b decreases to 85(4) GPa, whereas K_a increases of about 80% and K_c doubled (Tab. 7.1).

In phillipsite, even though it was not observed any H_2O adsorption, the change of the elastic compressibility as a consequence of the rearrangement of the extra-framework H_2O molecules leads to

a considerable softening of the structure (*i.e.*, K_V falls from 89(8) to 18.8(7) GPa). Such a softening is coupled with a drastic change of the elastic anisotropy scheme, from $K_c > K_a, > K_b$ (107(8), 81(12), and 50(5) GPa, respectively) to $K_a > K_c, > K_b$ (30(2), 21(1), and 11(1) GPa, respectively).

Such peculiar behaviors are all a consequence of the crystal-fluid interaction through selective sorption on the new H_2O molecules, or, in the case of phillipsite, to a simple rearrangement of (the pre-existing) H_2O molecules inside the zeolitic channels.

Also armstrongite is characterized by a marked elastic anisotropy, as $K_c \sim K_b \sim \frac{1}{3} K_a$ for the low-*P* form, $K_c \sim K_b \sim 1.4\ K_a$ for the high-*P* form. In this case, the lack of structure solution and refinement of the high-pressure phase prevents a discussion about the reason of such a drastic change of the compressional pattern. However, the structure refinements of the low-pressure form suggest that, for this zeolite-like material, the extra-framework population does not play a significant role on the compressional behavior. In fact, similarly to elpidite, the phase transition is likely induced by the rotation of the ZrO_6 octahedra (Table 6.7 and 6.8). More in general, the case of armstrongite shows a clear difference about the role played by the extra-framework population on the compressional behavior if compared to zeolites: secondary in armstrongite, very important in zeolites.

7.3 Effects of crystal-fluid interaction on the framework deformation

The framework deformation mechanisms at high pressure can be deduced from the relevant structural parameters reported in Tables 3.2 ($AlPO_4$-5), 4.6 (leonhardite and laumontite), 5.4, 5.6, 5.7, 5.8, 5.9, 5.11 (phillipsite), 6.5, 6.7, 6.8 (armstrongite). According to Gatta et al. (2010a), the structure refinements confirm that the main mechanism through which the bulk compression is accommodated is the *tilting* of the quasi-rigid tetrahedra, which leads to a compression of the structural cavities. Such a behavior is predominant to the distortion of the TO_4 units as well as to the contraction of the T-O bonds. Tilting is reported in all the open-framework materials and has been proposed as the energetically less costly way for accommodating the *T*- and *P*-induced strain (Gatta 2008, Gatta et al. 2010a). The tilting of the TO_4 tetrahedra induces a framework deformation that mainly affects the rings of tetrahedra, which confine the channel and often represent the SBUs of a given framework type. Overall, in all the studied compounds of this study, the rings increase their ellipticity, even though differently in the different structures. For instance, in $AlPO_4$-5, the increase of the 4-, 6- and 12-mRs ellipticity is coupled with a major deviation from planarity on the (001) plane for the 4- and the 6-mRs [001] (Table 3.2). This particular behavior is observed in both the samples compressed in silicone oil and in *m.e.w.,* although the extra-H_2O molecules adsorbed by the sample compressed in the aqueous medium bestows a sort of stiffness to the framework. As a result, the deformation of the rings in the sample of $AlPO_4$-5 compressed in *m.e.w.* is modest if compared to that observed in silicone oil

(Table 3.2, Fig. 3.6). This is an outcome of the "pillar effect", caused by the adsorption of the H_2O molecules from the *P*- transmitting fluid. In $AlPO_4$-5 refined structure model, it is confirmed the presence of clusters of H-bonded H_2O molecules into the 12-mRs channels, with a helical configurations along the *c*-axis (Table 3.4), in fair agreement with the results of Floquet et al. (2004) and Demontis et al. (2012). Notably, the deviation from planarity of the 4- and the 6-mRs [001] in $AlPO_4$-5 at high pressure is not observed in laumontite, leonhardite, phillipsite and armstrongite.

Nevertheless, the "pillar effect" of the H_2O molecules acting as fillers, partially counteracting the effect of pressure, is observed also in hydrated laumontite (LAU·$18H_2O$), leading to a lower magnitude of the same deformation mechanisms observed in leonhardite, which is also reflected at the macroscopic scale by the different isothermal *bulk modulus* (Table 7.1). Comparing the ε parameters of the tetrahedra rings in laumontite and leonhardite, it is interesting to note that the 10-mRs are considerably less affected by the pressure-induced deformation with respect to the 6-mRs (Table 4.6). Within 3σ, there are no changes in the ellipticity ratio of the 10-mRs ($\varepsilon_{10m\text{-}Rs}$) up to 2.40 GPa in leonhardite and up to 2.65 GPa in laumontite and the most deformed rings are the 6-mRs. In leonhardite, this distortion is driven by a significant decrease of the O5-O5 diameter coupled with an increase of the O4-O4 one (Fig. 4.1, Fig. 4.9 and Table 4.6). The same distortion mechanism is observed also in the fully hydrated laumontite, although less pronounced (Fig. 4.9 and Table 4.6). The fact that the rings with a lower number of TO_4 units are the most affected by the stiffening induced by the adsorption of H_2O molecules is observed also in $AlPO_4$-5. In fact, up to 1.43 GPa in silicone oil and 1.36 GPa in *m.e.w.*, the $\varepsilon_{12\text{-}mRs}$ decreases by about 5.5% and then remains constant with *P* (Table 3.2). This is surely quite a difference, but it is considerable lower than the changes of the $\varepsilon_{6R[hk0]1\text{-}2}$ which remain almost constant if $AlPO_4$-5 is compressed in *m.e.w.* whereas change of about 35% and 20% respectively if $AlPO_4$-5 is compressed in silicone oil.

In phillipsite, despite no intrusion of molecules from the pressure transmitting fluid is detected, the H_2O configuration inside the 8-mRs changes dramatically and, as a result, it is observed a sort of "reverse pillar effect". In fact, at 2.57 GPa, the *s.o.f.* of the W4 H_2O site begins to decreases, leaving the W4 site completely empty at 4.85 GPa. Such a behavior is not commonly observed in zeolites, though it was previously observed by Ori at al. (2008) in gismondine. The lack of the W4 site leads to a drastic change of the deformation mechanisms, and of the elastic parameters as well, of phillipsite, as quantitatively represented by the ε parameters of the 8-mRs (001) and 8-mRs [010] SBUs. Until the occupancy factor of W4 is constant (within 3σ), *i.e.,* up to 2.57 GPa, $\varepsilon_{8\text{-}mRs(001)}$ and $\varepsilon_{8\text{-}mRs[010]}$ decrease by only 2% and 4%, respectively. From 2.57 GPa until 4.85 GPa, $\varepsilon_{8\text{-}mRs(001)}$ and $\varepsilon_{8\text{-}mRs[010]}$ decrease by 6% and 12%, respectively, which means that the deformation of the rings triplicates in magnitude, consistently with the fact that the K_{V0} decreases from 89(8) GPa to 18.8(7) GPa.

Overall, if we consider the comparative analysis of the compressional behavior (sections 7.1, *Comparative compressional behavior* and 7.2, *Elastic anisotropy and difference between zeolite and zeolite-like materials*) and the effects at the atomic scale described in this section, it can be argued that in all the zeolites studied in this research project, a strong dependence between framework geometry, extra-framework population (nature and configuration) and compressional behavior occurs. The rings (or channels) configuration affect drastically the compressional anisotropy. The extra-framework population, stable at room conditions, governs the sorption of new molecules at high pressure, and the penetration of new guest molecules in turn affect the compressional behavior (through the "pillar effect"). Nevertheless, even a *P*-induced re-arrangement of the extra-framework molecules (without any sorption of new molecules) can have a drastic effect on the bulk compression, as observed in phillipsite. In contrast, in the zeolite-like armstrongite, in which only minor changes in the H_2O distances occur, and where neither adsorption nor *P*-induced H_2O rearrangement is observed, the role of the extra-framework population is secondary.

7.4. Framework composition: deformation and adsorption

Can the chemical composition of the framework sites influence the behavior at high pressure? Moreover, which is the role played in terms of crystal-fluid interaction? The experimental findings obtained on $AlPO_4$-5 can allows us to answer to these questions. For this synthetic zeolite, the experimental findings suggest a considerable uptake of H_2O already at 0.2 GPa. This represents a further evidence that the adsorption of guest molecules is driven not only by the configuration of the framework and by the pre-existing extra-framework population, but it is also chemically dependent. In fact, compressing in *m.e.w.* (16:3:1) the pure SiO_2-analogue of $AlPO_4$-5, the synthetic SSZ-24, Kim et al. (2013) observed a monotonic contraction of the unit-cell volume, with a steeper slope than that observed for $AlPO_4$-5, leading to a lower *bulk modulus* (*i.e.*, 21.7(3) GPa, Kim et al. 2013). The authors suggested that the reason for the two compressional behaviors of the AFI frameworks would be related to the difference in the hydrophobicity of the framework and hence to the H_2O distribution into the channels. Compressing the synthetic SSZ-24 zeolite in the non-penetrating silicone oil, the *bulk modulus* was found similar to that obtained in *m.e.w.* (16:3:1), demonstrating that the measured compressibility of SSZ-24 is inherent to the AFI framework type. It can be argued that, despite having the same AFI topology, the *bulk modulus* of $AlPO_4$-5 in silicone oil (K_{V0} = 13.2 GPa) is different (lower) than its SiO_2-analougue. This is probably a consequence of the fact that the compressibility of the SiO_4 units differs (and it is lower) from the compressibility of the AlO_4 and PO_4 tetrahedra,

coupled with a more pronounced tilting effect of the AlO_4 and PO_4 tetrahedra if compared to the pure SiO_2 framework.

These considerations point out that, if the framework topology is critical in order to determine the compressibility of zeolites, even the chemical nature of the tetrahedral site plays an important role. Furthermore, it seems that chemical composition of the framework is critical also to determine whether the zeolite can adsorb polar molecules such as H_2O, CH_3OH, CH_3CH_2OH, *etc*... Cruciani et al. (2006) reported that the Si/Al ratio of the framework has a strong control on the hydration/dehydration processes in zeolites. Such a ratio influences also the number of extra-framework cations in the zeolitic structure, giving to the H_2O molecules the opportunity to be H-bonded to the oxygen atoms of the framework or coordinated to the extra-framework cations.

7.5 Fluid adsorption and particle size

It is commonly believed that small particle size, especially in polycrystalline samples, promotes the adsorption kinetics of the guest molecules. In this view, as already reported in the Chapter 3 (*High-pressure behavior and crystal-fluid interactions in $AlPO_4$-5*) and Chapter 4 (*High-pressure behavior and crystal-fluid interactions in laumontite*), a comparison between the high-pressure studies of this research project on leonhardite and $AlPO_4$-5 and the respectively previous studies of Lee et al. (2004b) and Kim et al. (2013) could result fruitful. The K_{V0} of the $AlPO_4$-5 crystal compressed in *m.e.w.* of our experiments is found clearly lower with respect to the one obtained by Kim et al. (2013) using a polycrystalline sample (22.2(9) GPa *vs*. 50.5(7) GPa, respectively). As already discussed in the Chapter 3 (*High-pressure behavior and crystal-fluid interactions in $AlPO_4$-5*), this is likely due to a more pronounced intrusion of H_2O molecules into the structural cavities of the polycrystalline material, enhanced by the higher surface/volume ratio of the powder with respect to single crystals.

Such a phenomenon is also found in our single-crystal experiments at room and high pressure on the hydration of leonhardite with respect to the powder studies of Fridriksson et al. (2003) and Lee et al. (2004b). In fact, the powder samples of Ca-leonhardite respond almost instantaneously to the RH change or to pressure increases. Instead, in the case of single crystals, at ambient pressure the hydration of leonhardite takes several hours, even if the crystal is immersed in pure H_2O. Furthermore, room-pressure experiments performed with several H_2O-rich mixture show that the hydration process in single crystals is probably also influenced and hindered by the presence of local defects which, generating occlusions of the structural voids, hinder the intra-crystalline diffusion of the adsorbed molecules. Concerning the high-pressure experiments, we observe that the sample of laumontite has to be compressed in a very H_2O-rich mixture, in order to maintain all the H_2O molecules adsorbed at

ambient pressure. On the contrary, Lee et al. (2004b) observed an almost instantaneous hydration of Ca-leonhardite powder compressed in the 16:3:1 *m.e.w.* mixture. This discrepancy confirm what already reported by Lotti et al. (2015a, b): the different behavior of polycrystalline *vs.* single crystal can be ascribed to the particle size of the zeolite samples, which strongly influences the magnitude of the H*P*-intrusion of fluid molecules in the structural voids.

7.6. Reversibility of the high-pressure phenomena

All the studied compounds, with the exception of $AlPO_4$-5, show a fully reversible behavior upon decompression, as can be inferred by the evolution of the unit-cell volumes *vs*. *P* (Fig. 3.5, 4.6, 5.2 and 6.5 for $AlPO_4$-5, leonhardite and laumontite, phillipsite and armstrongite, respectively), compressed in penetrating or in non-penetrating fluids. Unfortunately, structure refinements during decompression were not possible for all the materials here investigated. For $AlPO_4$-5 and leonhardite, the reversibility has to be inferred only on the basis of the unit-cell parameters data.

In the case of laumontite, phillipsite and armstrongite, the complete reversibility of the deformation behaviors induced by pressure can also be deduced by the Table 4.6 (pertaining the O-O distances in the 6-mRs and 10-mRs in laumontite), Fig. 5.3 and 5.4 (which show the evolution of the ε parameters of the different 8-mRs in phillipsite) and Fig. 6.6 (in which the O-O distances pertaining the 6-mRs in armstrongite are displayed). Notably, in armstrongite the structure refinements performed in decompression suggest a complete reversibility of the phase transition occurring between 4 and 5 GPa. Nevertheless, in this particular case, there is a broad hysteresis effect and the high-pressure phase of armstrongite seems to be stable (in decompression) at least down to 2.91(5) GPa.

7.7 Industrial and geological implications

As reported in the Chapter 1 (*Introduciton*), microporous materials can be useful as storage of mechanical energy; in this light, it is worth to examine the decompression path of $AlPO_4$-5. In $AlPO_4$-5, the unit-cell parameters refined from the data collected in decompression at 0.82(P15d) and 0.75 (P16d) GPa (Table 3.1) reveal that the bulk compression is not fully recovered at these pressures. This fact, along with the results here reported (which show that the zeolite $AlPO_4$-5 is a promising material for the *P*-induce selective sorption of a relatively high number of H_2O molecules per unit cell), suggest that this zeolite could represent a system for the storage/dissipation of mechanical energy. In particular, because the volume of $AlPO_4$-5 after decompression is lower than its initial value (before compression), it seems that this microporous compound could be used as a *bumper*, thus as a sink of mechanical energy. The fact that the *P*-induced hydration occurs already at very low pressure is also

promising for potential industrial applications, as the use of modest pressures would be highly desirable for practical applications (Gatta et al. 2018).

As far as the geological implications are concerned, the experiments here reported suggests that the penetration phenomenon is likely to be active even at very low pressures (2 kbar or lower, for instance in $AlPO_4$-5 and in leonhardite). This is very interesting because zeolites (in particular some Ca-zeolites as laumontite) are believed to be stable at those pressures. Geological fluids can, therefore, interact efficiently with zeolites, enhancing a significant fluid-to-crystal mass transfer. Thus, pressure can promote the ability of zeolites, as microporous materials, to act as geochemical traps of small molecules, even at room temperature. In this light, the role of zeolites as fluids-carrier in geological environments, such as oceanic crust subductions, should be carefully re-considered in geophysical modelling, especially in view of the recent findings of the Ocean Drilling Project: zeolites are pervasively diffused in oceanic basalts, which will be subducted at *P* and *T* in which they can uptake and then release significant mass of fluids.

As pointed out by several studies (*e.g.,* Lotti et al. 2016, Gatta et al. 2018, Kong et al. 2018), and observed in this thesis, there must be several variables that govern the sorption phenomena at high pressure beyond the "free diameters" of the framework cavities. This is probably the case of the chemical nature and the configuration of the extra-framework population and the partial pressure of the penetrating molecule in the fluid (if mixed with other non-penetrating molecules, *e.g.,* the $P(H_2O)$ in a mixture of alcohol–H_2O, as shown for hydration of leonhardite). Moreover, is also likely that the rate of the *P*-increase, the surface/volume ratio of the crystallites under investigations, and the temperature at which the experiment is conducted (Gatta et al. 2018) play a critical role in the hydration process. In particular, it is highly likely that the combined effect of pressure and temperature would improve the magnitude of the pressure induce hydration, as previously observed in other zeolites (Gatta and Lee 2014 and references therein, Kong et al. 2018). Therefore, combining the effect of (moderate) temperature and pressure: 1) would allow to verify the behavior of zeolites at the *P*-*T* conditions in which are stable in hydrothermal systems (and therefore also investigate their role as potential carrier of H_2O, CO_2 or even H_2S, CH_4, Ar, Xe, or Kr); 2) could results relevant in order to employ zeolites in sustainable industrial applications.

Acknowledgments

First of all, I would like to thank my supervisor Prof. Diego G. Gatta for his many advices, concerning not only the research experiments of my Ph.D., but also for his presence and supervision during the entire process of writing and publishing my first results. Dr. Paolo Lotti and Prof. Marco Melini are deeply thanked for their help during these three years, without them I would have had a very hard time. Dr. Michael Hanfland (ESRF, Grenoble) and Dr. Hans-Peter Liermann (DESY, Hamburg) are thanked for their assistance during the high-pressure synchrotron experiment at their respective beamlines. I would like also to thank all the co-authors of my articles along with all the people that gave me advices during the Ph.D. for their contributes.

I want to thanks my office mates Gianluca, Justine and Luca: having them in these years (or months) was really funny and positive. In this acknowledgments, I cannot forget to mention all the people of the “Kitchen” and my present flat mates.

Finally, I’d like to thank my family and my friends for their continuous support.

APPENDIX: TABLES

Table 3.1: Unit-cell parameters of the zeolite $AlPO_4$-5 based on the experiment performed with the crystal in air and on the high-*P* experiments in silicone oil and in *m.e.w.*

Experiment	*P*	(GPa)	*a* (Å)	*c* (Å)	*V* (Å^3)
AIR		0.0001	13.7175(12)	8.4350(8)	1374.6(2)
Silicone oil	P_1	0.25(5)	13.6921(8)	8.326(3)	1351.8(4)
"	P_2	0.39(5)	13.6470(8)	8.302(3)	1339.0(4)
"	P_3	0.54(5)	13.6031(8)	8.264(3)	1324.4(4)
"	P_4	0.70(5)	13.5723(8)	8.228(3)	1312.5(4)
"	P_5	0.94(5)	13.5122(8)	8.185(3)	1294.1(4)
"	P_6	1.17(5)	13.4663(7)	8.152(3)	1280.3(4)
"	P_7	1.43(5)	13.3984(7)	8.108(2)	1260.6(3)
"	P_8	1.65(5)	13.3568(10)	8.080(3)	1248.4(5)
m.e.w.	P_0	0.0001	13.7179(10)	8.4191(5)	1372.06(17)
"	P_1	0.18(5)	13.6747(15)	8.4316(6)	1365.4(2)
"	P_2	0.36(5)	13.6472(15)	8.4175(6)	1357.7(3)
"	P_3	0.58(5)	13.6095(14)	8.3996(6)	1347.3(2)
"	P_4	0.77(5)	13.5656(14)	8.3823(6)	1335.9(3)
"	P_5	1.02(5)	13.5264(14)	8.3654(6)	1325.5(2)
"	P_6	1.36(5)	13.4498(14)	8.3307(6)	1305.1(2)
"	P_7	1.65(5)	13.4068(13)	8.3126(6)	1293.9(2)
"	P_8	2.05(5)	13.3258(11)	8.2754(7)	1272.64(18)
"	P_9	2.44(5)	13.2539(11)	8.2459(6)	1254.46(19)
"	P_{10}	2.94(5)	13.1668(11)	8.2068(5)	1232.15(18)
"	P_{11}	3.77(5)	13.0366(14)	8.1474(6)	1199.2(2)
"	P_{12}	4.77(5)	12.8980(14)	8.0776(7)	1163.7(2)
"	P_{13}	5.48(5)	12.8084(18)	8.0399(12)	1142.3(3)
"	P_{14}	6.51(5)	12.717(2)	7.9967(14)	1120.0(3)
"	P_{15d}	0.82(5)	13.2975(14)	8.3213(6)	1274.3(2)
"	P_{16d}	0.75(5)	13.3356(14)	8.3412(6)	1284.6(2)
d = in decompression					

Table 3.2. High-pressure evolution of: 12-mRs-channels and pseudo-cages volumes and relevant interatomic distances. 4-mRs- and 6-mRs[001]-deviate from planarity on the (001) plane. ε = $d1/d2$ = $(O1–O3/O1–O3)_1$ and $(O1–O4/O1–O4)_2$ are the distortion parameters of the 6-mRs $[hk0]_{1,2}$ windows, (see section 3.5, *Discussion*, and Fig. 3.2)

Exp.	P	(GPa)	V_{ch} (Å^3)	V_{cg} (Å^3)	$O1–O1_{ch}$ (Å)	$O3–O3_{ch}$ (Å)	$O3\text{-}O3_{4R}$ (Å)	$O4–O4_{4R}$ (Å)	Δz_{4R} (Å)	$\Delta z_{6R[001]}$ (Å)	$\varepsilon_{6R[hk0]1}$	$\varepsilon_{6R[hk0]2}$
AIR		0.0001	671(3)	358.5(9)	10.11(1)	10.015(8)	3.702(8)	3.52(2)	0.1080(7)	0.155(1)	1.056(9)	1.008(6)
Sil.	P_1	0.25(5)	652(4)	360(1)	10.02(2)	9.95(1)	3.75(1)	3.64(2)	0.0416(7)	0.225(5)	1.11(2)	1.08(2)
"	P_2	0.39(5)	645(4)	357.0(9)	9.96(2)	9.93(1)	3.73(1)	3.639(19)	0.174(3)	0.174(3)	1.09(2)	1.01(2)
"	P_3	0.54(5)	640(4)	351(1)	9.94(2)	9.93(1)	3.70(1)	3.59(2)	0.174(4)	0.306(7)	1.15(3)	1.07(2)
"	P_4	0.70(5)	637(4)	344(1)	9.99(2)	9.86(1)	3.73(1)	3.53(2)	0.115(6)	0.44(2)	1.24(7)	1.17(6)
"	P_5	0.94(5)	626(6)	334.6(9)	9.92(3)	9.82(2)	3.65(2)	3.45(2)	0.090(1)	0.434(6)	1.25(2)	1.18(2)
"	P_6	1.17(5)	622(6)	322(1)	9.82(3)	9.90(2)	3.59(2)	3.31(3)	0.302(8)	0.66(1)	1.39(4)	1.20(4)
"	P_7	1.43(5)	617(6)	305(1)	9.71(3)	9.98(2)	3.52(2)	3.05(3)	0.284(8)	0.74(2)	1.41(4)	1.32(4)
m.e.w.	P_0	0.0001	632(5)	369(1)	9.85(2)	9.71(2)	4.02(2)	3.70(3)	0.008420(7)	0.2484(2)	1.103(9)	1.096(9)
"	P_1	0.18(5)	631(5)	371(1)	9.84(2)	9.68(2)	4.00(2)	3.76(2)	0.06914(5)	0.3221(2)	1.121(9)	1.096(9)
"	P_2	0.36(5)	629(5)	367(1)	9.86(2)	9.65(2)	4.00(2)	3.70(2)	0.05892(5)	0.3207(3)	1.126(9)	1.103(9)
"	P_3	0.58(5)	619(5)	365(1)	9.74(2)	9.64(2)	3.97(2)	3.71(2)	0.10332(8)	0.3351(3)	1.130(9)	1.085(9)
"	P_4	0.77(5)	612(5)	361(1)	9.67(2)	9.61(2)	3.96(2)	3.69(3)	0.08634(7)	0.3688(3)	1.15(1)	1.108(9)
"	P_5	1.02(5)	606(5)	362(1)	9.70(2)	9.51(2)	4.02(2)	3.74(3)	0.08365(7)	0.3430(3)	1.15(1)	1.090(9)
"	P_6	1.36(5)	613(5)	350(1)	9.74(2)	9.62(2)	3.83(2)	3.62(3)	0.06665(6)	0.3416(3)	1.16(1)	1.094(9)
"	P_7	1.65(5)	600(5)	345(1)	9.76(2)	9.41(2)	4.01(2)	3.57(3)	0.09310(8)	0.3741(3)	1.16(1)	1.077(9)
"	P_8	2.05(5)	571(5)	341(1)	9.51(2)	9.24(2)	4.11(2)	3.58(3)	0.05793(6)	0.3807(4)	1.16(1)	1.087(9)
"	P_9	2.44(5)	548(7)	339(1)	9.28(2)	9.13(3)	4.16(3)	3.59(4)	0.1897(2)	0.1979(3)	1.07(2)	1.12(1)

Table 3.3. Details pertaining to the structure refinements of zeolite $AlPO_4$-5 from the experimental data with the crystal in air and from the high-pressure experiments in silicone oil and *m.e.w.*(Lotti et al. 2016).

	AIR	P_1 s.o. 0.25(5) GPa	P_2 s.o. 0.39(5) GPa	P_3 s.o. 0.54(5) GPa	P_4 s.o. 0.70(5) GPa	P_5 s.o. 0.94(5) GPa	P_6 s.o. 1.17(5) GPa	P_7 s.o. 1.43(5) GPa
min≤*h*≤max	-16; 16	-13; 13	-13; 13	-13; 13	-13; 13	-13; 13	-13; 13	-13; 13
min≤*k*≤max	-12; 16	-13; 13	-13; 13	-13; 13	-13; 13	-13; 13	-13; 13	-13; 13
min≤*l*≤max	-10; 10	-4; 5	-4; 5	-4; 5	-4; 5	-4; 5	-4; 5	-4; 5
Unique reflections	871	289	291	290	287	281	280	263
Observed reflections $I > 3\sigma(I)$	388	121	128	124	127	111	96	60
R_{int} (obs)	0.0322	0.0322	0.0319	0.0304	0.0313	0.0376	0.0417	0.0585
R_{int} (all)	0.0397	0.0397	0.0392	0.0401	0.0416	0.0493	0.0565	0.0833
Number l.s. parameters	73	33(+36)*	33(+36)*	33(+36)*	33(+36)*	31(+36)*	31(+36)*	31(+36)*
R_1 (obs)	0.0649	0.0507	0.0505	0.0616	0.0761	0.0728	0.1007	0.0881
R_1 (all)	0.1213	0.1331	0.1326	0.1507	0.1724	0.1968	0.2480	0.3386
wR_1 (obs)	0.0669	0.0464	0.0502	0.0542	0.0631	0.0654	0.0902	0.0658
wR_1 (all)	0.0714	0.0519	0.0551	0.0602	0.0705	0.0762	0.1010	0.0849
Residuals (e^-/Å^3)	+0.27; -0.26	+0.46; -0.38	+0.43; -0.34	+ 0.36; -0.33	+0.48; -0.49	+ 0.46; -0.46	+0.51; -0.62	+0.52; -0.78

	P_0 *m.e.w.* 0.0001 GPa	P_1 *m.e.w.* 0.18(5) GPa	P_2*m.e.w.* 0.36(5) GPa	P_3 *m.e.w.* 0.58(5) GPa	P_4 *m.e.w.* 0.77(5) GPa	P_5 *m.e.w.* 1.02(5) GPa	P_6 *m.e.w.* 1.36(5) GPa	P_7 *m.e.w.* 1.65(5) GPa
min≤*h*≤max	-6; 10	-6; 10	-6; 10	-5; 9	-6; 10	-6; 10	-6; 10	-6; 10
min≤*k*≤max	-11; 7	-11; 7	-11; 7	-11; 6	-10; 7	-10; 7	-11; 7	-10; 7
min≤*l*≤max	-9; 9	-9; 9	-9; 9	-9; 9	-9; 9	-9; 9	-9; 9	-9; 9
Unique reflections	441	428	431	403	409	415	402	394

Observed reflections $I > 3\sigma(I)$	281	249	227	209	197	182	160	148
R_{int} (obs)	0.0584	0.0863	0.0826	0.0808	0.0931	0.0666	0.0695	0.0890
R_{int} (all)	0.0606	0.0896	0.0863	0.0845	0.0983	0.0732	0.0756	0.0958
Number l.s.	35(+36)*	35(+36)*	35(+36)*	35(+36)*	35(+36)*	35(+36)*	35(+36)*	35(+36)*
R_1 (obs)	0.0918	0.0912	0.0921	0.0826	0.0875	0.0941	0.0887	0.0819
R_1 (all)	0.1326	0.1386	0.1540	0.1385	0.1634	0.1792	0.2002	0.1927
wR_1 (obs)	0.0857	0.0871	0.0883	0.0794	0.0880	0.0912	0.0789	0.0781
wR_1 (all)	0.0894	0.0907	0.0926	0.0827	0.0933	0.0968	0.0862	0.0855
Residuals (e^-/Å^3)	+0.43 -0.44	+ 0.44 -0.36	+ 0.40 -0.41	+0.28 -0.33	+ 0.36 -0.41	+ 0.38 -0.43	+ 0.33 -0.36	+0.30 -0.30

	P_8 *m.e.w.* 2.05(5) GPa	P_9 *m.e.w.* 2.44(5) GPa
min≤*h*≤max	-14; 14	-14; 13
min≤*k*≤max	-7; 11	-6; 9
min≤*l*≤max	-8; 8	-8; 8
Unique reflections	398	379
Observed reflections $I > 3\sigma(I)$	136	112
R_{int} (obs)	0.0599	0.0760
R_{int} (all)	0.0708	0.0875

	P_8 *m.e.w.* 2.05(5) GPa	P_9 *m.e.w.* 2.44(5) GPa
Number l.s. parameters	35(+36)*	35(+36)*
R_1 (obs)	0.0805	0.0863
R_1 (all)	0.2038	0.2541
wR_1 (obs)	0.0780	0.0939
wR_1 (all)	0.0899	0.1061
Residuals (e^-	+0.43; -0.42	+ 0.53; -0.55

* (+36): The anisotropic displacement parameters of the framework atoms (36 variables) have been refined, not simultaneously, in successive cycles. See Chpater 3 (*High-pressure behavior and crystal-fluid interaction in $AlPO_4$-5*), for further details.

Table 3.4. Site fractional coordinates, occupancy factors (*s.o.f.*) and equivalent/isotropic displacement parameters ($U_{eq/iso}$, Å^2), from the structure refinements based on the experiment with the crystal in air and the high-pressure experiments in silicone oil and *m.e.w.*

Site	*P* (GPa)	*s.o.f.*	*x*	*y*	*z*	$U_{eq/iso}$
AIR experiment						
Al	0.0001	1.0	0.45295(19)	0.33062(17)	0.0888(8)	0.082(1)
P	"	1.0	0.4566(3)	0.3356(3)	0.4602(9)	0.119(4)
O1	"	1.0	0.4256(5)	0.2077(7)	0.0042(15)	0.144(4)
O2	"	1.0	0.4452(6)	0.3269(6)	0.2829(14)	0.163(5)
O3	"	1.0	0.3661(5)	0.3640(6)	0.5098(14)	0.143(4)
O4	"	1.0	0.5785(8)	0.4303(9)	0.0226(19)	0.172(5)
W1	"	0.100(8)	-0.287(3)	0.367(3)	0.209(4)	0.08
W2	"	0.085(8)	0.122(4)	0.223(4)	0.211(6)	0.08
W3	"	0.17(1)	0.162(2)	0.198(2)	0.314(2)	0.08
W4	"	0.140(8)	0.110(2)	0.175(3)	0.087(3)	0.08
W5	"	0.20(2)	0	0	0.489(5)	0.08
Silicone oil high-*P* experiment						
Al	0.25(5)	1.0	0.4557(8)	0.3345(6)	0.075(3)	0.080
	0.39(5)	1.0	0.4554(7)	0.3355(5)	0.082(3)	0.083
	0.54(5)	1.0	0.4557(8)	0.3365(6)	0.081(5)	0.091
	0.70(5)	1.0	0.4591(8)	0.3406(7)	0.08(1)	0.108
	0.94(5)	1.0	0.4623(9)	0.3415(8)	0.030(2)	0.127
	1.17(5)	1.0	0.462(1)	0.341(1)	0.183(5)	0.154
	1.43(5)	1.0	0.448(1)	0.339(1)	0.180(6)	0.210
P	0.25(5)	1.0	0.4557(7)	0.3327(6)	0.445(3)	0.099
	0.39(5)	1.0	0.4561(7)	0.3327(6)	0.453(3)	0.101
	0.54(5)	1.0	0.4566(7)	0.3320(6)	0.451(5)	0.102
	0.70(5)	1.0	0.4544(7)	0.3308(7)	0.45(1)	0.107
	0.94(5)	1.0	0.4540(8)	0.3298(8)	0.387(2)	0.117
	1.17(5)	1.0	0.4570(9)	0.327(1)	0.532(5)	0.127
	1.43(5)	1.0	0.4681(8)	0.3230(9)	0.530(6)	0.206
O1	0.25(5)	1.0	0.4224(8)	0.208(1)	-0.013(5)	0.110
	0.39(5)	1.0	0.4214(7)	0.204(1)	0.012(5)	0.130
	0.54(5)	1.0	0.4217(8)	0.207(1)	0.000(6)	0.125
	0.70(5)	1.0	0.425(1)	0.215(1)	-0.02(1)	0.147
	0.94(5)	1.0	0.424(1)	0.215(1)	-0.074(4)	0.161
	1.17(5)	1.0	0.421(2)	0.219(2)	0.064(6)	0.272
	1.43(5)	1.0	0.418(2)	0.223(2)	0.053(7)	0.255

Site	*P* (GPa)	*s.o.f.*	*x*	*y*	*z*	$U_{eq/iso}$ (Å^2)
O2	0.25(5)	1.0	0.434(1)	0.316(2)	0.273(3)	0.196
	0.39(5)	1.0	0.438(1)	0.318(1)	0.280(3)	0.181
	0.54(5)	1.0	0.432(1)	0.312(2)	0.279(5)	0.239
	0.70(5)	1.0	0.425	0.302(2)	0.28(1)	0.214
	0.94(5)	1.0	0.414(2)	0.293(2)	0.218(3)	0.242
	1.17(5)	1.0	0.402(2)	0.303(3)	0.369(5)	0.228
	1.43(5)	1.0	0.392(2)	0.291(2)	0.377(6)	0.188
O3	0.25(5)	1.0	0.3680(6)	0.3586(9)	0.509(4)	0.107
	0.39(5)	1.0	0.3692(7)	0.3582(9)	0.512(3)	0.106
	0.54(5)	1.0	0.3714(7)	0.3579(9)	0.516(6)	0.106
	0.70(5)	1.0	0.3700(8)	0.356(1)	0.52(1)	0.108
	0.94(5)	1.0	0.3724(9)	0.359(1)	0.468(4)	0.145
	1.17(5)	1.0	0.374(1)	0.360(1)	0.608(8)	0.131
	1.43(5)	1.0	0.387(1)	0.356(1)	0.609(8)	0.154
O4	0.25(5)	1.0	0.5869(9)	0.4339(10)	0.014(5)	0.142
	0.39(5)	1.0	0.5898(8)	0.4366(8)	0.033(4)	0.140
	0.54(5)	1.0	0.5914(8)	0.4399(9)	0.037(5)	0.081
	0.70(5)	1.0	0.5932(8)	0.4445(9)	0.04(1)	0.207
	0.94(5)	1.0	0.5938(8)	0.448(1)	-0.021(3)	0.258
	1.17(5)	1.0	0.595(1)	0.457(1)	0.145(5)	0.214
	1.43(5)	1.0	0.584(1)	0.454(1)	0.144(6)	0.251
W1	0.25(5)	0.14(2)	2/3	1/3	0.17(2)	0.08
	0.39(5)	0.09(2)	2/3	1/3	0.19(3)	0.08
	0.54(5)	0.06(2)	2/3	1/3	0.20(6)	0.08
	0.70(5)	0.02(3)	2/3	1/3	0.18(16)	0.08
W2	0.25(5)	0.15(2)	0.112(5)	-0.025(5)	0.20(2)	0.08
	0.39(5)	0.21(3)	0.146(7)	0.008(7)	0.148(7)	0.08
	0.54(5)	0.26(4)	0.150(6)	0.015(6)	0.136(9)	0.08
	0.70(5)	0.28(2)	0.143(5)	0.000(5)	0.14(1)	0.08
	0.94(5)	0.35(2)	0.152(3)	0.017(3)	0.054(8)	0.08
	1.17(5)	0.19(5)	0.207(8)	0.11(1)	0.25(3)	0.08
	1.43(5)	0.44(6)	0.189(6)	0.127(8)	0.22(1)	0.08
W3	0.25(5)	0.30(2)	0.197(2)	0.141(3)	-0.327(7)	0.08
	0.39(5)	0.29(4)	0.203(5)	0.138(3)	-0.327(8)	0.08
	0.54(5)	0.22(4)	0.208(7)	0.141(5)	-0.32(1)	0.08
	0.70(5)	0.24(3)	0.205(4)	0.140(4)	-0.31(2)	0.08
	0.94(5)	0.16(2)	0.216(5)	0.164(6)	-0.25(2)	0.08
	1.17(5)	0.39(3)	0.164(4)	0.132(4)	-0.30(1)	0.08
	1.43(5)	0.10(4)	0.10(3)	0.10(2)	-0.34(7)	0.08

Site	*P* (GPa)	*s.o.f.*	*x*	*y*	*z*	$U_{eq/iso}$ (Å^2)
W4	0.25(5)	0.18(2)	0.156(4)	0.050(4)	-0.026(15)	0.08
	0.39(5)	0.19(2)	.155(4)	0.065(4)	-0.089(8)	0.08
	0.54(5)	0.22(2)	0.162(4)	0.074(4)	-0.09(1)	0.08
	0.70(5)	0.25(2)	0.162(3)	0.088(3)	-0.06(1)	0.08
	0.94(5)	0.31(2)	0.165(3)	0.087(4)	-0.12(1)	0.08
	1.17(5)	0.25(4)	0.172(7)	0.098(5)	0.05(2)	0.08
	1.43(5)	0.29(6)	0.18(1)	0.06(1)	0.14(2)	0.08
(16:3:1) methanol:ethanol:water high-*P* experiment						
Al	0.0001	1.0	0.4486(5)	0.3312(5)	0.071(1)	0.076
	0.18(5)	1.0	0.4514(7)	0.3328(6)	0.0862(9)	0.107
	0.36(5)	1.0	0.4515(7)	0.3326(6)	0.0857(8)	0.108
	0.58(5)	1.0	0.4502(7)	0.331(6)	0.0865(8)	0.122
	0.77(5)	1.0	0.4491(8)	0.3311(7)	0.086(1)	0.135
	1.02(5)	1.0	0.4477(8)	0.3335(8)	0.0897(8)	0.144
	1.36(5)	1.0	0.4470(9)	0.3340(8)	0.0911(9)	0.169
	1.65(5)	1.0	0.4454(8)	0.3361(8)	0.0891(9)	0.184
	2.05(5)	1.0	0.4433(9)	0.3373(8)	0.089(1)	0.202
	2.44(5)	1.0	0.442(1)	0.334(1)	0.085(1)	0.229
P	0.0001	1.0	0.4594(5)	0.3335(5)	0.442(1)	0.081
	0.18(5)	1.0	0.4558(4)	0.3317(5)	0.4560(9)	0.094
	0.36(5)	1.0	0.4557(4)	0.3319(5)	0.4551(8)	0.094
	0.58(5)	1.0	0.4549(5)	0.3308(5)	0.4562(8)	0.103
	0.77(5)	1.0	0.4561(5)	0.3306(5)	0.4555(9)	0.104
	1.02(5)	1.0	0.4581(5)	0.3312(6)	0.4606(9)	0.102
	1.36(5)	1.0	0.4578(6)	0.3311(6)	0.4629(8)	0.113
	1.65(5)	1.0	0.4585(6)	0.3290(7)	0.4619(9)	0.123
	2.05(5)	1.0	0.4589(7)	0.3275(7)	0.461(1)	0.141
	2.44(5)	1.0	0.4582(8)	0.3240(8)	0.452(1)	0.143
O1	0.0001	1.0	0.415(1)	0.198(1)	0.015(2)	0.127
	0.18(5)	1.0	0.415(1)	0.200(1)	0.029(2)	0.139
	0.36(5)	1.0	0.417(1)	0.199(1)	0.030(2)	0.148
	0.58(5)	1.0	0.413(1)	0.199(1)	0.028(2)	0.155
	0.77(5)	1.0	0.412(1)	0.197(1)	0.030(2)	0.165
	1.02(5)	1.0	0.414(2)	0.202(1)	0.024(2)	0.160
	1.36(5)	1.0	0.418(2)	0.206(1)	0.018(2)	0.183
	1.65(5)	1.0	0.420(2)	0.207(1)	0.026(2)	0.195
	2.05(5)	1.0	0.412(2)	0.203(1)	0.030(2)	0.224
	2.44(5)	1.0	0.404(2)	0.192(2)	0.043(3)	0.227

Site	*P* (GPa)	*s.o.f.*	*x*	*y*	*z*	$U_{eq/iso}$ (Å^2)
O2	0.0001	1.0	0.462	0.350(2)	0.272(1)	0.135
	0.18(5)	1.0	0.465(1)	0.352(2)	0.287(1)	0.140
	0.36(5)	1.0	0.464(1)	0.352(2)	0.286(1)	0.149
	0.58(5)	1.0	0.458(1)	0.345(2)	0.286(1)	0.156
	0.77(5)	1.0	0.456(1)	0.344(2)	0.287(1)	0.179
	1.02(5)	1.0	0.465(2)	0.357(2)	0.288(1)	0.207
	1.36(5)	1.0	0.473(2)	0.369(2)	0.290(1)	0.232
	1.65(5)	1.0	0.479(2)	0.372(2)	0.290(2)	0.239
	2.05(5)	1.0	0.479(2)	0.374(2)	0.289(2)	0.273
	2.44(5)	1.0	0.474(3)	0.375(3)	0.283(2)	0.320
O3	0.0001	1.0	0.359(1)	0.349(1)	0.485(2)	0.114
	0.18(5)	1.0	0.358(1)	0.350(2)	0.499(2)	0.144
	0.36(5)	1.0	0.357(1)	0.350(2)	0.499(2)	0.162
	0.58(5)	1.0	0.359(1)	0.350(2)	.501(2)	0.169
	0.77(5)	1.0	0.359(1)	0.349(1)	0.496(2)	0.173
	1.02(5)	1.0	0.355(1)	0.348(2)	0.493(2)	0.170
	1.36(5)	1.0	0.361(1)	0.355(2)	0.485(2)	0.186
	1.65(5)	1.0	0.357(1)	0.344(2)	0.492(2)	0.190
	2.05(5)	1.0	0.355(2)	0.338(2)	0.491(2)	0.209
	2.44(5)	1.0	0.354(2)	0.334(2)	0.496(3)	0.203
O4	0.0001	1.0	0.580(1)	0.424(1)	-0.014(2)	0.141
	0.18(5)	1.0	0.583(1)	0.424(1)	-0.009(2)	0.144
	0.36(5)	1.0	0.582(1)	0.425(1)	-0.008(2)	0.146
	0.58(5)	1.0	0.5808(9)	0.424(1)	-0.012(2)	0.153
	0.77(5)	1.0	0.578(2)	0.421(1)	-0.014(2)	0.162
	1.02(5)	1.0	0.575(1)	0.415(1)	-0.017(2)	0.167
	1.36(5)	1.0	0.570(1)	0.415(1)	-0.023(2)	0.203
	1.65(5)	1.0	0.572(1)	0.418(1)	-0.019(2)	0.211
	2.05(5)	1.0	0.573(2)	0.418(1)	-0.016(3)	0.213
	2.44(5)	1.0	0.583(2)	0.427(2)	0.019(3)	0.199
W1	0.0001	0.30(3)	2/3	1/3	0.205(4)	0.08
	0.18(5)	0.33(3)	2/3	1/3	0.207(4)	0.08
	0.36(5)	0.36(3)	2/3	1/3	0.204(4)	0.08
	0.58(5)	0.36(3)	2/3	1/3	0.212(3)	0.08
	0.77(5)	0.33(3)	2/3	1/3	0.215(4)	0.08
	1.02(5)	0.36(3)	2/3	1/3	0.217(4)	0.08
	1.36(5)	0.41(3)	2/3	1/3	0.225(4)	0.08
	1.65(5)	0.30(3)	2/3	1/3	0.219(5)	0.08
	2.05(5)	0.33(3)	2/3	1/3	0.217(5)	0.08

Site	*P* (GPa)	*s.o.f.*	*x*	*y*	*z*	$U_{eq/iso}$ (Å^2)
	2.44(5)	0.45(6)	2/3	1/3	0.208(4)	0.08
W2	0.0001	0.29(2)	0.224(3)	0.229(3)	0.209(2)	0.08
	0.18(5)	0.27(2)	0.210(3)	0.240(3)	0.22(3)	0.08
	0.36(5)	0.32(2)	0.212(2)	0.233(3)	0.225(2)	0.08
	0.58(5)	0.30(2)	0.201(2)	0.230(3)	0.227(2)	0.08
	0.77(5)	0.27(2)	0.197(2)	0.231(3)	0.227(3)	0.08
	1.02(5)	0.37(2)	0.211(3)	0.247(3)	0.220(2)	0.08
	1.36(5)	0.39(2)	0.205(2)	0.243(2)	0.227(2)	0.08
	1.65(5)	0.34(2)	0.216(3)	0.254(3)	0.226(2)	0.08
	2.05(5)	0.28(2)	0.220(4)	0.256(4)	0.229(3)	0.08
	2.44(5)	0.28(3)	0.222(5)	0.245(4)	0.233(4)	0.08
W3	0.0001	0.21(2)	0.06(2)	0.084(7)	0.349(3)	0.08
	0.18(5)	0.22(2)	0.08(1)	0.104(4)	0.343(3)	0.08
	0.36(5)	0.22(2)	0.08(1)	0.108(5)	0.344(3)	0.08
	0.58(5)	0.22(2)	0.088(8)	0.115(5)	0.341(3)	0.08
	0.77(5)	0.26(2)	0.087(8)	0.115(4)	0.338(2)	0.08
	1.02(5)	0.31(2)	0.077(7)	0.109(3)	0.327(2)	0.08
	1.36(5)	0.29(2)	0.065(6)	0.101(4)	0.326(2)	0.08
	1.65(5)	0.33(2)	0.070(4)	0.114(3)	0.327(2)	0.08
	2.05(5)	0.34(2)	0.069(3)	0.118(3)	0.325(2)	0.08
	2.44(5)	0.45(3)	0.059(4)	0.114(3)	0.324(3)	0.08
W4	0.0001	0.16(2)	0.087(5)	0.170(6)	0.447(5)	0.08
	0.18(5)	0.27(2)	0.100(3)	0.179(4)	0.467(3)	0.08
	0.36(5)	0.29(2)	0.099(3)	0.176(3)	0.465(2)	0.08
	0.58(5)	0.28(1)	0.107(3)	0.176(3)	0.460(2)	0.08
	0.77(5)	0.30(2)	0.107(3)	0.171(3)	0.459(3)	0.08
	1.02(5)	0.29(2)	0.107(4)	0.162(3)	0.459(3)	0.08
	1.36(5)	0.25(2)	0.113(5)	0.161(3)	0.458(3)	0.08
	1.65(5)	0.25(2)	0.103(5)	0.143(4)	0.467(3)	0.08
	2.05(5)	0.28(2)	0.091(4)	0.132(4)	0.465(3)	0.08
	2.44(5)	0.40(3)	0.082(5)	0.117(4)	0.461(3)	0.08
W5	0.0001	0.22(5)	0.0	0.0	0.555(9)	0.08
	0.18(5)	0.30(6)	0.0	0.0	0.395(7)	0.08
	0.36(5)	0.42(6)	0.0	0.0	0.395(5)	0.08
	0.58(5)	0.32(5)	0.0	0.0	0.392(6)	0.08
	0.77(5)	0.24(6)	0.0	0.0	0.400(8)	0.08
	1.02(5)	0.54(6)	0.0	0.0	0.400(5)	0.08
	1.36(5)	0.48(6)	0.0	0.0	0.393(5)	0.08
	1.65(5)	0.30(6)	0.0	0.0	0.379(8)	0.08
	2.05(5)	0.30(6)	0.0	0.0	0.382(9)	0.08
	2.44(5)	0.6(1)	0.0	0.0	0.384(7)	0.08

Table 3.5. Refined anisotropic displacement parameters of the framework atoms from the structure refinements based on the experiment with the crystal in air and the high-pressure experiments in silicone oil and *m.e.w.* The anisotropic displacement parameters from the high-pressure data have been refined, not simultaneously, in successive cycles. See the text, section 3 (*High-pressure behavior and crystal-fluid interaction in $AlPO_4$-5*), for further details.

Site	*P* (GPa)	U_{11}	U_{22}	U_{33}	U_{12}	U_{13}	U_{23}
AIR experiment							
Al	0.0001	0.101(2)	0.084(2)	0.081(2)	0.061(1)	0.001(3)	0.001(2)
P	"	0.157(3)	0.113(3)	0.105(3)	0.080(2)	-0.022(3)	-0.014(2)
O1	"	0.140(4)	0.112(6)	0.172(5)	0.059(5)	-0.026(5)	-0.066(4)
O2	"	0.215(6)	0.183(6)	0.089(4)	0.098(5)	0.002(9)	0.024(5)
O3	"	0.113(5)	0.121(5)	0.208(6)	0.068(3)	-0.017(6)	-0.062(6)
O4	"	0.120(5)	0.166(7)	0.237(8)	0.077(4)	0.020(6)	0.023(7)
Silicone oil high-*P* experiment							
Al	0.25(5)	0.13443	0.08795	0.05518	0.08345	0.01549	0.00837
	0.39(5)	0.13347	0.08588	0.06176	0.07881	-0.00181	0.01328
	0.54(5)	0.13467	0.08547	0.08088	0.07661	-0.00521	0.01685
	0.70(5)	0.14424	0.08568	0.1078	0.06684	-0.00455	0.02474
	0.94(5)	0.14062	0.10288	0.14012	0.06361	0.02786	0.05874
	1.17(5)	0.18666	0.12647	0.13776	0.0692	0.03769	0.03344
	1.43(5)	0.24347	0.0816	0.2822	0.06488	0.0837	0.09569
P	0.25(5)	0.10356	0.09973	0.11952	0.06973	-0.05174	-0.05524
	0.39(5)	0.1114	0.0921	0.12579	0.07069	-0.04959	-0.03627
	0.54(5)	0.11711	0.08963	0.12932	0.07459	-0.04705	-0.02767
	0.70(5)	0.12605	0.08781	0.14282	0.08084	-0.05421	-0.0337
	0.94(5)	0.1346	0.0901	0.1645	0.08435	-0.0462	-0.04
	1.17(5)	0.11354	0.11233	0.1888	0.08212	-0.05311	-0.04672
	1.43(5)	0.12228	0.11532	0.39265	0.0681	-0.08174	-0.07754
O1	0.25(5)	0.11573	0.08317	0.15139	0.06409	-0.07311	-0.05381
	0.39(5)	0.10864	0.09353	0.19004	0.05231	-0.0002	-0.01259
	0.54(5)	0.11191	0.10738	0.15991	0.05693	-0.01818	-0.02922
	0.70(5)	0.11475	0.12969	0.17646	0.04631	-0.06056	-0.02628
	0.94(5)	0.14256	0.15496	0.13016	0.03282	-0.05011	0.04933
	1.17(5)	0.12564	0.15395	0.49004	0.03427	-0.05812	0.06309
	1.43(5)	0.13377	0.16454	0.43877	0.05344	-0.02377	0.17795
O2	0.25(5)	0.24049	0.24049	0.09956	0.11423	0.01618	0.04022
	0.39(5)	0.22502	0.22502	0.09316	0.11348	0.01608	0.03997
	0.54(5)	0.2393	0.2393	0.09907	0.11275	0.01595	0.03966
	0.70(5)	0.25675	0.25675	0.10629	0.11224	0.01585	0.0394

Site	*P* (GPa)	U_{11}	U_{22}	U_{33}	U_{12}	U_{13}	U_{23}
	0.94(5)	0.28377	0.28377	0.11748	0.11125	0.0157	0.03902
	1.17(5)	0.26987	0.26987	0.11173	0.11049	0.01558	0.03873
	1.43(5)	0.2305	0.2305	0.09543	0.10938	0.01542	0.03833
O3	0.25(5)	0.07796	0.16395	0.10899	0.08282	-0.00465	-0.0832
	0.39(5)	0.08467	0.15193	0.10232	0.0744	0.0125	-0.06201
	0.54(5)	0.08116	0.15019	0.1087	0.075	0.02534	-0.04918
	0.70(5)	0.08036	0.14947	0.10768	0.06854	0.05041	-0.02722
	0.94(5)	0.06847	0.16272	0.17938	0.03965	0.08552	0.00368
	1.17(5)	0.07718	0.10612	0.14141	-0.00521	0.04494	-0.00129
	1.43(5)	0.09401	0.13125	0.20723	0.03457	-0.0195	0.08061
O4	0.25(5)	0.09509	0.12982	0.19173	0.04945	-0.05754	-0.04456
	0.39(5)	0.0947	0.12714	0.18788	0.04808	-0.05608	-0.0787
	0.54(5)	0.08107	0.14825	0.23897	0.04437	-0.08101	-0.12956
	0.70(5)	0.05571	0.18574	0.35961	0.04576	-0.10751	-0.1974
	0.94(5)	0.05548	0.22302	0.46394	0.04536	-0.13504	-0.21803
	1.17(5)	0.05068	0.1821	0.39131	0.04505	-0.10569	-0.19405
	1.43(5)	0.04991	0.22809	0.46716	0.06305	-0.07699	-0.24361

(16:3:1) methanol:ethanol:water high-*P* experiment							
Al	0.0001	0.12269	0.08706	0.04905	0.07654	0.00771	0.0126
	0.18(5)	0.1736	0.09272	0.06781	0.07722	0.00874	0.00875
	0.36(5)	0.17491	0.09163	0.06662	0.074	0.00542	0.00467
	0.58(5)	0.18533	0.09968	0.08118	0.07238	0.00804	0.00483
	0.77(5)	0.19501	0.11148	0.08968	0.07056	0.0068	0.00558
	1.02(5)	0.21067	0.125	0.07966	0.07096	0.01866	0.00665
	1.36(5)	0.24497	0.13588	0.09081	0.06856	0.03627	0.00804
	1.65(5)	0.25745	0.14086	0.10567	0.06322	0.04285	0.01257
	2.05(5)	0.2803	0.14538	0.11931	0.06044	0.04189	0.01565
	2.44(5)	0.29534	0.15488	0.11805	0.02282	-0.01315	0.04698
P	0.0001	0.08077	0.09558	0.09413	0.06564	-0.01652	-0.00763
	0.18(5)	0.09427	0.10206	0.11045	0.06867	-0.01588	-0.00704
	0.36(5)	0.09871	0.10006	0.11104	0.0698	-0.01472	-0.00515
	0.58(5)	0.11397	0.09918	0.11764	0.07023	-0.01173	-0.00803
	0.77(5)	0.11936	0.09918	0.1146	0.07129	-0.01054	-0.01038
	1.02(5)	0.11135	0.10251	0.11526	0.07092	-0.00992	-0.01068
	1.36(5)	0.1186	0.11384	0.12097	0.06948	-0.01287	-0.01965
	1.65(5)	0.12754	0.12096	0.1326	0.07049	-0.01376	-0.01764
	2.05(5)	0.15378	0.12741	0.14207	0.07126	-0.00797	-0.01698

Site	P (GPa)	U_{11}	U_{22}	U_{33}	U_{12}	U_{13}	U_{23}
	2.44(5)	0.16373	0.11692	0.14979	0.07076	-0.00435	0.00138
O1	0.0001	0.08379	0.12341	0.1877	0.06248	-0.05318	-0.07367
	0.18(5)	0.11068	0.13148	0.18376	0.06685	-0.04971	-0.06627
	0.36(5)	0.11478	0.13594	0.20643	0.0732	-0.0373	-0.05764
	0.58(5)	0.09903	0.14475	0.23612	0.07261	-0.04593	-0.05695
	0.77(5)	0.12826	0.1428	0.23049	0.07251	-0.05407	-0.05307
	1.02(5)	0.15677	0.09973	0.22325	0.06327	-0.07512	-0.07314
	1.36(5)	0.21522	0.10126	0.21118	0.062	-0.0748	-0.07149
	1.65(5)	0.26885	0.07781	0.21306	0.0676	-0.07095	-0.05973
	2.05(5)	0.35438	0.06813	0.19943	0.06865	-0.05132	-0.04419
	2.44(5)	0.30374	0.06498	0.26684	0.05802	-0.07087	-0.06403
O2	0.0001	0.15162	0.22924	0.07397	0.13234	0.03893	0.05137
	0.18(5)	0.16298	0.21885	0.07783	0.12479	0.04778	0.03789
	0.36(5)	0.19489	0.2127	0.07802	0.1298	0.02998	0.03256
	0.58(5)	0.2022	0.21478	0.08379	0.12809	0.02385	0.03007
	0.77(5)	0.22315	0.24376	0.08772	0.12951	0.02503	0.0222
	1.02(5)	0.25493	0.27026	0.09179	0.1286	0.03139	-0.02553
	1.36(5)	0.26432	0.27191	0.14224	0.12053	0.01709	-0.07335
	1.65(5)	0.27257	0.25833	0.17786	0.12648	0.0283	-0.06967
	2.05(5)	0.32285	0.28188	0.19922	0.14093	0.04209	-0.07439
	2.44(5)	0.38899	0.38899	0.16104	0.17892	0.05446	-0.12562
O3	0.0001	0.09168	0.14081	0.14827	0.08624	0.02625	-0.02135
	0.18(5)	0.08375	0.20696	0.15352	0.08223	0.01454	-0.04088
	0.36(5)	0.08469	0.23194	0.16784	0.07705	0.02013	-0.03829
	0.58(5)	0.08511	0.22776	0.18334	0.06924	0.01064	-0.05634
	0.77(5)	0.08696	0.24275	0.17668	0.07317	0.00254	-0.05941
	1.02(5)	0.09854	0.2327	0.1695	0.07631	0.02065	-0.06616
	1.36(5)	0.10574	0.26058	0.17216	0.07585	0.01604	-0.06615
	1.65(5)	0.10491	0.2697	0.18065	0.08163	0.01689	-0.06892
	2.05(5)	0.1085	0.31881	0.16962	0.08347	0.02453	-0.06462
	2.44(5)	0.13424	0.28245	0.19123	0.10273	0.0607	0.01083
O4	0.0001	0.14667	0.1157	0.17116	0.07439	0.08115	0.01765
	0.18(5)	0.11464	0.14191	0.17132	0.06052	0.09935	0.0451
	0.36(5)	0.11088	0.13377	0.18378	0.05485	0.10802	0.06305
	0.58(5)	0.11126	0.12666	0.20983	0.0514	0.11473	0.06218
	0.77(5)	0.11155	0.13976	0.22265	0.05436	0.12751	0.07378
	1.02(5)	0.11846	0.14806	0.22982	0.06264	0.12666	0.07978
	1.36(5)	0.13138	0.21863	0.26127	0.0889	0.12812	0.0552

Site	P (GPa)	U_{11}	U_{22}	U_{33}	U_{12}	U_{13}	U_{23}
	1.65(5)	0.13826	0.22353	0.28441	0.10038	0.12449	0.034
	2.05(5)	0.12042	0.25504	0.2853	0.11051	0.10525	0.01349
	2.44(5)	0.1357	0.18696	0.3255	0.11856	0.10433	0.0343

Table 3.6 Refined elastic parameters of $AlPO_4$-5, based on III-BM equations of state fits, with the crystal compressed in silicone oil (P_1-P_8 range) and in *m.e.w.* (P_1-P_{14} range) (see section 3.4.2, *Compressibility*, for further details).

Silicone oil experiment				
	V_0, l_0 (Å^3, Å)	$K_{V0,\,l0}$ (GPa)	K'	$\beta_{V,l}$ (GPa^{-1})
V	1376(3)	13.2(11)	5.1(14)	0.076(6)
a	13.759(5)	15.5(3)	4*	0.0215(4)
c	8.369(4)	9.6(2)	7*	0.0347(7)
(16:3:1) methanol:ethanol:water experiment				
	V_0, l_0 (Å^3, Å)	$K_{V0,\,l0}$ (GPa)	K'	$\beta_{V,l}$ (GPa^{-1})
V	1360(2)	22.2(9)	3.0(3)	0.045(2)
a	13.734(9)	19.7(7)	3.0(3)	0.0169(6)
c	8.453(3)	29.3(10)	2.9(4)	0.0114(4)

* fixed parameter; $K_0 = (1/\beta_{V,x})_{\text{room-}P,T}$; $K' = (\partial K/\partial P)_T$

Table 4.1. Unit-cell parameters of leonhardite with pressure (* in decompression) (from Comboni et al. 2018).

P (GPa)	*V* (Å^3)	*a* (Å)	*b* (Å)	*c* (Å)	*β* (°)
0.0001	1346.9(6)	14.7342(19)	13.0562(7)	7.5533(5)	112.035(11)
0.06(5)	1344.6(5)	14.7262(9)	13.0524(3)	7.5501(3)	112.096(5)
0.14(5)	1342.6(5)	14.7240(10)	13.0485(3)	7.5435(2)	112.126(5)
0.31(5)	1338.3(7)	14.7192(11)	13.0435(4)	7.5273(2)	112.175(6)
0.53(5)	1329.2(6)	14.7025(13)	13.0280(4)	7.5004(3)	112.298(7)
0.86(5)	1316.3(6)	14.6745(15)	13.0069(4)	7.4633(3)	112.476(8)
1.11(5)	1310.8(6)	14.6603(12)	13.0009(4)	7.4464(3)	112.549(7)
1.69(5)	1290.4(5)	14.592(3)	12.9919(9)	7.3886(6)	112.895(16)
2.38(5)	1263.6(5)	14.4842(13)	12.9848(4)	7.3228(3)	113.433(7)
3.01(5)	1245.6(5)	14.3866(18)	12.9949(5)	7.2861(4)	113.872(11)
3.37(5)	1237.2(5)	14.3381(10)	12.9947(3)	7.2696(2)	114.015(6)
4.40(5)	1212.2(5)	14.2038(12)	12.9866(4)	7.2217(3)	114.495(8)
4.79(5)	1205.3(5)	14.1660(12)	12.9851(3)	7.2083(3)	114.630(8)
5.38(5)	1187.9(5)	14.0783 (12)	12.9766(3)	7.1729(3)	114.975(7)
6.52(5)	1160.6(5)	13.9584(18)	12.9754(4)	7.1184(4)	115.818(12)
7.46(5)	1134(6)	13.863(5)	12.9795(13)	7.0707(13)	116.960(4)
*4.01(5)	1227(2)	14.17(2)	13.02(7)	7.239(5)	113.23(13)

Table 4.2. Unit-cell parameters of hydrated laumontite with pressure (* in decompression) (from Comboni et al. 2018).

P (GPa)	*V* (Å^3)	*a* (Å)	*b* (Å)	*c* (Å)	*β* (°)
0.00(5)	1394.4(3)	14.9193(6)	13.1805(5)	7.54296(13)	109.939(3)
0.03(5)	1393.1(4)	14.9132(11)	13.1775(9)	7.5405(2)	109.932(5)
0.11(5)	1391.1(3)	14.9096(10)	13.1708(8)	7.5319(2)	109.854(4)
0.27(5)	1386.8(4)	14.9036(6)	13.1542(5)	7.51924(13)	109.813(3)
0.49(5)	1382.0(4)	14.8932(10)	13.1422(9)	7.5048(2)	109.806(4)
0.67(5)	1377.1(3)	14.8789(6)	13.1358(5)	7.49105(13)	109.850(3)
0.90(5)	1372.4(4)	14.8644(7)	13.1268(6)	7.4789(2)	109.878(3)
1.10(5)	1366.8(4)	14.8445(6)	13.1169(6)	7.46626 (14)	109.918(3)
1.40(5)	1360.3(4)	14.8202(13)	13.1067(11)	7.4517(3)	109.987(5)
1.72(5)	1353.1(4)	14.796(2)	13.090 (2)	7.4361(4)	110.032(9)
2.03(5)	1346.8(7)	14.777(4)	13.0810(11)	7.4236(7)	110.19(2)
2.35(5)	1339.2(5)	14.7337(9)	13.0792(7)	7.4069(2)	110.242(4)
2.65(5)	1333.7(6)	14.703(2)	13.0917(5)	7.3974(3)	110.500(9)
*2.36(5)	1339.5(7)	14.737(2)	13.0865(5)	7.4083(3)	110.354(9)
*1.99(5)	1347.0(7)	14.778(2)	13.0810(4)	7.4233(2)	110.170(7)
*1.69(5)	1352.8(6)	14.8009(12)	13.0859(3)	7.4367(2)	110.080(6)
*0.58(5)	1380.7(5)	14.8914(9)	13.1374(8)	7.5008(2)	109.795(4)
*0.05(5)	1392.2(8)	14.928(3)	13.1573(7)	7.5339(6)	109.81(2)

Table 4.3. Evolution of the unit-cell parameters of leonhardite as a function of time of immersion for the samples Wat100, Wat15, Wat10 and Wat5, respectively (see text for further details) (from Comboni et al. 2018).

Leonhardite Wat100 sample					
time* (min)	V(Å^3)	a (Å)	b (Å)	c (Å)	β (°)
0	1351.56(17)	14.7372(8)	13.0754(5)	7.5604(3)	111.916(5)
78	1356(2)	14.75(2)	13.120(2)	7.532(11)	111.42(15)
198	1364.9(10)	14.758(1)	13.151(6)	7.525(4)	110.84(6)
305	1367(1)	14.788(12)	13.140(14)	7.526(6)	110.80(8)
428	1368(1)	14.795(11)	13.142(13)	7.523(6)	110.70(8)
545	1374(1)	14.849(13)	13.134(13)	7.533(6)	110.72(8)
979	1378(7)	14.813(6)	13.149(7)	7.562(3)	110.67(4)
1502	1383(1)	14.807(12)	13.213(10)	7.552(6)	110.62(8)
1708	1383(1)	14.809(13)	13.211(11)	7.551(6)	110.63(8)
2054	1383(1)	14.806(11)	13.220(11)	7.551(5)	110.60(7)
Leonhardite Wat15 sample					
time* (min)	V(Å^3)	a (Å)	b (Å)	c (Å)	β (°)
0	1349.1(7)	14.764(7)	13.072(5)	7.555(2)	112.29(4)
240	1360.2(6)	14.757(7)	13.134(5)	7.5505(16)	111.65(4)
1710	1385.6(4)	14.886(4)	13.180(3)	7.5321(9)	110.35(2)
2370	1385.7(4)	14.880(4)	13.184(3)	7.5302 (9)	110.29(2)
Leonhardite Wat10 sample					
time* (min)	V(Å^3)	a (Å)	b (Å)	c (Å)	β (°)
0	1350.18(18)	14.7568(11)	13.0649(5)	7.5574(5)	112.080(8)
250	1354.8(4)	14.755(4)	13.0962(13)	7.5618(8)	111.99(2)
812	1360.6(3)	14.769(5)	13.1232(15)	7.562(14)	111.83(3)
1998	1384.1(4)	14.861(3)	13.1772(11)	7.5455(7)	110.497(16)
2464	1384.1(3)	14.860(3)	13.1798(12)	7.5419(8)	110.446(18)
Leonhardite Wat5 sample					
time* (min)	V(Å^3)	a (Å)	b (Å)	c (Å)	β (°)
0	1349.6(5)	14.856(3)	13.063(3)	7.5554(15)	112.07(2)
95	1351.4(8)	14.757(3)	13.072(2)	7.556(14)	112.00(2)
212	1354.7(3)	14.763(3)	13.083(3)	7.5655(16)	112.02(2)
351	1357.7(3)	14.779(3)	13.088(2)	7.570(15)	111.99(2)
493	1359.6(3)	14.785(3)	13.099(2)	7.5708(13)	111.98(2)
623	1360.8(4)	14.786(7)	13.104(5)	7.575 (3)	112.01(4)
1468	1361.4(6)	14.776(5)	13.120(4)	7.567 (2)	111.87(3)
1734	1361.7(5)	14.776(6)	13.123(4)	7.569 (2)	111.90(4)
1878	1361.5(7)	14.767(6)	13.121(4)	7.571 (3)	111.85(4)
2184	1362.4(5)	14.778(6)	13.123(4)	7.569 (3)	111.85(4)
2637	1363.8(5)	14.784(7)	13.135(4)	7.566 (3)	111.85(4)
3266	1364.0(6)	14.785(7)	13.135(5)	7.565 (3)	111.80(4)
3479	1363.8(5)	14.786(8)	13.125(6)	7.568 (3)	111.78(5)
3933	1364.3(4)	14.782(6)	13.138(4)	7.565 (2)	111.78(3)

Table 4.4. Refined interatomic distances (in Å) pertaining to the samples Wat15 and Wat10 as a function of time (from Comboni et al. 2018).

Wat15 sample							
time (min)	O1-O1	O7-O7	W2-W2	W5-W5	W2-Ca	W8-O7	W1-07
0	6.68(4)	8.12(3)	1.010(4)	1.753(7)	2.487(14)	3.208(10)	-
240	6.75(4)	8.14(3)	0.802(3)	1.333(5)	2.471(14)	3.219(10)	2.907(8)
1710	6.96(4)	8.16(3)	0.475(2)	0.780(3)	2.396(14)	3.384(11)	2.802(8)
2370	7.00(4)	8.15(3)	0.494(2)	0.801(3)	2.398(14)	3.377(10)	2.792(8)

Wat10 sample							
time (min)	O1-O1	O7-O7	W2-W2	W5-W5	W2-Ca	W8-O7	W1-O7
0	6.67(4)	8.11(3)	0.928(8)	1.715(7)	2.48(1)	3.20(1)	-
250	6.73(4)	8.13(3)	0.933(8)	1.591(6)	2.47(1)	3.22(1)	2.89(5)
812	6.74(4)	8.14(3)	0.706(6)	1.298(5)	2.44(1)	3.23(1)	2.84(8)
1998	6.92(4)	8.16(3)	0.445(4)	0.778(3)	2.40(1)	3.28(1)	2.79(8)
2464	6.93(4)	8.16(3)	0.471(4)	0.727(3)	2.40(1)	3.47(1)	2.78(8)

Table 4.5. Relevant interatomic distances (in Å) of leonhardite and hydrated laumontite pertaining to the H_2O sites at different pressure (* in decompression) (from Comboni et al. 2018).

Leonhardite									
P (GPa)	W2-W2	W2-Ca	W5-W8	W5-W2	W8-Ca	W8-O5	W8-O7	W8'-Ca	W8'-O4
0.0001	0.979(2)	2.525(4)	2.480(2)	3.133(5)	2.424(1)	2.927(4)	3.265(2)	2.358(5)	2.867(6)
0.06(5)	0.902(2)	2.493(4)	2.595(2)	3.126(5)	2.364(1)	2.905(4)	3.278(2)	2.351(5)	2.807(6)
0.14(5)	0.925(2)	2.489(4)	2.610(2)	3.120(5)	2.368(1)	2.925(4)	3.238(2)	2.353(5)	2.789(6)
0.31(5)	0.896(2)	2.475(4)	2.625(2)	3.110(5)	2.368(1)	2.920(4)	3.224(2)	2.363(5)	2.780(6)
0.53(5)	0.883(2)	2.483(4)	2.618(2)	3.081(5)	2.381(1)	2.912(4)	3.177(2)	2.377(5)	2.759(6)
0.86(5)	0.840(2)	2.485(4)	2.667(2)	3.030(5)	2.363(1)	2.900(4)	3.148(2)	2.384(5)	2.759(6)
1.11(5)	0.848(2)	2.512(4)	2.662(2)	3.003(4)	2.370(1)	2.894(4)	3.127(2)	2.345(5)	2.727(6)
1.69(5)	0.693(2)	2.438(4)	2.750(2)	2.960(5)	2.344(1)	2.846(4)	3.100(2)	2.402(5)	2.711(6)
2.38(5)	0.676(2)	2.421(4)	2.857(2)	2.877(4)	2.329(1)	2.844(4)	3.040(2)		
3.01(5)	0.659(2)	2.423(4)	2.918(2)	2.813(4)	2.334(1)	2.795(4)	3.000(2)		
3.26(5)	0.623(2)	2.408(4)	2.901(2)	2.808(4)	2.339(1)	2.788(4)	2.975(2)		
4.40(5)	0.612(2)	2.394(4)	2.928(2)	2.754(4)	2.327(1)	2.750(4)	2.913(2)		
4.79(5)	0.646(2)	2.356(4)	2.940(2)	2.756(4)	2.310(1)	2.745(4)	2.929(2)		
5.38(5)	0.604(2)	2.370(4)	2.928(2)	2.698(4)	2.323(1)	2.749(4)	2.876(2)		
6.52(5)	0.630(2)	2.330(4)	2.921(2)	2.619(4)	2.289(1)	2.755(4)	2.871(2)		
7.46(5)	0.497(2)	2.243(4)	3.006(2)	2.540(4)	2.316(1)	2.855(4)	2.857(2)		
Laumontite									
P (GPa)	W2-Ca	W5-W8	W5-W2	W8-Ca	W8-O5	W8-O7	W8'-Ca	W1-W2	W1-O7
0.00(5)	2.355(3)	3.117(2)	3.515(5)	2.392(1)	2.935(4)	3.293(2)	2.391(1)	2.739(1)	2.813(2)
0.03(5)	2.337(3)	3.211(2)	3.529(5)	2.3881)	2.898 (4)	3.320(2)	2.408(1)	2.737(1)	2.817(2)
0.11(5)	2.345(3)	3.366(2)	3.528(5)	2.356(1)	2.903(4)	3.395(2)	2.421(1)	2.746(1)	2.816(2)
0.27(5)	2.341(3)	3.266(2)	3.523(5)	2.388(1)	2.889(4)	3.317(2)	2.407(1)	2.739(1)	2.809(2)
0.49(5)	2.335(3)	3.208(2)	3.512(5)	2.389(1)	2.869(4)	3.303(2)	2.386(1)	2.746(1)	2.807(2)
0.67(5)	2.342(3)	3.176(2)	3.482(5)	2.396(1)	2.853(4)	3.270(2)	2.390(1)	2.741(1)	2.806(2)
0.90(5)	2.344(3)	3.136(2)	3.469(5)	2.395(1)	2.864(4)	3.254(2)	2.383(1)	2.727(1)	2.815(2)
1.10(5)	2.345(3)	3.130(2)	3.448(5)	2.389(1)	2.842(4)	3.260(2)	2.391(1)	2.733(1)	2.808(2)
1.40(5)	2.351(3)	3.145(2)	3.431(5)	2.385(1)	2.821(4)	3.263(2)	2.379(1)	2.721(1)	2.810(2)
1.72(5)	2.346(3)	3.203(2)	3.409(5)	2.381(1)	2.832(4)	3.239(2)	2.361(1)	2.724(1)	2.801(2)
2.03(5)	2.336(3)	3.073(2)	3.384(5)	2.334(1)	2.832(4)	3.238(2)	2.377(1)	2.732(1)	2.779(2)
2.35(5)	2.335(3)	3.258(2)	3.360(5)	2.256(1)	2.816(4)	3.396(2)	2.380(1)	2.737(1)	2.820(2)
2.65(5)	2.346(3)	3.084(2)	3.312(5)	2.332(1)	2.812(4)	3.207(2)	2.368(1)	2.739(1)	2.771(2)
*2.36(5)	2.345(3)	3.132(2)	3.343(5)	2.299(1)	2.820(4)	3.276(2)	2.370(1)	2.731(1)	2.776(2)

Laumontite									
P (GPa)	W2-Ca	W5-W8	W5-W2	W8-Ca	W8-O5	W8-O7	W8'-Ca	W1-W2	W1-O7
*1.99(5)	2.362(3)	3.095(2)	3.366(5)	2.324(1)	2.831(4)	3.271(2)	2.391(1)	2.728(1)	2.777(2)
*1.69(5)	2.340(3)	3.123(2)	3.405(5)	2.318(1)	2.861(4)	3.284(2)	2.406(1)	2.736(1)	2.779(2)
*0.58(5)	2.342(3)	3.191(2)	3.505(5)	2.412(1)	2.871(4)	3.270(2)	2.378(1)	2.728(1)	2.819(2)
*0.05(5)	2.325(3)	3.186(2)	3.549(5)	2.427(1)	2.914(4)	3.292(2)	2.371(1)	2.742(1)	2.834(2)

Table 4.6. Relevant interatomic distances (in Å) and ε parameter (see section 4.5.2, *High-pressure behavior of leonhardite and fully-hydrated Ca-laumontite*) of leonhardite \ hydrated laumontite pertaining to the 6- and 10-mRs at different pressure $\left[\varepsilon_{10-\mathrm{mRs}} = \frac{\mathrm{O1-O1}}{\mathrm{O7-O7}}\right]$ (* in decompression) (from Comboni et al. 2018).

Leonhardite							
P (GPa)	O3-O3	O4-O4	O5-O5	O1-O6	O1-O1	O7-O7	$\varepsilon_{10\text{-mRs}}$
0.0001	4.859(3)	4.841(6)	5.339(5)	3.162(2)	6.683(8)	8.095(6)	0.826(3)
0.06(5)	4.856(3)	4.841(6)	5.316(5)	3.208(2)	6.661(8)	8.092(6)	0.823(3)
0.14(5)	4.850(3)	4.862(6)	5.294(5)	3.224(2)	6.662(8)	8.078(6)	0.825(3)
0.31(5)	4.841(3)	4.872(6)	5.269(5)	3.219(2)	6.651(8)	8.074(6)	0.824(3)
0.53(5)	4.843(3)	4.897(6)	5.217(5)	3.210(2)	6.663(8)	8.050(6)	0.828(3)
0.86(5)	4.842(3)	4.939(6)	5.131(5)	3.226(2)	6.638(8)	8.018(6)	0.828(3)
1.11(5)	4.839(3)	4.961(6)	5.083(5)	3.256(2)	6.608(8)	8.010(6)	0.825(3)
1.69(5)	4.832(3)	5.042(6)	4.930(5)	3.254(2)	6.598(8)	7.980(6)	0.827(3)
2.38(5)	4.823(3)	5.198(7)	4.708(4)	3.312(2)	6.548(8)	7.942(6)	0.824(3)
3.01(5)	4.804(3)	5.277(7)	4.554(4)	3.409(2)	6.409(8)	7.921(6)	0.801(3)
3.26(5)	4.781(3)	5.362(7)	4.492(4)	3.399(2)	6.406(8)	7.902(6)	0.811(3)
4.40(5)	4.744(3)	5.474(7)	4.399(6)	3.450(2)	6.300(8)	7.837(6)	0.804(3)
4.79(5)	4.739(3)	5.495(7)	4.298(6)	3.445(2)	6.261(8)	7.835(6)	0.799(3)
5.38(5)	4.729(3)	5.557(7)	4.204(4)	3.444(2)	6.212(8)	7.789(6)	0.797(3)
6.52(5)	4.707(3)	5.576(7)	4.060(4)	3.449(3)	6.081(8)	7.777(6)	0.782(3)
7.46(5)	4.847(3)	5.659(7)	3.943(4)	3.422(3)	6.026(8)	7.851(6)	0.768(3)

Table 4.6. Relevant interatomic distances (in Å) and ε parameter (see Section 4.5.2, *High-pressure behavior of leonhardite and fully-hydrated Ca-laumontite*) of leonhardite \ hydrated laumontite pertaining to the 6- and 10-mRs at different pressure $\left[\varepsilon_{10-\mathrm{mRs}} = \frac{\mathrm{O1-O1}}{\mathrm{O7-O7}}\right]$ (* in decompression) (from Comboni et al. 2018).

Laumontite							
P (GPa)	O3-O3	O4-O4	O5-O5	O1-O6	O1-O1	O7-O7	$\varepsilon_{10\text{-mRs}}$
0.00(5)	4.971(3)	5.113(6)	5.230(5)	3.279(2)	7.008(8)	8.147(6)	0.860(3)
0.03(5)	4.973(3)	5.118(6)	5.218(5)	3.266(2)	7.010(8)	8.161(6)	0.860(3)
0.11(5)	5.000(3)	5.109(6)	5.226(5)	3.267(2)	7.026(8)	8.160(6)	0.861(3)
0.27(5)	4.975(3)	5.098(6)	5.202(5)	3.235(2)	7.030(8)	8.115(6)	0.866(3)
0.49(5)	4.973(3)	5.095(6)	5.191(5)	3.247(2)	7.011(8)	8.128(6)	0.863(3)
0.67(5)	4.964(3)	5.119(6)	5.170(5)	3.243(2)	7.032(8)	8.110(6)	0.867(3)
0.90(5)	4.962(3)	5.121(6)	5.154(5)	3.251(2)	6.989(8)	8.105(6)	0.862(3)
1.10(5)	4.969(3)	5.125(6)	5.143(5)	3.233(2)	6.969(8)	8.096(6)	0.861(3)
1.40(5)	4.950(3)	5.129(6)	5.105(5)	3.222(2)	6.962(8)	8.088(6)	0.861(3)
1.72(5)	4.933(3)	5.140(6)	5.092(5)	3.232(2)	6.957(8)	8.079(6)	0.861(3)
2.03(5)	4.915(3)	5.162(6)	5.057(5)	3.226(2)	6.948(8)	8.057(6)	0.862(3)
2.35(5)	4.887(3)	5.167(6)	5.032(5)	3.210(2)	6.933(8)	8.124(6)	0.853(3)
2.65(5)	4.873(3)	5.230(6)	4.980(5)	3.242(2)	6.881(8)	8.055(6)	0.854(3)
*2.36(5)	4.888(3)	5.200(6)	5.018(5)	3.229(2)	6.937(8)	8.063(6)	0.860(3)
*1.99(5)	4.908(3)	5.164(6)	5.058(5)	3.191(2)	6.999(8)	8.057(6)	0.869(3)
*1.69(5)	4.915(3)	5.132(6)	5.123(5)	3.244(2)	6.925(8)	8.060(6)	0.859(3)
*0.58(5)	4.952(3)	5.114(6)	5.178(5)	3.256(2)	6.997(8)	8.137(6)	0.860(3)
*0.05(5)	4.947(3)	5.108(6)	5.242(5)	3.269(2)	6.994(8)	8.176(6)	0.855(3)

Table 4.7a. Details pertaining to the structure refinements of the Wat15 and Wat10 sample as in function of time (in minutes) (from Comboni et al. 2018).

Wat15 sample	t_0	t_{240}	t_{1710}	t_{2370}
min≤*h*≤max	-16; +17	-17; +17	-17; +17	-17; +17
min≤*k*≤max	-15; +15	+14; -15	-15; +15	-15; +15
min≤*l*≤max	-9; +10	-10; +9	-9; +10	-10; +9
Unique reflections	987	1162	1177	1142
Observed reflections	382	496	522	527
R_{int} (obs)	0.060	0.054	0.035	0.052
R_{int} (all)	0.082	0.075	0.052	0.037
R_1 (obs)	0.068	0.095	0.065	0.069
R_1 (all)	0.173	0.200	0.159	0.148
wR_1 (obs)	0.068	0.083	0.063	0.068
wR_1 (all)	0.056	0.085	0.067	0.071
Residuals (e^-/Å^3)	+0.34; -0.33	+0.60; -0.71	+0.40;-0.35	+0.53; -0.43

Wat10 sample	t_0	t_{250}	t_{812}	t_{1998}
min≤*h*≤max	-18; +13	-14; +9	-13; +14	-9; +14
min≤*k*≤max	-16; +16	-16; +17	-16; +16	-16; +17
min≤*l*≤max	-9; +9	-9; +9	-10; +9	-9; +10
Unique reflections	1545	1087	1276	1115
Observed reflections	900	467	579	483
R_{int} (obs)	0.049	0.044	0.059	0.040
R_{int} (all)	0.061	0.063	0.083	0.056
R_1 (obs)	0.074	0.084	0.094	0.082
R_1 (all)	0.120	0.159	0.0166	0.160
wR_1 (obs)	0.077	0.080	0.083	0.080
wR_1 (all)	0.079	0.083	0.086	0.083
Residuals (e^-/Å^3)	+0.55; -0.67	+0.51; -0.50	+0.80; -0.59	+0.48; -0.59

Table 4.7b. Details pertaining to the structure refinements of leonhardite and laumontite as in function of pressures (from Comboni et al. 2018).

P (GPa)	0.0001	0.06(5)	0.14(5)	0.31(5)	0.53(5)	0.86(5)	1.11(5)	1.69(5)
min≤*h*≤max	-12; +15	-14; +15	-15; +13	-15; +13	-15;	-13;	-	-15;
min≤*k*≤max	-14; +16	-12; +16	-12; +16	-12; +16	-12;	-12;	-12;	-13;
min≤*l*≤max	-9; +10	-9; +10	-8: +9	-8; +9	-8; +9	-9; +9	-8; +8	-8; +8
Unique	633	607	601	593	579	614	583	578
Observed reflections	512	516	503	445	431	416	456	438
R_{int} (obs)	0.04	0.017	0.022	0.024	0.028	0.025	0.027	0.027
R_{int} (all)	0.04	0.017	0.023	0.025	0.029	0.027	0.028	0.028
R_1 (obs)	0.061	0.051	0.050	0.041	0.052	0.043	0.064	0.064
R_1 (all)	0.069	0.058	0.058	0.057	0.069	0.070	0.079	0.079
wR_1 (obs)	0.071	0.067	0.060	0.044	0.056	0.044	0.071	0.076
wR_1 (all)	0.072	0.067	0.060	0.045	0.057	0.045	0.072	0.076
Residuals (e^-/Å^3)	-0.23; +0.23	-0.16; +0.17	-0.18; +0.19	-0.12; +0.15	-0.16; +0.16	-0.16; +0.11	-0.16; +0.18	-0.34; +0.36

P (GPa)	2.38(5)	3.01(5)	3.26(5)	4.40(5)	4.79(5)	5.38(5)	6.52(5)	7.46(5)
min≤*h*≤max	-13;+15	-15; +13	-15; +13	-14; +13	-14;	-13;	-13;	-13;
min≤*k*≤max	-13; +16	-13; +16	-13; +16	-13; +16	-13;	-13;	-13;	-13;
min≤*l*≤max	-8; +8	-8; +8	-8; +8	-8; +8	-8; +8	-8; +8	-8;+8	-8;+8
Unique	596	575	569	554	542	531	519	496
Observed reflections	426	452	463	444	430	422	382	264
R_{int} (obs)	0.029	0.030	0.016	0.025	0.019	0.017	0.021	0.057
R_{int} (all)	0.030	0.030	0.016	0.025	0.019	0.017	0.021	0.064
R_1 (obs)	0.071	0.072	0.061	0.065	0.067	0.067	0.070	0.119
R_1 (all)	0.089	0.084	0.071	0.077	0.080	0.078	0.088	0.168
wR_1 (obs)	0.076	0.085	0.074	0.080	0.079	0.083	0.083	0.116
wR_1 (all)	0.077	0.085	0.074	0.081	0.080	0.083	0.084	0.118
Residuals (e^-/Å^3)	-0.21; +0.24	-0.24; +0.22	-0.16; +0.21	-0.19; +0.22	-0.36; +0.41	-0.21; +0.28	-0.26; +0.33	-0.42; +0.55

Table 4.7c. Details pertaining to the structure refinements of hydrated laumontite at different pressure. (from Comboni et al. 2018).

P (GPa)	0.0001	0.03	0.11	0.27	0.49	0.67	0.90	1.10	1.40
min≤*h*≤max	-17;	-17;	-17;	-17;	-17;	-17;	-17;	-17;	-17;
min≤*k*≤max	-16;	-16;	-15;	-15;	-15;	-15;	-15;	-15;	-15;
min≤*l*≤max	-9; +9	-9; +9	-9; +9	-9; +9	-9; +9	-9; +9	-9; +9	-9; +9	-9; +9
Unique	913	892	888	884	883	876	874	870	868
Observed reflections $I > 3\sigma(I)$	736	635	625	626	632	623	624	619	607
R_{int} (obs)	0.019	0.023	0.023	0.031	0.029	0.028	0.023	0.024	0.023
R_{int} (all)	0.020	0.024	0.024	0.032	0.030	0.029	0.024	0.025	0.024
R_1 (obs)	0.065	0.084	0.089	0.081	0.074	0.072	0.073	0.073	0.076
R_1 (all)	0.075	0.107	0.114	0.104	0.096	0.095	0.094	0.093	0.099
wR_1 (obs)	0.080	0.085	0.090	0.086	0.077	0.077	0.075	0.079	0.081
wR_1 (all)	0.081	0.086	0.091	0.087	0.078	0.078	0.075	0.080	0.082
Residuals (e^-/Å^3)	-0.33; +0.54	-0.37; +0.51	-0.32; +0.44	-0.36; +0.38	-0.31; +0.42	-0.39; +0.42	-0.26; +0.40	-0.29; +0.35	-0.30; +0.33

P (GPa)	1.72	2.03	2.35	2.65	2.36	1.99	1.69	0.58	0.05
min≤*h*≤max	-17;	-15;	-17;	-15;	-14;	-14;	-15;	-14;	-13;
min≤*k*≤max	-15;	-16;	-15;	-18;	-18;	-18;	-17;	-15;	-15;
min≤*l*≤max	-10;	-10;	-9; +9	-9; +9	-10;	-10;	-10;	-10;	-9; +9
Unique	886	838	848	836	827	832	818	936	833
Observed reflections $I > 3\sigma(I)$	574	612	574	620	597	565	562	590	562
R_{int} (obs)	0.038	0.051	0.031	0.034	0.060	0.078	0.062	0.027	0.036
R_{int} (all)	0.039	0.053	0.033	0.036	0.063	0.082	0.065	0.030	0.039
R_1 (obs)	0.068	0.065	0.090	0.06	0.066	0.063	0.064	0.066	0.090
R_1 (all)	0.115	0.081	0.117	0.075	0.084	0.084	0.084	0.123	0.124
wR_1 (obs)	0.073	0.072	0.094	0.068	0.072	0.069	0.068	0.063	0.080
wR_1 (all)	0.074	0.073	0.095	0.068	0.072	0.070	0.069	0.065	0.082
Residuals (e^-/Å^3)	-0.30; +0.33	-0.37; +0.35	-0.39; +0.34	-0.21; +0.20	-0.26; +0.31	-0.25; +0.31	-0.25; +0.22	-0.33; +0.36	-0.42; +0.42

Table 4.8a. Refined positional and displacement parameters of the Wat15 sample as in function of time (from Comboni et al. 2018).

Site	t (min)	*s.o.f.*	*x*	*y*	*z*	U_{iso} (Å^2)
Si(1)	0	1	0.2393(3)	0.3820(3)	0.1593(4)	0.0058(8)
	240	1	0.2384(3)	0.3819(3)	0.1558(5)	0.0087(9)
	1710	1	0.2366(2)	0.3831(2)	0.1518(3)	0.0078(7)
	2370	1	0.2366(2)	0.3830(3)	0.1516(3)	0.0079(7)
Si(2)	0	1	0.0831(3)	0.3839(3)	0.3272(4)	0.0065(8)
	240	1	0.0807(3)	0.3839(3)	0.3256(4)	0.0088(9)
	1710	1	0.0783(2)	0.3842(3)	0.3233(3)	0.0084(7)
	2370	1	0.0783(2)	0.3841(3)	0.3231(3)	0.0078(7)
Al	0	1	0.1275(3)	0.3089(3)	0.7338(5)	0.0084(10)
	240	1	0.1280(3)	0.3082(3)	0.7348(5)	0.0099(10)
	1710	1	0.1288(2)	0.3065(3)	0.7365(3)	0.0090(7)
	2370	1	0.1289(3)	0.3066(3)	0.7365(4)	0.0090(8)
O1	0	1	0.2611(7)	0.5	0.2286(10)	0.0047(8)
	240	1	0.2601(9)	0.5	0.2268(13)	0.0098(9)
	1710	1	0.2580(7)	0.5	0.2212(10)	0.0083(7)
	2370	1	0.2570(7)	0.5	0.2200(10)	0.0087(7)
O2	0	1	0.2091(5)	0.3779(6)	0.9291(8)	0.0047(8)
	240	1	0.2082(6)	0.3779(6)	0.9258(9)	0.0098(9)
	1710	1	0.2083(5)	0.3783(5)	0.9225(6)	0.0083(7)
	2370	1	0.2084(5)	0.3781(5)	0.9227(7)	0.0087(7)
O3	0	1	0.1482(5)	0.3827(6)	0.5554(8)	0.0047(8)
	240	1	0.1470(6)	0.3825(7)	0.5552(9)	0.0098(9)
	1710	1	0.1400(4)	0.3801(5)	0.5488(6)	0.0083(7)
	2370	1	0.1394(5)	0.3804(6)	0.5480(7)	0.0087(7)
O4	0	1	0.1492(5)	0.3385(5)	0.2106(9)	0.0047(8)
	240	1	0.1489(6)	0.3408(6)	0.2113(9)	0.0098(9)
	1710	1	0.1462(5)	0.3437(5)	0.2073(7)	0.0083(7)
	2370	1	0.1462(5)	0.3439(5)	0.2075(7)	0.0087(7)
O5	0	1	0.3359(6)	0.3170(5)	0.2662(9)	0.0047(8)
	240	1	0.3338(6)	0.3159(6)	0.2643(10)	0.0098(9)
	1710	1	0.3287(5)	0.3287(5)	0.2600(7)	0.0083(7)
	2370	1	0.3290(5)	0.3150(5)	0.2602(7)	0.0087(7)
O6	0	1	0.0508(7)	0.5	0.263(1)	0.0047(8)
	240	1	0.0500(8)	0.5	0.266(1)	0.0098(9)
	1710	1	0.0450(6)	0.5	0.2663(10)	0.0083(7)
	2370	1	0.0455(7)	0.5	0.2674(10)	0.0087(7)
O7	0	1	0.0078(5)	0.3106(6)	0.7181(8)	0.0047(8)
	240	1	0.0086(6)	0.3099(6)	0.7220(9)	0.0098(9)
	1710	1	0.0107(5)	0.3094(5)	0.7284(7)	0.0083(7)
	2370	1	0.0109(5)	0.3092(6)	0.7287(7)	0.0087(7)

Site	t (min)	*s.o.f.*	*x*	*y*	*z*	U_{iso} (Å^2)
Ca	0	1	0.2726(3)	0.5	0.7581(4)	0.014(1)
	240	1	0.2699(3)	0.5	0.7513(5)	0.018(1)
	1710	1	0.2606(2)	0.5	0.7349(3)	0.0137(8)
	2370	1	0.2604(3)	0.5	0.7346(4)	0.0136(8)
W2	0	0.53(2)	0.4170(1)	0.461(1)	0.0550(2)	0.059(5)
	240	0.50(1)	0.4140(1)	0.469(2)	0.044(2)	0.045(2)
	1710	0.56(1)	0.3989(7)	0.482(2)	0.016(1)	0.029(2)
	2370	0.56(1)	0.3985(7)	0.481(2)	0.015(1)	0.028(2)
W5	0	0.52(2)	0.5	0.433(2)	0.5	0.059(5)
	240	0.48(2)	0.5	0.449(2)	0.5	0.045(2)
	1710	0.42(2)	0.5	0.470(2)	0.5	0.029(2)
	2370	0.42(2)	0.5	0.469(2)	0.5	0.028(2)
W8	0	0.65(3)	0.120(1)	0.106(1)	0.344(3)	0.059(5)
	240	0.73(2)	0.125(1)	0.109(1)	0.342(2)	0.045(2)
	1710	0.34(8)	0.124(4)	0.096(4)	0.366(4)	0.029(2)
	2370	0.38(1)	0.126(3)	0.098(4)	0.366(4)	0.028(2)
W8'	0	0.45(3)	0.111(2)	0.127(2)	0.223(4)	0.059(5)
	240	0.27(2)	0.109(3)	0.127(3)	0.208(6)	0.045(2)
	1710	0.66(8)	0.147(2)	0.125(2)	0.355(2)	0.029(2)
	2370	0.62(7)	0.149(2)	0.126(2)	0.354(2)	0.028(2)
W1	240	0.26(2)	0	0.161(4)	0	0.045(2)
	1710	0.88(2)	0	0.1692(9)	0	0.029(2)
	2370	0.89(2)	0	0.1700(9)	0	0.028(2)

Table 4.8b. Refined positional and displacement parameters of the Wat10 sample as in function of time (from Comboni et al. 2018).

Site	t (min)	*s.o.f.*	*x*	*y*	*z*	U_{iso} (Å^2)
Si(1)	0	1	0.2390(2)	0.3821(1)	0.1583(2)	0.0171(5)
	250	1	0.2396(3)	0.3821(3)	0.1581(5)	0.0188(10)
	812	1	0.2387(3)	0.3823(2)	0.1565(4)	0.0210(8)
	1998	1	0.2374(3)	0.3833(3)	0.1516(4)	0.0200(9)
	2464	1	0.2373(3)	0.3832(3)	0.1514(4)	0.0194(9)
	7395	1	0.2374(3)	0.3831(3)	0.1520(5)	0.0190(9)
Si(2)	0	1	0.0824(2)	0.3832(1)	0.3275(3)	0.0173(5)
	250	1	0.0814(3)	0.3838(3)	0.3276(4)	0.0182(10)
	812	1	0.0810(3)	0.3836(2)	0.3270(4)	0.0202(8)
	1998	1	0.0774(3)	0.3839(3)	0.3236(4)	0.0188(9)
	2464	1	0.0777(3)	0.3840(3)	0.3235(4)	0.0189(9)
	7395	1	0.0775(3)	0.3845(3)	0.3235(5)	0.017(1)
Al	0	1	0.1285(2)	0.3098(2)	0.7341(3)	0.0184(6)
	250	1	0.1285(3)	0.3098(9)	0.7346(5)	0.020(1)
	812	1	0.1291(3)	0.3089(2)	0.7353(5)	0.0227(9)
	1998	1	0.1299(3)	0.3076(3)	0.7365(5)	0.021(1)
	2464	1	0.1297(3)	0.3076(3)	0.7367(5)	0.021(1)
	7395	1	0.1296(4)	0.3075(4)	0.7363(5)	0.020(1)
O1	0	1	0.2617(5)	0.5	0.2314(9)	0.0200(5)
	250	1	0.2601(9)	0.5	0.227(1)	0.0194(9)
	812	1	0.2606(8)	0.5	0.226(1)	0.2260(8)
	1998	1	0.2594(9)	0.5	0.220(1)	0.0196(9)
	2464	1	0.2594(9)	0.5	0.220(1)	0.0191(9)
	7395	1	0.2598(10)	0.5	0.220(1)	0.018(1)
O2	0	1	0.2095(3)	0.3774(3)	0.9294(6)	0.0200(5)
	250	1	0.2076(6)	0.3755(6)	0.9278(9)	0.0194(9)
	812	1	0.2085(5)	0.3768(5)	0.9291(8)	0.2260(8)
	1998	1	0.2078(6)	0.3764(6)	0.9240(9)	0.0196(9)
	2464	1	0.2074(6)	0.3765(5)	0.9235(8)	0.0191(9)
	7395	1	0.2079(6)	0.3752(7)	0.9241(9)	0.018(1)
O3	0	1	0.1479(4)	0.3823(3)	0.5531(6)	0.0200(5)
	250	1	0.1473(6)	0.3823(6)	0.5540(9)	0.0194(9)
	812	1	0.1458(5)	0.3811(5)	0.5531(9)	0.2260(8)
	1998	1	0.1407(6)	0.3798(6)	0.5483(9)	0.0196(9)
	2464	1	0.1404(6)	0.3799(6)	0.5488(9)	0.0191(9)
	7395	1	0.1398(7)	0.3814(7)	0.5492(9)	0.018(1)
O4	0	1	0.1487(3)	0.3393(3)	0.2116(7)	0.0200(5)
	250	1	0.1477(6)	0.3395(5)	0.2086(9)	0.0194(9)
	812	1	0.1484(6)	0.3410(4)	0.2091(9)	0.2260(8)

Site	t (min)	*s.o.f.*	*x*	*y*	*z*	U_{iso} (Å^2)
	1998	1	0.1463(6)	0.3448(5)	0.2045(9)	0.0196(9)
	2464	1	0.1463(6)	0.3448(5)	0.2046(9)	0.0191(9)
	7395	1	0.1469(7)	0.3434(6)	0.205(1)	0.018(1)
O5	0	1	0.3358(4)	0.3166(3)	0.2672(7)	0.0200(5)
	250	1	0.3355(6)	0.3167(6)	0.266(1)	0.0194(9)
	812	1	0.3336(6)	0.3164(5)	0.2644(10)	0.2260(8)
	1998	1	0.3296(6)	0.3155(5)	0.2619(10)	0.0196(9)
	2464	1	0.3296(7)	0.3154(5)	0.2619(9)	0.0191(9)
	7395	1	0.3303(7)	0.3146(6)	0.261(1)	0.018(1)
O6	0	1	0.0504(5)	0.5	0.2620(9)	0.0200(5)
	250	1	0.0506(8)	0.5	0.264(1)	0.0194(9)
	812	1	0.0494(8)	0.5	0.266(1)	0.2260(8)
	1998	1	0.0441(8)	0.5	0.266(1)	0.0196(9)
	2464	1	0.0444(8)	0.5	0.267(1)	0.0191(9)
	7395	1	0.0435(9)	0.5	0.268(1)	0.018(1)
O7	0	1	0.0086(4)	0.3103(3)	0.7206(7)	0.0200(5)
	250	1	0.0084(7)	0.3105(6)	0.7200(9)	0.0194(9)
	812	1	0.0089(6)	0.3101(5)	0.7215(9)	0.2260(8)
	1998	1	0.0108(6)	0.3096(6)	0.7285(9)	0.0196(9)
	2464	1	0.0105(6)	0.3095(5)	0.7284(9)	0.0191(9)
	7395	1	0.0097(7)	0.3088(7)	0.7284(9)	0.018(1)
Ca	0	1	0.2726(2)	0.5	0.7580(3)	0.0237(6)
	250	1	0.2721(1)	0.5	0.7573(5)	0.028(1)
	812	1	0.2701(3)	0.5	0.7532(5)	0.029(1)
	1998	1	0.2621(3)	0.5	0.7374(5)	0.026(1)
	2464	1	0.2618(3)	0.5	0.7370(5)	0.026(1)
	7395	1	0.2615(4)	0.5	0.7368(5)	0.026(1)
W2	0	0.52(1)	0.4145(8)	0.4645(8)	0.056(2)	0.057(2)
	250	0.52(1)	0.414(1)	0.464(1)	0.054(2)	0.054(3)
	812	0.50(1)	0.411(1)	0.473(1)	0.047(2)	0.060(3)
	1998	0.59(1)	0.3998 (10)	0.483(2)	0.021(2)	0.060(4)
	2464	0.58(1)	0.3996(9)	0.483(2)	0.020(2)	0.055(3)
	7395	0.57(1)	0.399(1)	0.479(2)	0.023(2)	0.056(3)
W5	0	0.49(2)	0.5	0.434(1)	0.5	0.057(2)
	250	0.51(2)	0.5	0.439(2)	0.5	0.054(3)
	812	0.48(2)	0.5	0.451(2)	0.5	0.060(3)
	1998	0.49(2)	0.5	0.470(2)	0.5	0.060(4)
	2464	0.47(2)	0.5	0.472(2)	0.5	0.055(3)
	7395	0.46(2)	0.5	0.469(3)	0.5	0.056(3)
W8	0	0.60(1)	0.1211(9)	0.1069(9)	0.346(2)	0.057(2)
	250	0.62(2)	0.122(1)	0.106(1)	0.351(3)	0.054(3)

Site	t (min)	*s.o.f.*	*x*	*y*	*z*	U_{iso} (Å^2)
	812	0.69(2)	0.128(1)	0.110(1)	0.354(3)	0.060(3)
	1998	1.03(2)	0.1373(7)	0.1157(7)	0.357(1)	0.060(4)
	2464	1	0.1376(7)	0.1160(7)	0.357(1)	0.055(3)
	7395	1	0.1361(8)	0.1142(9)	0.358(1)	0.056(3)
W8'	0	0.40(1)	0.109(1)	0.126(1)	0.229(3)	0.057(2)
	250	0.38(2)	0.112(2)	0.128(2)	0.228(5)	0.054(3)
	812	0.31(2)	0.112(2)	0.127(2)	0.235(6)	0.060(3)
W1	250	0.11(2)	0	0.165(1)	0	0.054(3)
	812	0.27(2)	0	0.169(3)	0	0.060(3)
	1998	0.83(2)	0	0.171(1)	0	0.060(4)
	2464	0.82(2)	0	0.171(1)	0	0.055(3)
	7395	0.83(2)	0	0.171(1)	0	0.056(3)

Table 4.8c. Refined positional and displacement parameters of leonhardite as a function of pressure (from Comboni et al. 2018)

Site	*P* (GPa)	*s.o.f.*	*x*	*y*	*z*	U_{iso} (Å^2)
Si(1)	0.0001	1	0.2394(2)	0.3822(1)	0.1580(3)	0.0114(6)
	0.06(5)	1	0.2391(2)	0.3821(1)	0.1584(3)	0.0102(5)
	0.14(5)	1	0.2391(2)	0.3821(1)	0.1584(2)	0.0095(5)
	0.31(5)	1	0.2385(2)	0.3821(1)	0.1580(2)	0.0107(4)
	0.53(5)	1	0.2378(2)	0.3821(2)	0.1576(3)	0.0109(5)
	0.86(5)	1	0.2374(2)	0.3821(1)	0.1579(2)	0.0106(4)
	1.11(5)	1	0.2379(3)	0.3822(2)	0.1589(3)	0.0129(6)
	1.69(5)	1	0.2361(3)	0.3823(2)	0.1578(4)	0.0113(7)
	2.38(5)	1	0.2344(3)	0.3824(2)	0.1576(4)	0.0126(7)
	3.01(5)	1	0.2333(3)	0.3825(2)	0.1573(4)	0.0144(7)
	3.26(5)	1	0.2332(3)	0.3828(2)	0.1577(4)	0.0127(6)
	4.40(5)	1	0.2325(3)	0.3829(2)	0.1579(4)	0.0114(7)
	4.79(5)	1	0.2323(3)	0.3835(2)	0.1580(4)	0.0127(7)
	5.38(5)	1	0.2322(4)	0.3835(2)	0.1589(4)	0.0130(7)
	6.52(5)	1	0.2321(4)	0.3840(2)	0.1615(5)	0.0164(8)
	7.46(5)	1	0.2338(9)	0.3844(6)	0.1669(1)	0.025(2)
Si(2)	0.0001	1	0.0835(2)	0.3833(2)	0.3273(3)	0.0131(6)
	0.06(5)	1	0.0827(2)	0.3837(1)	0.3268(3)	0.0105(5)
	0.14(5)	1	0.0824(2)	0.3836(1)	0.3262(2)	0.0104(5)
	0.31(5)	1	0.0820(2)	0.3836(1)	0.3248(2)	0.0117(4)
	0.53(5)	1	0.0811(2)	0.3837(2)	0.3227(3)	0.0125(5)
	0.86(5)	1	0.0795(2)	0.3839(1)	0.3196(2)	0.0119(4)
	1.11(5)	1	0.0784(3)	0.3841(2)	0.3177(3)	0.0137(6)
	1.69(5)	1	0.0760(3)	0.3847(2)	0.3134(4)	0.0125(7)
	2.38(5)	1	0.0723(3)	0.3849(2)	0.3077(4)	0.0146(7)
	3.01(5)	1	0.0700(3)	0.3852(2)	0.3046(4)	0.0160(7)
	3.26(5)	1	0.0686(3)	0.3858 (2)	0.3030(4)	0.0141(6)
	4.40(5)	1	0.0657(3)	0.3864(2)	0.2992(4)	0.0118(7)
	4.79(5)	1	0.0655(3)	0.3866(2)	0.2986(4)	0.0138(7)
	5.38(5)	1	0.0632(4)	0.3868(2)	0.2956(4)	0.0127(7)
	6.52(5)	1	0.0609(4)	0.3877(2)	0.2924(5)	0.0160(8)
	7.46(5)	1	0.0601(9)	0.3872(6)	0.2915(1)	0.0249(2)
Al	0.0001	1	0.1282(2)	0.3094(2)	0.7338(3)	0.0131(6)
	0.06(5)	1	0.1283(2)	0.3096(1)	0.7340(3)	0.0108(5)
	0.14(5)	1	0.1282(2)	0.3095(1)	0.7335(2)	0.0108(5)
	0.31(5)	1	0.1284(2)	0.3094(1)	0.7325(2)	0.0120(4)
	0.53(5)	1	0.1288(3)	0.3093(2)	0.7311(3)	0.0125(6)
	0.86(5)	1	0.1296(2)	0.3092(1)	0.7301(3)	0.0121(5)

Site	P (GPa)	*s.o.f.*	x	y	z	U_{iso} (Å^2)
	1.11(5)	1	0.1297(3)	0.3093(2)	0.7290(4)	0.0135(7)
	1.69(5)	1	0.1314(3)	0.3087(2)	0.7263(4)	0.0122(7)
	2.38(5)	1	0.1331(3)	0.3085(2)	0.7216(4)	0.0130(7)
	3.01(5)	1	0.1349(4)	0.3080(2)	0.7191(5)	0.0142(8)
	3.26(5)	1	0.1354(3)	0.3086(2)	0.7181(4)	0.0129(6)
	4.40(5)	1	0.1374(4)	0.3088(2)	0.7159(5)	0.0115(7)
	4.79(5)	1	0.1377(4)	0.3086(2)	0.7147(5)	0.0134(8)
	5.38(5)	1	0.1395(4)	0.3086(2)	0.7138(5)	0.0125(7)
	6.52(5)	1	0.1405(5)	0.3088(2)	0.7114(6)	0.0173(9)
	7.46(5)	1	0.141(1)	0.3087(5)	0.710(1)	0.0272(2)
O(1)	0.0001	1	0.2601(7)	0.5	0.231(1)	0.011(2)
	0.06(5)	1	0.2614(7)	0.5	0.2319 (9)	0.013(1)
	0.14(5)	1	0.2613(7)	0.5	0.2316(9)	0.012(1)
	0.31(5)	1	0.2613(6)	0.5	0.2324(8)	0.013(1)
	0.53(5)	1	0.2599(8)	0.5	0.233(1)	0.014(2)
	0.86(5)	1	0.2595(6)	0.5	0.2351(8)	0.014(1)
	1.11(5)	1	0.2601(9)	0.5	0.236(1)	0.015(2)
	1.69(5)	1	0.258(1)	0.5	0.238(1)	0.017(2)
	2.38(5)	1	0.257(1)	0.5	0.239(1)	0.017(2)
	3.01(5)	1	0.2591(8)	0.5	0.243(1)	0.018(2)
	3.26(5)	1	0.258(1)	0.5	0.242(1)	0.017(2)
	4.40(5)	1	0.259(1)	0.5	0.245(1)	0.015(2)
	4.79(5)	1	0.259(1)	0.5	0.245(2)	0.018(2)
	5.38(5)	1	0.259(1)	0.5	0.248(2)	0.017(2)
	6.52(5)	1	0.259(1)	0.5	0.252(2)	0.019(2)
	7.46(5)	1	0.257(3)	0.5	0.255(3)	0.016(5)
O(2)	0.0001	1	0.2100(6)	0.3778(3)	0.9307(7)	0.014(1)
	0.06(5)	1	0.2106(5)	0.3777(3)	0.9307(6)	0.012(1)
	0.14(5)	1	0.2115(5)	0.3778(3)	0.9315(6)	0.012(1)
	0.31(5)	1	0.2121(4)	0.3778(3)	0.9311(5)	0.014(9)
	0.53(5)	1	0.2139(6)	0.3776(4)	0.9311(7)	0.014(1)
	0.86(5)	1	0.2148(5)	0.3774(3)	0.9312(5)	0.014(9)
	1.11(5)	1	0.2156(7)	0.3777(5)	0.9309(8)	0.015(1)
	1.69(5)	1	0.2191(8)	0.3760(5)	0.9322(9)	0.013(2)
	2.38(5)	1	0.2213(8)	0.3744(5)	0.931(1)	0.017(2)
	3.01(5)	1	0.2228(8)	0.3741(5)	0.931(1)	0.018(2)
	3.26(5)	1	0.2234(7)	0.3745(4)	0.9311 (9)	0.015(1)
	4.40(5)	1	0.2260(8)	0.3740(5)	0.932(1)	0.014(1)
	4.79(5)	1	0.2266(8)	0.3732(5)	0.933(1)	0.015(2)
	5.38(5)	1	0.2287(9)	0.3736(5)	0.934(1)	0.016(2)
	6.52(5)	1	0.231(1)	0.3719(6)	0.938(1)	0.020(2)

Site	*P* (GPa)	*s.o.f.*	*x*	*y*	*z*	U_{iso} (Å^2)
	7.46(5)	1	0.239(2)	0.369(1)	0.9519(3)	0.027(4)
O(3)	0.0001	1	0.1467(5)	0.3826(4)	0.5551(7)	0.015(1)
	0.06(5)	1	0.1482(5)	0.3827(3)	0.5550(6)	0.014(1)
	0.14(5)	1	0.1481(5)	0.3826(3)	0.5546(6)	0.013(1)
	0.31(5)	1	0.1480(4)	0.3827(3)	0.5531(5)	0.014(9)
	0.53(5)	1	0.1480(6)	0.3836(4)	0.5514(7)	0.014(1)
	0.86(5)	1	0.1472(5)	0.3839(3)	0.5488(6)	0.015(1)
	1.11(5)	1	0.1477(7)	0.3846(5)	0.5481(9)	0.017(1)
	1.69(5)	1	0.1464(8)	0.3853(5)	0.542(1)	0.015(2)
	2.38(5)	1	0.1475(8)	0.3877(5)	0.539(1)	0.017(2)
	3.01(5)	1	0.1482(8)	0.3886(5)	0.536 (1)	0.019(2)
	3.26(5)	1	0.1492(7)	0.3887(5)	0.5356(9)	0.017(1)
	4.40(5)	1	0.1506(8)	0.3897(5)	0.533(1)	0.013(1)
	4.79(5)	1	0.1503(8)	0.3897(5)	0.532(1)	0.015(2)
	5.38(5)	1	0.1512(8)	0.3910(5)	0.531(1)	0.013(2)
	6.52(5)	1	0.1536(9)	0.3925(5)	0.531(1)	0.015(2)
	7.46(5)	1	0.148(2)	0.3966(1)	0.525(3)	0.026(4)
O(4)	0.0001	1	0.1492(5)	0.3396(4)	0.2126(7)	0.016(1)
	0.06(5)	1	0.1490(5)	0.3393(4)	0.2123(6)	0.013(1)
	0.14(5)	1	0.1481(5)	0.3394(4)	0.2107(6)	0.013(1)
	0.31(5)	1	0.1477(4)	0.3394(3)	0.2090(5)	0.015(9)
	0.53(5)	1	0.1462(5)	0.3393(4)	0.2058(7)	0.015(1)
	0.86(5)	1	0.1442(4)	0.3398(3)	0.2011(6)	0.015(1)
	1.11(5)	1	0.1432(6)	0.3400(5)	0.1989(8)	0.017(1)
	1.69(5)	1	0.1398(8)	0.3416(5)	0.190(1)	0.016(2)
	2.38(5)	1	0.1337(8)	0.3450(5)	0.178(1)	0.018(2)
	3.01(5)	1	0.1284(8)	0.3485(6)	0.168(1)	0.021(2)
	3.26(5)	1	0.1270(7)	0.3490(5)	0.1655(9)	0.020(1)
	4.40(5)	1	0.1216(8)	0.3512(5)	0.155(1)	0.018(2)
	4.79(5)	1	0.1207(9)	0.3524(5)	0.154(1)	0.021(2)
	5.38(5)	1	0.1176(9)	0.3543(6)	0.148 (1)	0.020(2)
	6.52(5)	1	0.114(1)	0.3562(6)	0.142(1)	0.023(2)
	7.46(5)	1	0.106(2)	0.3595(1)	0.134(3)	0.036(5)
O(5)	0.0001	1	0.3344(5)	0.3170(4)	0.2675(7)	0.017(1)
	0.06(5)	1	0.3362(5)	0.3164(4)	0.2692(6)	0.017(1)
	0.14(5)	1	0.3357(5)	0.3163(3)	0.2698(6)	0.016(1)
	0.31(5)	1	0.3358(4)	0.3166(3)	0.2717(6)	0.017(1)
	0.53(5)	1	0.3352(6)	0.3171(4)	0.2745(7)	0.017(1)
	0.86(5)	1	0.3344(5)	0.3163(3)	0.2784(6)	0.018(1)
	1.11(5)	1	0.3338(7)	0.3154(4)	0.2800(9)	0.019(2)
	1.69(5)	1	0.3320(8)	0.3160(5)	0.288(1)	0.019(2)
	2.38(5)	1	0.3279(9)	0.3143(5)	0.296(1)	0.021(2)

Site	*P* (GPa)	*s.o.f.*	*x*	*y*	*z*	U_{iso} (Å^2)
	3.01(5)	1	0.3252(9)	0.3137(5)	0.303(1)	0.020(2)
	3.26(5)	1	0.3239(8)	0.3132(4)	0.304(1)	0.020(1)
	4.40(5)	1	0.3213(9)	0.3124(5)	0.311(1)	0.016(2)
	4.79(5)	1	0.3207(9)	0.3121(5)	0.312(1)	0.019(2)
	5.38(5)	1	0.3194(9)	0.3115(5)	0.316 (1)	0.018(2)
	6.52(5)	1	0.319(1)	0.3108 (5)	0.326(1)	0.022(2)
	7.46(5)	1	0.314(2)	0.3103(1)	0.326(3)	0.021(4)
O(6)	0.0001	1	0.0511(8)	0.5	0.262(1)	0.016(2)
	0.06(5)	1	0.0489(7)	0.5	0.2576(9)	0.014(1)
	0.14(5)	1	0.0473(7)	0.5	0.2562(9)	0.013(1)
	0.31(5)	1	0.0474(6)	0.5	0.2557(8)	0.014(1)
	0.53(5)	1	0.0459(9)	0.5	0.253(1)	0.016(2)
	0.86(5)	1	0.0427(7)	0.5	0.2491(9)	0.014(1)
	1.11(5)	1	0.040(1)	0.5	0.245(1)	0.014(2)
	1.69(5)	1	0.035(1)	0.5	0.241(1)	0.016(2)
	2.38(5)	1	0.028(1)	0.5	0.237(1)	0.017(2)
	3.01(5)	1	0.020(1)	0.5	0.234(2)	0.019(2)
	3.26(5)	1	0.019(1)	0.5	0.235(1)	0.017(2)
	4.40(5)	1	0.013(1)	0.5	0.232(1)	0.016(2)
	4.79(5)	1	0.013(1)	0.5	0.232(1)	0.017(2)
	5.38(5)	1	0.010(1)	0.5	0.231(2)	0.018(2)
	6.52(5)	1	0.008(2)	0.5	0.231(2)	0.025(3)
	7.46(5)	1	0.005(3)	0.5	0.233(4)	0.036(6)
O(7)	0.0001	1	0.0100(6)	0.3100(4)	0.7212(7)	0.017(1)
	0.06(5)	1	0.0094(5)	0.3100(3)	0.7210(7)	0.016(1)
	0.14(5)	1	0.0093(5)	0.3095(3)	0.7211(7)	0.015(1)
	0.31(5)	1	0.0109(5)	0.3095(3)	0.7225(6)	0.016(1)
	0.53(5)	1	0.0116(6)	0.3089(4)	0.7229(8)	0.017(1)
	0.86(5)	1	0.0122(5)	0.3082(3)	0.7232(6)	0.016(1)
	1.11(5)	1	0.0126(7)	0.3080(5)	0.7243(9)	0.017(2)
	1.69(5)	1	0.0147(8)	0.3073(5)	0.7252(1)	0.016(2)
	2.38(5)	1	0.0171(8)	0.3058(5)	0.7253(1)	0.019(2)
	3.01(5)	1	0.0183(8)	0.3047(5)	0.7240(1)	0.020(2)
	3.26(5)	1	0.0186(7)	0.3040(4)	0.7239(9)	0.020(1)
	4.40(5)	1	0.0175(8)	0.3015(5)	0.721(1)	0.017(2)
	4.79(5)	1	0.0197(9)	0.3017(5)	0.722(1)	0.020(2)
	5.38(5)	1	0.0201(9)	0.3000(5)	0.721(1)	0.018(2)
	6.52(5)	1	0.021(1)	0.2997(5)	0.719(1)	0.019(2)
	7.46(5)	1	0.022(2)	0.302(1)	0.720(3)	0.023(4)
Ca	0.0001	1	0.2721(2)	0.5	0.7586(3)	0.0176(6)
	0.06(5)	1	0.2725(2)	0.5	0.7585(3)	0.0159(5)
	0.14(5)	1	0.2727(2)	0.5	0.7582(3)	0.0154(5)

Site	*P* (GPa)	*s.o.f.*	*x*	*y*	*z*	U_{iso} (Å^2)
	0.31(5)	1	0.2731(2)	0.5	0.7576(3)	0.0165(5)
	0.53(5)	1	0.2737(3)	0.5	0.7572(3)	0.0175(6)
	0.86(5)	1	0.2746(2)	0.5	0.7565(3)	0.0168(5)
	1.11(5)	1	0.2746(3)	0.5	0.7551(4)	0.0178(7)
	1.69(5)	1	0.2768(3)	0.5	0.7551(5)	0.0161(8)
	2.38(5)	1	0.2791(4)	0.5	0.7558(5)	0.0174(8)
	3.01(5)	1	0.2809(4)	0.5	0.7569(5)	0.0184(8)
	3.26(5)	1	0.2813(3)	0.5	0.7569(4)	0.0171(7)
	4.40(5)	1	0.2831(4)	0.5	0.7576(5)	0.0161(7)
	4.79(5)	1	0.2843(4)	0.5	0.7584(5)	0.0172(8)
	5.38(5)	1	0.2854(4)	0.5	0.7594(5)	0.0176(8)
	6.52(5)	1	0.2893(4)	0.5	0.7659(6)	0.0213(9)
	7.46(5)	1	0.293(1)	0.5	0.774(1)	0.0311(2)
W(2)	0.0001	0.47(3)	0.425(3)	0.464(1)	0.055(2)	0.059(9)
	0.06(5)	0.54(2)	0.418(2)	0.4655(9)	0.057(1)	0.056(4)
	0.14(5)	0.57(2)	0.417(2)	0.4646(9)	0.057(2)	0.058(4)
	0.31(5)	0.55(2)	0.415(2)	0.4657(7)	0.058(2)	0.054(3)
	0.53(5)	0.53(2)	0.417(2)	0.4662(9)	0.060(2)	0.049(4)
	0.86(5)	0.54(2)	0.417(2)	0.468(3)	0.063(2)	0.045(3)
	1.11(5)	0.55(2)	0.419(2)	0.468(1)	0.066(2)	0.044(4)
	1.69(5)	0.58(3)	0.415(2)	0.473(1)	0.065(2)	0.046(5)
	2.38(5)	0.63(3)	0.419(2)	0.474(1)	0.073(2)	0.055(4)
	3.01(5)	0.63(3)	0.422(2)	0.475(1)	0.078(2)	0.052(4)
	3.26(5)	0.60(2)	0.422(2)	0.476(1)	0.078(2)	0.047(3)
	4.40(5)	0.60(2)	0.424(2)	0.476(1)	0.082(2)	0.038(3)
	4.79(5)	0.61(2)	0.422(2)	0.475(1)	0.081(2)	0.042(4)
	5.38(5)	0.58(2)	0.424(2)	0.476(1)	0.088(2)	0.041(4)
	6.52(5)	0.55(2)	0.424(2)	0.475(1)	0.100(3)	0.042(4)
	7.46(5)	0.45(4)	0.422(5)	0.480(4)	0.110(6)	0.048(7)
W(5)	0.0001	0.48(3)	0.5	0.435(2)	0.5	0.059(9)
	0.06(5)	0.44 (2)	0.5	0.435(2)	0.5	0.056(4)
	0.14(5)	0.43(1)	0.5	0.434(2)	0.5	0.058(4)
	0.31(5)	0.41(1)	0.5	0.434(2)	0.5	0.054(3)
	0.53(5)	0.38(1)	0.5	0.434(2)	0.5	0.049(4)
	0.86(5)	0.36(1)	0.5	0.439(2)	0.5	0.045(3)
	1.11(5)	0.39(1)	0.5	0.439(2)	0.5	0.044(4)
	1.69(5)	0.40(2)	0.5	0.452(2)	0.5	0.046(5)
	2.38(5)	0.42(2)	0.5	0.461(2)	0.5	0.055(4)
	3.01(5)	0.42(2)	0.5	0.469(2)	0.5	0.052(4)
	3.26(5)	0.42(1)	0.5	0.467(2)	0.5	0.047(3)
	4.40(5)	0.35(1)	0.5	0.469(2)	0.5	0.038(3)
	4.79(5)	0.37(2)	0.5	0.464(2)	0.5	0.042(4)

Site	*P* (GPa)	*s.o.f.*	*x*	*y*	*z*	U_{iso} (Å^2)
	5.38(5)	0.33(2)	0.5	0.459(3)	0.5	0.041(4)
	6.52(5)	0.35 (2)	0.5	0.436(3)	0.5	0.042(4)
	7.46(5)	0.54 (3)	0.5	0.434(3)	0.5	0.048(7)
W(8)	0.0001	0.58(2)	0.119(1)	0.102(1)	0.349(2)	0.055(1)
	0.06(5)	0.51(2)	0.129(2)	0.105(1)	0.351(3)	0.056(4)
	0.14(5)	0.55(2)	0.127(2)	0.107(1)	0.345(2)	0.058(4)
	0.31(5)	0.57(2)	0.126(1)	0.1093(8)	0.341(2)	0.054(3)
	0.53(5)	0.59(2)	0.123(2)	0.111 (1)	0.335(2)	0.049(4)
	0.86(5)	0.61(2)	0.123(1)	0.1137(8)	0.329(2)	0.045(3)
	1.11(5)	0.58(3)	0.122(2)	0.114(1)	0.328(3)	0.044(4)
	1.69(5)	0.72(4)	0.123(2)	0.118(1)	0.323(3)	0.046(5)
	2.38(5)	0.93(3)	0.118(1)	0.1223(9)	0.303(2)	0.055(4)
	3.01(5)	0.94(3)	0.117(1)	0.1256(8)	0.298(2)	0.052(4)
	3.26(5)	0.91(2)	0.116(1)	0.1264(7)	0.295(1)	0.047(3)
	4.40(5)	0.87(3)	0.114(1)	0.1285(8)	0.289(2)	0.038(3)
	4.79(5)	0.87(3)	0.117(1)	0.1306(8)	0.287(2)	0.042(4)
	5.38(5)	0.89(3)	0.113(1)	0.1328(8)	0.278(2)	0.041(4)
	6.52(5)	0.90(3)	0.112(1)	0.1353(8)	0.261(2)	0.042(4)
	7.46(5)	1.04(6)	0.106(3)	0.140(1)	0.237(3)	0.048(7)
W(8)'	0.0001	0.37(4)	0.112(2)	0.124(2)	0.233(3)	0.055(1)
	0.06(5)	0.37(2)	0.117(2)	0.129(2)	0.245(3)	0.056(4)
	0.14(5)	0.34(2)	0.116(2)	0.130(2)	0.235(4)	0.058(4)
	0.31(5)	0.34(2)	0.114(2)	0.131(1)	0.231(3)	0.054(3)
	0.53(5)	0.32(2)	0.112(3)	0.132(2)	0.226(4)	0.049(4)
	0.86(5)	0.30(2)	0.110(2)	0.132(2)	0.225(4)	0.045(3)
	1.11(5)	0.31(3)	0.119(3)	0.134(3)	0.247(6)	0.044(4)
	1.69(5)	0.22(3)	0.111(5)	0.134(4)	0.231(1)	0.046(5)

Table 4.8d. Refined positional and displacement parameters of hydrated laumontite as a function of pressure (from Comboni et al. 2018).

Site	*P* (GPa)	*s.o.f*	*x*	*y*	*z*	U_{iso} (Å^2)
Si(1)	0.0001	1	0.2368(1)	0.3834(1)	0.1509(2)	0.0134(4)
	0.03(5)	1	0.2365(2)	0.3832(2)	0.1507(3)	0.0140(5)
	0.11(5)	1	0.2366(2)	0.3834(2)	0.1505(3)	0.0163(6)
	0.27(5)	1	0.2364(2)	0.3832(2)	0.1503(3)	0.0150(5)
	0.49(5)	1	0.2365(2)	0.3834(2)	0.1500(2)	0.0147(5)
	0.67(5)	1	0.2365(2)	0.3834(2)	0.1503(2)	0.0140(5)
	0.90(5)	1	0.2365(2)	0.3833(2)	0.1505(2)	0.0121(5)
	1.10(5)	1	0.2366(2)	0.3831(2)	0.1506(3)	0.0129(5)
	1.40(5)	1	0.2367(2)	0.3832(2)	0.1509(3)	0.0124(5)
	1.72(5)	1	0.2365(2)	0.3833(2)	0.1508(2)	0.0149(5)
	2.03(5)	1	0.2364(2)	0.3833(1)	0.1507(2)	0.0121(4)
	2.35(5)	1	0.2366(2)	0.3833(2)	0.1507(3)	0.0172(7)
	2.65(5)	1	0.2363(2)	0.3834(1)	0.1512(2)	0.0120(4)
	2.36(5)	1	0.2361(2)	0.3834(1)	0.1510(2)	0.0109(5)
	1.99(5)	1	0.2362(2)	0.3831(1)	0.1510(2)	0.0117(4)
	1.69(5)	1	0.2362(2)	0.3831(1)	0.1502(3)	0.0126(5)
	0.58(5)	1	0.2362(2)	0.3837(2)	0.1500(2)	0.0105(4)
	0.05(5)	1	0.2362(2)	0.3837(2)	0.1504(3)	0.0118(6)
Si(2)	0.0001	1	0.0786(2)	0.3836(1)	0.3238(2)	0.0127(4)
	0.03(5)	1	0.0781(2)	0.3838(2)	0.3230(3)	0.0143(6)
	0.11(5)	1	0.0780(2)	0.3836(2)	0.3223(3)	0.0169(6)
	0.27(5)	1	0.0778(2)	0.3836(2)	0.3216(3)	0.0160(6)
	0.49(5)	1	0.0778(2)	0.3836(2)	0.3209(2)	0.0149(5)
	0.67(5)	1	0.0774(2)	0.3834(2)	0.3197(2)	0.0144(5)
	0.90(5)	1	0.0771(2)	0.3834(2)	0.3189(2)	0.0123(5)
	1.10(5)	1	0.0769(2)	0.3835(2)	0.3181(2)	0.0128(5)
	1.40(5)	1	0.0768(2)	0.3838(2)	0.3174(3)	0.0124(6)
	1.72(5)	1	0.0764(2)	0.3836(2)	0.3168(2)	0.0148(5)
	2.03(5)	1	0.0760(2)	0.3838(1)	0.3160(3)	0.0136(5)
	2.35(5)	1	0.0760(2)	0.3841(3)	0.3153(3)	0.0175(7)
	2.65(5)	1	0.0747(2)	0.3844(1)	0.3139(3)	0.0131(4)
	2.36(5)	1	0.0757(3)	0.3840(1)	0.3152(3)	0.0120(5)
	1.99(5)	1	0.0767(2)	0.3839(1)	0.3164(3)	0.0124(5)
	1.69(5)	1	0.0762(3)	0.3837(1)	0.3172(3)	0.0140(5)
	0.58(5)	1	0.0780(1)	0.3835(2)	0.3206(2)	0.0110(4)
	0.05(5)	1	0.0790(2)	0.3832(2)	0.3231(3)	0.0115(6)
Al	0.0001	1	0.1288(1)	0.3070(2)	0.7371(2)	0.0134(4)
	0.03(5)	1	0.1286(2)	0.3071(2)	0.7370(3)	0.0152(6)
	0.11(5)	1	0.1282(2)	0.3073(2)	0.7371(3)	0.0179(6)
	0.27(5)	1	0.1288(2)	0.3072(2)	0.7369(3)	0.0168(6)
	0.49(5)	1	0.1291(2)	0.3070(2)	0.7367(3)	0.0159(6)

Site	P (GPa)	s.o.f	x	y	z	U_{iso} (Å^2)
	0.67(5)	1	0.1292(2)	0.3071(2)	0.7361(3)	0.0155(6)
	0.90(5)	1	0.1294(2)	0.3073(2)	0.7357(3)	0.0134(5)
	1.10(5)	1	0.1297(2)	0.3077(2)	0.7352(3)	0.0135(6)
	1.40(5)	1	0.1300(2)	0.3078(2)	0.7345(3)	0.0129(6)
	1.72(5)	1	0.1302(2)	0.3080(2)	0.7342(3)	0.0157(5)
	2.03(5)	1	0.1315(3)	0.3079(2)	0.7335(3)	0.0142(5)
	2.35(5)	1	0.1314(3)	0.3083 (3)	0.7326(4)	0.0177(7)
	2.65(5)	1	0.1325(3)	0.3081(1)	0.7313(3)	0.0136(5)
	2.36(5)	1	0.1321(3)	0.3082(2)	0.7325(3)	0.0129(5)
	1.99(5)	1	0.1315(3)	0.3079(2)	0.7338(3)	0.0138(5)
	1.69(5)	1	0.1305(3)	0.3075(2)	0.7343(3)	0.0151(5)
	0.58(5)	1	0.1291(2)	0.3069(2)	0.7365(2)	0.0112(5)
	0.05(5)	1	0.1291(2)	0.3065(3)	0.7375(3)	0.0124(7)
O(1)	0.0001	1	0.2577(5)	0.5	0.2232(7)	0.018(1)
	0.03(5)	1	0.2577(6)	0.5	0.2225(9)	0.015(2)
	0.11(5)	1	0.2572(7)	0.5	0.2221(10)	0.019(2)
	0.27(5)	1	0.2568(6)	0.5	0.2235(9)	0.016(2)
	0.49(5)	1	0.2571(6)	0.5	0.2246(8)	0.016(2)
	0.67(5)	1	0.2559(6)	0.5	0.2246(8)	0.015(2)
	0.90(5)	1	0.2569(5)	0.5	0.2264(8)	0.014(2)
	1.10(5)	1	0.2572(6)	0.5	0.2271(8)	0.012(2)
	1.40(5)	1	0.2567(6)	0.5	0.2279(9)	0.013(2)
	1.72(5)	1	0.2563(6)	0.5	0.2274(8)	0.015(1)
	2.03(5)	1	0.2556(8)	0.5	0.2293(9)	0.014(1)
	2.35(5)	1	0.2553(8)	0.5	0.2294(10)	0.017(2)
	2.65(5)	1	0.2559(7)	0.5	0.2305(8)	0.013(1)
	2.36(5)	1	0.2549(8)	0.5	0.2295(9)	0.015(2)
	1.99(5)	1	0.2538(8)	0.5	0.2282(9)	0.012(1)
	1.69(5)	1	0.2574(8)	0.5	0.2286(10)	0.016(2)
	0.58(5)	1	0.2576(5)	0.5	0.2253(7)	0.010(1)
	0.05(5)	1	0.2587(7)	0.5	0.2236(9)	0.010(2)
O(2)	0.0001	1	0.2080(5)	0.3770(4)	0.9229(5)	0.0160(9)
	0.03(5)	1	0.2075(5)	0.3782(5)	0.9218(6)	0.017(1)
	0.11(5)	1	0.2081(5)	0.3791(5)	0.9211(7)	0.018(1)
	0.27(5)	1	0.2079(5)	0.3780(5)	0.9212(7)	0.019(1)
	0.49(5)	1	0.2083(4)	0.3778(5)	0.9214(6)	0.018(1)
	0.67(5)	1	0.2094(4)	0.3776(5)	0.9208(6)	0.017(1)
	0.90(5)	1	0.2100(4)	0.3778(4)	0.9207(6)	0.015(1)
	1.10(5)	1	0.2099(4)	0.3783(5)	0.9207(6)	0.014(1)
	1.40(5)	1	0.2110(5)	0.3781(5)	0.9208(6)	0.015(1)
	1.72(5)	1	0.2115(4)	0.3782(4)	0.9207(6)	0.017(1)

Site	P (GPa)	*s.o.f.*	x	y	z	U_{iso} (Å^2)
	2.03(5)	1	0.2132(6)	0.3765(3)	0.9213(6)	0.014(1)
	2.35(5)	1	0.2127(5)	0.3776(6)	0.9213(8)	0.020(1)
	2.65(5)	1	0.2144(6)	0.3769(3)	0.9212(6)	0.0142(10)
	2.36(5)	1	0.2144(6)	0.3766(3)	0.9211(6)	0.013(1)
	1.99(5)	1	0.2125(6)	0.3772(3)	0.9208(6)	0.013(1)
	1.69(5)	1	0.2107(6)	0.3769(4)	0.9213(7)	0.017(1)
	0.58(5)	1	0.2089(4)	0.3775(4)	0.9216(5)	0.0136(10)
	0.05(5)	1	0.2071(5)	0.3784(5)	0.9217(7)	0.014(1)
O(3)	0.0001	1	0.1384(3)	0.3787(3)	0.5471(5)	0.0156(9)
	0.03(5)	1	0.1382(5)	0.3788(5)	0.5468(7)	0.020(1)
	0.11(5)	1	0.1370(5)	0.3791(5)	0.5464(7)	0.020(1)
	0.27(5)	1	0.1379(5)	0.3790(5)	0.5462(7)	0.023(1)
	0.49(5)	1	0.1375(4)	0.3792(5)	0.5447(6)	0.021(1)
	0.67(5)	1	0.1380(4)	0.3795(5)	0.5443(6)	0.020(1)
	0.90(5)	1	0.1382(4)	0.3801(5)	0.5436(6)	0.018(1)
	1.10(5)	1	0.1382(4)	0.3809(5)	0.5433(6)	0.019(1)
	1.40(5)	1	0.1385(5)	0.3810(5)	0.5417(6)	0.019(1)
	1.72(5)	1	0.1388(4)	0.3806(5)	0.5424(6)	0.022(1)
	2.03(5)	1	0.1403(6)	0.3816(4)	0.5424(6)	0.017(1)
	2.35(5)	1	0.1405(6)	0.3812(7)	0.5402(8)	0.025(2)
	2.65(5)	1	0.1423(6)	0.3821(3)	0.5416(6)	0.016(1)
	2.36(5)	1	0.1410(7)	0.3815(3)	0.5410(7)	0.015(1)
	1.99(5)	1	0.1408(6)	0.3814(4)	0.5434(6)	0.016(1)
	1.69(5)	1	0.1405(7)	0.3811(4)	0.5438(7)	0.018(1)
	0.58(5)	1	0.1385(4)	0.3792(4)	0.5448(5)	0.016(1)
	0.05(5)	1	0.1383(5)	0.3777(6)	0.5462(7)	0.019(2)
O(4)	0.0001	1	0.1459(4)	0.3454(4)	0.2071(5)	0.0172(9)
	0.03(5)	1	0.1461(4)	0.3460(5)	0.2070(6)	0.019(1)
	0.11(5)	1	0.1462(5)	0.3452(6)	0.2066(7)	0.023(1)
	0.27(5)	1	0.1459(5)	0.3444(5)	0.2066(6)	0.020(1)
	0.49(5)	1	0.1457(4)	0.3441(5)	0.2056(6)	0.019(1)
	0.67(5)	1	0.1453(4)	0.3447(5)	0.2037(6)	0.018(1)
	0.90(5)	1	0.1444(4)	0.3440(5)	0.2027(6)	0.017(1)
	1.10(5)	1	0.1440(4)	0.3435(5)	0.2012(6)	0.018(1)
	1.40(5)	1	0.1439(5)	0.3434(5)	0.1996(6)	0.018(1)
	1.72(5)	1	0.1430(4)	0.3438(5)	0.1986(5)	0.019(1)
	2.03(5)	1	0.1419(6)	0.3433(3)	0.1953(6)	0.019(1)
	2.35(5)	1	0.1413(6)	0.3429(6)	0.1937(8)	0.024(2)
	2.65(5)	1	0.1391(6)	0.3446(3)	0.1897(6)	0.019(1)
	2.36(5)	1	0.1404(6)	0.3438(4)	0.1919(7)	0.018(1)
	1.99(5)	1	0.1419(6)	0.3433(3)	0.1953(6)	0.019(1)
	1.69(5)	1	0.14376)	0.3432(4)	0.1979(7)	0.019(1)

Site	P (GPa)	*s.o.f.*	x	y	z	U_{iso} (Å^2)
	0.58(5)	1	0.0150(4)	0.3442(4)	0.2043(5)	0.015(1)
	0.05(5)	1	0.1454(5)	0.3449(6)	0.2075(7)	0.017(2)
O(5)	0.0001	1	0.3287(5)	0.3157(4)	0.2605(5)	0.0186(10)
	0.03(5)	1	0.3283(5)	0.3161(5)	0.2609(6)	0.021(1)
	0.11(5)	1	0.3289(5)	0.3158(5)	0.2606(7)	0.022(1)
	0.27(5)	1	0.3283(5)	0.3150(5)	0.2604(7)	0.022(1)
	0.49(5)	1	0.3281(4)	0.3159(5)	0.2609(6)	0.021(1)
	0.67(5)	1	0.3282(4)	0.3165(5)	0.2627(6)	0.022(1)
	0.90(5)	1	0.3288(4)	0.3158(5)	0.2639(6)	0.019(1)
	1.10(5)	1	0.3295(4)	0.3157(5)	0.2653(6)	0.019(1)
	1.40(5)	1	0.3289(5)	0.3153(5)	0.2666(6)	0.018(1)
	1.72(5)	1	0.3289(4)	0.3158(5)	0.2673(6)	0.020(1)
	2.03(5)	1	0.3280(6)	0.3156(3)	0.2686(6)	0.019(1)
	2.35(5)	1	0.3289(6)	0.3156(6)	0.2709(8)	0.022(2)
	2.65(5)	1	0.3278(6)	0.3148(3)	0.2727(6)	0.018(1)
	2.36(5)	1	0.3286(6)	0.3158(4)	0.2720(7)	0.017(1)
	1.99(5)	1	0.3290(6)	0.3151(3)	0.2694(7)	0.019(1)
	1.69(5)	1	0.3294(6)	0.3160(3)	0.2659(7)	0.018(1)
	0.58(5)	1	0.3281(4)	0.3161(4)	0.2619(5)	0.017(1)
	0.05(5)	1	0.3283(5)	0.3161(6)	0.2587(7)	0.018(2)
O(6)	0.0001	1	0.0462(5)	0.5	0.2657(8)	0.020(1)
	0.03(5)	1	0.0470(7)	0.5	0.2652(9)	0.019(2)
	0.11(5)	1	0.0466(7)	0.5	0.266(1)	0.021(2)
	0.27(5)	1	0.0478(7)	0.5	0.2656(10)	0.020(2)
	0.49(5)	1	0.0468(6)	0.5	0.2647(9)	0.020(2)
	0.67(5)	1	0.0451(6)	0.5	0.2621(9)	0.020(2)
	0.90(5)	1	0.0446(6)	0.5	0.2601(9)	0.017(2)
	1.10(5)	1	0.0453(6)	0.5	0.2590(9)	0.017(2)
	1.40(5)	1	0.0449(7)	0.5	0.2580(9)	0.018(2)
	1.72(5)	1	0.0433(6)	0.5	0.2566(8)	0.018(2)
	2.03(5)	1	0.0419(9)	0.5	0.254(9)	0.017(2)
	2.35(5)	1	0.0418(8)	0.5	0.253(1)	0.022(2)
	2.65(5)	1	0.0397(8)	0.5	0.2535(9)	0.018(1)
	2.36(5)	1	0.0402(9)	0.5	0.2533(9)	0.015(2)
	1.99(5)	1	0.0431(9)	0.5	0.2561(9)	0.014(1)
	1.69(5)	1	0.0439(9)	0.5	0.2587(10)	0.017(2)
	0.58(5)	1	0.0459(5)	0.5	0.2618(7)	0.014(1)
	0.05(5)	1	0.0479(7)	0.5	0.2663(10)	0.014(2)
O(7)	0.0001	1	0.0121(3)	0.3091(4)	0.7308(5)	0.0162(9)
	0.03(5)	1	0.0118(5)	0.3097(5)	0.7309(6)	0.019(1)
	0.11(5)	1	0.0114(5)	0.3098(6)	0.7299(7)	0.020(1)
	0.27(5)	1	0.0120(5)	0.3084(6)	0.7308(6)	0.020(1)

Site	*P* (GPa)	*s.o.f.*	*x*	*y*	*z*	U_{iso} (Å^2)
	0.49(5)	1	0.0121(4)	0.3092(5)	0.7310(6)	0.020(1)
	0.67(5)	1	0.0125(4)	0.3087(5)	0.7308(6)	0.020(1)
	0.90(5)	1	0.0130(4)	0.3087(5)	0.7311(6)	0.017(1)
	1.10(5)	1	0.0137(5)	0.3085(5)	0.7312(6)	0.017(1)
	1.40(5)	1	0.0144(5)	0.3085(5)	0.7311(6)	0.016(1)
	1.72(5)	1	0.0132(4)	0.3086(5)	0.7304(6)	0.020(1)
	2.03(5)	1	0.0126(7)	0.3080(4)	0.7300(7)	0.020(1)
	2.35(5)	1	0.0151(6)	0.3106(6)	0.7298(8)	0.023(2)
	2.65(5)	1	0.0132(6)	0.3076(3)	0.7278(7)	0.020(1)
	2.36(5)	1	0.0148(7)	0.3081(4)	0.7309(7)	0.019(1)
	1.99(5)	1	0.0147(7)	0.3080(4)	0.7318(7)	0.021(1)
	1.69(5)	1	0.0137(7)	0.3080(4)	0.7307(8)	0.020(1)
	0.58(5)	1	0.0126(4)	0.3097(4)	0.7314(5)	0.017(1)
	0.05(5)	1	0.0127(5)	0.3107(6)	0.7311(7)	0.017(1)
Ca	0.0001	1.00(1)	0.2584(2)	0.5	0.7319(2)	0.0176(4)
	0.03(5)	0.97(1)	0.2586(2)	0.5	0.7320(3)	0.0169(8)
	0.11(5)	0.98(1)	0.2584(2)	0.5	0.7311(3)	0.1970(8)
	0.27(5)	0.98(1)	0.2583(2)	0.5	0.7300(3)	0.0189(8)
	0.49(5)	0.98(1)	0.2588(2)	0.5	0.7295(3)	0.0180(7)
	0.67(5)	0.98(1)	0.2595(2)	0.5	0.7287(3)	0.0170(7)
	0.90(5)	0.99(1)	0.2600(2)	0.5	0.7287(3)	0.0156(7)
	1.10(5)	0.99(1)	0.2607(2)	0.5	0.7289(3)	0.0160(8)
	1.40(5)	1.00(1)	0.2613(2)	0.5	0.7288(3)	0.0163(8)
	1.72(5)	0.99(1)	0.2618(2)	0.5	0.7290(3)	0.0172(7)
	2.03(5)	0.97(1)	0.2631(3)	0.5	0.7296(3)	0.0149(6)
	2.35(5)	0.99(1)	0.2638(2)	0.5	0.7298(4)	0.0198(10)
	2.65(5)	0.97(1)	0.2651(2)	0.5	0.7311(3)	0.0146(6)
	2.36(5)	0.97(1)	0.2645(3)	0.5	0.7300(3)	0.0143(7)
	1.99(5)	0.97(1)	0.2628(3)	0.5	0.7292(3)	0.0148(6)
	1.69(5)	0.98(1)	0.2622(3)	0.5	0.7295(3)	0.0168(7)
	0.58(5)	0.98(1)	0.2588(2)	0.5	0.7289(2)	0.0126(6)
	0.05(5)	0.98(1)	0.2575(2)	0.5	0.7307(3)	0.0144(9)
W(2)	0.0001	1.00(2)	0.3926(6)	0.5	0.0100(9)	0.0328(9)
	0.03(5)	1.02(2)	0.3920(8)	0.5	0.008(1)	0.036(1)
	0.11(5)	1.02(2)	0.3916(8)	0.5	0.009(1)	0.037(1)
	0.27(5)	1.02(2)	0.3905(8)	0.5	0.009(1)	0.037(1)
	0.49(5)	1.06(2)	0.3902(7)	0.5	0.0093(10)	0.037(1)
	0.67(5)	1.06(2)	0.3904(7)	0.5	0.0116(10)	0.035(1)
	0.90(5)	1.04(2)	0.3906(7)	0.5	0.0136(10)	0.032(1)
	1.10(5)	1.03(2)	0.3908(7)	0.5	0.016(1)	0.032(1)
	1.40(5)	1.04(2)	0.3919(8)	0.5	0.017(1)	0.032(1)
	1.72(5)	1.01(2)	0.3918(7)	0.5	0.0188(10)	0.032(1)

Site	*P* (GPa)	*s.o.f.*	*x*	*y*	*z*	U_{iso} (Å^2)
	2.03(5)	1.01(2)	0.393(1)	0.5	0.020(1)	0.031(1)
	2.35(5)	1.05(3)	0.3913(9)	0.5	0.024(1)	0.038(1)
	2.65(5)	0.97(2)	0.395(1)	0.5	0.027(1)	0.030(1)
	2.36(5)	1.00(2)	0.394(1)	0.5	0.024(1)	0.030(1)
	1.99(5)	1.00(2)	0.394(1)	0.5	0.023(1)	0.029(1)
	1.69(5)	1.02(2)	0.392(1)	0.5	0.018(1)	0.032(1)
	0.58(5)	1.04(2)	0.3909(6)	0.5	0.0091(8)	0.0297(10)
	0.05(5)	1.07(2)	0.3897(9)	0.5	0.005(1)	0.031(1)
W(8)	0.0001	0.53(3)	0.150(1)	0.150(2)	0.350(2)	0.0328(9)
	0.03(5)	0.41(5)	0.158(2)	0.134(3)	0.356(3)	0.036(1)
	0.11(5)	0.29(3)	0.171(3)	0.141(3)	0.361(3)	0.037(1)
	0.27(5)	0.35(4)	0.162(3)	0.139(3)	0.358(3)	0.037(1)
	0.49(5)	0.39(4)	0.158(2)	0.136(3)	0.358(2)	0.037(1)
	0.67(5)	0.45(4)	0.154(2)	0.135(2)	0.356(2)	0.035(1)
	0.90(5)	0.46(3)	0.152(2)	0.135(2)	0.352(2)	0.032(1)
	1.10(5)	0.44(3)	0.154(2)	0.136(2)	0.354(2)	0.032(1)
	1.40(5)	0.44(3)	0.154(2)	0.137(2)	0.354(2)	0.032(1)
	1.72(5)	0.41(3)	0.156(2)	0.139(2)	0.351(2)	0.032(1)
	2.03(5)	0.55(3)	0.148(2)	0.129(1)	0.349(2)	0.031(1)
	2.35(5)	0.35(4)	0.165(3)	0.136(3)	0.355(3)	0.038(1)
	2.65(5)	0.55(2)	0.146(1)	0.130(1)	0.345(2)	0.030(1)
	2.36(5)	0.53(2)	0.151(2)	0.130(1)	0.347(2)	0.030(1)
	1.99(5)	0.53(2)	0.150(2)	0.129(1)	0.349(2)	0.029(1)
	1.69(5)	0.52(3)	0.151(2)	0.129(1)	0.350(2)	0.032(1)
	0.58(5)	0.48(3)	0.154(1)	0.136(2)	0.354(2)	0.0297(10)
	0.05(5)	0.43(5)	0.154(2)	0.135(3)	0.353(3)	0.032(1)
W(1)	0.0001	0.95(2)	0.5	0.667(7)	0	0.0328(9)
	0.03(5)	0.96(2)	0.5	0.667(9)	0	0.036(1)
	0.11(5)	1.00(2)	0.5	0.6672(9)	0	0.037(1)
	0.27(5)	1.02(2)	0.5	0.6659(9)	0	0.037(1)
	0.49(5)	1.02(2)	0.5	0.6664(9)	0	0.037(1)
	0.67(5)	1.02(2)	0.5	0.6659(8)	0	0.035(1)
	0.90(5)	1.03(2)	0.5	0.6646(8)	0	0.032(1)
	1.10(5)	1.04(2)	0.5	0.6652(8)	0	0.032(1)
	1.40(5)	1.05(2)	0.5	0.6650(8)	0	0.032(1)
	1.72(5)	1.03(2)	0.5	0.6654(7)	0	0.032(1)
	2.03(5)	0.99(2)	0.5	0.6668(6)	0	0.031(1)
	2.35(5)	1.02(2)	0.5	0.666(1)	0	0.038(1)
	2.65(5)	0.97(2)	0.5	0.6687(6)	0	0.030(1)
	2.36(5)	0.96(2)	0.5	0.6676(6)	0	0.030(1)
	1.99(5)	1.00(2)	0.5	0.6670(6)	0	0.029(1)
	1.69(5)	1.01(2)	0.5	0.6672(6)	0	0.032(1)

Site	*P* (GPa)	*s.o.f.*	*x*	*y*	*z*	U_{iso} (Å^2)
	0.58(5)	1.00(2)	0.5	0.6654(7)	0	0.0297(10)
	0.05(5)	0.97(2)	0.5	0.666 (1)	0	0.032(1)
W(8')	0.0001	0.47(3)	0.137(1)	0.100(2)	0.375(2)	0.0328(9)
	0.03(5)	0.60(5)	0.136(2)	0.106(2)	0.367(2)	0.036(1)
	0.11(5)	0.71(3)	0.136(1)	0.110(1)	0.364(1)	0.037(1)
	0.27(5)	0.65(4)	0.136(1)	0.107(2)	0.367(2)	0.037(1)
	0.49(5)	0.61(4)	0.136(1)	0.105(2)	0.368(2)	0.037(1)
	0.67(5)	0.55(4)	0.133(2)	0.102(2)	0.370(2)	0.035(1)
	0.90(5)	0.54(3)	0.133(1)	0.102(2)	0.371(2)	0.032(1)
	1.10(5)	0.56(3)	0.131(1)	0.103(2)	0.368(2)	0.032(1)
	1.40(5)	0.56(3)	0.131(2)	0.103(2)	0.366(2)	0.032(1)
	1.72(5)	0.59(3)	0.133(1)	0.104(1)	0.367(1)	0.032(1)
	2.03(5)	0.45(3)	0.130(2)	0.098(1)	0.378(2)	0.031(1)
	2.35(5)	0.65(4)	0.130(2)	0.111(2)	0.357(2)	0.038(1)
	2.65(5)	0.45(2)	0.127(2)	0.098(1)	0.374(2)	0.030(1)
	2.36(5)	0.47(2)	0.128(2)	0.099(1)	0.375(2)	0.030(1)
	1.99(5)	0.47(2)	0.129(2)	0.099(1)	0.377(2)	0.029(1)
	1.69(5)	0.48(3)	0.129(2)	0.100(1)	0.377(2)	0.032(1)
	0.58(5)	0.52(3)	0.135(1)	0.102(2)	0.372(2)	0.0297(10)
	0.05(5)	0.57(5)	0.139(2)	0.102(2)	0.372(2)	0.032(1)
W(5)	0.0001	0.34(2)	0.5	0.469(2)	0.5	0.0328(9)
	0.03(5)	0.35(2)	0.5	0.469(2)	0.5	0.036(1)
	0.11(5)	0.37(2)	0.5	0.464(2)	0.5	0.037(1)
	0.27(5)	0.37(2)	0.5	0.467(2)	0.5	0.037(1)
	0.49(5)	0.38(2)	0.5	0.468(2)	0.5	0.037(1)
	0.67(5)	0.37(2)	0.5	0.472(2)	0.5	0.035(1)
	0.90(5)	0.40(3)	0.5	0.468(2)	0.5	0.032(1)
	1.10(5)	0.41(3)	0.5	0.467(2)	0.5	0.032(1)
	1.40(5)	0.41(2)	0.5	0.465(2)	0.5	0.032(1)
	1.72(5)	0.39(2)	0.5	0.468(2)	0.5	0.032(1)
	2.03(5)	0.39(2)	0.5	0.472(1)	0.5	0.031(1)
	2.35(5)	0.45(2)	0.5	0.464(2)	0.5	0.038(1)
	2.65(5)	0.36(2)	0.5	0.475(1)	0.5	0.030(1)
	2.36(5)	0.37(2)	0.5	0.473(1)	0.5	0.030(1)
	1.99(5)	0.38(3)	0.5	0.471(1)	0.5	0.029(1)
	1.69(5)	0.39(2)	0.5	0.473(1)	0.5	0.032(1)
	0.58(5)	0.34(1)	0.5	0.472(2)	0.5	0.0297(10)
	0.05(5)	0.30(2)	0.5	0.471(3)	0.5	0.032(1)

Table 4.9. Refined isothermal elastic parameters of leonhardite and hydrated laumontite based on III- and II-BM equation of state fits (see the Section 4.2, *Experimental methods*, for further details).

	V_0, l_0 (Å^3, Å)	$K_{V0,\ l0}$ (GPa)	K'	$\beta_{V,l}$ (GPa^{-1})
Elastic parameters of leonhardite fitted with a third-order Birch-Murnaghan EoS				
V	1348(1)	36(1)	2.4(3)	0.0278(8)
a	14.76(1)	37(2)	1.1(5)	0.0090(5)
b	13.055(4)*	95(9)*	4*	0.0035(4)*
c	7.559(7)	20(2)	6.6(8)	0.017 (1)
* *b*-*V* data fitted up to 2.38 GPa				

	V_0, l_0 (Å^3, Å)	$K_{V0,\ l0}$ (GPa)	K'	$\beta_{V,l}$ (GPa^{-1})
Elastic parameters of fully hydrated laumontite fitted with a second-order Birch-Murnaghan EoS				
V	1393.9(6)	54.8(10)	4	0.0184(3)
a	14.923(3)	66(3)	4	0.0050(2)
b	13.174(2)**	85(4)**	4**	0.0039(2)**
c	7.537(2)	40(1)	4	0.0083(3)
** *b*-*V* data fitted up to 2.1 GPa				

Table 5.1. Unit-cell parameters of the zeolite phillipsite with *P*. $P_{19\text{-}21}$ in decompression.

P_n	*P*(GPa)	*V* ($Å^3$)	*a*(Å)	*b*(Å)	*c*(Å)	*β*(°)
P_1	0.20(5)	1001.6(3)	9.8934(4)	14.184(2)	8.6998(3)	124.874(6)
P_2	0.60(5)	1000.2(3)	9.8982(4)	14.153(2)	8.6941(4)	124.792(7)
P_3	0.94(5)	993.8(3)	9.8780(4)	14.105(2)	8.6790(4)	124.733(7)
P_4	1.22(5)	991.1(3)	9.8675(4)	14.082(2)	8.6739(4)	124.683(7)
P_{4b}	1.22(5)	991.6(3)	9.8689(4)	14.085(2)	8.6756(4)	124.685(6)
P_5	1.60(5)	988.8(3)	9.8546(5)	14.068(2)	8.6681(5)	124.631(8)
P_6	1.82(5)	985.3(3)	9.8402(4)	14.051(2)	8.6585(4)	124.612(7)
P_7	2.14(5)	973.4(3)	9.7930(4)	13.995(2)	8.6242(4)	124.560(6)
P_8	2.57(5)	965.2(3)	9.7643(4)	13.952(2)	8.6013(4)	124.539(7)
P_9	3.13(5)	956.9(3)	9.7536(5)	13.886(3)	8.5839(5)	124.610(8)
P_{10}	3.92(5)	941.8(3)	9.7283(7)	13.782(4)	8.5434(8)	124.70(1)
P_{11}	4.85(5)	913.0(3)	9.6822(9)	13.569(4)	8.468(1)	124.85(2)
P_{12}	5.26(5)	900.4(5)	9.6498(9)	13.490(4)	8.432(1)	124.88(2)
P_{13}	6.14(5)	881.0(3)	9.5903(7)	13.379(4)	8.3692(8)	124.88(1)
P_{14}	6.71(5)	864.6(3)	9.5410(9)	13.279(4)	8.323(1)	124.93(2)
P_{15}	7.48(5)	853.8(3)	9.514(1)	13.203(5)	8.300(1)	125.02(2)
P_{16}	8.20(5)	841.7(3)	9.477(1)	13.137(6)	8.264(1)	125.11(2)
P_{17}	8.73(5)	829.6(4)	9.435(2)	13.092(7)	8.220(2)	125.20(3)
P_{18}	9.44(5)	821.1(4)	9.393(2)	13.084(8)	8.187(2)	125.31(3)
P_{19}	1.93(5)	989.8(3)	9.8283(7)	14.103(3)	8.6691(5)	124.539(9)
P_{20}	1.93(5)	971.9(3)	9.7718(5)	14.008(2)	8.6196(4)	124.537(7)
P_{21}	0.50(5)	1007.9(4)	9.925(1)	14.181(5)	8.730(1)	124.88(2)

Table 5.2. Details pertaining to the structure refinements of phillipsite at different pressures.

	P_1 0.20 GPa	P_2 0.60 GPa	P_3 0.94 GPa	P_4 1.22 GPa	P_5 1.60 GPa	P_6 1.82 GPa	P_7 2.14 GPa
min≤*h*≤max	-16; 16	-15; 15	-16; 15	-16; 15	-16; 15	-16; 15	-15; 15
min≤*k*≤max	-10; 10	-10; 12	-10; 11	-11; 11	-11; 11	-10; 11	-11; 11
min≤*l*≤max	-13; 12	-14; 14	-14; 14	-13; 14	-13; 14	-13; 14	-13; 14
Unique	1934	1999	1860	1841	1839	1812	1823
Observed reflections	1181	1500	1395	1360	1356	1312	1349
Number of refined	82	84	84	84	84	83	84
Number of restrains	2	1	1	1	1	1	1
R_{int} (obs)	0.067	0.078	0.078	0.084	0.081	0.083	0.089
R_{int} (all)	0.080	0.088	0.087	0.092	0.091	0.093	0.097
R_1 (obs)	0.0224	0.0232	0.0250	0.0269	0.0253	0.0278	0.0229
R_1 (all)	0.0255	0.0244	0.0261	0.0279	0.0262	0.0289	0.0240
wR_1 (obs)	0.0803	0.0928	0.0907	0.0974	0.0955	0.0980	0.1063
wR_1 (all)	0.0809	0.0945	0.0911	0.0978	0.0960	0.0985	0.1067
Residuals (e^-/Å^3)	+0.23; -0.17	+0.22; -0.24	+0.25; -0.26	+0.24; -0.28	+0.19; -0.19	+0.22; -0.23	+0.20; -0.23

	P_8 2.57 GPa	$P_9$3.13 GPa	P_{10} 3.92 GPa	P_{11} 4.85 GPa	P_{21} 0.50
min≤*h*≤max	-15; 16	-15; 15	-15; 15	-15; 14	-13; 10
min≤*k*≤max	-10; 11	-10; 11	-9; 10	-9; 10	-11; 8
min≤*l*≤max	-13; 14	-12; 14	-11; 13	-11; 13	-8; 14
Unique	1803	1762	1888	1559	1884
Observed reflections	1297	1232	1022	813	1154
Number of refined	83	84	83	83	80
Number of restrains	1	2	2	2	1
R_{int} (obs)	0.102	0.114	0.130	0.162	0.090
R_{int} (all)	0.110	0.126	0.153	0.192	0.010
R_1 (obs)	0.0718	0.0444	0.0392	0.0570	0.0826
R_1 (all)	0.0729	0.0457	0.0440	0.0612	0.0862
wR_1 (obs)	0.1167	0.1297	0.1458	0.1673	0.1027
wR_1 (all)	0.1174	0.1303	0.1469	0.1685	0.1033
Residuals(e^-/Å^3)	+0.26; -0.27	+0.29; -0.25	+0.21; -0.23	+0.34; -0.33	+0.29; -0.23

Table 5.3. Refined positional and displacement parameters of phillipsite at different pressures. (*) fixed value; (**) value refined with a restrain.

Site	*P* (GPa)	*s.o.f.*	*x*	*y*	*z*	U_{iso} (Å^2)
Ca	P_1(0.20)	0.31(1)	0.6672(9)	0.372(1)	0.562(1)	0.041(4)
	P_2(0.60)	0.308*	0.674(1)	0.370(1)	0.572(1)	0.048(2)
	P_3(0.94)	0.308*	0.678(1)	0.367(1)	0.574(1)	0.048(2)
	P_4(1.22)	0.308*	0.681(1)	0.365(1)	0.575(1)	0.049(2)
	P_5(1.60)	0.308*	0.684(1)	0.362(1)	0.577(1)	0.049(2)
	P_6(1.82)	0.308*	0.685(1)	0.362(1)	0.577(1)	0.050(2)
	P_7(2.14)	0.308*	0.687(1)	0.360(1)	0.578(1)	0.047(2)
	P_8(2.57)	0.308*	0.687(1)	0.359(1)	0.577(1)	0.042(2)
	P_9(3.13)	0.308*	0.690(2)	0.356(2)	0.577(2)	0.055(3)
	P_{10}(3.92	0.308*	0.682(2)	0.357(3)	0.576(3)	0.075(5)
	P_{11}(4.85	0.308*	0.684(4)	0.361(5)	0.580(5)	0.12(1)
	P_{21}(0.50	0.308*	0.669(1)	0.367(1)	0.566(1)	0.060(3)
T1(Si)	P_1(0.20)	1.00	0.7264(3)	0.0073(3)	0.2855(3)	0.0139(6)
	P_2(0.60)	1.00	0.7256(2)	0.0068(3)	0.2861(3)	0.0113(6)
	P_3(0.94)	1.00	0.7254(2)	0.0073(3)	0.2863(3)	0.0112(6)
	P_4(1.22)	1.00	0.7250(3)	0.0074(3)	0.2865(3)	0.0114(6)
	P_5(1.60)	1.00	0.7249(2)	0.0073(3)	0.2870(3)	0.0127(6)
	P_6(1.82)	1.00	0.7246(3)	0.0071(3)	0.2867(3)	0.0127(6)
	P_7(2.14)	1.00	0.7241(3)	0.0071(3)	0.2869(3)	0.0142(7)
	P_8(2.57)	1.00	0.7234(3)	0.0063(4)	0.2871(4)	0.0144(8)
	P_9(3.13)	1.00	0.7231(4)	0.0042(4)	0.2883 (4)	0.0178(9)
	P_{10}(3.92	1.00	0.7212(5)	0.0003(6)	0.2891(6)	0.024(1)
	P_{11}(4.85	1.00	0.7213(6)	-0.0050(8)	0.2923(7)	0.031(1)
	P_{21}(0.50	1.00	0.7258(3)	0.0078(3)	0.2862(3)	0.0181(7)
T2(Si)	P_1(0.20)	1.00	0.4207(2)	0.1390(3)	0.0435(3)	0.0147(6)
	P_2(0.60)	1.00	0.4210(2)	0.1384(3)	0.0454(3)	0.0135(6)
	P_3(0.94)	1.00	0.4211(2)	0.1383(3)	0.0458(3)	0.0140(6)
	P_4(1.22)	1.00	0.4213(3)	0.1377(3)	0.0461(3)	0.0145(6)
	P_5(1.60)	1.00	0.4214(3)	0.1376(3)	0.0461(3)	0.0162(6)
	P_6(1.82)	1.00	0.4213(3)	0.1375(3)	0.0458(3)	0.0166(6)
	P_7(2.14)	1.00	0.4213(3)	0.1374(3)	0.0459(4)	0.0187(7)
	P_8(2.57)	1.00	0.4221(4)	0.1371(4)	0.0488(4)	0.0181(8)
	P_9(3.13)	1.00	0.4209(4)	0.1361(5)	0.0532(5)	0.0250(9)
	P_{10}(3.92	1.00	0.4193(5)	0.1342(6)	0.0618(6)	0.032(1)
	P_{11}(4.85	1.00	0.4167(7)	0.1308(9)	0.0725(8)	0.040(2)
	P_{21}(0.50	1.00	0.4214(3)	0.1384(3)	0.0453(4)	0.0206(7)

Site	P (GPa)	*s.o.f.*	x	y	z	U_{iso}(Å^2)
T3(Si)	P_1(0.20)	1.00	0.0434(3)	0.0251(3)	0.2807(3)	0.0140(6)
	P_2(0.60)	1.00	0.0430(2)	0.0271(3)	0.2803(3)	0.0105(6)
	P_3(0.94)	1.00	0.0432(2)	0.0275(3)	0.2804(3)	0.0114(6)
	P_4(1.22)	1.00	0.0435(3)	0.0279(3)	0.2806(3)	0.0116(6)
	P_5(1.60)	1.00	0.0441(2)	0.0286(3)	0.2810(3)	0.0126(6)
	P_6(1.82)	1.00	0.0441(3)	0.0288(3)	0.2810(3)	0.0128(6)
	P_7(2.14)	1.00	0.0442(3)	0.0297(3)	0.2810(3)	0.0152(7)
	P_8(2.57)	1.00	0.0436(3)	0.0307(4)	0.2807(4)	0.0140(7)
	P_9(3.13)	1.00	0.0426(4)	0.0332(4)	0.2814(4)	0.0190(9)
	P_{10}(3.92	1.00	0.0389(4)	0.0348(6)	0.2813(5)	0.023(1)
	P_{11}(4.85	1.00	0.0352(6)	0.0396(8)	0.2816(8)	0.033(1)
	P_{21}(0.50	1.00	0.0438(3)	0.0270(3)	0.2809(3)	0.0183(7)
T4(Si)	P_1(0.20)	1.00	0.0855(3)	0.1408(3)	0.0053(3)	0.0155(6)
	P_2(0.60)	1.00	0.0838(2)	0.1406(3)	0.0039(3)	0.0122(6)
	P_3(0.94)	1.00	0.0832(2)	0.1401(3)	0.0027(3)	0.0122(6)
	P_4(1.22)	1.00	0.0826(3)	0.1400(3)	0.0022(3)	0.0119(6)
	P_5(1.60)	1.00	0.0816(3)	0.1401(3)	0.0014(3)	0.0134(6)
	P_6(1.82)	1.00	0.0815(3)	0.1403(3)	0.0013(3)	0.0131(6)
	P_7(2.14)	1.00	0.0803(3)	0.1399(3)	0.0003(3)	0.0146(7)
	P_8(2.57)	1.00	0.0785(3)	0.1399(4)	-0.0014(4)	0.0140(8)
	P_9(3.13)	1.00	0.0750(4)	0.1398(4)	-0.0042(4)	0.0185(9)
	P_{10}(3.92	1.00	0.0702(4)	0.1387(6)	-0.0090(5)	0.023(1)
	P_{11}(4.85	1.00	0.0624(6)	0.1378(8)	-0.0176(7)	0.030(1)
	P_{21}(0.50	1.00	0.0842(3)	0.1403(3)	0.0044(4)	0.0194(7)
O1	P_1(0.20)	1.00	0.0637(7)	0.1122(9)	0.1739(8)	0.027(2)
	P_2(0.60)	1.00	0.0625(7)	0.1160(8)	0.1738(8)	0.021(1)
	P_3(0.94)	1.00	0.0616(7)	0.1178(8)	0.1747(8)	0.020(1)
	P_4(1.22)	1.00	0.0628(7)	0.1187(8)	0.1763(9)	0.021(2)
	P_5(1.60)	1.00	0.0625(7)	0.1199(8)	0.1765(8)	0.023(1)
	P_6(1.82)	1.00	0.0633(7)	0.1197(8)	0.1772(9)	0.022(2)
	P_7(2.14)	1.00	0.0620(8)	0.1232(9)	0.1782(9)	0.024(2)
	P_8(2.57)	1.00	0.0598(9)	0.123(1)	0.175(1)	0.025(2)
	P_9(3.13)	1.00	0.051(1)	0.124(1)	0.170(1)	0.033(2)
	P_{10}(3.92	1.00	0.036(1)	0.124(2)	0.155(2)	0.042(3)
	P_{11}(4.85	1.00	0.024(2)	0.124(2)	0.149(2)	0.046(4)
	P_{21}(0.50	1.00	0.0654(8)	0.1145(9)	0.1769(9)	0.028(2)

Site	P (GPa)	*s.o.f.*	x	y	z	U_{iso}(Å^2)
O2	P_1(0.20)	1.00	0.6325(8)	0.5868(9)	0.1517(9)	0.027(2)
	P_2(0.60)	1.00	0.6276(7)	0.5864(8)	0.1470(8)	0.025(1)
	P_3(0.94)	1.00	0.6262(7)	0.5844(9)	0.1470(8)	0.026(1)
	P_4(1.22)	1.00	0.6230(8)	0.585(1)	0.1441(9)	0.027(2)
	P_5(1.60)	1.00	0.6226(8)	0.5847(9)	0.1445(9)	0.027(2)
	P_6(1.82)	1.00	0.6215(8)	0.585(1)	0.144(1)	0.029(2)
	P_7(2.14)	1.00	0.6194(9)	0.584(1)	0.142(1)	0.030(2)
	P_8(2.57)	1.00	0.618(1)	0.583(1)	0.141(1)	0.030(2)
	P_9(3.13)	1.00	0.614(1)	0.585(1)	0.139(1)	0.036(2)
	P_{10}(3.92	1.00	0.615(2)	0.588(2)	0.135(2)	0.054(3)
	P_{11}(4.85	1.00	0.620(2)	0.585(3)	0.128(2)	0.069(5)
	P_{21}(0.50	1.00	0.6272(9)	0.5849(9)	0.148(1)	0.033(2)
O3	P_1(0.20)	1.00	0.5951(8)	0.0981(9)	0.2257(9)	0.028(2)
	P_2(0.60)	1.00	0.5940(7)	0.0975(8)	0.2282(9)	0.027(2)
	P_3(0.94)	1.00	0.5952(7)	0.0971(8)	0.2305(8)	0.026(1)
	P_4(1.22)	1.00	0.5952(8)	0.0978(9)	0.2319(9)	0.026(2)
	P_5(1.60)	1.00	0.5962(8)	0.0989(9)	0.2333(9)	0.027(2)
	P_6(1.82)	1.00	0.5959(8)	0.0988(9)	0.233(1)	0.028(2)
	P_7(2.14)	1.00	0.5964(9)	0.099(1)	0.235(1)	0.030(2)
	P_8(2.57)	1.00	0.595(1)	0.099(1)	0.237(1)	0.031(2)
	P_9(3.13)	1.00	0.597(1)	0.094(1)	0.245(1)	0.038(2)
	P_{10}(3.92	1.00	0.592(1)	0.086(2)	0.250(2)	0.044(3)
	P_{11}(4.85	1.00	0.587(2)	0.080(2)	0.256(2)	0.042(4)
	P_{21}(0.50	1.00	0.5964(9)	0.0962(9)	0.230(1)	0.036(2)
O4	P_1(0.20)	1.00	0.0371(8)	0.922(1)	0.1834(9)	0.029(2)
	P_2(0.60)	1.00	0.0359(7)	0.9267(9)	0.1792(9)	0.028(2)
	P_3(0.94)	1.00	0.0386(7)	0.9281(9)	0.1807(8)	0.026(1)
	P_4(1.22)	1.00	0.0404(8)	0.929(1)	0.181(1)	0.027(2)
	P_5(1.60)	1.00	0.0408(8)	0.930(1)	0.1798(9)	0.029(2)
	P_6(1.82)	1.00	0.0413(8)	0.929(1)	0.180(1)	0.029(2)
	P_7(2.14)	1.00	0.0439(9)	0.931(1)	0.181(1)	0.030(2)
	P_8(2.57)	1.00	0.045(1)	0.930(1)	0.182(1)	0.034(2)
	P_9(3.13)	1.00	0.047(1)	0.928(1)	0.185(1)	0.039(3)
	P_{10}(3.92	1.00	0.054(2)	0.934(2)	0.191(2)	0.056(4)
	P_{11}(4.85	1.00	0.061(2)	0.928(2)	0.212(2)	0.057(4)
	P_{21}(0.50	1.00	0.0360(9)	0.925(1)	0.180(1)	0.037(2)

Site	P (GPa)	*s.o.f.*	x	y	z	U_{iso}(Å^2)
O5	P_1(0.20)	1.00	0.8765(7)	0.0448(8)	0.2738(8)	0.026(2)
	P_2(0.60)	1.00	0.8756(7)	0.0441(8)	0.2719(8)	0.023(1)
	P_3(0.94)	1.00	0.8762(7)	0.0451(8)	0.2734(8)	0.026(1)
	P_4(1.22)	1.00	0.8768(8)	0.0454(9)	0.2744(9)	0.026(2)
	P_5(1.60)	1.00	0.8749(8)	0.0456(9)	0.2723(9)	0.029(2)
	P_6(1.82)	1.00	0.8755(8)	0.0461(9)	0.273(1)	0.029(2)
	P_7(2.14)	1.00	0.8732(9)	0.045(1)	0.270(1)	0.034(2)
	P_8(2.57)	1.00	0.873(1)	0.046(1)	0.272(1)	0.032(2)
	P_9(3.13)	1.00	0.872(1)	0.045(1)	0.274(1)	0.043(3)
	P_{10}(3.92	1.00	0.871(1)	0.048(2)	0.278(2)	0.047(3)
	P_{11}(4.85	1.00	0.871(2)	0.046(2)	0.289(2)	0.053(4)
	P_{21}(0.50	1.00	0.8756(8)	0.0470(9)	0.2730(9)	0.030(2)
O6	P_1(0.20)	1.00	0.2804(8)	0.3763(9)	0.0861(8)	0.028(1)
	P_2(0.60)	1.00	0.2804(7)	0.3778(8)	0.0876(9)	0.024(1)
	P_3(0.94)	1.00	0.2790(7)	0.3784(8)	0.0855(9)	0.024(1)
	P_4(1.22)	1.00	0.2785(8)	0.3793(9)	0.084(1)	0.026(2)
	P_5(1.60)	1.00	0.2766(8)	0.3789(9)	0.0824(9)	0.028(2)
	P_6(1.82)	1.00	0.2775(8)	0.3794(9)	0.084(1)	0.028(2)
	P_7(2.14)	1.00	0.2749(9)	0.380(1)	0.081(1)	0.030(1)
	P_8(2.57)	1.00	0.272(1)	0.381(1)	0.078(1)	0.030(2)
	P_9(3.13)	1.00	0.271(1)	0.383(1)	0.082(1)	0.040(3)
	P_{10}(3.92	1.00	0.266(1)	0.388(2)	0.086(2)	0.045(3)
	P_{11}(4.85	1.00	0.262(2)	0.393(2)	0.093(2)	0.049(4)
	P_{21}(0.50	1.00	0.2808(9)	0.3764(9)	0.087(1)	0.036(2)
O7	P_1(0.20)	1.00	0.7934(7)	0.5203(8)	0.5026(7)	0.022(1)
	P_2(0.60)	1.00	0.7937(7)	0.5216(8)	0.5014(8)	0.022(1)
	P_3(0.94)	1.00	0.7938(7)	0.5224(8)	0.5021(8)	0.023(1)
	P_4(1.22)	1.00	0.7925(8)	0.5227(9)	0.5012(9)	0.024(2)
	P_5(1.60)	1.00	0.7925(8)	0.5243(9)	0.5013(9)	0.027(2)
	P_6(1.82)	1.00	0.7917(8)	0.5241(9)	0.501(1)	0.027(2)
	P_7(2.14)	1.00	0.7931(9)	0.526(1)	0.503(1)	0.032(2)
	P_8(2.57)	1.00	0.794(1)	0.529(1)	0.504(1)	0.033(2)
	P_9(3.13)	1.00	0.792(1)	0.535(1)	0.505(1)	0.040(2)
	P_{10}(3.92	1.00	0.790(1)	0.543(2)	0.500(2)	0.042(3)
	P_{11}(4.85	1.00	0.788(2)	0.554(2)	0.498(2)	0.049(4)
	P_{21}(0.50	1.00	0.7941(8)	0.5229(9)	0.5024(9)	0.028(2)

Site	P (GPa)	*s.o.f.*	x	y	z	U_{iso}(Å^2)
O8	P_1(0.20)	0.50	0.550(1)	3/4	-0.019(1)	0.033(2)
	P_2(0.60)	0.50	0.551(1)	3/4	-0.019(1)	0.030(2)
	P_3(0.94)	0.50	0.552(1)	3/4	-0.018(1)	0.036(2)
	P_4(1.22)	0.50	0.554(1)	3/4	-0.017(1)	0.033(3)
	P_5(1.60)	0.50	0.557(1)	3/4	-0.014(2)	0.040(3)
	P_6(1.82)	0.50	0.556(1)	3/4	-0.014(2)	0.038(3)
	P_7(2.14)	0.50	0.558(2)	3/4	-0.011(2)	0.044(3)
	P_8(2.57)	0.50	0.554(2)	3/4	-0.017(2)	0.047(4)
	P_9(3.13)	0.50	0.552(2)	3/4	-0.029(2)	0.059(5)
	P_{10}(3.92	0.50	0.545(3)	3/4	-0.050(3)	0.080(7)
	P_{11}(4.85	0.50	0.546(4)	3/4	-0.069(5)	0.10(1)
	P_{21}(0.50	0.50	0.550(1)	3/4	-0.020(1)	0.040(3)
O9	P_1(0.20)	0.50	0 .026(1)	1/4	-0.061(1)	0.029(2)
	P_2(0.60)	0.50	0.028(1)	1/4	-0.063(1)	0.026(2)
	P_3(0.94)	0.50	0.028(1)	1/4	-0.067(1)	0.027(2)
	P_4(1.22)	0.50	0.028(1)	1/4	-0.068(1)	0.025(2)
	P_5(1.60)	0.50	0.027(1)	1/4	-0.071(1)	0.028(2)
	P_6(1.82)	0.50	0.026(1)	1/4	0.071(1)	0.028(2)
	P_7(2.14)	0.50	0.026(1)	1/4	-0.073(1)	0.032(2)
	P_8(2.57)	0.50	0.023(1)	1/4	-0.079(2)	0.033(3)
	P_9(3.13)	0.50	0.022(2)	1/4	-0.084(2)	0.040(3)
	P_{10}(3.92	0.50	0.017(2)	1/4	-0.097(3)	0.050(5)
	P_{11}(4.85	0.50	0.022(3)	1/4	-0.097(4)	0.069(7)
	P_{21}(0.50	0.50	0.026(1)	1/4	-0.064(1)	0.035(3)
K1	P_1(0.20)	0.59(2)	0.862(1)	1/4	0.226(2)	0.048(2)
	P_2(0.60)	0.49(2)	0.854(1)	1/4	0.220(1)	0.041(2)
	P_3(0.94)	0.46(2)	0.848(1)	1/4	0.215(2)	0.039(1)
	P_4(1.22)	0.44(2)	0.845(1)	1/4	0.212(3)	0.038(2)
	P_5(1.60)	0.42(3)	0.842(2)	1/4	0.209(3)	0.041(2)
	P_6(1.82)	0.42(3)	0.841(2)	1/4	0.208(3)	0.039(2)
	P_7(2.14)	0.50(4)	0.836(2)	1/4	0.199(3)	0.040(2)
	P_8(2.57)	0.51(4)	0.833(2)	1/4	0.199(3)	0.037(2)
	P_9(3.13)	0.50(4)	0.827(2)	1/4	0.197(4)	0.041(2)
	P_{10}(3.92	0.48(4)	0.825(3)	1/4	0.208(5)	0.059(3)
	P_{11}(4.85	0.53(7)	0.819(5)	1/4	0.211(8)	0.106(6)
	P_{21}(0.50	0.51(2)	0.853(1)	1/4	0.217(2)	0.048(2)

Site	P (GPa)	*s.o.f.*	x	y	z	U_{iso}(Å^2)
K2	P_1(0.20)	0.33**	0.823(2)	1/4	0.152(3)	0.048(2)**
	P_2(0.60)	0.43**	0.817(1)	1/4	0.147(2)	0.041(2)**
	P_3(0.94)	0.46**	0.817(1)	1/4	0.147(2)	0.039(1)**
	P_4(1.22)	0.48**	0.816(1)	1/4	0.147(2)	0.038(2)**
	P_5(1.60)	0.50**	0.815(2)	1/4	0.148(3)	0.041(2)**
	P_6(1.82)	0.50**	0.811(2)	1/4	0.142(4)	0.040(2)**
	P_7(2.14)	0.42**	0.808(2)	1/4	0.139(4)	0.037(2)**
	P_8(2.57)	0.41**	0.808(2)	1/4	0.139(4)	0.037(2)**
	P_9(3.13)	0.42**	0.803(2)	1/4	0.137(4)	0.041(2)**
	P_{10}(3.92	0.44**	0.797(3)	1/4	0.136(5)	0.059(3)**
	P_{11}(4.85	0.39**	0.787*	1/4	0.135*	0.106(6)*
	P_{21}(0.50	0.41**	0.814(2)	1/4	0.141(3)	0.048(2)**
W1	P_1(0.20)	0.62(4)	0.787(3)	1/4	0.530(3)	0.079(4)
	P_2(0.60)	0.32(4)	0.787(6)	1/4	0.531(7)	0.075*
	P_3(0.94)	0.21(4)	0.782(8)	1/4	0.54(1)	0.075*
	P_4(1.22)	0.17(4)	0.77(1)	1/4	0.56(1)	0.075*
	P_5(1.60)	0.20(4)	0.72(1)	1/4	0.56(1)	0.075*
	P_6(1.82)	0.16(4)	0.73(1)	1/4	0.56(1)	0.075*
	P_7(2.14)	0.19(4)	0.72(1)	1/4	0.55(1)	0.075*
	P_8(2.57)	0.30(5)	0.712(8)	1/4	0.559(9)	0.075*
	P_9(3.13)	0.46(5)	0.699(9)	1/4	0.550(7)	0.075*
	P_{10}(3.92	0.35(5)	0.709(9)	1/4	0.568(9)	0.075*
	P_{11}(4.85	0.36(6)	0.72(1)	1/4	0.57(1)	0.075*
	P_{21}(0.50	0.42(3)	0.761(4)	1/4	0.582(5)	0.075*
W2	P_1(0.20)	0.60(4)	0.779(3)	3/4	0.430(3)	0.079(4)**
	P_2(0.60)	0.40(4)	0.791(5)	3/4	0.429(6)	0.075*
	P_3(0.94)	0.33(4)	0.792(7)	3/4	0.426(7)	0.075*
	P_4(1.22)	0.28(4)	0.798(8)	3/4	0.427(9)	0.075*
	P_5(1.60)	0.29(4)	0.791(8)	3/4	0.424(9)	0.075*
	P_6(1.82)	0.29(4)	0.788(8)	3/4	0.421(9)	0.075*
	P_7(2.14)	0.32(4)	0.791(7)	3/4	0.422(8)	0.075*
	P_8(2.57)	0.30(6)	0.72(1)	3/4	0.39(1)	0.075*
	P_9(3.13)	0.51(4)	0.670(5)	3/4	0.357(6)	0.075*
	P_{10}(3.92	0.78(5)	0.659(4)	3/4	0.344(4)	0.075*
	P_{11}(4.85	0.44(6)	0.65(1)	3/4	0.33(1)	0.075*
	P_{21}(0.50	0.47(4)	0.761(4)	3/4	0.418(5)	0.075*

Site	P (GPa)	*s.o.f.*	x	y	z	U_{iso}(Å^2)
W3	P_1(0.20)	0.96(4)	0.342(1)	0.642(1)	0.158(1)	0.079(4)**
	P_2(0.60)	0.98(3)	0.342(1)	0.635(1)	0.156(2)	0.075*
	P_3(0.94)	0.98(3)	0.341(1)	0.632(1)	0.153(2)	0.075*
	P_4(1.22)	0.99(3)	0.341(1)	0.632(1)	0.154(2)	0.075*
	P_5(1.60)	0.99(3)	0.340(1)	0.631(1)	0.151(2)	0.075*
	P_6(1.82)	1.00*	0.340(1)	0.632(1)	0.153(2)	0.075*
	P_7(2.14)	1.00(3)	0.339(1)	0.630(2)	0.152(2)	0.075*
	P_8(2.57)	1.00*	0.342(2)	0.633(2)	0.158(2)	0.075*
	P_9(3.13)	0.98(3)	0.343(2)	0.636(2)	0.163(2)	0.075*
	P_{10}(3.92	0.80(3)	0.343(2)	0.632(3)	0.162(3)	0.075*
	P_{11}(4.85	0.69(4)	0.347(3)	0.631(4)	0.159(4)	0.075*
	P_{21}(0.50	0.96(2)	0.347(1)	0.637(1)	0.163(2)	0.075*
W4	P_1(0.20)	0.55(4)	0.427(3)	1/4	0.437(3)	0.079(4)**
	P_2(0.60)	0.47(4)	0.426(4)	1/4	0.432(5)	0.075*
	P_3(0.94)	0.43(4)	0.421(4)	1/4	0.427(5)	0.075*
	P_4(1.22)	0.42(5)	0.422(5)	1/4	0.429(6)	0.075*
	P_5(1.60)	0.36(5)	0.419(6)	1/4	0.425(7)	0.075*
	P_6(1.82)	0.38(5)	0.418(5)	1/4	0.424(7)	0.075*
	P_7(2.14)	0.32(5)	0.419(7)	1/4	0.426(8)	0.075*
	P_8(2.57)	0.45(6)	0.417(6)	1/4	0.417(6)	0.075*
	P_9(3.13)	0.25(5)	0.41(1)	1/4	0.41(1)	0.075*
	P_{21}(0.50	0.57(4)	0.423(3)	1/4	0.431(4)	0.075*
W5	P_1(0.20)	0.55(3)	0.526(3)	0.987(3)	0.545(3)	0.079(4)**
	P_2(0.60)	0.61(3)	0.534(2)	0.973(3)	0.545(3)	0.075*
	P_3(0.94)	0.60(3)	0.533(2)	0.975(3)	0.547(3)	0.075*
	P_4(1.22)	0.60(3)	0.536(2)	0.975(3)	0.547(3)	0.075*
	P_5(1.60)	0.60(3)	0.538(2)	0.976(3)	0.551(3)	0.075*
	P_6(1.82)	0.59(3)	0.536(2)	0.974(3)	0.547(3)	0.075*
	P_7(2.14)	0.62(3)	0.539(2)	0.977(3)	0.554(3)	0.075*
	P_8(2.57)	0.58(3)	0.538(3)	0.974(4)	0.552(4)	0.075*
	P_9(3.13)	0.51(3)	0.534(4)	0.977(4)	0.544(4)	0.075*
	P_{10}(3.92	0.67(3)	0.533(3)	0.982(5)	0.536(4)	0.075*
	P_{11}(4.85	0.68(4)	0.534(3)	1.021(5)	0.543(4)	0.075*
	P_{21}(0.50	0.62(2)	0.531(2)	0.973(3)	0.542(3)	0.075*

Site	*P* (GPa)	*s.o.f.*	*x*	*y*	*z*	U_{iso}(Å^2)
W6	P_1(0.20)	0.29(2)	0.590(5)	0.870(6)	0.552(5)	0.079(4)**
	P_2(0.60)	0.41(3)	0.590(3)	0.856(4)	0.549(4)	0.075*
	P_3(0.94)	0.50(3)	0.589(3)	0.857(4)	0.544(3)	0.075*
	P_4(1.22)	0.56(3)	0.587(3)	0.856(4)	0.545(3)	0.075*
	P_5(1.60)	0.56(3)	0.590(3)	0.855(3)	0.546(3)	0.075*
	P_6(1.82)	0.59(3)	0.590(2)	0.856(3)	0.547(3)	0.075*
	P_7(2.14)	0.57(3)	0.591(3)	0.852(4)	0.547(3)	0.075*
	P_8(2.57)	0.56(3)	0.591(3)	0.857(4)	0.555(4)	0.075*
	P_9(3.13)	0.51**	0.593(4)	0.851(5)	0.545(4)	0.075*
	P_{10}(3.92	0.52**	0.595(4)	0.844(4)	0.554(5)	0.075*
	$\grave{P}_{11}$(4.85	0.47**	0.609(5)	0.848(5)	0.566(6)	0.075*
	$\grave{P}_{21}$(0.50	0.46**	0.591(3)	0.863(4)	0.547(4)	0.075*
W2’	$\grave{P}_2$(0.60)	0.29(3)	0.668(7)	3/4	0.369(8)	0.075*
	P_3(0.94)	0.34(7)	0.676(6)	3/4	0.376(7)	0.075*
	P_4(1.22)	0.36(4)	0.673(6)	3/4	0.374(8)	0.075*
	P_5(1.60)	0.33(4)	0.673(7)	3/4	0.376(8)	0.075*
	P_6(1.82)	0.34(4)	0.665(6)	3/4	0.370(8)	0.075*
	P_7(2.14)	0.37(4)	0.671(7)	3/4	0.368(8)	0.075*
	P_8(2.57)	0.40(6)	0.624(9)	3/4	0.346(8)	0.075*
W1’	P_9(3.13)	0.36(4)	0.005(7)	1/4	0.550(8)	0.075*
	P_{10}(3.92	0.20(5)	0.02(1)	1/4	0.57(2)	0.075*
	$\grave{P}_{11}$(4.85	0.36(6)	0.051(9)	1/4	0.58(1)	0.075*
W2’’	$\grave{P}_{10}$(3.92	0.27(5)	0.46(1)	1/4	0.77(1)	0.075*
	$\grave{P}_{11}$(4.85	0.58(0)	0.446(8)	1/4	0.755(8)	0.075*

Table 5.4 Refined T-O distances (Å) in phillipsite structure at different pressures. *P* values in Table 5.3.

P_n	*P*(GPa)	T1-O5	T1-O7	T1-O2	T1-O3	T2-O8	T2-O2	T2-O6	T2-O3
P_1	0.20(5)	1.635(1)	1.652(1)	1.661(2)	1.685(1)	1.634(2)	1.638(1)	1.644(1)	1.645(2)
P_2	0.60(5)	1.645(1)	1.637(1)	1.675 (2)	1.688(1)	1.642(2)	1.628(1)	1.645(1)	1.640(2)
P_3	0.94(5)	1.646(1)	1.643(1)	1.657(2)	1.668(1)	1.636(2)	1.645(1)	1.641(1)	1.650(2)
P_4	1.22(5)	1.647(1)	1.636(1)	1.679(2)	1.669(1)	1.641(2)	1.633(1)	1.637(1)	1.646(2)
P_5	1.60(5)	1.645(1)	1.639(1)	1.674(2)	1.678(1)	1.640(2)	1.630(1)	1.643(1)	1.650(2)
P_6	1.82(5)	1.649(1)	1.633(1)	1.673(2)	1.676(1)	1.641(2)	1.625(1)	1.641(1)	1.647(2)
P_7	2.14(5)	1.636(1)	1.647(1)	1.666(2)	1.666(1)	1.637(2)	1.618(1)	1.642(1)	1.651(2)
P_8	2.57(5)	1.633(1)	1.652(1)	1.656(2)	1.676(1)	1.637(2)	1.632(1)	1.638(1)	1.630(2)
P_9	3.13(5)	1.626(1)	1.662(1)	1.655(2)	1.643(1)	1.632(2)	1.641(1)	1.629(1)	1.665(2)
P_{10}	3.92(5)	1.655(1)	1.635(1)	1.651(1)	1.619(1)	1.650(2)	1.647(1)	1.645(1)	1.664(2)
P_{11}	4.85(5)	1.632(1)	1.628(1)	1.605(1)	1.639(1)	1.681(2)	1.657(1)	1.643(1)	1.654(1)
P_{21}	0.50(5)	1.647(1)	1.652(1)	1.668(2)	1.652(1)	1.643(2)	1.643(1)	1.638(1)	1.660(2)

P_n	*P*(GPa)	T3-O1	T3-O7	T3-O5	T3-O4	T4-O9	T4-O4	T4-O1	T4-O6
P_1	0.20(5)	1.622(1)	1.641(2)	1.642(1)	1.669(2)	1.637(2)	1.638(1)	1.650(1)	1.651(1)
P_2	0.60(5)	1.637(1)	1.650(1)	1.635(1)	1.651(2)	1.636(2)	1.641(1)	1.644(1)	1.664(1)
P_3	0.94(5)	1.639(1)	1.642(2)	1.635(1)	1.635(2)	1.641(2)	1.650(1)	1.653(1)	1.657(1)
P_4	1.22(5)	1.638(1)	1.650(2)	1.633(1)	1.631(2)	1.638(2)	1.655(2)	1.654(1)	1.657(1)
P_5	1.60(5)	1.640(1)	1.644(2)	1.643(1)	1.632(2)	1.638(2)	1.656(1)	1.657(1)	1.650(1)
P_6	1.82(5)	1.634(1)	1.649(2)	1.640(1)	1.644(2)	1.636(2)	1.649(1)	1.657(1)	1.657(1)
P_7	2.14(5)	1.644(2)	1.628(2)	1.639(1)	1.630(2)	1.636(2)	1.657(1)	1.659(1)	1.638(1)
P_8	2.57(5)	1.637(1)	1.619(2)	1.637(1)	1.651(2)	1.640(2)	1.637(1)	1.648(1)	1.634(1)
P_9	3.13(5)	1.611(1)	1.612(2)	1.633(1)	1.682(2)	1.634(2)	1.620(1)	1.655(1)	1.642(2)
P_{10}	3.92(5)	1.656(1)	1.656(2)	1.625(1)	1.634(2)	1.657(2)	1.657(1)	1.632(1)	1.633(1)
P_{11}	4.85(5)	1.576(1)	1.687(2)	1.633(1)	1.718(2)	1.643(2)	1.652(1)	1.672(1)	1.654(1)
P_{21}	0.50(5)	1.618(1)	1.637(2)	1.651(1)	1.666(2)	1.645(2)	1.633(1)	1.654(1)	1.662(1)

Table 5.5 Refined interatomic distances (Å) in the structure of phillipsite at different pressures. *P* values in Table 5.3.

P_n	*P*(GPa)	K1-O1(x2)	K1-O8	K2-O1(x2)	K2-O8	Ca-O4	Ca-O7
P_1	0.20(5)	3.004(2)	3.391(3)	2.995(2)	3.181(2)	2.564(3)	2.642(2)
P_2	0.60(5)	2.995(2)	3.337(3)	2.981(2)	3.148(2)	2.541(3)	2.678(2)
P_3	0.94(5)	2.978(2)	3.300(3)	2.953(2)	3.148(2)	2.517(3)	2.707(3)
P_4	1.22(5)	2.976(2)	3.282(3)	2.948(2)	3.143(2)	2.493(3)	2.712(3)
P_5	1.60(5)	2.972(2)	3.283(3)	2.946(2)	3.153(2)	2.489(2)	2.747(3)
P_6	1.82(5)	2.981(2)	3.260(3)	2.941(2)	3.151(2)	2.474(2)	2.740(3)
P_7	2.14(5)	2.924(2)	3.226(2)	2.901(2)	3.118(2)	2.458(2)	2.771(3)
P_8	2.57(5)	2.927(2)	3.170(2)	2.894(2)	3.070(2)	2.440(2)	2.793(3)
P_9	3.13(5)	2.897(2)	3.109(2)	2.856(2)	3.027(2)	2.407(2)	2.867(3)
P_{10}	3.92(5)	2.908(2)	3.038(2)	2.827(2)	2.965(2)	2.419(2)	2.974(3)
P_{11}	4.85(5)	2.907(2)	3.025(2)	2.831(2)	2.952(1)	2.261(2)	3.048(3)
P_{21}	0.50(5)	3.008(2)	3.320(3)	3.016(2)	3.117(2)	2.591(3)	2.732(3)

P_n	*P*(GPa)	W1-Ca	W1-W6	W2-W6	W2-O8	W1-O9	W1-O3(x2)
P_1	0.20(5)	2.202(2)	3.790(2)	3.123(2)	3.207(3)	2.940(3)	3.081(3)
P_2	0.60(5)	2.174(2)	3.700(2)	3.104(1)	3.205(3)	2.923(3)	3.081(3)
P_3	0.94(5)	2.039(2)	3.613(2)	3.120(1)	3.175(3)	2.821(3)	3.121(3)
P_4	1.22(5)	1.879(2)	3.435(2)	3.164(1)	3.174(4)	2.753(4)	3.167(3)
P_5	1.60(5)	1.658(2)	3.059(2)	3.104(1)	3.129(3)	2.896(3)	3.161(2)
P_6	1.82(5)	1.653(1)	3.088(3)	3.096(1)	3.104(3)	2.842(3)	3.187(2)
P_7	2.14(5)	1.612(2)	2.980(2)	3.068(1)	3.085(3)	2.944(4)	3.092(2)
P_8	2.57(5)	1.565(2)	2.939(2)	2.809(3)	2.880(2)	2.860(3)	3.137(2)
P_9	3.13(5)	1.496(2)	2.844(2)	2.544(1)	2.826(2)	2.919(4)	3.087(2)
P_{10}	3.92(5)	1.512(2)	2.827(2)	2.563(1)	2.878(2)	2.720(3)	3.197(3)
P_{11}	4.85(5)	1.562(2)	2.986(2)	2.641(1)	2.938(2)	2.690(3)	3.229(3)
P_{21}	0.50(5)	2.114(2)	3.698(2)	2.958(2)	3.129(3)	2.957(3)	3.053(3)

Table 5.6. High-pressure evolution of the 8-mRs(001) in phillipsite structure: relevant interatomic distances (Å), angles (°), and the ellipticity ratio $\varepsilon_{8\text{-mRs}(001)}$ (calculated as O5-O5/O9-O8, with O5-O5>O9-O8). *P* values in Table 5.3.

P_n	*P*(GPa)	O5-O5	O9-O8	O1-O1	O3-O3	O1-O3	$\varepsilon_{8\text{-mRs}(001)}$
P_1	0.20(5)	5.810(8)	6.121(2)	3.901(6)	4.299(6)	4.913(2)	0.948(2)
P_2	0.60(5)	5.828(8)	6.166(2)	3.794(5)	4.318(6)	4.929(2)	0.945(2)
P_3	0.94(5)	5.780(8)	6.180(2)	3.730(5)	4.314(6)	4.908(2)	0.935(2)
P_4	1.22(5)	5.756(8)	6.181(2)	3.693(5)	4.284(6)	4.907(2)	0.932(2)
P_5	1.60(5)	5.752(8)	6.203(2)	3.661(5)	4.252(6)	4.901(2)	0.927(2)
P_6	1.82(5)	5.731(8)	6.179(2)	3.661(5)	4.249(6)	4.899(2)	0.928(2)
P_7	2.14(5)	5.724(8)	6.161(2)	3.550(5)	4.233(6)	4.869(2)	0.929(2)
P_8	2.57(5)	5.706(8)	6.141(2)	3.532(5)	4.218(6)	4.869(2)	0.929(2)
P_9	3.13(5)	5.673(8)	6.194(2)	3.483(5)	4.316(6)	4.826(2)	0.915(2)
P_{10}	3.92(5)	5.555(8)	6.261(3)	3.465(5)	4.507(7)	4.849(2)	0.887(2)
P_{11}	4.85(5)	5.596(8)	6.431(3)	3.465(5)	4.678(7)	4.866(2)	0.870(2)
P_{21}	0.50(5)	5.747(8)	6.145(2)	3.836(5)	4.354(6)	4.924(2)	0.935(2)

P_n	*P*(GPa)	O1-O9-O1	O1-O5-O3	O5-O3-O8	O3-O8-O3
P_1	0.20(5)	92.90(5)	135.32(2)	116.62(3)	108.97(6)
P_2	0.60(5)	90.37(5)	134.76(2)	115.86(3)	108.84(7)
P_3	0.94(5)	88.20(5)	134.80(2)	115.62(3)	107.99(7)
P_4	1.22(5)	87.02(6)	134.71(2)	115.60(3)	106.92(7)
P_5	1.60(5)	85.93(5)	134.61(2)	115.84(2)	105.24(6)
P_6	1.82(5)	85.92(5)	134.89(2)	115.62(2)	105.40(7)
P_7	2.14(5)	83.56(5)	134.20(2)	115.17(2)	104.29(6)
P_8	2.57(5)	82.66(5)	133.92(2)	114.67(2)	105.55(6)
P_9	3.13(5)	81.13(5)	134.44(2)	113.40(3)	107.78(6)
P_{10}	3.92(5)	80.21(5)	136.65(3)	109.59(3)	114.45(7)
P_{11}	4.85(5)	79.23(4)	135.53(3)	109.20(3)	119.58(7)
P_{21}	0.50(5)	133.73(2)	137.03(3)	115.07(6)	109.09(6)

Table 5.7. High-pressure evolution of the 8-mRs[010] in phillipsite structure: relevant interatomic distances (Å), angles (°), and the ellipticity ratio $\varepsilon_{8\text{-mRs}[010]}$ (calculated as O3-O3/O1-O1, with O1-O1 > O3-O3). *P* values in Table 5.3.

P_n	*P*(GPa)	$\varepsilon_{8\text{-mRs}[010]}$	O6-O6	O7-O7	O1-O1	O3-O3
P_1	0.20(5)	0.852(5)	6.874(6)	5.810(2)	7.807(7)	6.652(3)
P_2	0.60(5)	0.838(5)	6.834(6)	5.833(2)	7.868(7)	6.592(3)
P_3	0.94(5)	0.831(5)	6.842(6)	5.818(2)	7.888(7)	6.553(3)
P_4	1.22(5)	0.829(5)	6.837(6)	5.789(2)	7.870(8)	6.528(3)
P_5	1.60(5)	0.828(5)	6.869(6)	5.793(2)	7.888(7)	6.532(3)
P_6	1.82(5)	0.829(5)	6.838(6)	5.775(2)	7.865(7)	6.522(3)
P_7	2.14(5)	0.820(5)	6.850(6)	5.762(2)	7.890(7)	6.466(3)
P_8	2.57(5)	0.811(5)	6.846(6)	5.758(2)	7.905(7)	6.409(3)
P_9	3.13(5)	0.777(5)	6.743(6)	5.725(2)	8.014(7)	6.230(3)
P_{10}	3.92(5)	0.729(5)	6.606(6)	5.762(2)	8.216(7)	5.986(3)
P_{11}	4.85(5)	0.687(5)	6.452(6)	5.801(2)	8.356(7)	5.737(2)
P_{21}	0.50(5)	0.844(5)	6.866(6)	5.833(2)	7.805(7)	6.590(3)

P_n	*P*(GPa)	O3-O7-O1	O7-O1-O6	O1-O6-O3	O6-O3-O7
P_1	0.20(5)	159.93(2)	107.69(2)	142.31(2)	124.73(2)
P_2	0.60(5)	159.38(2)	106.53(2)	142.82(2)	125.41(2)
P_3	0.94(5)	159.78(2)	106.10(2)	142.02(2)	125.74(2)
P_4	1.22(5)	159.75(3)	106.04(2)	141.39(2)	125.61(2)
P_5	1.60(5)	159.49(2)	106.15(2)	140.69(2)	125.42(2)
P_6	1.82(5)	159.51(2)	106.02(2)	140.98(2)	125.18(2)
P_7	2.14(5)	159.71(2)	105.57(2)	139.96(2)	125.63(2)
P_8	2.57(5)	158.78(2)	105.26(2)	139.31(2)	125.87(2)
P_9	3.13(5)	158.15(3)	101.97(2)	140.30(2)	126.64(2)
P_{10}	3.92(5)	154.43(3)	97.617(2)	143.43(3)	128.75(3)
P_{11}	4.85(5)	150.49(3)	93.749(2)	145.67(3)	130.10(3)
P_{21}	0.50(5)	159.19(2)	107.91(2)	141.50(2)	125.72(2)

Table 5.8. High-pressure evolution of the 8-mRs[100]-1 in phillipsite structure: relevant interatomic distances (Å), angles (°), and the ellipticity ratio $\varepsilon_{8\text{-mRs}[100]\text{-}1}$ (calculated as O9-O8/O7-O7, with O7-O7 > O9-O8). *P* values in Table 5.3.

P_n	*P*(GPa)	O7-O7	O9-O8	O3-O3	O3-O4	O3-O8-O3	O4-O7-O3	$\varepsilon_{8\text{-mRs}[001]\text{-}1}$
P_1	0.20(5)	7.650(5)	6.669(7)	4.299(6)	4.288(5)	108.97(6)	38.50(2)	0.872(2)
P_2	0.60(5)	7.688(5)	6.657(7)	4.318(6)	4.306(5)	108.84(7)	38.27(2)	0.866(2)
P_3	0.94(5)	7.686(5)	6.635(7)	4.314(6)	4.274(5)	107.99(7)	37.98(2)	0.863(2)
P_4	1.22(5)	7.673(5)	6.638(8)	4.284(6)	4.262(5)	106.92(7)	37.93(2)	0.865(2)
P_5	1.60(5)	7.717(5)	6.650(7)	4.252(6)	4.261(5)	105.24(6)	37.76(2)	0.862(2)
P_6	1.82(5)	7.704(5)	6.637(7)	4.249(6)	4.258(5)	105.40(7)	37.82(2)	0.862(2)
P_7	2.14(5)	7.733(5)	6.621(7)	4.233(6)	4.219(5)	104.29(6)	37.39(2)	0.856(2)
P_8	2.57(5)	7.775(5)	6.515(7)	4.218(6)	4.192(5)	105.55(6)	37.16(2)	0.838(2)
P_9	3.13(5)	7.896(5)	6.385(7)	4.316(6)	4.089(4)	107.78(6)	35.97(2)	0.809(2)
P_{10}	3.92(5)	8.079(5)	6.133(7)	4.507(7)	3.999(4)	114.45(7)	34.35(2)	0.759(2)
P_{11}	4.85(5)	8.338(5)	6.007(7)	4.678(7)	3.817(4)	119.58(7)	32.38(2)	0.720(2)
P_{21}	0.50(5)	7.726(5)	6.640(7)	4.354(6)	4.285(5)	109.09(6)	38.03(2)	0.859(2)

Table 5.9. High-pressure evolution of the 8-mRs[100]-1in phillipsite: relevant interatomic distances (Å), angles (°), and the ellipticity ratio $\varepsilon_{8\text{-mRs}[100]\text{-}1}$ (calculated as O7-O7/O9-O8, with O9-O8 > O7-O7). *P* values in Table 5.3.

P_n	*P*(GPa)	O7-O7	O9-O8	O1-O9-O1	O7-O1-O9	O1-O7-O2	O2-O8-O2	$\varepsilon_{8\text{-mRs}[001]\text{-}1}$
P_1	0.20(5)	6.503(5)	7.794(6)	92.90(5)	156.53(2)	130.09(2)	124.44(8)	0.834(2)
P_2	0.60(5)	6.495(5)	7.820(6)	90.37(5)	157.16(2)	130.20(2)	125.64(8)	0.831(2)
P_3	0.94(5)	6.414(5)	7.835(6)	88.20(5)	157.57(1)	130.76(2)	126.30(8)	0.819(2)
P_4	1.22(5)	6.395(5)	7.837(7)	87.02(6)	158.06(3)	130.59(2)	127.12(9)	0.816(2)
P_5	1.60(5)	6.351(5)	7.832(6)	85.93(5)	158.13(2)	131.21(2)	127.92(8)	0.811(2)
P_6	1.82(5)	6.347(5)	7.827(6)	85.92(5)	158.44(2)	131.19(2)	128.07(9)	0.811(2)
P_7	2.14(5)	6.262(5)	7.798(6)	83.56(5)	158.89(2)	131.72(2)	129.45(8)	0.803(2)
P_8	2.57(5)	6.177(5)	7.866(6)	82.66(5)	158.66(2)	133.25(2)	127.98(8)	0.785(2)
P_9	3.13(5)	5.974(5)	7.955(6)	81.14(5)	154.94(2)	136.44(2)	124.53(7)	0.751(2)
P_{10}	3.92(5)	5.703(4)	8.163(7)	80.21(5)	149.88(3)	141.67(2)	119.02(7)	0.699(2)
P_{11}	4.85(5)	5.386(4)	8.318(7)	79.23(4)	143.77(3)	148.71(2)	116.21(7)	0.648(2)
P_{21}	0.50(5)	6.427(5)	7.831(6)	90.46(5)	157.60(2)	131.44(2)	125.70(8)	0.821(2)

Table 5.10. Refined elastic parameters of phillipsite for the first and the second compressional regime (see text for further details), based on II-BM equations of state fits. (*) fixed parameter.

Elastic parameters of phillipsite in the first compressional regime (*P1-P6*)				
	V_0, l_0 (Å^3, Å)	$K_{V0,\,l0}$ (GPa)	K'	$\beta_{V,l}$ (GPa^{-1})
V	1005(1)	89(8)	4*	0.011(1)
a	9.914(7)	81(12)	4*	0.012(2)
b	14.201(9)	50(5)	4*	0.020(2)
c	8.707(2)	107(8)	4*	0.0093(7)
Elastic parameters of phillipsite in the second compressional regime (*P9-P20*)				
	V_0, l_0 (Å^3, Å)	$K_{V0,\,l0}$ (GPa)	K'	$\beta_{V,l}$ (GPa^{-1})
V	1098(2)	18.8(7)	4*	0.053(2)
a	10.07(2)	30(2)	4*	0.033(2)
b	14.8(1)	11(1)	4*	0.091(8)
c	8.94(2)	21(1)	4*	0.048(2)

Table 5.11. Evolution of some selected T-O-T angles (°) of the structure of phillipsite with pressure (GPa). *P* values in Table 5.3.

P_n	*P*(GPa)	T4-O1-T3	T2-O8-T2	T1-O7-T3	T4-O6-T2
P_1	0.20(5)	144.74(4)	147.99(5)	144.38(3)	144.79(4)
P_2	0.60(5)	141.95(4)	148.39(5)	145.22(3)	143.87(4)
P_3	0.94(5)	139.95(4)	148.61(5)	144.95(3)	144.45(4)
P_4	1.22(5)	139.06(4)	148.76(9)	144.68(3)	144.53(4)
P_5	1.60(5)	138.28(4)	148.99(5)	144.39(3)	145.45(4)
P_6	1.82(5)	138.48(4)	148.79(9)	144.34(3)	144.59(4)
P_7	2.14(5)	135.34(4)	148.46(5)	144.18(3)	145.63(4)
P_8	2.57(5)	135.83(4)	148.46(5)	143.89(3)	146.20(4)
P_9	3.13(5)	135.58(4)	150.71(5)	140.88(3)	144.28(4)
P_{10}	3.92(5)	136.57(4)	150.65(5)	137.30(4)	141.34(4)
P_{11}	4.85(5)	137.37(4)	153.79(5)	132.80(4)	137.37(4)
P_{21}	0.50(5)	142.66(4)	148.03(5)	144.51(3)	145.10(4)

Table 6.1. Unit-cell parameters of armstrongite at high pressure (* in decompression).

P (GPa)	*V* (Å^3)	*a* (Å)	*b* (Å)	*c* (Å)	*β* (°)
0.0001	1469.3(5)	14.0312(6)	14.1385(2)	7.851(2)	109.37(1)
0.01(5)	1466.7(6)	14.0248(9)	14.1368(2)	7.843(2)	109.39(2)
0.15(5)	1456.6(6)	14.016(1)	14.0970(3)	7.822(3)	109.53(2)
0.28(5)	1450.3(6)	14.0079(9)	14.0670(2)	7.814(2)	109.62(2)
0.48(5)	1440.3(6)	13.997(1)	14.0286(3)	7.793(3)	109.73(2)
0.71(5)	1430.5(6)	13.9810(8)	13.9877(2)	7.774(2)	109.80(2)
1.15(5)	1416.1(5)	13.958(1)	13.9303(3)	7.746(2)	109.92(2)
1.48(5)	1405.8(5)	13.940(1)	13.8924(3)	7.725(3)	109.99(2)
2.03(5)	1391.4(6)	13.914(1)	13.8345(3)	7.698(3)	110.11(2)
2.76(5)	1371.5(6)	13.874(2)	13.7579(4)	7.658(4)	110.23(3)
3.27(5)	1358.1(6)	13.840(1)	13.7064(2)	7.633(2)	110.29(2)
4.01(5)	1340.7(6)	13.801(2)	13.6435(5)	7.596(4)	110.38(4)
5.07(5)	3813(1)	12.684(1)	13.4750(4)	22.917(8)	103.23(2)
5.67(5)	3779(1)	12.642(2)	13.4402(6)	22.84(1)	103.16(3)
6.33(5)	3742(1)	12.596(2)	13.3944(7)	22.78(1)	103.15(3)
7.18(5)	3701(1)	12.535(3)	13.359(1)	22.68(2)	102.98(5)
7.68(5)	3674(1)	12.498(2)	13.3415(9)	22.61(2)	102.91(4)
8.01(5)	3654(1)	12.476(2)	13.3124(9)	22.56(2)	102.96(4)
*7.31(5)	3682(1)	12.501(2)	13.3443(9)	22.65(2)	102.90(4)
*5.31(5)	3792(1)	12.651(3)	13.459(1)	22.86(2)	103.05(5)
*4.19(5)	3860(1)	12.740(3)	13.544(1)	22.96(2)	103.06(5)
*3.45(5)	3912(1)	12.812(2)	13.5791(9)	23.11(2)	103.32(4)
*2.91(5)	3957(1)	12.865(2)	13.6428(7)	23.16(2)	103.24(3)
*2.00(5)	1382.7(7)	13.904(3)	13.8099(6)	7.676(6)	110.26(5)
*1.15(5)	1411.2(7)	13.991(4)	13.9608(10)	7.694(9)	110.11(7)

Table 6.2. Details pertaining to the structure refinements of armstrongite as a function of pressures.

P (GPa)	0.0001	0.01(5)	0.28(5)	0.48(5)	0.71(5)	1.15(5)	1.48(5)
min≤h≤max	-20; +20	-18; +18	-18; +19	-19; +18	-18; +19	-19; +18	-19; +18
min≤k≤max	+20; -21	-18; +18	-18; +18	-18; +18	-18; +18	-18; +18	-18; +18
min≤l≤max	+5; -6	+3; -5	-5; +4	-4; +5	-4; +5	-4; +5	-4; +5
Unique reflections	755	699	690	688	682	680	674
Observed reflections $I > 3\sigma(I)$	503	515	525	528	518	511	511
R_{int} (obs)	0.021	0.022	0.025	0.025	0.027	0.024	0.030
R_{int} (all)	0.023	0.022	0.026	0.026	0.029	0.026	0.031
R_1 (obs)	0.047	0.056	0.059	0.057	0.059	0.057	0.060
R_1 (all)	0.065	0.064	0.067	0.065	0.072	0.072	0.068
wR_1 (obs)	0.048	0.065	0.066	0.065	0.058	0.058	0.068
wR_1 (all)	0.049	0.065	0.067	0.065	0.059	0.058	0.068
Residuals (e^-/Å^3)	+0.21;-0.17	+0.26;-0.29	+0.25;-0.27	+0.25;-0.29	+0.28;-0.22	+0.34;-0.25	+0.36;-0.29

P (GPa)	2.03(5)	2.76(5)	3.27(5)	4.01(5)	1.15(5)
min≤h≤max	-18; +19	-19; +18	-18; +18	-18; +16	-18; +19
min≤k≤max	-18; +18	-18; +18	-18; +18	-17; +18	-18; +18
min≤l≤max	-5; +4	-4; +5	+3; -5	+5; -3	-5; +4
Unique reflections	678	660	646	642	659
Observed reflections $I > 3\sigma(I)$	502	479	462	440	428
R_{int} (obs)	0.035	0.034	0.044	0.046	0.043
R_{int} (all)	0.036	0.035	0.045	0.049	0.046
R_1 (obs)	0.071	0.069	0.08	0.088	0.084
R_1 (all)	0.083	0.083	0.098	0.113	0.103
wR_1 (obs)	0.078	0.076	0.091	0.099	0.089
wR_1 (all)	0.078	0.077	0.092	0.100	0.090
Residuals (e^-/Å^3)	+0.48;-0.31	+0.49;-0.28	+0.51;-0.38	+0.72;-0.42	+0.47;-0.40

Table 6.3. Refined positional and displacement parameters of armstrongite as a function of pressure (* in decompression).

Site	*P* (GPa)	*s.o.f.*	*x*	*y*	*z*	U_{iso} (Å^2)
Ca(1)	0.0001	1.00(1)	0.2538(2)	0.5	0.045(1)	0.0173(9)
	0.01(5)	0.98(2)	0.2545(3)	0.5	0.048(1)	0.015(1)
	0.15(5)	0.98(2)	0.2554(3)	0.5	0.051(1)	0.015(1)
	0.28(5)	0.98(2)	0.2558(3)	0.5	0.052(1)	0.015(1)
	0.48(5)	0.99(1)	0.2556(3)	0.5	0.053(1)	0.0148(9)
	0.71(5)	0.98(1)	0.2559(3)	0.5	0.056(1)	0.0158(9)
	1.15(5)	0.98(2)	0.256 (4)	0.5	0.061(2)	0.018(1)
	1.48(5)	0.96(2)	0.2562 (4)	0.5	0.064(2)	0.017(2)
	2.03(5)	0.94(2)	0.2557(4)	0.5	0.063(2)	0.016(2)
	2.76(5)	0.94(3)	0.2542(6)	0.5	0.069(2)	0.023(2)
	3.27(5)	0.97(3)	0.2526(7)	0.5	0.065(3)	0.029(3)
	4.01(5)	0.99(3)	0.2519(9)	0.5	0.066(4)	0.035(3)
	*1.15(5)	0.96(3)	0.2569(6)	0.5	0.062(3)	0.024(2)
Zr(1)	0.0001	1.00(1)	0.25	0.25	0	0.0076(3)
	0.01(5)	1.00(1)	0.25	0.25	0	0.0086(5)
	0.15(5)	1.00(1)	0.25	0.25	0	0.0082(5)
	0.28(5)	1.00(1)	0.25	0.25	0	0.0084(5)
	0.48(5)	1.00(1)	0.25	0.25	0	0.0071(3)
	0.71(5)	1.00(1)	0.25	0.25	0	0.0084(3)
	1.15(5)	1.00(1)	0.25	0.25	0	0.0092(5)
	1.48(5)	1.00(1)	0.25	0.25	0	0.0090(6)
	2.03(5)	1.00(1)	0.25	0.25	0	0.0089(6)
	2.76(5)	1.00(1)	0.25	0.25	0	0.0130(8)
	3.27(5)	1.00(1)	0.25	0.25	0	0.0140(9)
	4.01(5)	1.00(1)	0.25	0.25	0	0.0173(9)
	*1.15(5)	1.00(1)	0.25	0.25	0	0.0133(2)
Si(1)	0.0001	1	0.1872(2)	0.6146(2)	0.341(1)	0.0110(6)
	0.01(5)	1	0.1868(3)	0.6144(2)	0.340(1)	0.0123(9)
	0.15(5)	1	0.1879(3)	0.6147(2)	0.343(1)	0.0132(9)
	0.28(5)	1	0.1888(3)	0.6150(2)	0.346(1)	0.0128(9)
	0.48(5)	1	0.1890(2)	0.6154(2)	0.347(1)	0.0103(6)
	0.71(5)	1	0.1895(3)	0.6157(2)	0.350(1)	0.0114(6)
	1.15(5)	1	0.1907(4)	0.6161(2)	0.354(2)	0.0143(9)
	1.48(5)	1	0.1910(4)	0.6162(3)	0.356(2)	0.013(1)

Site	*P* (GPa)	*s.o.f.*	*x*	*y*	*z*	U_{iso} (Å^2)
	2.03(5)	1	0.1914(4)	0.6167(3)	0.358(2)	0.013(1)
	2.76(5)	1	0.1919(6)	0.6166(3)	0.363(2)	0.019(1)
	3.27(5)	1	0.1927(6)	0.6173(4)	0.371(3)	0.018(2)
	4.01(5)	1	0.1921(7)	0.6183(4)	0.373(3)	0.021(2)
	*1.15(5)	1	0.1908(5)	0.6164(4)	0.353(2)	0.016(1)
Si(2)	0.0001	1	0.3400(2)	0.6104(2)	0.730(1)	0.0100(6)
	0.01(5)	1	0.3400(3)	0.6105(2)	0.730(1)	0.0106(8)
	0.15(5)	1	0.3423(3)	0.6105(2)	0.735(1)	0.0106(9)
	0.28(5)	1	0.3436(3)	0.6105(2)	0.738(1)	0.0106(8)
	0.48(5)	1	0.3455(2)	0.6106(1)	0.741(1)	0.0081(6)
	0.71(5)	1	0.3469(2)	0.6108(1)	0.744(1)	0.0095(6)
	1.15(5)	1	0.3494(3)	0.6109(2)	0.749(1)	0.0115(9)
	1.48(5)	1	0.3510(4)	0.6109(3)	0.752(2)	0.011(1)
	2.03(5)	1	0.3533(4)	0.6112(3)	0.757(2)	0.011(1)
	2.76(5)	1	0.3562(5)	0.6109(3)	0.763(2)	0.014(1)
	3.27(5)	1	0.3588(6)	0.6113(4)	0.769(2)	0.015(1)
	4.01(5)	1	0.3582(7)	0.6121(4)	0.767(3)	0.019(2)
	*1.15(5)	1	0.3502(5)	0.6109(4)	0.750(2)	0.015(1)
Si(3)	0.0001	1	0.0034(2)	0.7429(2)	0.3037(9)	0.0109(5)
	0.01(5)	1	0.0036(3)	0.7426(2)	0.303(1)	0.0121(8)
	0.15(5)	1	0.0031(3)	0.7421(2)	0.303(1)	0.0121(9)
	0.28(5)	1	0.0027(3)	0.7418(2)	0.303(1)	0.0121(9)
	0.48(5)	1	0.0025(2)	0.7414(1)	0.304(1)	0.0102(6)
	0.71(5)	1	0.0027(2)	0.7413(1)	0.307(1)	0.0109(6)
	1.15(5)	1	0.0022(3)	0.7413(2)	0.306(1)	0.013(1)
	1.48(5)	1	0.0015(4)	0.7412(2)	0.304(2)	0.011(1)
	2.03(5)	1	0.0015(4)	0.7412(2)	0.309(2)	0.012(1)
	2.76(5)	1	0.0009(5)	0.7413(3)	0.309(2)	0.015(1)
	3.27(5)	1	0.0001(5)	0.7410(4)	0.309(2)	0.015(2)
	4.01(5)	1	0.9989(6)	0.7406(4)	0.306(3)	0.018(2)
	*1.15(5)	1	0.0020(5)	0.7411(3)	0.304(2)	0.015(1)
O(1)	0.0001	1	0	0.7674(6)	0.5	0.031(3)
	0.01(5)	1	0	0.7672(7)	0.5	0.026(3)
	0.15(5)	1	0	0.7697(8)	0.5	0.027(4)
	0.28(5)	1	0	0.7714(8)	0.5	0.028(3)
	0.48(5)	1	0	0.7745(6)	0.5	0.027(3)

Site	*P* (GPa)	*s.o.f.*	*x*	*y*	*z*	U_{iso} (Å^2)
	0.71(5)	1	0	0.7768(6)	0.5	0.026(3)
	1.15(5)	1	0	0.7792(9)	0.5	0.026(4)
	1.48(5)	1	0	0.780(1)	0.5	0.024(4)
	2.03(5)	1	0	0.784(1)	0.5	0.023(4)
	2.76(5)	1	0	0.787(1)	0.5	0.024(5)
	3.27(5)	1	0	0.788(1)	0.5	0.023(5)
	4.01(5)	1	0	0.791(2)	0.5	0.032(7)
	*1.15(5)	1	0	0.778(1)	0.5	0.028(6)
O(2)	0.0001	1	0.2597(6)	0.6398(4)	0.537(3)	0.021(1)
	0.01(5)	1	0.0250(8)	0.6396(5)	0.539(4)	0.025(7)
	0.15(5)	1	0.2618(8)	0.6405(5)	0.543(4)	0.025(2)
	0.28(5)	1	0.2634(8)	0.6407(5)	0.547(4)	0.023(2)
	0.48(5)	1	0.2642(6)	0.6409(4)	0.548(3)	0.020(2)
	0.71(5)	1	0.2657(6)	0.6413(4)	0.549(3)	0.023(2)
	1.15(5)	1	0.2682(9)	0.6418(6)	0.561(4)	0.021(3)
	1.48(5)	1	0.269(1)	0.6417(6)	0.562(4)	0.018(3)
	2.03(5)	1	0.270(1)	0.6427(6)	0.558(5)	0.020(3)
	2.76(5)	1	0.271(1)	0.6452(8)	0.556(6)	0.024(4)
	3.27(5)	1	0.274(1)	0.6441(9)	0.560(6)	0.024(4)
	4.01(5)	1	0.270(2)	0.644(1)	0.547(8)	0.025(5)
	*1.15(5)	1	0.271(1)	0.6405(9)	0.566(6)	0.028(4)
O(3)	0.0001	1	0.2966(5)	0.6286(3)	0.891(2)	0.012(1)
	0.01(5)	1	0.2979(7)	0.6282(4)	0.893(3)	0.012(2)
	0.15(5)	1	0.2997(7)	0.6273(4)	0.897(3)	0.011(2)
	0.28(5)	1	0.3006(7)	0.6270(4)	0.900(3)	0.011(2)
	0.48(5)	1	0.3020(6)	0.6262(4)	0.902(3)	0.012(1)
	0.71(5)	1	0.3041(6)	0.6258(4)	0.907(3)	0.014(1)
	1.15(5)	1	0.3071(8)	0.6251(5)	0.913(3)	0.012(2)
	1.48(5)	1	0.3098(9)	0.6244(6)	0.912(4)	0.014(2)
	2.03(5)	1	0.3110(9)	0.6242(6)	0.917(4)	0.011(2)
	2.76(5)	1	0.313(1)	0.6245(7)	0.915(5)	0.012(3)
	3.27(5)	1	0.315(1)	0.6239(8)	0.922(5)	0.012(3)
	4.01(5)	1	0.317(1)	0.6237(9)	0.922(6)	0.015(4)
	*1.15(5)	1	0.310(1)	0.6259(7)	0.923(5)	0.015(3)

Site	*P* (GPa)	*s.o.f.*	*x*	*y*	*z*	U_{iso} (Å^2)
O(4)	0.0001	1	0.2285(5)	0.6536(4)	0.189(2)	0.019(1)
	0.01(5)	1	0.2298(7)	0.6536(5)	0.191(3)	0.019(2)
	0.15(5)	1	0.2291(7)	0.6548(5)	0.191(3)	0.018(2)
	0.28(5)	1	0.2295(7)	0.6552(5)	0.193(3)	0.018(2)
	0.48(5)	1	0.2297(6)	0.6553(4)	0.193(2)	0.014(1)
	0.71(5)	1	0.2300(6)	0.6567(4)	0.198(2)	0.017(1)
	1.15(5)	1	0.2291(8)	0.6574(6)	0.201(4)	0.018(2)
	1.48(5)	1	0.2280(9)	0.6581(7)	0.202(4)	0.018(3)
	2.03(5)	1	0.227(1)	0.6588(7)	0.203(4)	0.022(3)
	2.76(5)	1	0.226(1)	0.6610(8)	0.212(5)	0.024(3)
	3.27(5)	1	0.227(1)	0.6609(9)	0.215(6)	0.024(4)
	4.01(5)	1	0.231(1)	0.664(1)	0.223(7)	0.023(4)
	*1.15(5)	1	0.231(1)	0.6588(9)	0.209(6)	0.027(4)
O(5)	0.0001	1	0.1819(7)	0.5	0.312(3)	0.012(2)
	0.01(5)	1	0.181(1)	0.5	0.311(4)	0.017(3)
	0.15(5)	1	0.183(1)	0.5	0.312(4)	0.015(3)
	0.28(5)	1	0.184(1)	0.5	0.316(4)	0.016(3)
	0.48(5)	1	0.1850(8)	0.5	0.319(3)	0.014(2)
	0.71(5)	1	0.1857(8)	0.5	0.316(3)	0.016(2)
	1.15(5)	1	0.188(1)	0.5	0.326(5)	0.015(3)
	1.48(5)	1	0.188(1)	0.5	0.334(6)	0.016(3)
	2.03(5)	1	0.189(1)	0.5	0.330(6)	0.017(4)
	2.76(5)	1	0.192(2)	0.5	0.333(7)	0.014(4)
	3.27(5)	1	0.189(2)	0.5	0.325(8)	0.022(5)
	4.01(5)	1	0.192(2)	0.5	0.34(1)	0.024(6)
	*1.15(5)	1	0.189(2)	0.5	0.324(7)	0.020(5)
O(6)	0.0001	1	0.3699(7)	0.5	0.730(3)	0.014(2)
	0.01(5)	1	0.3701(9)	0.5	0.727(4)	0.017(3)
	0.15(5)	1	0.374(1)	0.5	0.731(4)	0.017(3)
	0.28(5)	1	0.375(1)	0.5	0.734(4)	0.019(3)
	0.48(5)	1	0.3789(8)	0.5	0.737(3)	0.017(2)
	0.71(5)	1	0.3801(8)	0.5	0.738(3)	0.016(2)
	1.15(5)	1	0.384(1)	0.5	0.744(5)	0.018(3)
	1.48(5)	1	0.385(1)	0.5	0.741(5)	0.017(4)

Site	*P* (GPa)	*s.o.f.*	*x*	*y*	*z*	U_{iso} (Å^2)
	2.03(5)	1	0.387(1)	0.5	0.742(5)	0.017(4)
	2.76(5)	1	0.388(2)	0.5	0.743(7)	0.021(5)
	3.27(5)	1	0.391(2)	0.5	0.745(8)	0.021(5)
	4.01(5)	1	0.395(2)	0.5	0.748(9)	0.024(6)
	*1.15(5)	1	0.383(2)	0.5	0.742(7)	0.022(5)
O(7)	0.0001	1	0.4442(5)	0.6679(4)	0.761(2)	0.016(1)
	0.01(5)	1	0.4444(7)	0.6678(5)	0.760(3)	0.018(2)
	0.15(5)	1	0.4462(7)	0.6689(5)	0.763(3)	0.016(2)
	0.28(5)	1	0.4475(7)	0.6694(5)	0.766(3)	0.017(2)
	0.48(5)	1	0.4493(5)	0.6700(4)	0.670(4)	0.017(2)
	0.71(5)	1	0.4510(5)	0.6708(4)	0.778(2)	0.017(1)
	1.15(5)	1	0.4528(7)	0.6724(5)	0.781(3)	0.017(2)
	1.48(5)	1	0.4547(8)	0.6733(6)	0.789(3)	0.014(3)
	2.03(5)	1	0.4566(9)	0.6735(6)	0.794(3)	0.016(3)
	2.76(5)	1	0.458(1)	0.6752(8)	0.804(4)	0.021(3)
	3.27(5)	1	0.459(1)	0.6763(9)	0.804(5)	0.021(4)
	4.01(5)	1	0.463(1)	0.678(1)	0.818(6)	0.022(4)
	*1.15(5)	1	0.454(1)	0.6730(8)	0.781(4)	0.022(4)
O(8)	0.0001	1	0.0730(5)	0.6496(4)	0.313(2)	0.016(1)
	0.01(5)	1	0.0741(7)	0.6490(4)	0.314(3)	0.014(2)
	0.15(5)	1	0.0758(7)	0.6487(4)	0.324(3)	0.013(2)
	0.28(5)	1	0.0757(7)	0.6486(5)	0.326(3)	0.015(2)
	0.48(5)	1	0.0774(6)	0.6489(4)	0.332(2)	0.015(1)
	0.71(5)	1	0.0777(6)	0.6487(4)	0.332(2)	0.016(1)
	1.15(5)	1	0.0783(8)	0.6482(5)	0.340(3)	0.016(2)
	1.48(5)	1	0.079(1)	0.6486(6)	0.343(4)	0.019(3)
	2.03(5)	1	0.080(1)	0.6478(6)	0.347(4)	0.017(3)
	2.76(5)	1	0.082(1)	0.6487(7)	0.358(5)	0.016(3)
	3.27(5)	1	0.081(1)	0.6486(9)	0.361(6)	0.021(4)
	4.01(5)	1	0.085(2)	0.650(1)	0.376(7)	0.026(4)
	*1.15(5)	1	0.079(1)	0.6490(8)	0.344(5)	0.020(3)
O(9)	0.0001	1	0.8954(5)	0.7237(3)	0.165(2)	0.016(1)
	0.01(5)	1	0.8949(7)	0.7233(5)	0.162(3)	0.017(2)
	0.15(5)	1	0.8942(7)	0.7205(5)	0.161(3)	0.018(2)
	0.28(5)	1	0.8937(7)	0.7184(5)	0.163(3)	0.018(2)

Site	P (GPa)	*s.o.f.*	x	y	z	U_{iso} (Å^2)
	0.48(5)	1	0.8940(5)	0.7160(4)	0.166(2)	0.016(2)
	0.71(5)	1	0.8938(5)	0.7136(4)	0.171(2)	0.018(2)
	1.15(5)	1	0.8933(8)	0.7114(6)	0.172(3)	0.018(2)
	1.48(5)	1	0.8924(9)	0.7100(7)	0.175(6)	0.019(3)
	2.03(5)	1	0.892(1)	0.7074(7)	0.179(4)	0.023(3)
	2.76(5)	1	0.892(1)	0.7065(8)	0.185(5)	0.020(3)
	3.27(5)	1	0.891(1)	0.7048(9)	0.181(6)	0.024(4)
	4.01(5)	1	0.890(1)	0.702(1)	0.184(6)	0.025(4)
	*1.15(5)	1	0.892(1)	0.7106(8)	0.173(5)	0.023(3)
O(10)	0.0001	1	0.0886(9)	0.5	0.861(4)	0.043(3)
	0.01(5)	1	0.088(1)	0.5	0.855(6)	0.044(4)
	0.15(5)	1	0.089(1)	0.5	0.860(6)	0.047(4)
	0.28(5)	1	0.090(1)	0.5	0.861(6)	0.049(4)
	0.48(5)	1	0.092(1)	0.5	0.861(5)	0.051(4)
	0.71(5)	1	0.091(1)	0.5	0.853(5)	0.051(4)
	1.15(5)	1	0.093(2)	0.5	0.860(7)	0.059(6)
	1.48(5)	1	0.096(2)	0.5	0.850(9)	0.059(7)
	2.03(5)	1	0.097(2)	0.5	0.86(1)	0.074(8)
	2.76(5)	1	0.097(3)	0.5	0.86(1)	0.09(1)
	3.27(5)	1	0.097(4)	0.5	0.84(1)	0.09(1)
	4.01(5)	1	0.108(4)	0.5	0.83(2)	0.09(1)
	*1.15(5)	1	0.097(3)	0.5	0.85(1)	0.064(9)
O(11)	0.0001	1	0.4161(9)	0.5	0.262(4)	0.037(3)
	0.01(5)	1	0.418(1)	0.5	0.271(5)	0.039(4)
	0.15(5)	1	0.419(1)	0.5	0.278(6)	0.043(4)
	0.28(5)	1	0.418(1)	0.5	0.285(6)	0.046(4)
	0.48(5)	1	0.419(1)	0.5	0.290(5)	0.048(4)
	0.71(5)	1	0.419(1)	0.5	0.294(5)	0.047(3)
	1.15(5)	1	0.418(2)	0.5	0.303(7)	0.055(5)
	1.48(5)	1	0.418(2)	0.5	0.306(8)	0.054(6)
	2.03(5)	1	0.418(2)	0.5	0.309(8)	0.062(7)
	2.76(5)	1	0.416(2)	0.5	0.31(1)	0.055(7)
	3.27(5)	1	0.413(3)	0.5	0.31(1)	0.053(8)
	4.01(5)	1	0.421(4)	0.5	0.33(2)	0.09(1)
	*1.15(5)	1	0.418(3)	0.5	0.31(1)	0.070(9)

Table 6.4. Si-O, Zr-O and Ca-O distances (in Å) of armstrongite at different pressure (* in decompression).

P (GPa)	Si1-O2	Si1-O4	Si1-O8	Si1-O5	Si2-O3	Si2-O2
0.0001	1.576(3)	1.590(2)	1.621(1)	1.634(1)	1.598(3)	1.614(3)
0.01(5)	1.595(4)	1.581(3)	1.602(1)	1.631(1)	1.600(3)	1.601(4)
0.15(5)	1.605(6)	1.587(4)	1.602(6)	1.633(1)	1.586(5)	1.606(5)
0.28(5)	1.610(5)	1.591(3)	1.611(1)	1.633(1)	1.593(3)	1.595(4)
0.48(5)	1.603(6)	1.595(4)	1.597(4)	1.633(1)	1.585(5)	1.608(5)
0.71(5)	1.603(5)	1.584(3)	1.589(1)	1.637(1)	1.592(3)	1.604(4)
1.15(5)	1.642(5)	1.565(3)	1.601(1)	1.630(1)	1.586(3)	1.568(4)
1.48(5)	1.630(5)	1.564(3)	1.590(1)	1.622(1)	1.542(3)	1.581(4)
2.03(5)	1.610(6)	1.556(4)	1.576(1)	1.627(1)	1.553(5)	1.611(5)
2.76(5)	1.551(7)	1.525(6)	1.579(7)	1.621(1)	1.495(6)	1.688(8)
3.27(5)	1.532(4)	1.551(3)	1.576(1)	1.645(1)	1.495(3)	1.687(5)
4.01(5)	1.430(4)	1.548(3)	1.552(1)	1.636(1)	1.486(3)	1.747(5)
*1.15(5)	1.67(2)	1.53(1)	1.615(4)	1.640(1)	1.63(2)	1.53(2)

P (GPa)	Si2-O6	Si2-O7	Si3-O9	Si3-O1	Si3-O7	Si3-O8
0.0001	1.616(1)	1.618(1)	1.569(2)	1.596(3)	1.625(1)	1.629(1)
0.01(5)	1.612(1)	1.620(1)	1.581(4)	1.603(4)	1.616(1)	1.637(1)
0.15(5)	1.624(1)	1.624(1)	1.585(4)	1.606(6)	1.610(1)	1.639(1)
0.28(5)	1.620(1)	1.625(1)	1.586(4)	1.608(4)	1.609(4)	1.634(1)
0.48(5)	1.623(1)	1.622(1)	1.576(4)	1.610(1)	1.616(1)	1.635(1)
0.71(5)	1.623(1)	1.622(1)	1.573(3)	1.597(4)	1.628(1)	1.637(1)
1.15(5)	1.621(1)	1.623(1)	1.577(3)	1.604(4)	1.608(1)	1.641(1)
1.48(5)	1.623(1)	1.625(1)	1.568(3)	1.613(4)	1.614(1)	1.644(1)
2.03(5)	1.624(1)	1.615(1)	1.567(3)	1.598(5)	1.633(2)	1.656(1)
2.76(5)	1.609(1)	1.604(2)	1.553(5)	1.594(7)	1.654(3)	1.653(1)
3.27(5)	1.624(1)	1.599(1)	1.571(3)	1.597(3)	1.644(2)	1.643(1)
4.01(5)	1.631(1)	1.629(1)	1.564(3)	1.619(4)	1.659(2)	1.662(1)
*1.15(5)	1.620(1)	1.632(4)	1.58(1)	1.60(2)	1.591(5)	1.633(3)

P (GPa)	Zr1-O9 x2	Zr1-O3 x2	Zr1-O4x2
0.0001	2.055(3)	2.115(1)	2.107(2)
0.01(5)	2.043(4)	2.120(1)	2.114(3)
0.15(5)	2.037(5)	2.121(2)	2.101(4)
0.28(5)	2.037(4)	2.116(1)	2.101(3)
0.48(5)	2.050(5)	2.121(2)	2.100(4)
0.71(5)	2.068(5)	2.115(1)	2.108(3)
1.15(5)	2.061(5)	2.117(1)	2.117(3)
1.48(5)	2.059(5)	2.141(1)	2.116(3)
2.03(5)	2.079(5)	2.118(5)	2.128(1)
2.76(5)	2.082(7)	2.136(2)	2.149(7)
3.27(5)	2.060(5)	2.122(1)	2.153(4)
4.01(5)	2.054(5)	2.132(1)	2.152(4)
*1.15(5)	2.05(2)	2.094(4)	2.14(2)

P (GPa)	Ca-O3x2	Ca-O4x2	Ca-O5	Ca-O10	Ca-O11
0.0001	2.371(2)	2.524(1)	2.604(4)	2.290(3)	2.346(4)
0.01(5)	2.369(2)	2.522(2)	2.595(6)	2.325(5)	2.380(6)
0.15(5)	2.355(3)	2.525(2)	2.564(8)	2.311(5)	2.388(6)
0.28(5)	2.347(2)	2.525(2)	2.573(6)	2.304(5)	2.388(6)
0.48(5)	2.334(3)	2.517(2)	2.581(8)	2.277(5)	2.402(7)
0.71(5)	2.325(2)	2.533(1)	2.535(6)	2.304(5)	2.403(6)
1.15(5)	2.323(2)	2.533(2)	2.542(6)	2.277(5)	2.396(6)
1.48(5)	2.348(2)	2.530(1)	2.574(6)	2.281(6)	2.383(6)
2.03(5)	2.320(3)	2.536(2)	2.548(8)	2.229(6)	2.395(7)
2.76(5)	2.376(4)	2.562(3)	2.461(11)	2.211(8)	2.377(10)
3.27(5)	2.335(2)	2.568(2)	2.432(5)	2.210(6)	2.326(6)
4.01(5)	2.348(2)	2.599(2)	2.479(2)	2.151(6)	2.505(7)
*1.15(5)	2.307(8)	2.569(7)	2.51(2)	2.26(2)	2.40(2)

Table 6.5. Relevant interatomic distances (in Å) of armstrongite pertaining to the 6- and 8-mRs diameters at different pressure (* in decompression).

P (GPa)	O7-O7$_{(6\text{-mRs})}$	O8-O8	O1-O1	O6-O6	O7-O7$_{(8\text{-mRs})}$
0.0001	6.091(8)	5.630(6)	6.577(1)	5.922(8)	6.792(6)
0.01(5)	6.080(13)	5.606(9)	6.581(1)	5.875(11)	6.765(8)
0.15(5)	6.108(14)	5.531(9)	6.493(1)	5.833(14)	6.790(11)
0.28(5)	6.133(13)	5.517(8)	6.430(1)	5.896(11)	6.800(8)
0.48(5)	6.174(14)	5.450(8)	6.326(1)	5.797(14)	6.837(12)
0.71(5)	6.223(14)	5.436(8)	6.246(1)	5.775(11)	6.885(8)
1.15(5)	6.238(14)	5.391(8)	6.151(1)	5.764(11)	6.908(8)
1.48(5)	6.297(14)	5.345(8)	6.126(1)	5.680(11)	6.975(9)
2.03(5)	6.335(2)	5.306(8)	5.967(1)	5.64 (14)	6.981(13)
2.76(5)	6.378(2)	5.223(11)	5.859(2)	5.62(2)	7.07(2)
3.27(5)	6.381(2)	5.20(2)	5.808(1)	5.544(11)	7.076(9)
4.01(5)	6.478(2)	5.075(6)	5.702(1)	5.511(11)	7.163(9)
*1.15(5)	6.23(5)	5.37(3)	6.21(4)	5.75(5)	6.90(4)

Table 6.6. Refined elastic parameters pertaining the low- and the high-*P* polymorphs of armstrongite based on isothermal III- and II-BM Equation of State fits.

	V_0, l_0 (Å^3, Å)	$K_{V0,\,l0}$ (GPa)	K'	$\beta_{V0,\,l0}$ (GPa^{-1})
Elastic parameters of the low pressure polymorph of armstrongite fitted to a third-order Birch-Murnaghan EoS				
V	1465(1)	31.2(6)	8.6*	0.0321(5)
a	14.028(1)	78(4)	2(2)	0.0043(2)
b	14.131(4)	23(2)	10*	0.015(1)
c	7.844(2)	26(2)	10*	0.0128(9)

	V_0, l_0 (Å^3, Å)	$K_{V0,\,l0}$ (GPa)	K'	$\beta_{V0,\,l0}$ (GPa^{-1})
Elastic parameters of the high pressure polymorph of armstrongite fitted with a second-order Birch-Murnaghan EoS				
V	4185(8)	45(1)	4*	0.0222(5)
a	13.17(2)	35(1)	4*	0.0095(3)
b	13.87(1)	50(2)	4*	0.0067(3)
c	23.62(4)	46(3)	4*	0.0072(5)

Note: The value of $K' = \partial K_{V0}/\partial P$ for the unit-cell volume of the low-*P* polymorph was fixed to 8.6: the free refined value was too high to be reasonable (*e.g.* ~12.5(8)), likely biased by the impending phase transition.* fixed value.

Table 6.7. Relevant O-O-O angles (in °) of armstrongite, pertaining to the 5-mRs, at different pressure (* in decompression).

P (GPa)	O7-O1-O9	O1-O9-O4	O2-O4-O9	O4-O2-O7	O4-O3-O9
0.0001	131.34(1)	89.42(1)	104.22(1)	118.26(5)	58.67(1)
0.01(5)	131.39(1)	88.52(1)	105.38(1)	117.09(6)	58.33(1)
0.15(5)	132.12(2)	87.64(1)	104.88(1)	117.63(8)	58.70(1)
0.28(5)	132.54(3)	86.87(2)	104.77(2)	117.71(7)	58.87(1)
0.48(5)	133.03(2)	86.20(1)	104.23(1)	118.22(8)	58.97(1)
0.71(5)	133.06(1)	85.74(1)	103.90(1)	118.99(6)	58.93(1)
1.15(5)	133.26(2)	84.51(1)	103.85(1)	118.56(6)	59.25(1)
1.48(5)	133.20(2)	84.85(1)	103.16(1)	120.11(6)	59.12(1)
2.03(5)	132.52(2)	84.33(1)	101.77(1)	121.49(8)	59.45(1)
2.76(5)	132.00(2)	83.49(2)	102.16(2)	124.07(11)	59.82(1)
3.27(5)	131.95(1)	82.31(1)	102.29(1)	125.05(6)	59.92(1)
4.01(5)	131.46(1)	80.58(1)	105.52(1)	124.83(6)	59.14(1)
*1.15(5)	132.73(5)	84.01(4)	105.34(4)	117.6(3)	58.64(2)

Table 6.8. Others O-O-O angles (in °) of the 5-mRS of armstrongite at different pressure (* in decompression).

P (GPa)	O1-O7-O2	O8-O1-O9	O1-O9-O3	O2-O4-O3
0.0001	90.59(1)	102.59(2)	116.23(1)	104.43(1)
0.01(5)	91.40(1)	102.31(2)	115.92(1)	104.90(1)
0.15(5)	90.78(1)	99.37(2)	117.16(1)	105.55(1)
0.28(5)	90.39(3)	97.94(3)	118.25(2)	106.15(1)
0.48(5)	89.19(2)	95.26(2)	119.81(1)	106.39(1)
0.71(5)	87.89(1)	93.43(1)	122.49(1)	108.09(1)
1.15(5)	88.29(2)	90.94(2)	123.24(1)	109.15(1)
1.48(5)	86.47(2)	89.59(1)	124.23(1)	109.46(1)
2.03(5)	84.90(2)	86.14(1)	126.94(1)	110.31(1)
2.76(5)	81.95(3)	83.24(2)	127.31 (1)	111.50(1)
3.27(5)	81.39(2)	82.25(1)	127.69(1)	112.89(1)
4.01(5)	78.06(2)	78.47(1)	128.58(1)	115.14(1)
*1.15(5)	89.33(6)	90.18(5)	125.11(4)	112.25(3)

Table 7.1: elastic parameter of the studied compounds.

	$AlPO_4$-5	$AlPO_4$-5	Leonhardite	Laumontite	Phillipsite low-pressure regime	Phillipsite high-pressure regime	Armstrongite low-pressure form	Armstrongite high-pressure form
Space group	*P6cc*	*P6cc*	*C2/m*	*C2/m*	$P2_1/m$	$P2_1/m$	*C2/m*	*C2/m*
Pressure medium	*s. oil*	*m.e.w.* (16:3:1)	*m.e.* (4:1)	*m.e.w.* (1:1:2)	*m.e.w.* (16:3:1)	*m.e.w.* (16:3:1)	*m.e.w.* (16:3:1)	*m.e.w.* (16:3:1)
P- range (GPa)	0.25-1.65	0.0001-6.51	0.0001-7.46	0.0001-2.65	0.0001-1.82	3.1-9.4	0.0001-4	5-8.01
EoS	3-BM EoS	3-BM EoS	3-BM EoS	2-BM EoS	2-BM EoS	2-BM EoS	3-BM EoS	2-BM EoS
V_0(Å^3)	1376(3)	1360(2)	1348(1)	1393.9(6)	1005(1)	1098(2)	1465(1)	4185(8)
K_{V0} (GPa)	13.2(11)	22.2(9)	36(1)	54.8(10)	89(8)	18.8(7)	31.2(6)	45(1)
K'	5.1(14)	3.0(3)	2.4(3)	4*	4*	4*	8.6*	4*
a_0(Å)	13.759(5)	13.734(9)	14.76(1)	14.923(3)	9.914(7)	10.07(2)	14.028(1)	13.17(2)
K_{a0} (GPa)	15.5(3)	19.7(7)	37(2)	66(3)	81(12)	30(2)	78(4)	35(1)
K_a'	4*	3.0(3)	1.1(5)	4*	4*	4*	2(2)	4*
b_0 (Å)	-	-	13.055(4)*	13.174(2)**	14.201(9)	14.8(1)	14.131(4)	13.87(1)
K_{b0} (GPa)	-	-	95(9)*	85(4)**	50(5)	11(1)	23(2)	50(2)
K_b'	-	-	4*	4*	4*	4*	10*	4*
c_0 (Å)	8.369(4)	8.453(3)	7.559(7)	7.537(2)	8.707(2)	8.94(2)	7.844(2)	23.62(4)
K_{c0} (GPa)	9.6(2)	29.3(10)	20(2)	40(1)	107(8)	21(1)	26(2)	46(3)
K_c'	7*	2.9(4)	6.6(8)	4*	4*	4*	10*	4*

*= fixed parameter; **= fitted up to 2.1 GPa

References

Adams D.M., Shaw A.C. (1982). A computer-aided design study of the behavior of diamond anvils under stress. Journal of Physics D: Applied Physics, 15, 1609-1617.

Agilent (2012). CrysAlis RED, Agilent Technologies Ltd, Yarnton, Oxfordshire, England.

Alt J.C. and Honnorez J. (1984). Alteration of the Upper Oceanic-Crust, Dsdp Site-417 - Mineralogy and Chemistry. Contributions to Mineralogy and Petrology, 87, 149-169.

Altomare A., Cuocci C., Gatta G.D., Moliterni A., Rizzi R. (2017). Methods of crystallography: powder X-ray diffraction. EMU Notes in Mineralogy, Vol. 19, Chapter 1, 1–59.

Ames L.L.J. (1960). Cation sieve properties of clinoptilolite. American Mineralogist, 45, 689–700.

Anderson O.L. (1995). Equations of State of Solids for Geophysics and Ceramic Science, Oxford University Press, Oxford (UK).

Angel R.J. (2000). High-temperature and High pressure Crystal Chemistry. In: Reviews in Mineralogy and Geochemistry (R.M. Hazen, R.T. Downs Eds.), 41, Mineralogical Society of America, Washington DC (USA), pp. 35-60.

Angel R.J., Allan D.R., Miletich R., Finger L.W. (1997). The use of quartz as internal pressure calibrant in high-pressure crystallography. Journal of Applied Crystallography, 30, 461-466.

Angel R.J., Alvaro M., Gonzalez-Platas J. (2014). EosFit7c and a Fortran module (library) for equation of state calculations. Zeitschrift für Kristallographie, 229, 405-419.

Angel R.J., Bujak M., Zhao J., Gatta G.D. and Jacobsen S.J. (2007). Effective hydrostatic limits of pressure media for high-pressure crystallographic studies. Journal of Applied Crystallography, 40, 26-32.

Arletti R., Quartieri S., Vezzalini G. (2010). Elastic behavior of zeolite boggsite in *silicon oil* and aqueous medium: a case of high-pressure-induced over-hydration. American Mineralogist, 95, 1247-1256.

Arletti R., Vezzalini G., Morsli A., Di Renzo F., Dmitriev V., Quartieri S. (2011). Elastic behavior of MFI-type zeolites: 1-Compressibility of Na-ZSM-5 in penetrating and non-penetrating media. Microporous and Mesoporous Materials 142, 696-707.

Armbruster, T., Gunter, M. E. (1991). Stepwise dehydration of heulandite-clinoptilolite from Succor Creelq Oregon, U.S.A.: A single-crystal X-ray study at 100 K. American Mineralogist, 76, 1872-1883.

Armbruster T. and Gunter M.E. (2001). Crystal structures of natural zeolites. In: Natural zeolites: occurrence, properties, application (Bish D.L., Ming D.W., Eds), 45, Mineralogical Society of America, Washington DC (USA), pp. 1-57.

Armbruster T. and Kohler T. (1992). Rehydration and dehydration of laumontite: a single-crystal X-ray study at 100-K. Neues Jahrbuch für Mineralogie Monatshefte, 9, 385-397.

Artioli G., Smith J.V., and Kvick A. (1989). Single-crystal neutron-diffraction study of partially dehydrated laumontite at 15K. Zeolites, 9, 377–391.

Artioli G. and Ståhl K. (1993). Fully hydrated laumontite: a structure study by flat plate and capillary powder diffraction techniques. Zeolites, 13, 249–255.

Aumento F. (1966). Thermal transformations of stilbite. Canadian Journal of Earth Sciences, 3, 351-366.

Bacakova L., Vandrovcova M., Kopova I., Jirka I. (2018). Applications of zeolites in biotechnology and medicine - a review. Biomaterials Science, 6, 974-689.

Baykal B.B. and Guven D.A. (1997). Performance of clinoptilolite alone and in combination with sand filters for removal of ammonia peaks from domestic wastewater. Water Science Technology Journal, 35, 47-54.

Baerlocher C., McCusker L.B. and Olson D.H. (2007). Atlas of Zeolite framework types, sixth ed., Elsevier Science, New York (USA).

Barnett J.D., Block S., Piermarini G.J. (1973). An optical fluorescence system for quantitative pressure measurement in the diamond-anvil cell. Review of Scientific Instruments, 44, 1-9.

Barrer R.M. (1978). Cation-exchange equilibria in zeolites and feldspathoids. In: Natural Zeolites: Occurrence, Properties (Sand L.B., Mumpton F.A., Eds), Use. Pergamon Press, New York (USA), pp 385-395.

Barrer R.M. and Klinowski J. (1974). Ion exchange in mordenite. Journal of the Chemical Society Faraday Transactions, 70, 2362-2367.

Bartolini R., John Adams Institute, Public Domain. [Online]. Available: https://commons.wikimedia.org/w/index.php?curid=15588142 [2018].

Berlie A., Kearley G.J., Liu Y., Yu D., Mole R.A., Ling C.D., Withers R.L. (2015). Energy and temperature dependence of rigid unit modes in $AlPO_4$-5. Physical Chemistry Chemical Physics. 17, 21547-21554.

Besson J.M., Nelmes R.J., Hamel G., Loveday J.S., Weill G., Hull S. (1992). Neutron powder diffraction above 10 GPa. Journal of physics B: Atomic, Molecular and Optical Physics, 180, 907-910.

Betti C., Fois E., Mazzucato E., Medici C., Quartieri S., Tabacchi G., Vezzalini G., Dmitriev V. (2007). Gismondine under H*P*: Deformation mechanism and re-organization of the extra-framework species. Microporous and mesoporous materials, 103, 190-209.

Bhagwanjee J. and Devendra N. S. (2016). Basics of Zeolites, in: Fly Ash Zeolites, innovations, applications and directions. Springer, Advanced Structured Materials 78.

Birch F. (1947). Finite Elastic Strain of Cubic Crystals. Physical Review Journals, 71, 809-824.

Bish D.L. and Carey J.W. (2001). Thermal behavior of natural zeolites, in: Natural Zeolites: Occurrence, Properties, Applications (Bish D.L., Ming D.W., Eds), 45, Reviews in Mineralogy and Geochemistry, Washington DC (USA), pp 403-452.

Bish D.L., Vaniman D.T., Chipera S.J., Carey J.W. (2003). The distribution of zeolites and their effects on the performance of a nuclear waste repository at Yucca Mountain, Nevada, USA. American Mineralogist, 88, 1889-1902.

Boles J.R. and Wise W.S. (1978). Nature and origin of deep-sea clinoptilolite. In: Natural Zeolites: Occurrence, Properties, Use (Sand L.B., Mumpton F.A., Eds). Pergamon Press, New York (USA), pp 235-244.

Bohlke J.K., Honnorez J. and Honnorez-Guerstein B.M. (1980). Alteration of basalts from Site 396B, DSDP: Petrographic and mineralogic studies. Contributions to Mineralogy and Petrology, 73, 341-364.

Bonferoni M.C., Cerri G., de' Gennaro M., Juliano C., Caramella C. (2007) Zn2+-exchanged clinoptilolite-rich rock as active carrier for antibiotics in anti-acne topical therapy - In-vitro characterization and preliminary formulation studies. Applied Clay Science, 36, 95-102.

Borai E.H., Harjula R., Malinen L., Paajanen A. (2007). Efficient removal of cesium from low-level radioactive liquid waste using natural and impregnated zeolite minerals. Journal of Hazardous Materials, 172, 416-422.

Bordat P., Kirstein J., Labeguerie P., Merawa M., Brown R. (2007). Structure and dynamics of $AlPO_4$-5 and other aluminophosphates: Classical molecular dynamics and ab initio calculations. Journal of Physical Chemistry C, 10972-10981.

Breck D.W. (1974). Zeolite Molecular Sieves, structure chemistry and use, John Wiley and Sons inc., New York (USA).

Brunner G.O and Meier W.M. (1989). Framework density distribution of zeolite-type tetrahedral nets. Nature, 337,146-147.

Cappelletti P., Colella A., Langella A., Mercurio M., Catalanotti L., Vincenzo M., de Gennaro B. (2017)Use of surface modified natural zeolite (SMNZ) in pharmaceutical preparations Part 1. Mineralogical and technological characterization of some industrial zeolite-rich rocks. Microporous and Mesoporous Materials 250, 232-244.

Čejka, J., Corma, A. and Zones S. (2010). Zeolite and Catalysis. Synthesis, Reactions and Applications. Wyley-YCH, Weinheim (DE).

Cerri G., de' Gennaro M., Bonferoni M.C., Caramella C. (2004) Zeolites in biomedical application: Zn-exchanged clinoptilolite-rich rock as active carrier for antibiotics in anti-acne topical therapy. Applied Clay Science, 27, 141-150.

Chatterjee N.D., Krüger R., Haller G., Olbricht W. (1998). The Bayesian approach to an internally consistent thermodynamic database: theory, database, and generation of phase diagrams. Contributions to Mineralogy and Petrology, 133, 149-168.

Cheetham A.K. and Wilkinson A.P. (1992). Synchrotron X-ray and Neutron Diffraction Studies in Solid-State Chemistry. Angewandte Chemie, 31, 1557-1570.

Chen Y., Zhang Y., Li D., Gao F., Feng C., Wen S., Ruan S. (2015). Humidity sensor based on $AlPO_4$-5 zeolite with high responsivity and its sensing mechanism. Sensors and Actuators B-Chemical, 212, 242-247.

Cho M., Maruyama S. and Liou J.G. (1987). An experimental investigation of heulandite-laumontite equilibrium at 1000 to 2000 bar P_{fluid}. Contributions to mineralogy and petrology, 97, 43-50.

Close D.J. and Dunkle R.V. (1977). Use of adsorbent beds for energy storage in drying of heating systems. Solar Energy, 19, 233-238.

Colella C., de' Gennaro M. and Aiello R. (2001). Use of Zeolitic Tuff in the Building Industry. Reviews in Mineralogy and Geochemistry, 45, 552-587.

Colligan, M., Foster, P.M., Cheetman, A.K., Lee, Y., Vogt, T., and Hriljac, J.A. (2004). Synchrotron X-ray powder diffraction and computational investigation of purely siliceus zeolite Yunder pressure. Journal of American Chemical Society, 126, 12015–12022.

Colligan M., Lee Y., Vogt T., Celestian A ., Parise J.B., Marshall W. and Hriljac, J. (2005). High pressure Neutron powder diffraction study of superhydrated natrolite. Journal of Physical Chemistry B, 109, 18223-18225.

Comboni D., Gatta G.D, Lotti P., Merlini M., Liermann H-P. (2017). On the P-induced behavior of the zeolite phillipsite: an *in situ* single-crystal synchrotron X-ray diffraction study. Physics and chemistry of the minerals, 44, 1-20.

Comboni D., Gatta G.D, Lotti P., Merlini, Hanfland M. (2018). Crystal-fluid interactions in laumontite Microporous and mesoporous materials, 263, 86-95.

Comboni D., Lotti P., Gatta D., Lacalamita M., Mesto E., Merlini M., Hanfland M. (2018). Armstrongite at non-ambient conditions: An *in-situ* high-pressure single-crystal X-ray diffraction study. Microporous and mesoporous materials, 274, 171-175.

Coombs D.S., Alberti A., Armbruster T., Artioli G., Colella C., Galli E., Grice J.D., Liebau F., Mandarino J.A., Minato H., Nickel E.H., Passaglia E., Peacor D.R., Quartieri S., Rinaldi R., Ross M., Sheppard R.A.,Tillmanns E., Vezzalini G. (1998). Recommended nomenclature for zeolite minerals:

report of the subcommittee on zeolites of the International Mineralogical Association, Commission on New Minerals and Mineral Names. Mineralogical Magazine, 62, 533–571.

Coombs D.S., Ellis A.J., Fyfe W.S., Taylor A.M. (1959). The zeolite facies, with comments on the interpretation of hydrothermal syntheses. Geochimica et Cosmochimica Acta, 17, 53-107.

Couture I.A. (1977). Composition and origin of palygorskite-rich and montmorillonite-rich zeolite-containing sediments from the Pacific Ocean. Chemical Geology, 19, 113–130.

Cruciani G. (2006). Zeolites upon heating: Factors governing their thermal stability and structural changes. Journal of Physics and Chemistry of Solids, 67, 1973-1994.

Cundy C.S. and Cox P.A. (2003). The Hydrothermal Synthesis of Zeolites: History and Development from the Earliest Days to the Present Time. Chemical Reviews, 103, 663-701.

Danisi R.M., Armbruster T. and Nagashima M. (2015). Structural intergrowth of merlinoite/phillipsite and its temperature-dependent dehydration behavior: a single-crystal X-ray study. Minerogical Magazine, 79, 191-203.

De' Gennaro M., Colella C., Franco E., Stanzione D. (1988). Hydrothermal conversion of trachytic glass into zeolite I: Reactions with deionized water. Neues Jahrbuch für Mineralogie, 4,149-158.

de' Gennaro M., Petrosino P., Conte M.T., Munno R., Colella C. (1990). Zeolite chemistry and distribution in a Neapolitan yellow tuff deposit. European Journal of Mineralogy, 2, 779-786.

Deffeyes K.S. (1968). Natural zeolites deposits of potential commercial use, in: Molecular Sieves (Barrer R.M., Ed). London Society of Chemical Industry, London (UK), pp 7-9.

Demontis P., Gulín-Gonzalez J. and Suffritti G.B. (2012). Water Adsorbed in $AlPO_4$-5 and SSZ-24 Studied by Molecular Dynamics Simulation. The Journal of Physical Chemistry C, 116, 11100-11109.

Doula M.K (2009). Simultaneous removal of Cu, Mn and Zn from drinking water with the use of clinoptilolite and its Fe-modified form. Water Research, 15, 3659-3672.

Downs R.T. (2000). Analysis of Harmonic Displacement Factors. Reviews in Mineralogy and Geochemistry, 41, 61-87.

Duffy T. S. and Wang Y. B. (1998). Pressure-volume-temperature equations of state. In: Ultrahigh-Pressure Mineralogy: Physics and Chemistry of the Earth's Deep Interior (Hemley R., Ed). Mineralogical Society of America, Washington DC (USA) , pp. 425-458.

Dunstan D.J. and Spain I.L. (1989). The technology of diamond anvil high-pressure cells: I. Principles, design, and construction. Journal of Physics E: Scientific Instruments, 22, 913-923.

Ennaert T., Van Aelst J., Dijkmans J., De Clercq R., Schutyser W., Dusselier M., Verboekend D., Sels B.F (2016). Potential and challenges of zeolite chemistry in the catalytic conversion of biomass. Chemical Society Reviews, 45, 584-611.

Eroshenko V. and Acad C. R (1990). Science Ukraine Ser A, 10, 79–82.

Eroshenko V., Brevet Inter. (Europe, USA, Japan) WO 96/18040, 13 juin 1996 ; Brevet français No 9414856, 30 may 1997.

Eroshenko V., Regis R.C., Soulard M., Patarin J. (2001). Energetics: A New Field of Applications for hydrophobic Zeolites. Journal of the American Chemical Society, 123, 8129-8130.

Eroshenko V., Regis R.C., Soulard M., Patarin J. (2002). Les systèmes hétérogènes « eau–zéolithe hydrophobe » : de nouveaux ressorts moléculaires. Comptes Rendus Physique, 3, 111-119.

Fikri N. (1999). Zeolites based composites in energy storage. Master Thesis in Materials Science and Engineering.

Flanigen E.M., Lok B.M., Patton R.L., Wilson S.T. (1986). Aluminophosphate molecular sieves and the periodic table, Pure and Applied Chemistry, 58, 1351-1358.

Floquet N., Coulomb J.P., Dufau N., Andre G. (2004). Structure and Dynamics of Confined Water in $AlPO_4$-5 Zeolite. The Journal of Physical Chemistry B, 108, 13107-13115.

Fridriksson T., Bish D.L. and Bird D.K. (2003). Hydrogen-bonded water in laumontite I: X-ray powder diffraction study of water site occupancy and structural changes in laumontite during room-temperature isothermal hydration/dehydration. American Mineralogist, 88, 277- 287.

Galli E. and Loschi Ghittoni A. (1972). The crystal chemistry of phillipsites. American Mineralogist, 57, 1125-1145.

Galloway W.E. (1979). Diagenetic control of reservoir quality in arc-derived sandstones: implications for petroleum exploration. Aspects of Diagenesis: Society of Economic Paleontologists and Mineralogists Special Publications, 26, 251–261.

Gascon J., Kapteijn F., Zornoza B., Sebastian V., Casado C., Coronas J. (2012). Practical Approach to Zeolitic Membranes and Coatings: State of the Art, Opportunities, Barriers, and Future Perspectives. Chemistry of materials, 24, 2829-2844.

Gatta G.D. (2008). Does porous mean soft? On the elastic behavior and structural evolution of zeolites under pressure. Zeitschrift für Kristallographie, 223, 160-170.

Gatta G.D. (2010a). Extreme deformation mechanisms in open-framework silicates at high-pressure: evidence of anomalous intertetrahedral angles. Microporous and Mesoporous Materials, 128,78–84.

Gatta G.D. (2010b). Microporous materials at high pressure: Are they really soft?. In: High-Pressure Crystallography: From Fundamental Phenomena to Technological Applications, NATO Science for Peace and Security - Series B (Physics and Biophysics) (E. Boldyreva and P. Dera, eds), Springer, pp. 481-491.

Gatta G.D., Cappelletti P., Langella A. (2010). Crystal-chemistry of phillipsites from the Neapolitan Yellow Tuff. European Journal of Mineralogy, 22, 779-786.

Gatta G.D., Cappelletti P., Rotiroti N., Slebodnick C., Rinaldi R. (2009a). New insights into the crystal structure and crystal chemistry of the zeolite phillipsite. American Mineralogist, 94, 190-199.

Gatta G.D., Cappelletti P., de' Gennaro B., Rotiroti N., Langella A. (2015). New data on Cu-exchanged phillipsite: a multi-methodological study. Physics and Chemistry of Minerals 42, 723-733.

Gatta G.D., Comboni D., Alvaro M., Lotti P., Càmara F., Domeneghetti M.C. (2014). Thermoelastic behavior and dehydration process of cancrinite. Physics and Chemistry of Minerals, 41, 373-386.

Gatta G.D., Comodi P., Zanazzi P.F., Boffa Ballaran T. (2005). Anomalous elastic behavior and high-pressure structural evolution of zeolite levyne. American Mineralogist 90, 645-652.

Gatta G.D. and Lee Y. (2007). Anisotropic elastic behavior and structural evolution of zeolite phillipsite at high pressure: a synchrotron powder diffraction study. Microporous and Mesoporous Materials, 105, 239-250.

Gatta G.D. and Lee Y. (2014). Zeolites at high pressure: a review. Mineralogical Magazine, 78, 267-291.

Gatta G.D., Lotti P., Nestola F., Pasqual D. (2012). On the high-pressure behavior of gobbinsite, the natural counterpart of the synthetic zeolite Na-P2. Microporous and Mesoporous Materials, 163, 259-269.

Gatta G.D., Lotti P. and Tabacchi G. (2018). The effect of pressure on open-framework silicates: elastic behavior and crystal-fluid interaction. Physics and Chemistry of Minerals, 45,115-138.

Gatta G.D., Nestola F. and Boffa Ballaran T. (2006). Elastic behavior, phase transition and pressure-induced structural evolution of analcime. American Mineralogist 91, 568-578.

Gatta G.D., Rotiroti N., Boffa Ballaran T., Pavese A. (2008). Leucite at high-pressure: elastic behavior, phase stability and petrological implications. American Mineralogist 93, 1588-1596.

Gatta G.D., Rotiroti N., Boffa Ballaran T., Sanchez-Valle C., Pavese A. (2009b). Elastic behavior and phase stability of pollucite, a potential host for nuclear waste. American Mineralogist, 94, 1137-1143.

Ghasemi Z., Sourinejad I., Kazemian H., Rohani S. (2018). Application of zeolites in aquaculture industry: a review. Reviews in aquaculture, 10, 75-95.

Gottardi G. (1978). Mineralogy and crystal chemistry of zeolites. In: Natural Zeolites: Ocurrence, Properties,Use (Sand L.B. and Mumpton, F.A., Eds). Pergamon press, Elmsford, New York (USA), pp. 31-44.

Gottardi G. and Galli E. (1985). Natural zeolites. Minerals and rocks series. Springer, Berlin (DE), pp. 409.

Gualtieri A.F., Caputo D. and Colella C. (1999a). Ion-exchange selectivity of phillipsite for Cs^+ : a structural investigation using the Rietveld method. Microporous and Mesoporous Materials, 32, 319-329.

Gualtieri A.F., Passaglia E., Galli E., Viani A. (1999b). Rietveld structure refinement of Sr- exchanged phillipsites. Microporous and Mesoporous Materials, 31, 33-43.

Gualtieri A.F., Passaglia E. and Galli E. (2000). Rietveld structure refinement of natural and Na^-, K^-, Ca^-, and Ba-exchanged phillipsites. In: Natural zeolites for the third millennium (Colella C., Mumpton F.A., Eds). De Frede, Naples (ITA), pp. 93-110.

Guan H., Bestland E., Zhu C., Zhu H., Albertsdottir D., Hutson J., Simmons C.T., Ginic-Markovic M., Tao X., Ellis A.V. (2010) Variation in performance of surfactant loading and resulting nitrate removal among four selected natural zeolites. Journal of Hazardous Materials 183, 616-621.

Haile S.M. and Wuensch B.J. (1997). Comparison of the crystal chemistry of selected MSi_6O_{15}-based silicates. American Mineralogist, 82, 1141-1149.

Hay R.L. (1966) Zeolites and zeolitic reactions in sedimentary rocks. Geological Society of America Special Papers, 85, 130.

Hay R.L. and Sheppard R.A. (2001). Occurrence of Zeolites in Sedimentary Rocks: An Overview. Reviews in Mineralogy and Geochemistry 45, 217-234.

Harbottle M.J., Mantle M.D., Johns M.L., Tabbaa A.L., Hutchings T.R., Moffat A.J., Ouki S.K. (2007). Magnetic resonance imaging of the effect of zeolite on lithium uptake in poplar. Environmental Science and Tecnology, 41, 3444-3448.

Hazen R.M., Downs R.T. and Prewitt C.T. (2000). Principles of Comparative Crystal Chemistry. Reviews in Mineralogy and Geochemistry, 41, 1-33.

Hazen R.M. (1983). Zeolite Molecular Sieve 4A: Anomalous Compressibility and Volume Discontinuities at High Pressure. Science, 219, 1065-1067.

Hazen R.M. and Finger L.W. (1984). Compressibility of zeolite 4A is dependent on the molecular size of the hydrostatic pressure medium. Journal of Applied Physics, 56, 1838-1840.

Holland T.J.B. and Powell R. (1998). An internally consistent thermodynamic data set for phases of petrological interest. Journal of Metamorphic Geology, 16, 309-343.

Höller H. and Wirsching U. (1980). Experiments on the hydrothermal formation of zeolites from nepheline and nephelinite. In: Fifth International Conference on Zeolites (Rees L.V.C., Ed), Heyden, London (UK), pp. 164-170.

Ievtushenko O.V., Eroshenko V.A., Grosu Y.G., Nedelec J-M., Grolier J-P.E. (2013). Evolution of the energetic characteristics of {silicalite-1 + water} repulsive clathrates in a wide temperature range. Physical Chemistry Chemical Physics, 15, 4451-4457.

Iijima A. (2001). Zeolites in Petroleum and Natural Gas Reservoirs. Reviews in Mineralogy and Geochemistry, 45, 348-402.

Jambor J.L., Roberts A.L. and Grice J.D. (1987). Armstrongite from the Strange Lake Alkalic Complex, on the Quebec-Labrador Boundary, Canada. Powder Diffraction, 2, 2-4.

Johnson M., O'Connor D., Barnes P., Catlow C.R.A., Owens S.L., Sankar G., Bell S., Teat S.J., Stephenson R. (2003). Cation exchange, dehydration, and calcination in clinoptilolite: *in situ* x-ray diffraction and computer modeling. The journal of physical chemistry B, 107, 942-951.

Jove C. and Hacker B.R. (1997). Experimental investigation of laumontite->wairakite + H_2O: A model diagenetic reaction. American Mineralogist, 82, 781-789.

Juan V.C. and Lo H-J. (1971). The stability fields of natural laumontite and wairakite and their bearing on the zeolite facies. Proceedings of the geological society of China, 14, 34-44.

Kabalov Yu.K., Zubkova N.V., Pushcharovsky D.Yu., Schneider J., and Sapozhnikov A.N. (2000). Powder Rietveld refinement of armstrongite, $CaZr[Si_6O_{15}]\cdot 3H_2O$. Zeitschrift für Kristallographie, 215, 757-761.

Kalló D. (1990). Exploitation of ammonia with ion exchange. Unpublished research report. Hungarian Academy of Sciences, Budapest, Hungary.

Kalló D. (2001). Applications of Natural Zeolites in Water and Wastewater Treatment. Reviews in Mineralogy and Geochemistry, 45, 519-549.

Kaneva E., Lacalamita M., Mesto E., Schingaro E., Scordari F., Vladykin N. (2014) Structure and modeling of disorder in miserite from the Murun (Russia) and Dara-i-Pioz (Tajikistan) massifs. Physichs and Chemistry of Minerals, 41, 49-63.

Karashaev A.A. and Sapozhnikov A.N. (1978). Crystal structure of armstrongite. Soviet physics, crystallography, 23, 539-542.

Kazansky V.B. (1994). The catalytic site from a chemical point of view. In: Stöcker M., Karge H.G., Jansen J.C., Weitkamp J. (eds) Advanced Zeolite Science and Applications, pp 251-272.

Kenichi T. (1999). Absence of the *c*/*a* anomaly in Zn under high pressure with a helium-pressure medium. Physics review B, 60, 6171–6174.

Kim T., Lee Y., Jang Y.-N., Shin J., Hong S.B. (2013). Contrasting high-pressure compression behaviors of $AlPO_4$-5 and SSZ-24 with the same AFI framework topology. Microporous and Mesoporous Materials, 169, 42-46.

Klap G.J., van Koningsveld H., Graafsma H., Shreurs A.M.M. (2000). Absolute configuration and domain structure of $AlPO_4$-5 studied by single crystal X-ray diffraction. Microporous and Mesoporous Materials, 38, 403-412.

Klotz S., Chervin J.C., Munsch P., Le Marchand G. (2009). Hydrostatic limits of 11 pressure transmitting media. Journal of Physics D: Applied Physics, 42, 7.

Kong M., Lee Y., Gatta G.D., Lee Y. (2018). Comparative compressional behavior of chabazite with Li+, Na+, Ag+, K+, Rb+, and Cs+ as extra-framework cations. American Mineralogist, 103, 207-215.

Koporulin V.I. (2013). Formation of laumontite in sedimentary rocks: a case study of sedimentary sequences in Russia. Lithology and Mineral Resources, 48, 122-137.

Kortunov P., Chmelik C., Karger J., Rakoczy R.A., Ruthven D.M., Traa Y., Vasenkov S., Weitkamp J. (2005). Sorption kinetics and intracrystalline diffusion of methanol in ferrierite: An example of disguised kinetics. Journal of the International Adsorption Society, 11, 235-244.

Lacalamita M., Cametti G., Mesto E., Schingaro E. (2018). Armstrongite at non ambient conditions: An *in-situ* high temperature single crystal X-ray diffraction study. Microporous and mesoporous materials, in press.

Langella A., Cappelletti P. and de′ Gennaro R. (2001). Zeolites in Closed Hydrologic Systems. Reviews in Mineralogy and Geochemistry,45, 235-260.

Lee Y., Vogt T., Hriljac J.A., Parise J.B. and Artioli G. (2002a) Pressure-induced volume expansion of zeolites in the natrolite family. Journal of the American Chemical Society, 124, 5466-5475.

Lee Y., Vogt T., Hriljac J.A., Parise J.B., Hanson J.C. and Kimk S.J. (2002b) Non-framework cation migration and irreversible pressure-induced hydration in a zeolite. Nature, 420, 485-489.

Lee Y., Hriljac J.A., Studer A., Vogt T. (2004a). Anisotropic compression of edingtonite and thomsonite to 6 GPa at room temperature. Physics and Chemistry of Minerals, 31, 22-27.

Lee Y., Hriljac J.A. and Vogt T. (2004b). Pressure induced migration of zeolitic water in laumontite. Physics and Chemistry of Minerals, 31, 421-428.

Lee Y., Hriljac J.A. and Vogt T. (2010). Pressure-induced argon insertion into an auxetic small pore zeolite. The Journal of Physical Chemistry C, 114, 6922–6927.

Lee Y., Seoung D., Jang Y.N., Vogt T., Lee Y. (2013). Pressure-Induced Hydration and Insertion of CO_2 into Ag-Natrolite. Chemistry-A European journal, 19, 5806-5811.

Lercher J.A and Jentys A. (2011). Basic concepts in zeolite acid-base catalysis. In: Zeolites and ordered porous solids: Fundamentals and applications, 5 th International FEZA conference, pp. 181-210.

Li D., Yao J. and Wang H. (2012). Hydrothermal synthesis of $AlPO_4$-5: Effect of precursor gel preparation on the morphology of crystals. Progress in Natural Science, 22, 684-692.

Li Z., Beachner R., McManama Z., Hanlie H. (2007) Sorption of arsenic by surfactant modified zeolite and kaolinite. Microporous and Mesoporous Materials, 105, 291–297.

Likhacheva A.Y., Seryotkin Y.V., Manakov A.Y., Goryainov S.V., Ancharov A.I. and Sheromov M.A. (2006). Anomalous compression of scolecite and thomsonite in aqueous medium to 2 GPa. High Pressure Research, 26, 449-453.

Likhacheva A.Y., Seryotkin Y.V., Manakov A.Y., Goryainov S.V., Ancharov A.I. and Sheromov M.A. (2007). Pressure-induced over-hydration of thomsonite: A synchrotron powder diffraction study. American Mineralogist, 92, 1610-1615.

Liebau F. (1985). Structural Chemistry of Silicates: Structure, Bonding and Classification, Springer-Verlag, Berlin (DE), pp. 14-30.

Liou J.G. (1971). *P-T* stabilities of laumontite, wairakite, lawsonite, and related minerals in the system $CaAl_2Si_2O_8$-SiO_2-H_2O. Journal of Petrology, 12, 379-411.

Liou J.G. (1979). Zeolite facies metamorphism of basaltic rocks from the East Taiwan Ophiolite. American Mineralogist, 64, 1-14.

Liu Z., Fujita N., Terasaki O., Ohsuna T., Hiraga K., Camblor M.A., Diaz-Cabanas M.J., and Cheetham A.K. (2002). Incommensurate Modulation in the Microporous Silica SSZ-24. Chemistry - A European Journal, 4549-4556.

Liu D., Zhang B., Liu X., Li J. (2015). Cyclohexane oxidation over AFI molecular sieves: effects of Cr, Co incorporation and crystal size. Catalysis Science & Technology, 5, 3394-3402.

Löwenstein W. (1954). The distribution of aluminum in the tetrahedral of silicates and aluminates. American Mineralogist, 39, 92–96.

Lotti P., Arletti R., Gatta G.D., Quartieri S., Vezzalini G., Merlini M., Dmitriev V., Hanfland M. (2015a). Compressibility and crystal-fluid interactions in all-silica ferrierite at high pressure. Microporous and Mesoporous Materials, 218, 42-54.

Lotti P., Gatta G.D., Merlini M., Liermann H-P. (2015b). High-pressure behavior of synthetic mordenite-Na: an *in situ* single-crystal synchrotron X-ray diffraction study. Zeitschrift für Kristallographie, 230, 201-211.

Lotti P., Gatta G.D., Comboni D., Merlini M., Pastero L., Hanfland M. (2016). $AlPO_4$-5 zeolite at high pressure: crystal–fluid interaction and elastic behavior. Microporous and Mesoporous Materials, 228, 158-167.

Lv H., Yao M., Li Q., Liu R., Liu B., Lu S., Jiang L., Cui W., Liu Z., Liu J., Chen Z., Zou B., Cui T., Liu B (2012). The structural stability of $AlPO_4$-5 zeolite under pressure: Effect of the pressure transmission medium Journal of Applied Physics, 111, 112615.

Malla P.B. and Komarneni S. (1995). Effect of pore size on the chemical removal of organic template molecules from synthetic molecular sieves. Zeolites, 15, 324-332.

Mao H.K., Bell P.M., Dunn K.J., Chrenko R.M., DeVries R.C. (1979). Absolute pressure measurements and analysis of diamonds subjected to maximum static pressures of 1.3-1.7 Mbar. Review of Scientific Instruments, 50, 1002-1009.

Mao H.K., Xu J. and Bell P.M. (1986). Calibration of the ruby pressure gauge to 800-kbar under quasi-hydrostatic conditions. Journal of Geophysical Research, 91, 4673-4676.

Mesto E., Kaneva E., Schingaro E., Vladykin N., Lacalamita M., and Scordari, F. (2014). Armstrongite from Khan Bogdo (Mongolia): Crystal structure determination and implications for zeolite-like cation exchange properties. American Mineralogist, 99, 2424-2432.

Merlini M. and Hanfland M. (2013). single crystal diffraction at megabar conditions by synchrotron radiation. High Pressure Research, 33, 511-522.

Merrill L. and Basset W.A. (1974). The Crystal Structure of CaCO3(II), a High-Pressure Metastable Phase of Calcium Carbonate. Acta crystallographica, 31, 343.

Mier M,V., Callejas R. L., Gehr R., Cisnerosc B.E. J., Alvarez P.J.J. (2001). Heavy metal removal with mexican clinoptilolite: multi-component ionic exchange. Water Research. 35, 373-378.

Miletich R., Allan D.R., Kuhs W.F. (2000). High-Pressure Single-Crystal Techniques. Reviews in Mineralogy and Geochemistry, Vol. 41, 445-520.

Millini R. (2011). Zeolites in refining and petrochemistry. In: Zeolites and ordered porous solids: Fundamentals and applications (Martínez C. and Pérez-Pariente J., Eds), Editorial Universitat Politècnica de València, Valencia (SPA), pp. 211- 253.

Ming W.D. and Allen E.R. (2001). Use of Natural Zeolites in Agronomy, Horticulture and Environmental Soil Remediation Reviews in Mineralogy and Geochemistry, 45, 620-654.

Ming D.G. and Boettinger J.L. (2001). Zeolites in Soil Environments. Reviews in Mineralogy and Geochemistry, 45, 323-345.

Misaelides P. (2011). Application of natural zeolites in environmental remediation: A short review. Microporous and Mesoporous Materials, 144, 15-18.

Motsi T., Rowson N.A. and Simmons M.J.H. (2009). Adsorption of heavy metals from acid mine drainage by natural zeolite. International Journal of Mineral Processing, 92, 42-48.

Murnaghan F.D. (1937). Finite deformations of an elastic solid. American Journal of Mathematics, 49, 235-260

Nakhli S.A.A., Delkash M., Bakhshayesh B.E., Kazemian H. (2017). Application of Zeolites for Sustainable Agriculture: a Review on Water and Nutrient Retention. Water, Air, & Soil Pollution, 228-463.

Newalkar B.L., Jasra R.V., Kamath V., Bhat S.G.T. (1998). Sorption of water in aluminophosphate molecular sieve $AlPO_4$-5. Microporous and Mesoporous Materials, 20, 129-137.

Nye J.F. (1957). Physical Properties of Crystals. Oxford University Press, Oxford.

Neuhoff P.S. and Bird D.K. (2001). Partial dehydration of laumontite: thermodynamic constraints and petrogenetic implications. Mineralogical magazine, 65, 59-70.

Olsbye U., Svelle S., Bjørgen M., Beato P., Janssens T.V.W., Joensen F., Bordiga S., Lillerud K.P. (2012). Conversion of Methanol to Hydrocarbons: How Zeolite Cavity and Pore Size Controls Product Selectivity. Angewandte chemie-international edition, 51, 5810-5831.

Ostroski, I.C., Barros, M.A.S.D., Silvab, E.A., Dantas, J.H., Arroyo, P.A., Lima, O.C.M., (2009). A comparative study for the ion exchange of Fe(III) and Zn(II) on zeolite NaY. Journal of Hazardous Materials, 161, 1404-1412.

Ori S., Quartieri S., Vezzalini G., Dmitriev V. (2008) Pressure-induced over-hydration and water ordering in gismondine: A synchrotron powder diffraction study. American Mineralogist, 93, 1393-1403.

Pabalan R.T. and Bertetti F.P. (2001). Cation-Exchange Properties of Natural Zeolites. Reviews in Mineralogy & Geochemistry, 45, 453-518.

Palatinus L. and Chapuis G. (2007). SUPERFLIP - a computer program for the solution of crystal structures by charge flipping in arbitrary dimensions. Journal of Applied Crystallography, 41, 786-790.

Passaglia E., Vezzalini G. and Carnevali R. (1990). Diagenetic chabazites and phillipsites in Italy: Crystal chemistry and genesis. European Journal of Mineralogy, 2, 827-839.

Passaglia E., Galli E. and Gualtieri A.F. (2000). Variations of the physical and chemical properties in cation exchanged phillipsites. In: Natural Zeolites for the Third Millennium (Colella C. and Mumpton F.A., Eds.), De Frede Editore, Napoli (ITA), pp. 259-267.

Passaglia E. and Sheppard R.A. (2001). The Crystal Chemistry of Zeolites. Reviews in Mineralogy and Geochemistry, 45, 69-116.

Pécsi-Donàth É. (1965). On the individual properties of some Hungarian zeolites. Acta Geologica Hungarica, 9, 235-257.

Pécsi-Donàth É. (1968). Some contributions to the knowledge of zeolites. Acta Mineralogica-Petrografica, 18, 127-141.

Petříček V., Dušek M. and Palatinus L. (2014). Crystallographic computing system JANA2006: general features. Zeitschrift für Kristallographie, 229, 345-352.

Piermarini G.J., Block S., Barnett J.D., Forman R.A. (1975). Calibration of the R_1 ruby fluorescence line to 195 kbar. Journal of Applied Physics, 46, 2774-2780.

Plank C.J. and Rosinski E. J. (1967). Kinetics and Catalysis. In: Chemical Engineering Progress Symposium Series, New York (USA), volume 73, pp. 26.

Plank C.J. and Rosinski E.J. (1964). Catalytic Cracking of Hydrocarbons with a Crystalline Zeolite Catalyst Composite. U.S. Patent 3, 140, 249, assigned to Socony Mobil Oil Corp.

Poirier JP. and Tarantola A. (1998). A logarithmic equation of state. Physics of the Earth and Planetary Interiors, 109, 1-8.

Ramesh K., Damodar Reddy D., Kumar Biswas A., Subba Rao A. (2011). 4 zeolites and their potential uses in agriculture. Advances in Agronomy, 113, 215.

Rashchenko S.V., Seryotkin Y.V. and Bakakin V.V. (2012a). An X-ray single crystal study of alkaline cations influence on laumontite hydration ability: I. Humidity-induced hydration of Na,K-rich laumontite. Microporous and Mesoporous Materials, 151, 93-98.

Rashchenko S.V., Seryotkin Y.V. and Bakakin V.V. (2012b). An X-ray single crystal study of alkaline cations influence on laumontite hydration ability: II. Pressure-induced hydration of Na,K-rich laumontite. Microporous and Mesoporous Materials, 159, 126-131

Richard L.H. and Sheppard A.R. (2001). Occurrence of Zeolites in sedimentary Rocks: an Overview. Reviews in Mineralogy & Geochemistry, 45, 217-234.

Rinaldi R. (1983). Mineralogy of natural zeolites: present status. Conference Paper, Sixth International Zeolite Conference, pp. 570-583.

Rinaldi R., Pluth J.L. and Smith J.V. (1974). Zeolites of the phillipsite family. Refinement of the crystal structure of phillipsite and harmotome. Acta Crystallographica Section B, 30, 2426-2433.

Rinaldi R., Smith J.V. and Jung G. (1975). Chemistry and paragenesis of faujasite, phillipsite, and offretite from Sasbach, Kaiserstuhl, Germany. Neues Jahrbuch für Mineralogie, 10, 433-443.

Rothkirch A., Gatta G.D., Meyer M., Merkel S., Merlini M., Liermann H.P. (2013). Single-crystal diffraction at the Extreme Conditions beamline P02.2: procedure for collecting and analyzing high pressure single-crystal data. Journal of Synchrotron Radiation, 20, 711-720.

Sani A., Cruciani G. and Gualtieri A.F. (2002). Dehydration dynamics of Ba-phillipsite: an *in situ* synchrotron powder diffraction study. Physics and Chemistry of Minerals 29, 351-361.

Schingaro E., Lacalamita M., Mesto E., Della Ventura G. (2018). Thermal stability and dehydration of armstrongite, a microporous zirconium silicate. Microporous and Mesoporous Materials, 272, 137-142.

Seki Y., Onuki H., Okumura K., Takashima I. (1969). Zeolite distribution in the Katayama geothermal area, Onikobe, Japan. Japanese journal of geology and geography, 15, 63-79.

Serri C., de Gennaro B., Catalanotti L., Cappelletti P., Langella A., Mercurio M. (2016) Surfactant-modified phillipsite and chabazite as novel excipients for pharmaceutical applications? Microporous and Mesoporous Materials, 224, 143-148.

Seryotkin Y.V., Bakakin V.V., Fursenko B.A., Belitsky I.A., Joswig W. and Radaelli P.G. (2005). Structural evolution of natrolite during overhydration: a high-pressure neutron diffraction study. European Journal of Mineralogy, 17, 305-313.

Seryotkin Y.V., Bakakin V.V. and Pekov I.V. (2014). Structural evolution of microporous zirconosilicate elpidite under high pressure. Journal of Structural Chemistry, 55, 1252-1259.

Sheppard R.A. (1973). Zeolites in sedimentary rocks. In: United States mineral resources (Brobst D.A., and Pratt P.W., Eds), U.S. Government Printing Office, Washington D.C. (USA), pp. 689-695.

Sheppard R.A. and Hay R.L. (2001). Formation of Zeolites in Open Hydrologic Systems. Reviews in Mineralogy and Geochemistry,45, 261-275.

Shi W.Y., Shao H., Li H., Shao M., Du S. (2009). The remediation of heavy metals contaminated sediment, Journal of Hazardous Materials, 161, 633-640.

Shigeishi R.A., Langford C.H. and Holleborne B.R. (1979). Solar energy storage using chemical potential changes associated with drying of zeolites. Solar Energy, 23,489-495.

Smičiklas I., Dimovic S. and Plecas I. (2006). Removal of Cs^{+}, Sr^{2+} and Co^{2+} from aqueous solutions by adsorption on natural clinoptilolite. Applied Clay Science. Volume 35, pag 139-144.

Smith J.V. (1963). Structural classification of zeolites. Mineralogical Society of America, 1, 281-290.

Sokolova E., Hawthorne F.C., Ball N.A., Mitchell R.H., and Della Ventura G. (2006). Vlasovite, $Na_2Zr(Si_4O_{11})$, from the Kipawa alkaline complex, Quebec, Canada: Crystal-structure refinement and infrared spectroscopy. Canadian Mineralogist, 44, 1349-1356.

Soulard M., Patarin J. and Eroshenko V. (2004). Molecular spring or bumper: A new application for hydrophobic zeolitic materials. Studies in Surface Science and Catalysis, 154, 1830-1837.

Spain I.L. and Dunstan D.J. (1989). The technology of diamond anvil high-pressure cells: II. Operation and use. Journal of Physics E: Scientific Instruments, 22, 913-923.

Stacey F.D., Brennan B.J. and Irvine R.D. (1981). Finite strain theories and comparisons with seismological data. Geophys Surveys 4,189-232.

Ståhl K. and Artioli G. (1993). A neutron powder diffraction study of fully deuterated laumontite. European Journal of Mineralogy, 5, 851-856.

Ståhl K., Artioli G. and Hanson J.C. (1993). The dehydration process in the zeolite laumontite: A real-time synchrotron X-ray powder diffraction study. Physics and Chemistry of Minerals, 23, 328-336.

Steinfink H. (1962). The crystal structure of the zeolite phillipsite. Acta Crystallographica 15, 644-651.

Stöcker M. (1999). Methanol-to-hydrocarbons: catalytic materials and their behavior. Microporous and mesoporous materials, 29, 3-48.

Surdam R.C. and Boles J.R. (1979). Diagenesis of volcanic sandstones. In: Aspects of Diagenesis: Society of Economic Paleontologists and Mineralogists Special Publication 26 (Scholle P.A. and Schluger P.R., Eds.), Tulsa, OK (USA), 26, pp. 227-242.

Stuckenschmidt E., Fuess H. and Kvick A. (1990). Investigation of the structure of harmotome by X-ray (293 K, 100 K) and neutron diffraction (15 K). European Journal of Mineralogy, 2, 861-874.

Taffarel S.R. and Rubio J. (2009). On the removal of Mn^{2+} ions by adsorption onto natural and activated Chilean zeolites. Minerals Engineering, 22, 336-343.

Taylor M.W. and Surdam R.C. (1981). Zeolite reactions in the tuffaceous sediments at Teels Marsh, Nevada. Clays & Clay Minerals, 29, 341-352.

Tavolaro A. and Drioli E. (1999). Zeolite Membranes. Advanced materials, 12, 975-996.

Tarasevich Y.I. (1994). Natural, modified, and semisynthetic sorbents in water-treatment processes. Khimiya i Tekhnoliya Vody, 16, 626-640.

Tchernev D.I. (2001). Natural Zeolites in Solar Energy Heating, Cooling, and Energy Storage. Reviews in Mineralogy and Geochemistry, 45, 589-617.

Tran H.N., Van Viet P. and Chao H.P. (2018). Surfactant modified zeolite as amphiphilic and dual-electronic adsorbent for removal of cationic and oxyanionic metal ions and organic compounds. Ecotoxicology and Environmental Safety, 147, 55-63.

Tsitsishvili G.V., Skhirtladze N.S., Andronikashvili T.G., Tsitsishvili V.G., Dolidze A.V. (1999). Natural zeolites of Georgia: occurrences, properties, and application. Studies in Surface Science and Catalysis, 125, 715, 722.

Tsutsumi K., Mizoe K. and Chubachi K. (1999). Adsorption characteristics and surface free energy of $AlPO_4$-5. Colloid and polymer science, 277, 83-88.

U.S. Geological Survey (2017). Mineral commodity summaries 2016. U.S. Geological Survey, Reston, Virginia.

Utada M. (2001a). Zeolites in Burial Diagenesis and Low-grade Metamorphic rocks. Reviews in Mineralogy and Geochemistry, 45, 277-304.

Utada M. (2001b). Zeolites in Hydrothermally Altered Rocks. Reviews in Mineralogy and Geochemistry, 45, 1-18.

van Koningsveld H. (2007). Compendium of Zeolite Framework Types. In: Building Schemes and Type Characteristics, Elsevier, Amsterdam (NL).

Van Reeuwijk L.P. (1971). The dehydration of gismondite. American Mineralogist, 56, 1655-1659.

Van Reeuwijk L.P. (1974). The thermal dehydration of natural zeolites (with a summary in Dutch) (Wageningen H. and Zonen B.V., Eds), Mededelingen Landbouwhogeschool Wageningen (NL), pp.74-79.

Vinet P., Ferrante J., Smith J.R., Rose J.H. (1986). A universal equation of state for solids. Journal of Physics C: Solid State Physics, 19, 467-473.

Vitali F., Blanc G. and Larqué P. (1995). Zeolite distribution in volcaniclastic deep-sea sediments from the Tonga Trench margin (SW Pacific). Clays & Clay Minerals, 43, 92-104.

Vladykin N.V., Kovalenko V.I., Kashaev A.N., Sapozhnikov A.N., and Pisarskaya V.A. (1973). A new mineral of calcium and zirconium, armstrongite. Doklady Akademii Nauk SSSR, 209, 1185–1188 (in Russian).

Wirsching U. (1976). Experiments on hydrothermal alteration processes of rhyolitic glass in closed and “open” system. Neues Jahrbuch für Mineralogie, 203-213.

White C.L.I.M., Ruiz-Salvador A.R. and Lewis D.W. (2004). Pressure-induced hydration effects in the zeolite laumontite. Angewandte Chemie, 43, 469-472.

Wilson S.T, Lok B.M., Messina C.A., Cannan T.R., Flanigen E.M. (1982). Aluminophosphate molecular sieves: a new class of microporous crystalline inorganic solids. Journal of the American Chemical Society, 104, 1146-1147.

Wingenfelder U., Furrer G., Schulin R. (2006) Sorption of antimonate by HDTMA-modified zeolite. Microporous and Mesoporous Materials, 95, 265-271.

Wloch J. (2003). Effect of surface etching of ZSM-5 zeolite crystals on the rate of n-hexane sorption. Microporous and Mesoporous Materials, 62, 81-86.

Woszuk A. and Franus W. (2017). A Review of the Application of Zeolite Materials in Warm Mix Asphalt Technologies. Applied Sciences, 7, 293.

Yamazaki A., Shiraki T., Nishido H., Otsuka R. (1991). Phase change of laumontite under relative humidity-controlled conditions. Clay Science, 8, 79-86.

Yang W., Sun W., Zhao S., Yin X. (2016). Single-walled carbon nanotubes prepared in small $AlPO_4$-5 and CoAPO-5 molecular sieves by low-temperature hydrocracking. Microporous Mesoporous Materials, 219, 87-92.

Xu R., Pang W., Yu J., Huo Q., Chen J. (2007). Chemistry of Zeolites and Related Porous Materials: Synthesis and Structure. John Wiley & Sons (Asia) Pte Ltd.

Zanin E., Scapinello J., Oliveira M., Rambo C.L., Francescon F., Freitas L., de Mello J.M.M., Fior M.A., Oliveira J.V., Dal Magro J. (2017). Adsorption of heavy metals from wastewatergraphic industry using clinoptilolite zeolite as adsorbent. Process Safety and Environmental Protection, 105, 194-200.

Zhang L., Ahsbahs H. and Kutoglu A. (1998). Hydrostatic compression and crystal structure of pyrope to 33 GPa. Physics and Chemistry of Minerals, 25, 301-307.

Zion Research (2014). Zeolite (Natural and Synthetic) Market for Catalysts, Adsorbents, Detergent Builders and Other Applications - Global Industry Perspective, Comprehensive Analysis, and Forecast, 2014 -2020. Zion Research, Deerfield Beach, Florida.
http://www.marketresearchstore.com/news/global-zeolite-market-140 [4/4/2018]

Zubkova N.V. and Pushcharovsky D.Yu. (2008). New data on the crystal structures of natural zirconosilicates: Structure refinements and ion-exchange behavior. Zeitschrift für Kristallographie, 223, 98-108.